Solar and Solar Wind Studies Using Ground and Space Based Observations

A THESIS

submitted for the Award of Ph.D. degree of

MOHANLAL SUKHADIA UNIVERSITY

in the

Faculty of Science

by

Susanta Kumar Bisoi

Under the Supervision of

Prof. P. Janardhan

Physical Research Laboratory, Ahmedabad

Department of Physics

MOHANLAL SUKHADIA UNIVERSITY

UDAIPUR

Year of submission: 2013

DECLARATION

I, **Mr. Susanta Kumar Bisoi**, S/o Mr. Maheswar Bisoi, resident of RN-106, PRL student hostel campus, Thaltej, Ahmedabad 380059, hereby declare that the research work incorporated in the present thesis entitled, **"Solar and Solar Wind Studies Using Ground and Space Based Observations"** is my own work and is original. This work (in part or in full) has not been submitted to any University for the award of a Degree or a Diploma. I have properly acknowledged the material collected from secondary sources wherever required. I solely own the responsibility for the originality of the entire content.

Date:

Susanta Kumar Bisoi

(Author)

CERTIFICATE

I feel great pleasure in certifying that the thesis entitled, **"Solar and Solar Wind Studies Using Ground and Space Based Observations"** by Mr. Susanta Kumar Bisoi under my guidance. He has completed the following requirements as per Ph.D regulations of the University.

(a) Course work as per the university rules.

(b) Residential requirements of the university.

(c) Regularly submitted six monthly progress reports.

(d) Presented his work in the departmental committee.

(e) Published minimum of one research papers in a referred research journal.

I recommend the submission of thesis.

Date:

Dr. Janardhan Padmanabhan
Astronomy and Astrophysics Division,
Physical Research Laboratory,
Ahmedabad - 380 009.

Countersigned by

Head of the Department

Dedicated

to my mother

Contents

List of Tables

List of Figures

Acknowledgments

It gives me a great pleasure in presenting this thesis, the success of which is not only my efforts, but it is a collective contribution of so many people, in some or the other way, otherwise which the thesis might have been incomplete. At this juncture, I wholeheartedly thank and acknowledge all for helping me in the realization of this thesis. First of all, I express my sincere and deepest gratitude to Prof. P. Janardhan, under the guidance of whom, the work reported in this thesis has been carried out. Completely new to the subject of Solar Physics and have no experience in the field of research, he never made me feel like this, and always gave importance to my views and was always patient with me. From the very beginning, he encouraged and helped me immensely in learning and independently approaching research problems. I appreciate his interest to allow me for collaborative work with other research groups in India and abroad. These few words fell short to describe his contribution. It was a great experience to work with him and I consider myself most fortunate to have him as my supervisor.

I thank the free-use data policy of the National Solar Observatory (NSO) at Kitt Peak. NSO/Kitt Peak data, used in this thesis, were produced cooperatively by NSF/NSO, NASA/GSFC/, and NOAA/SEL. This thesis utilized SOLIS data obtained by the NSO Integrated Synoptic Program (NISP), managed by the National Solar Observatory, which is operated by the Association of Universities for Research in Astronomy (AURA), Inc. under a cooperative agreement with the National Science Foundation. IPS observations, used in this thesis, were carried out under the solar wind program of Solar Terrestrial Environment Laboratory (STEL), Japan. Wavelet software, used in this thesis, was provided by C. Torrence and G. Compo, and is available at URL: http://atoc.colorado.edu/research/wavelets/. I thank King, J.H. and Papatashvilli, N. of Adnet Systems, NASA, GSFC, the CDAWeb team, the ACE SWEPAM instrument team, the ACE Science Center and the EIT and

MDI/SOHO consortia for making data available in the public domain via the world wide web. SOHO is a project of international collaboration between ESA and NASA.

I thank Prof. J. N. Goswami, Director; Prof. Anjan Joshipura and Prof. A. K. Singhvi, former Deans; and Prof. Utpal Sarkar, Dean of PRL for providing necessary facilities and encouragements to carry out my research work. I also thank to Prof. Shyam Lal, former Academic Head, and to all former and present academic committee members for their key inputs that help in improving this thesis.

I specially thank to Prof. S. Ananthakrishnan of Pune University; Dr. P. Subramanian of IISER, Pune; Dr. Ishwar-Chandra of NCRA, Pune; Dr. Dibyendu Nandy of IISER, Kolkata; Dr. S. Gosain; and Prof. Rastogi for the fruitful discussion and the continuous encouragement, which I received from them. My special thanks are also due to Dr. Dibyendu Chakrabarty (Dipu) of PRL who was always ready for scientific discussion and cheered me up to carry out my work. Also, I thank him for his constructive suggestions that help in improving this thesis.

I thank A&A faculty members, Prof. B.G. Anandarao, Prof. T. Chandrasekhar, Prof. Hari Om Vats, Prof. N.M. Ashok, Dr. D.P.K. Banerjee, Dr. A. Singal, Dr. K.S. Baliyan, Dr. Abhijit Chakraborty, Dr. Santhosh Vadawale, and Dr. Shashikiran Ganesh who always shared their experience and knowledge to encourage me to pursue the thesis work during the last long five years period. Especially, one faculty member, Dr. Sachindra Naik, who cannot be left out still if I wish. My special thanks are due to him who always encouraged, criticized, and cheered me up. His lively nature made the work environment at Thaltej so full-of-live that I always enjoyed every shared moments with him, and surely I will miss these moments.

I thank all the staffs of PRL computer center for providing excellent computational and internet facilities. I also express my appreciation for all the library staff members for their kind cooperation and extended ever-willingly help. Especially, I thank Mrs. Pragya Pandey who always helped me in the library work.

I always enjoyed the visit to the GMRT, Pune for making solar observations. The wonderful company of all students at NCRA, staffs, and faculties has left pleasant memories.

I thank Murli bhai, Vadheer ji, Kayasthi ji, Nambiar ji, Mr. Vishal Shah, Mr. A.B. Shah, and Mr. Bhagirath for helping me in many official work at Thaltej. It would never been easy to complete this thesis unless I received help from Mr. Sandeep Doshi, and my special thanks are due to him. I thank all PRL administration staff for helping in many official works, and special thanks are due to Parul madam and Mr. Senthil Babu for their ever-willingly help.

Spending the last long five years at PRL would have never been easy without friends (especially my thaltej hostel friends). Although I couldn't name all, company of each made my life at Thaltej most enjoyable. I am specially thankful and grateful to my batch mates (Abhishek, Arun, Amerendra, Chinmay, Koushik, Siddartha, Sunil, Yogita, and Vema) for all those happiness they brought to me and also their unconditional support during bad periods of my life. Many thanks to Chinmay and Nigam with whom I spent many memorable moments that will always make me remember of my days at PRL. I am also thankful to Debashish, Dipti, Dillip, Deepak, Arko, Manu, Ranjith, Digu, Zulfi, Vimal, Arvind, and Pankaj for their wonderful company at Thaltej.

I enjoyed the company of Venkat, Ramakrishna, Lokesh, Vishal bhai, Priyanka, Anjali, Tanmoy, Gaurav, Varun, Vaibhav, Sunil, and Arun. They made my life in Thaltej more cheerful. I would also like to thank Blesson, Asish, and Tapas for the fruitful discussions and also suggestions for the submission of this thesis.

This thesis is incomplete if I do not acknowledge Google and ADSABS database. It had never been even one day, throughout my research period, when I didn't need Google. Google always tried to make my life easier and simple like a true friend.

My thanks are also due to my school friends (Sasmita, Kalia, Bidhu, Ranjit, and Titu), and my college friends (Balakrushna, Gaura Bhai, and Chandra) for their constant encouragement and support.

Finally, but not the least the devotion I got from my parents, my brother (Sukanta, Ranjan), my sisters (Puspa, Geeta, Papali), in-laws (Bhikari and Dasaratha), my family members, and Satyapriya is something beyond acknowledgment. They were always with me for whatever reason it may be and the encouragement that I received from them will never fade away. I am very much grateful to Satyapriya for providing the mental support and encouragement throughout the period, and for her proof-read of this thesis. Lastly, words of gratitude for my "mother", who always have been instrumental in my endeavor. Her innumerable sacrifices and unconditional support helped me to come all the way to carry out my research and completion of this thesis, and I, therefore, dedicate this thesis to my mother.

Susanta Kumar Bisoi

ABSTRACT

Stellar magnetic fields are crucial for the dynamical evolution of all stars, and in the Sun these magnetic fields contribute not only to the dynamics of the Sun, but also coupled with the changes in the solar wind and the frozen-in interplanetary magnetic field, eventually, drive space weather at 1 AU and in near-Earth space environment. Continuous solar observations, using both ground-based telescopes and advanced space-borne platforms, have channeled solar magnetic field research in a new direction to uncover how the solar magnetic activity evolves, and modulates heliospheric activity out to 1 AU and beyond.

In general, solar magnetic activity shows an 11-year periodicity, called as the solar cycle. However, we have witnessed, at the end of Solar Cycle 23, an unusually extended solar minimum, which has been the deepest minima experienced in the past 100 years, with $\sim 75\%$ and $\sim 80\%$ days in 2008 and 2009 respectively, showing a complete absence of sunspots. Utilizing such unique opportunity of quiet-sun conditions, not expected in the foreseeable future, we carried out, in this thesis, detailed investigations of solar magnetic fields, using ground-based and space-borne observations, to study and understand the solar cycle related magnetic activity changes both on the Sun and in the solar wind, and specifically addressed the long-term magnetic field changes that led to this extended solar minimum at the end of Solar Cycle 23. We also studied a specific type of geo-magnetic event to discuss space weather effects of the Sun and solar wind on the Earth's magnetic field variations.

A brief overview of solar magnetic fields, solar wind, and their space weather effects on the Earth, with respect to the current scenario in the field of solar and space physics, has been described in Chapter 1 while Chapter 2 gives details of ground-based and space-borne instruments and measurements used in this thesis.

In Chapter 3, using synoptic magnetograms from the ground-based NSO/KP

and space-based SoHO/MDI database, we examined solar photospheric magnetic fields for the last three Solar Cycles, *viz.*, Cycles 21, 22, and 23. Specifically, we examined polar magnetic fields at high latitudes (78°–90°) in both the solar hemispheres which showed a significant and steady decline in the unsigned polar fields from the late declining phase of Cycle 22 to the maximum of Cycle 23. We found a good correlation, in Cycle 23, between the long-term changes in these unsigned polar fields and changes in meridional flow speeds reported by (Hathaway & Rightmire, *Science*, 327, 1250, 2010). In addition, our observations of continuously weaker polar fields, in Cycle 23, led us to believe that these weaker fields were the cause of the extremely prolonged minimum, experienced at the end of Cycle 23 and would lead to a weaker Cycle 24.

Apart from the 11-year periodicity, the Sun also shows quasi-periodicities at longer and shorter scales than 11 years in various solar activity indicators. The periodic and quasi-periodic variations detected in solar activity features provide direct insights into the underlying dynamic processes that govern the nature and evolution of solar magnetic fields. We had, therefore, in Chapter 4 of this thesis, undertaken an investigation such quasi-periodic variations in solar photospheric fields in the build-up to one of the deepest solar minima experienced in recent times. Further, we found a hemispheric asymmetry in quasi-periodicities of the photospheric fields, confined to the latitude range 45° to 60°. This observed asymmetry, when coupled with the fact that both solar fields above ±45° and microturbulence levels in the inner-heliosphere have been decreasing steadily since the early to mid-1990s (Janardhan *et al., Geophys.Res.Lett.*, 382, 20108) suggested that active changes occurred in the solar dynamo around this time. These changes, in turn, probably initiated the build-up to the deep solar minimum around mid-1990s.

Any long term changes in solar photospheric magnetic fields (polar fields) during solar cycles must leave its signatures in the solar wind. These signatures can be effectively detected through interplanetary scintillation (IPS) measurements as enhanced or reduced scintillation levels (rms electron density fluctuations) compared to the long term mean value. We used, in Chapter 5 of this thesis, IPS observations at 327 MHz, obtained between 1983 and 2009, to investigate the long-term temporal variations in the scintillation levels (or solar wind microturbulence levels). We found a steady and significant decline in the microturbulence levels in the entire inner heliosphere, which was started since $\sim$1995. This large-scale heliospheric IPS signature, coupled with the similar steady decline of solar polar magnetic fields since $\sim$1995, provide a consistent result that showed the buildup to the deepest solar minima, experienced in the past 100 years, actually began in a decade earlier – that is, in the early- to mid-1990s.

Although most space weather disturbances at 1 AU are caused by explosive solar events like CMEs and solar flares, there are occasions when interplanetary double shocks, convected towards the Earth by the solar wind, cause sudden impulses (SI) in the Earth's magnetic fields. We studied, in Chapter 6, such a SI pair, first identified at the Indian magnetic observatories, on 23 – 24 April 1998. We discussed the close correlations between the SI pair and the corresponding variations in solar wind density, while the solar wind velocity and the southward component of the interplanetary magnetic field (IMF-Bz) did not show any correspondence. Further, we also showed that it is possible for a rear-side solar flare to propagate a shock towards the earth. Finally, in Chapter 7, we summarized our results and discussed the future scope of the investigations carried out in this thesis.

Keywords: Solar magnetic fields, Polar fields, Meridional flows, Solar Cycle, Deep solar minimum, Solar Periodicity, Solar wind microturbulence, Interplanetary scintillation, Sudden impulse pairs, Prompt penetration, and Overshielding.

LIST OF PUBLICATIONS

A. Referred Journals

1. **"Unique observations of a geomagnetic $\mathbf{SI^+ - SI^-}$ pair: Solar sources and associated solar wind fluctuations"**
   Rastogi, R.G., Janardhan, P., Ahmed, K., Das, A.C., and **Bisoi, S.K.**
   2010, *J. Geophys. Res.*, **115**, A12110, doi: 10.1029/2010JA015708.

2. **"Solar Polar Fields During Cycles 21 − 23: Correlation with Meridional Flows"**
   Janardhan, P., **Bisoi, S.K.**, and Gosain, S.
   2010, *Sol. Phys.*, **267**, 267–277, doi: 10.1007/s11207-010-9653-x.

3. **"The prelude to the deep minimum between solar Cycles 23 and 24: Interplanetary Scintillation signatures in the inner heliosphere"**
   Janardhan, P., **Susanta Kumar Bisoi**, Ananthakrishnan, S., Tokumaru, M. and Fujiki, K.
   2011. *Geophys. Res. Lett.*, **38**, L20108, doi: 10.1029/2011GL049227.

4. **"Deep GMRT 150 MHz Observations of the DEEP2 fields: Searching for High Red-shift Radio Galaxies Revisited [1]"**
   Susanta Kumar Bisoi, C.H. Ishwara-Chandra, S.K. Sirothia , and Janardhan, P.
   2011. *J. Astrophys. Astr.*, **32**, 613–614, doi: 10.1007/s12036-011-9116-2.

5. **"Changes in quasi-periodic variations of solar photospheric fields: precursor to the deep solar minimum in the cycle 23?"**
   Susanta Kumar Bisoi, Janardhan, P., D. Chakrabarty, Ananthakrishnan, S., and Divekar, A.
   2013. *Sol. Phys.*, doi: 10.1007/s11207-013-0335-3.

[1] The work carried out in this article is not part of this thesis.

B. Conference Proceedings

1. **"Observations of a geomagnetic $\mathbf{SI^+ - SI^-}$ pair and associated solar wind fluctuations"**
   Susanta Kumar Bisoi and Janardhan, P.
   2012, Solar and Astrophysical Dynamos and Magnetic Activity, *Proceedings of the IAU, IAU Symposium*, **294**, 543 – 544, doi: 10.1017/S1743921313003141.

2. **"Peculiar behavior of solar polar fields during solar cycles 21-23: Correlation with meridional flow speed"**
   Susanta Kumar Bisoi and Janardhan, P.
   2012, Solar and Astrophysical Dynamos and Magnetic Activity, *Proceedings of the IAU, IAU Symposium*, **294**, 81 – 82, doi: 10.1017/S1743921313002287.

3. **"Interplanetary scintillation signatures in the inner heliosphere of the deepest solar minimum in the past 100 years"**
   Susanta Kumar Bisoi and Janardhan, P.
   2012, Solar and Astrophysical Dynamos and Magnetic Activity, *Proceedings of the IAU, IAU Symposium*, **294**, 83 – 84, doi: 10.1017/S1743921313002299.

4. **"Asymmetry in the periodicities of solar photospheric fields: A probe to the unusual solar minimum prior to cycle 24 [2]"**
   Susanta Kumar Bisoi and Janardhan, P.
   2012, Solar and Astrophysical Dynamos and Magnetic Activity, *Proceedings of the IAU, IAU Symposium*, **294**, 85 – 86, doi: 10.1017/S1743921313002305.

[2]Won the Best Poster Competition in the International Astronomical Union (IAU) symposium, Aug 20–31, 2012, Beijing, China.

C. Presentations at Conferences and Symposia

1. **"Deep GMRT 150 MHz observations of the DEEP2 fields: Searching for high red-shift radio galaxies revisited"**
   Contributed Talk at 29th ASI Scientific meeting, Feb 23-25, 2011, Pt. Ravishankar Shukla University, Raipur, India.

2. **"Solar Polar Fields during Cycles $21-23$: Correlation with Meridional Flows"**
   Contributed Talk at 1st Asia-Pacific Solar Physics Meeting, Mar 24-26, 2011, IIA, Bangalore, India.

3. **"Composite synthesis imaging of the quiet-sun using simultaneous observations from the GMRT and the NRH"**
   Contributed Talk at Solar Radio Workshop, Nov 23-25, 2011, NCRA, Pune, India.

4. **"North-south asymmetry in periodicities of solar photospheric fields: signatures to the deep solar minimum prior to the solar cycle 24"**
   Contributed Talk at 39th COSPAR meeting, July 14-22, 2012, Infosys Campus, Mysore, India.

5. **"The buildup to the deep solar minimum of cycle 23: Quasi-periodic changes of the solar photospheric fields"**
   Contributed Talk at 30th ASI Scientific meeting, Feb 20-22, 2013, IISER-IIST, Trivandrum, India.

6. **"Deep GMRT 150 MHz observations of the DEEP2 fields: Searching for high red-shift radio galaxies revisited"**
   Poster presentation at Diffuse Relativistic Plasma Workshop, Mar 1-4, 2011, RRI, Bangalore, India.

7. **"The prelude the deep minimum between solar cycles 23 and 24: Earlier IPS signatures in the inner heliosphere"**
   Poster presentation at National Space Science Symposium (NSSS), Feb 14-17, 2012, Tirupati, India.

8. **"Observations of a geomagnetic $\mathbf{SI^{+} - SI^{-}}$ pair and associated solar wind fluctuations"**
   Poster presentation at IAU, Aug 20-31, 2012, Beijing, China.

9. **"Peculiar behavior solar polar fields during solar cycles 21-23: Correlation with meridional flow"**
   Poster presentation at IAU, Aug 20-31, 2012, Beijing, China.

10. **"Inner heliospheric interplanetary scintillation signatures of the deepest solar minimum in the past 100 years"**
    Poster presentation at IAU, Aug 20-31, 2012, Beijing, China.

11. **"Asymmetry in periodicities of solar photospheric fields: A probe to the unusual solar minimum prior to the solar cycle 24"**
    Poster presentation at IAU, Aug 20-31, 2012, Beijing, China.

Chapter 1

Introduction

To begin with it would be appropriate to place the work carried out in this thesis in the proper perspective with respect to current scenario in the field of research in solar and space physics. Research in solar and space physics is important not only for its intrinsic academic interest, but also because such studies have a profound and far-reaching influence on our understanding of the Earth's near-space environment, a study that is commonly referred to as "space weather". With society's increased dependence on space-based technology that occupies the Earth's near-space environment, and much of which is at risk due to a lack of a detailed understanding of how solar activity influences and controls space weather, it is imperative that research is focused towards addressing such issues. In addition, there has been strong speculation among the scientific community regarding the possible link between the reported anthropogenic influence of the unusual decline in solar activity and the terrestrial climate change that has already been known from the simultaneous occurrence of the solar Maunder minimum, a period of long declined solar activity, and the Little Ice Age on the Earth. It is therefore becoming increasingly important, in the long term, to distinguish and delineate the degree to which the solar cycle can affect terrestrial climate and such studies will go a long way in eventually understanding and addressing these aspects.

The Sun is our nearest star and the main source of energy. It provides all the necessary heat and light to maintain the temperature of the Earth for sustenance of life. It has, therefore, been of general interest to understand the Sun ever since the first observations were made by Gallelio Galilei who invented the telescope in the early 17th century, and made the very first observations of dark spots on the visible solar disk, called sunspots. The variation in the number count of sunspots over time revealed the existence of solar activity that continuously waxes and wanes with a periodicity of approximately 11 years, called the sunspot cycle. This solar activity is driven by an intense, variable magnetic field, which coupled with solar differential rotation, manifests itself as different structures from the photosphere to the outer solar atmosphere, namely the corona. These structures range from relatively stable structures, like sunspots, coronal loops, and solar prominences, to explosive solar outbursts, like solar flares and coronal mass ejections (CMEs). Detailed studies of solar magnetic fields are, therefore, always a topic of interest for solar physicists.

In the last few decades, vast amounts of solar magnetic field data have been accumulated using a network of worldwide ground-based and space-borne instruments, covering regions starting from the solar interior to the corona and beyond. In particular, daily full-disk photospheric line-of-sight (LOS) magnetic field data are easily available from ground-based observatories as well as from space-borne instruments dedicated to solar observations. A detailed description of these LOS photospheric magnetic field data have been given in Chapter 2 of this thesis.

The 11 years solar cycle that the Sun manifests is attributed to a solar dynamo that is believed to reside at the base of the convection zone in a region referred to as, the tachocline. Apart from the 11 year periodicity in sunspot numbers, the Sun also shows other periodic and quasi-periodic variations that give direct insights into the underlying dynamical processes governing the nature and evolution of magnetic fields. So one part of this thesis has used the ground-based and space-borne synoptic magnetograms, compiled from daily full-disk photospheric LOS magnetic fields, to study the solar cycle related magnetic field variations over time. This has been described in Chapter 3 and 4 of this thesis.

Photospheric magnetic fields are carried into interplanetary space by the ever expanding coronal plasma flow, namely the solar wind, to form the interplanetary magnetic field (IMF). It is, therefore, obvious that the long-term changes in the photospheric magnetic field activity would contribute to the corresponding variations in the IMF, and therefore must leave their signatures in the solar wind. Such changes could be detected through studies of solar wind microturbulence levels which are related to both rms electron density fluctuations and large-scale magnetic field fluctuations. The changes in rms electron density fluctuations can be effectively detected through a ground-based technique, called interplanetary scintillation (IPS). IPS is a scattering phenomenon in which coherent electromagnetic radiation, from distant radio sources, on passage through the turbulent and refracting solar wind, develops random temporal variations of the signal intensity (scintillation) as observed by large ground-based radio telescopes. In addition, IPS can also study a very large region of the inner heliosphere, ranging from 0.2 AU to 0.8 AU at an observing wavelength of ≈ 1 m. Such IPS measurements are used in Chapter 5 to study the solar cycle changes of the solar wind microturbulence levels in the inner heliosphere.

Although most space weather disturbances at 1 AU are caused by explosive solar events like CMEs, solar flares, and solar energetic particle events (SEPs), sometimes interplanetary shocks, convected towards the Earth by the solar wind, cause sudden impulses in the Earth's magnetic fields. A study of such a pair of sudden impulses, showing a close correspondence between the solar wind parameters and the geomagnetic field variations, is described in Chapter 6.

In the present Chapter, a brief overview of observational and theoretical aspects of solar magnetic fields, solar periodicities, the solar wind, the IPS technique as a probe to solar wind, and interactions of solar wind disturbances with the Earth's magnetosphere and ionosphere are described.

1.1 The Solar Cycle

1.1.1 Sunspot Activity

Sunspots have been systematically observed since the invention of telescopes by Galileo in the early 17th century. However, it was first noticed by Sammuel Schwabe in the early 1840s that the sunspot number count varies with an average periodicity of 11 years (Schwabe, 1843). This periodic variation of the sunspot number with time is known as the sunspot cycle. In any given sunspot cycle, the number of sunspots first rises from a minimum value (at sunspot minimum) to a maximum value (at sunspot maximum), and then falls back to a minimum value (at sunspot minimum). Shortly after the discovery of sunspot cyclic variation, Carrington (1858) reported the gradual drift of sunspots towards the equator. Systematic and daily sunspot observations were then begun at the Zurich observatory by J.R. Wolf (Wolf, 1861) who devised an easier method for finding the number of sunspots through a count of sunspot groups (instead of counting individual sunspots) and using a relative sunspot number, R, defined as

$$R = k(10g + f) \tag{1.1}$$

where k is a scaling factor for the observer, g is the number of sunspot groups observed, and f is the total number of sunspots within the sunspot group. Figure 1.1 shows the yearly averaged sunspot number variations during the period of 1610 − 2010. The sunspot cycle is clearly seen in Figure 1.1. The number of sunspots during the period of 1645 − 1715 is seen to be very low, and is well known as Maunder minimum.

In addition to the sunspot numbers, sunspot areas have also been used as a measure of solar activity. A very good correlation exists between sunspot

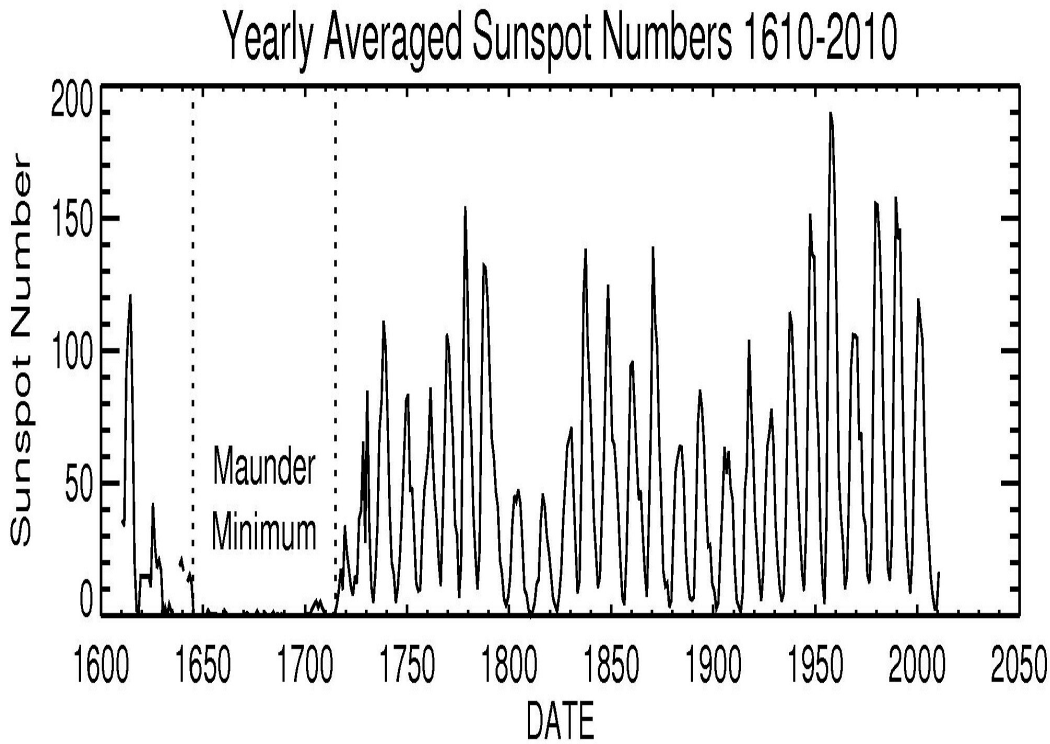

Figure 1.1: Shows the yearly averaged sunspot number variations during the period of 1610 − 2010. The period 1645 − 1715, demarcated by the vertical dotted lines, is known as Maunder minimum. Credit: (http://solarscience.msfc.nasa.gov/images/ssn_yearly.jpg).

numbers and sunspot areas. Additional positional information – latitude and longitude are inferred from sunspot areas. Figure 1.2 shows the distribution of sunspot areas with latitude and time. It is apparent from the upper panel of Figure 1.2 that at the start of each sunspot cycle, sunspots erupt at latitudes zone of 35° on either side of the equator. As the cycle advances, the latitude at which sunspot erupt drifts towards the equator, and eventually sunspots of the new cycle begin appearing at high latitudes while old sunspots of the previous cycle are still erupting at low latitudes. So two consecutive cycles generally overlap, and this behavior is known as Spörer's law (Maunder, 1903). It may be noted, however, that sunspots do not erupt or appear in the narrow latitude zone of ±10°. A plot of the latitudinal migration of sunspots resembles the wings of a butterfly (Figure 1.2), and is hence known as "butterfly diagram" (Maunder, 1904).

1.1.2 Magnetic Field Activity

In 1908, G.E. Hale discovered the sunspots as regions of intense, concentrated magnetic fields using the well known Zeeman effect (Hale, 1908). It is now known that sunspots have a magnetic field strength of ~ 3000 Gauss (G). In comparison to this, the terrestrial magnetic field strength is nearly 10,000 times weaker. Sunspots, generally, erupt as bipolar pairs and the magnetic regions in the solar atmosphere surrounding these bipolar sunspots are commonly referred to as "bipolar magnetic regions (BMRs)". BMRs are also referred to as "active regions", and are large bipoles with an absolute magnetic flux between $\sim 10^{20}$ Mx and 3×10^{22} Mx. Since sunspots are regions of intense magnetic activity, magnetic field activity, like sunspot activity, also shows a 11-year solar cycle variation.

The bipolar sunspot groups (or BMRs) often appear in pairs. The leading (in the direction of solar rotation) and following spots of the sunspot groups are, with few exceptions, of opposite polarity, and the corresponding spots of

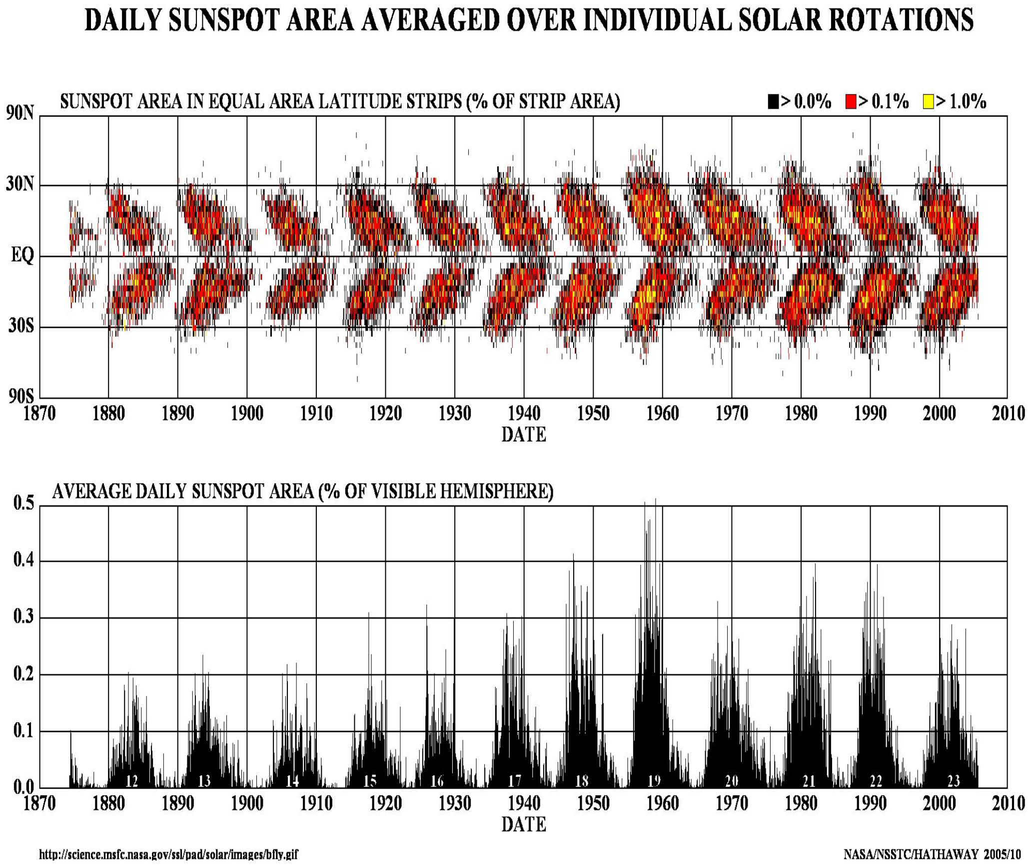

Figure 1.2: (Upper panel:) Shows the distribution of sunspot areas with latitudes. The changes in the sunspot area resemble the wings of a butterfly and therefore known as “butterfly diagram”, and (Lower panel:) Shows the distribution of daily sunspot areas with time for the Sunspot Cycles 12 − 23. The 11-year periodicity of sunspot cycle can be clearly noticed in temporal variation of daily sunspot areas. Credit: (http://solarscience.msfc.nasa.gov/images/bfly.gif).

the Northern and Southern hemisphere are also of opposite polarity, – that is, if the leading and following spots are respectively, of positive and negative polarity in the North, then the corresponding spots in the South are respectively, of negative and positive polarity. Furthermore, the polarity of spots in the next solar cycle is opposite to the polarity of spots in the previous cycle. This phenomenon is known as Hale's Polarity Law (Hale, Nicholson and Joy, 1919). Since sunspots resume their initial polarities after a gap of two sunspot cycles, a 22-year magnetic cycle also exists in addition to the 11-year solar cycle. The leading spot, usually, appears at lower latitudes than the following spot, so a line segment joining these two spots makes a tilt angle with the east-west direction. Observations of regular sunspot pairs have shown that the tilt angle often decreases with decrease in latitude. This phenomenon is known as Joy's Law (Hale, Nicholson and Joy, 1919).

Magnetographs, both ground- and space-based, are now commonly used to measure the Sun's magnetic field and presented in the form of full-disk solar magnetograms. Figure 1.3 shows such a magnetogram from the Magnetic Doppler Imager (MDI; Scherrer *et al.* (1995)) instrument on board the Solar and Heliospheric Observatory (SoHO; Domingo, Fleck and Poland (1995)). Systematic magnetograph observations have been carried out since the early 1950s, when the First magnetograph was installed by Babcock and Babcock (1955). Magnetograms, generally, measure the longitudinal component of magnetic field along the LOS. However, these days, vector magnetograms are also commonly used to measure the transverse component of photospheric magnetic field across the LOS. More details about such magnetograms are described in Chapter 2. Using magnetographic observations, Babcock and Babcock (1955) categorized the Sun's magnetic fields into – (1) A General Magnetic Field, mostly confined to latitudes beyond $\pm 55°$, of one polarity; (2) Bipolar Magnetic Regions (BMRs), generally found towards lower latitudes, having mixed polarity and obeying Hale's polarity law; and (3) occasionally extended Unipolar Magnetic Regions (UMRs), having low flux intensity that exist for months,

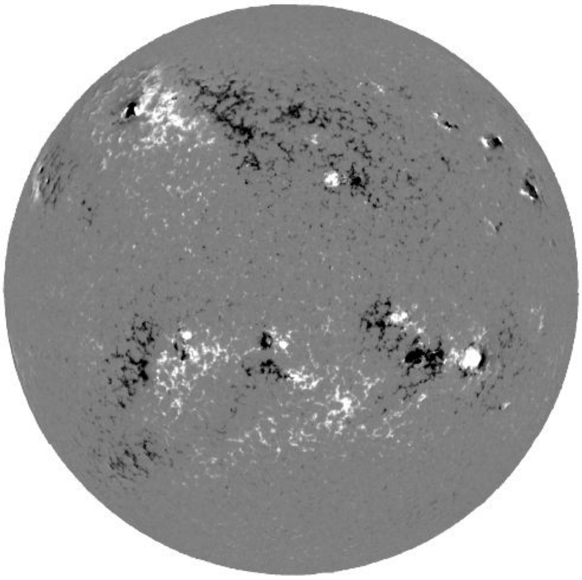

Figure 1.3: A MDI magnetogram showing the surface distribution and polarity of the solar magnetic fields during the active period of a solar cycle. The white and black patches indicate regions of strong magnetic fields while the grey patches indicate regions of no magnetic field. Further, these white and black patches respectively, represent the positive (directed outward from the Sun) and negative polarity (directed towards the Sun), of bipolar magnetic regions. It is clearly seen that the corresponding polarity of bipolar magnetic regions in the Northern and Southern hemispheres are opposite in nature with the leading and following polarities being of different signs in the two hemispheres. Credit: (http://solar-center.stanford.edu/solar-images/magnetograms.html).

and are thought to be remnants of BMRs. Using observations from 1953 to 1957, Babcock (1959) proposed that the General Magnetic Fields, reported by Babcock and Babcock (1955), reverse their polarity around the maximum of each solar cycle. These weak ($\sim$ 10 G) and diffuse general magnetic fields, which reverse the polarity at the solar maximum, are referred to as polar fields.

Figure 1.4 shows a magnetic butterfly diagram for the Solar Cycles 21, 22, and 23. This diagram is generated from magnetograms obtained from the National Solar Observatory at Kitt-Peak (NSO/Kitt Peak) since mid-1970s. The diagram represents the actual latitudinal distribution of magnetic fields in time. The red and green color respectively represent the positive and negative polarity flux. All the solar activity, *viz.* Solar cycle, Hale's polarity law, Joy's law, and Polar field reversal are clearly illustrated in this single figure.

1.1.3 Large-scale Solar Flows

Motions of small magnetic features on the solar surface are carried forward by different kind of solar flows, *viz.* granulation, supergranulation, differential rotation, and meridional flows. Granule and supergranule photospheric motions are usually caused by the convective flows of solar plasma. Granular motions are horizontal velocity flows with length scales ranging from $\sim$ 0.5 Mm to 2 Mm, and the associated velocity ranges from 500 m s^{-1} to 1500 m s^{-1} (Rieutord and Rincon, 2010). On the other hand, supergranular motions have typical length scales of $\sim$ 30 Mm, and velocities of $\sim$ 360 m s^{-1} (Rieutord and Rincon, 2010). Both of these flows primarily contribute to the Sun's chromospheric/magnetic network, and are key to the transport of the photospheric magnetic flux (Hathaway, 2012). However, on large spatial scales, magnetic flux transport occurs through the advective processes of differential rotation (Snodgrass, 1983) and meridional flows (Duvall, 1979).

The angular rotation of the Sun varies from the equator to the poles, being faster at the equator and becoming progressively slower as one moves pole-

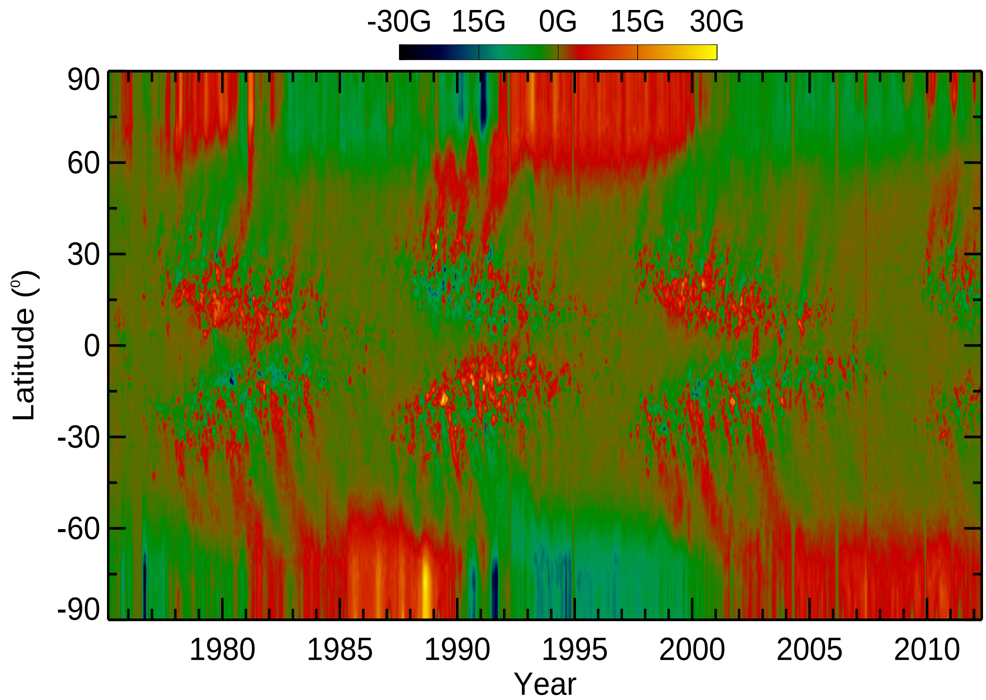

Figure 1.4: Shows a magnetic butterfly diagram for Solar Cycles 21, 22, and 23, covering the period from 1975 − 2012. The positive and negative polarities are shown in red and green respectively. The field strength is indicated by a color bar at the top of the figure.

wards. While solar equatorial rotation takes about 25 days, solar polar rotation takes about 29 days and this was first noticed by observations of the relative motions of sunspots (Newton and Nunn, 1951). The general expression for the differential rotation is expressed as

$$\Omega = \Omega_0 - \Delta\Omega sin^2\Psi \tag{1.2}$$

where Ψ denotes heliographic latitude, Ω_0 is the rotation rate at the equator, and $\Delta\Omega$ is the difference in rotation rate between the pole and the equator. In addition, Howard and Labonte (1980), using 12 years Mount Wilson velocity data, reported alternating latitude zones of faster and slower rotation, referred as zonal flows or torsional oscillations. Further, with the development of helioseismological techniques for probing the solar interior, it was found that these zonal bands extend much below the photosphere to the tachocline, a thin layer present at about 0.7 $R_\odot$ (Kosovichev *et al.*, 1997; Kosovichev and Schou, 1997) from the centre of the Sun. Using helioseismic data from both the space-borne MDI instrument and the Global Oscillations Network Group (GONG), Howe *et al.* (2000a) has shown that these zonal bands extend deep down to at least 60,000 km below the photosphere. However, the velocity of these zonal flows, about 5 ms^{-1}, is comparatively less than the Sun's equatorial rotation speed of $\sim$ 2000 ms^{-1}.

Meridional flows are axisymmetric flows which transport flux from the equator to the North and South poles along the meridional plane of the Sun. Meridional flows are, generally, weaker compared to other solar flows, and therefore difficult to measure. However, a few successful attempts have been made to measure meridional flows, and poleward meridional flows were first reported by Duvall (1979) using the Doppler velocity measurements of photospheric spectral lines from the Stanford Solar Observatory. Other researchers followed up on these early meridional flow measurements using Doppler velocity observations (Hathaway, 1996), magnetic feature tracking (Komm, Howard and Harvey, 1993a; Hathaway and Rightmire, 2010), and helioseismic techniques (Haber *et al.*, 2002) and confirmed a poleward meridional flows of $\sim$10 – 20 m s^{-1}. It has also been found that poleward meridional flows exist down to a depth of at least 0.04 $R_\odot$ with a peak flow ranging from $\sim$10 – 20 m s^{-1} (Giles *et al.*, 1997). Mass conservation would require the existence of an equatorward counter meridional flow somewhere near the base of the convection zone. However, such internal flows are very difficult to measure and quantify. More recently, using data from the Helioseismic Magnetic Imager (HMI; Schou *et al.* (2012)) on board the Solar Dynamic Observatory (SDO; Pesnell, Thompson and Chamberlin (2012)), an equatorward counter meridional flow of 10 m s^{-1} has been reported at about 0.82 to 0.91 $R_\odot$ from the centre of the Sun (Zhao *et al.*, 2013).

1.1.4 The Solar Dynamo

From the observational evidence of the solar magnetic fields, discussed in the earlier sections, it is tempting to conclude that a hydromagnetic dynamo action takes place in the convection zone, and operates and controls the origin and evolution of solar magnetic fields which eventually give rise to the solar magnetic cycle via a dynamo process. However, there is no direct observational evidence, till date, of the location or the underlying physical mechanism of such a dynamo. A large number of dynamo models, based on the theoretical ideas and numerical simulations, have been proposed to improve our understanding of the origin and dynamics of the solar cycle. In this section, we have attempted to describe the working of solar dynamo models as proposed by different researchers. However, a more detailed review of dynamo models with detailed mathematical formulation can be referred to in reviews by Ossendrijver (2003) and Charbonneau (2010).

1.1.4.1 The Induction Equation

It is known that matters in the solar interior exists in the state of a plasma, where electron and ions move freely to produce electric currents which subsequently gives rise to magnetic fields. The dynamics of these magnetic fields in the solar plasma is governed by the magnetohydrodynamic (MHD) induction equation

$$\frac{\partial \mathbf{B}}{\partial t} = \nabla \times (\mathbf{v} \times \mathbf{B} - \lambda \nabla \times \mathbf{B}), \tag{1.3}$$

where $\mathbf{B}$ is the magnetic field, $\mathbf{v}$ is the (plasma) velocity field and λ is the magnetic diffusivity of the system. If magnetic diffusivity is constant in space, this induction equation reduces to

$$\frac{\partial \mathbf{B}}{\partial t} = \nabla \times (\mathbf{v} \times \mathbf{B}) + \lambda \nabla^{\mathbf{2}} \mathbf{B} \tag{1.4}$$

The ratio of the first to the second term on the R.H.S. of the above equation is commonly referred to as magnetic Reynolds number (R_m). For astrophysical plasma systems, conductivity σ is very high – that is, in case of sunspots, it lies in the range $\approx 1 - 100\,\mathrm{A/Vm}$. Thus, in sunspots, R_m is reported to be $10^2 - 10^4$ – that is, $R_m >> 1$, and therefore, the term $\nabla^2 \mathbf{B}$ becomes negligible and the induction equation reduces to

$$\frac{\partial \mathbf{B}}{\partial t} = \nabla \times (\mathbf{v} \times \mathbf{B}) \tag{1.5}$$

This equation implies that magnetic fields remain frozen in the plasma flows, and this was first pointed out by Alfvén (1943) in a famous theorem known as "Alfvén's theorem of flux freezing".

1.1.4.2 Magnetic Buoyancy

The magnetic field lines inside the convection zone interact with the plasma and form "magnetic flux tubes". Strong solar differential rotation causes these flux tubes to be rotated and aligned in the toroidal direction. The pressure balance across the bounding surface of these flux tubes requires:

$$p_{out} = p_{in} + \frac{B^2}{8\pi} \tag{1.6}$$

where p_{out} and p_{in} are respectively, the pressure outside and inside of the flux tube, and B is the magnetic field strength of the flux tube. Under thermal equilibrium, $\rho_{in} < \rho_{out}$ since $p_{out} > p_{in}$, where ρ_{out} and ρ_{in} are respectively, the density outside and inside of the flux tube. Therefore, the flux tube is less dense than the ambient surrounding plasma, and rises to the surface due to buoyancy pressure. This is known as magnetic buoyancy.

1.1.4.3 Understanding of the Solar Cycle

The current understanding of the solar cycle is ascribed to a cyclic generation of the two components of the Sun's magnetic field, *viz.* the poloidal field or field in the meridional plane and the toroidal field or field twisted around the axis of rotation and perpendicular to the meridional plane. Using a hydrodynamic model, Parker (1955a) first proposed the generation of a toroidal field from a pre-existing poloidal field followed by the re-generation of a poloidal field, – that is, a sort of back and forth generation of poloidal field and toroidal field. It is known, as described earlier, that magnetic field in the solar convection zone is frozen into the solar plasma. Differential rotation in the convective plasma layers thus stretches out the poloidal field component (north – south direction or r – θ plane) to produce the toroidal field component (east – west direction or ϕ direction). Figure 1.5a shows a poloidal field component subjected to the differential rotation along the east – west direction to produce a toroidal field component, which is oppositely directed in the two hemispheres, that is shown in Figure 1.5b. This process of generation of the toroidal field from the poloidal field is commonly referred to as the "Ω-effect", where the Ω(r, θ) denotes the angular velocity of rotation, r is the solar radius and θ is the co-latitude.

While the generation of the toroidal field from the poloidal field is straightforward, the generation of the poloidal field, however, involves a complex mechanism. The first mechanism was proposed by Parker (1955a) in which the twisting of the mean toroidal field component by helical turbulent convection produces a poloidal field component in the $r-\theta$ plane. Figure 1.6 shows the stages for generation of the poloidal field from the toroidal field. A toroidal field, oppositely directed in the two hemispheres, is shown in Figure 1.6. Helical turbulent motions, caused by convective plasma, twist this toroidal field line and produce new magnetic loops which have the same sense of direction in both the hemispheres (Figure 1.6b). A large number of such loops, shown in Figure 1.6c, get smoothed out by turbulent diffusion to produce a large-scale poloidal field. The direction of the new poloidal field line is in the opposite direction to the former poloidal field line and it's generation thus completes one solar magnetic cycle. Parkers's original dynamo model was later modified by Steenbeck and Krause (1969) who worked out a detailed mathematical formalism to describe the evolution of mean (large-scale) magnetic fields as described below.

The velocity and magnetic fields in a turbulent system can be expressed as:

$$v = \bar{v} + v' \; B = \bar{B} + B', \tag{1.7}$$

where the bar indicates the mean (large-scale)s and the prime indicates the fluctuating (small-scale) part.

Substituting these terms in the induction equation 1.4, and separating the mean and fluctuating parts, the induction equation 1.4 reduces to a mean induction equation,

$$\frac{\partial \bar{\mathbf{B}}}{\partial t} = \nabla \times (\bar{\mathbf{v}} \times \bar{\mathbf{B}}) + \nabla \times \epsilon + \lambda \nabla^{\mathbf{2}} \bar{\mathbf{B}}, \tag{1.8}$$

where $\epsilon = \langle \mathbf{v}' \times \mathbf{B}' \rangle$ is the mean electromotive force (e.m.f), with $\langle \; \rangle$ denoting a spatial average over intermediate scales. Considering a first oder approximation for this emf, one obtains

$$\epsilon = \alpha \bar{B} + \beta \nabla \times \bar{B}, \tag{1.9}$$

where α represents the average helical motions of plasma, and β is the turbulent diffusivity.

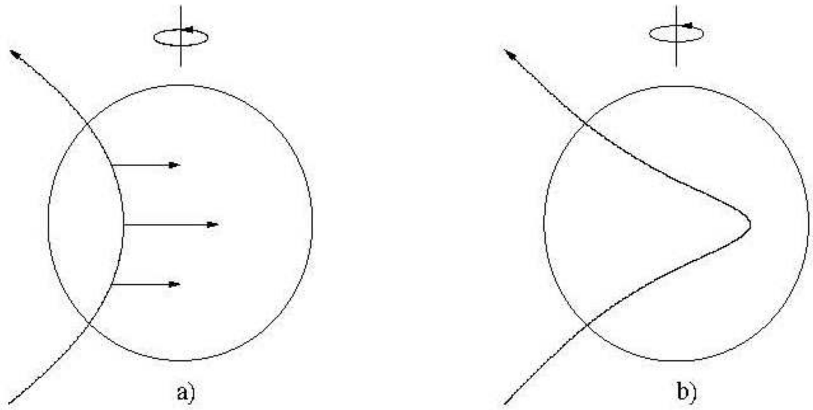

Figure 1.5: a) Differential rotation stretches out a poloidal field component in the direction of rotation b) Generation of a toroidal field component which is oppositely directed in the Northern and Southern hemispheres. Adapted from Choudhuri (2003).

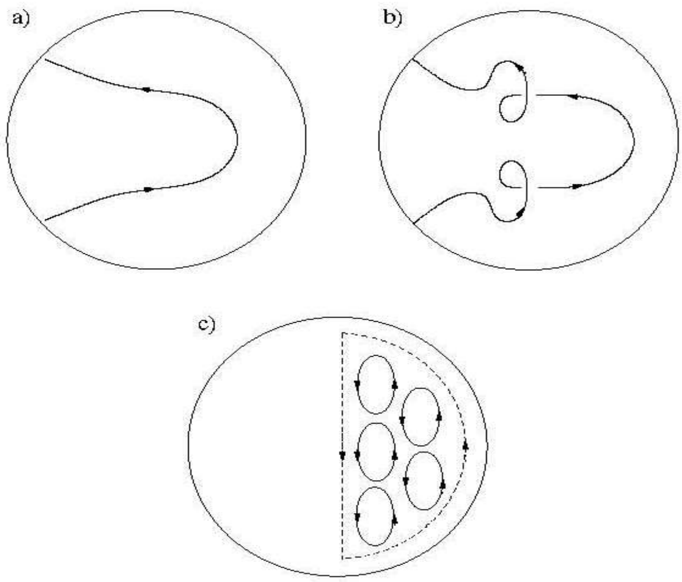

Figure 1.6: a) A toroidal field line b) Twisting of the toroidal field line by helical turbulence to produce magnetic loops of the same sense in both hemispheres c) A large number of such magnetic loops smoothen out, by turbulent diffusion, to produce the large-scale poloidal field. Adapted from Choudhuri (2003).

Substituting equation 1.9 in equation 1.8, one obtains

$$\frac{\partial \bar{\mathbf{B}}}{\partial t} = \nabla \times (\bar{\mathbf{v}} \times \bar{\mathbf{B}}) + \nabla \times \alpha \mathbf{B} + \eta\, \nabla^2 \bar{\mathbf{B}}, \tag{1.10}$$

where $\eta = \lambda + \beta$ is the net magnetic diffusivity. This equation is known as mean field dynamo equation and explains the dynamo generation of large-scale solar magnetic fields. In this mean field dynamo theory, the generation of poloidal field leads to an additional source term, $\nabla \times \alpha B$. Since then it has been known as "α-effect". This effect can only take place when toroidal fields are raised to the surface, and Parker (1955b) explained this rise of toroidal flux to the surface to form magnetic loops and bipolar sunspots by the process (as described earlier) of magnetic buoyancy. The magnetic field in such a loop comes out of the solar photosphere through one of the spots, while it goes into the photosphere through the other spot. Hence, sunspot pairs are generally of opposite polarity.

Figure 1.7 shows such a bipolar sunspot pair with magnetic field lines joining them. Further, since the toroidal field that emerged subsequently to form sunspots, has opposite direction in the two hemispheres (Figure 1.5b), the corresponding sunspot pairs in the two hemispheres are also of opposite polarity. The flux tubes, which rise due to buoyancy, are subjected to Coriolis force due to the rotation of the Sun, which imparts a tilt to the axis of the flux tubes. It is clear from the above discussion that mean field dynamo models were successful in explaining the observational features of sunspots and in sustaining the solar magnetic cycle. Since magnetic flux tubes in the convection zone always tend to rise to the surface (Spruit and van Ballegooijen, 1982), the question still remains of how the weak poloidal fields are converted to strong toroidal fields or in other words, how does the amplification and storage of toroidal fields occur.

Using helioseismology, Spiegel and Zahn (1992) discovered the tachocline, a thin transition region between the stratified radiative zone and the convection zone, which is also referred to as the overshoot layer. It is believed that the

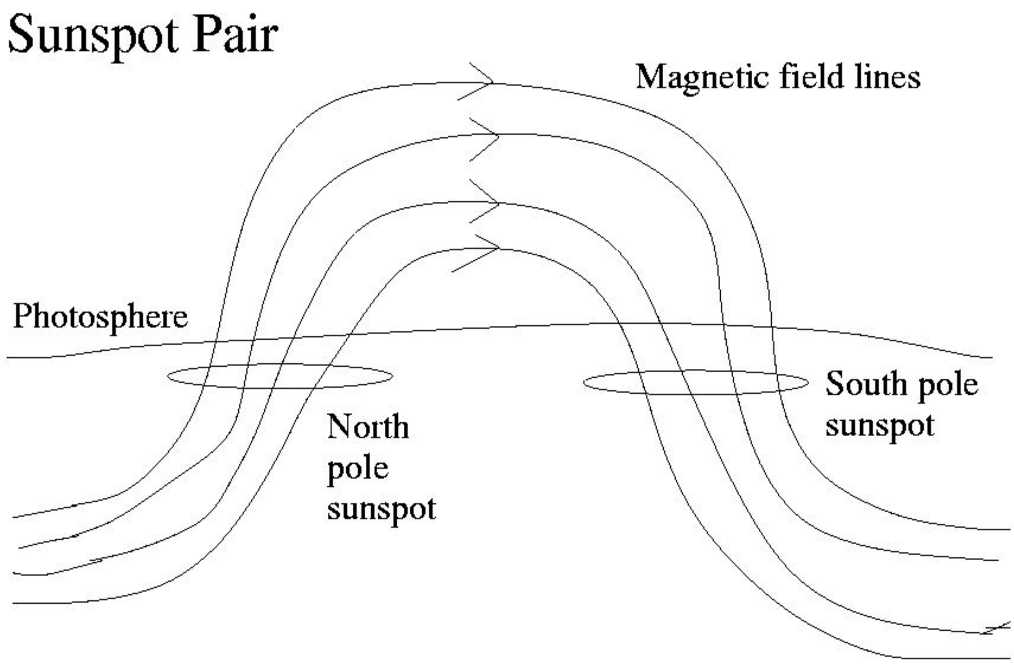

Figure 1.7: Shows a cartoon of a sunspot pair and magnetic field lines joining them. The magnetic field lines comes out of the solar photosphere through one of the spots (North pole sunspot), while goes into the photosphere through the other spot (South pole sunspot). Credit: http://www.nhn.ou.edu/~jeffery/astro/astlec/lec008.html.

sub-adiabatic temperature gradient condition in this region suppresses magnetic buoyancy of flux tubes, and thus helps in storage and amplification of the toroidal field (Spiegel and Weiss, 1980; van Ballegooijen, 1982). Very strong magnetic flux tubes comes out of this stable layer via a process of overshooting convection. Once in the convection zone, they rise to the surface due to magnetic buoyancy, as proposed by Parker (1955b), to form bipolar sunspot pairs. Sunspots are therefore surface manifestations of deep-seated toroidal flux tubes generated and amplified at the base of the convection zone. Simulations of thin flux tubes have shown that the toroidal field strength at the base of the convection zone is approximately $\sim 10^5$ G (D'Silva and Choudhuri, 1993; Fan, Fisher and Deluca, 1993). This field is an order of magnitude stronger than the equipartition strength (magnetic field strength at which the energy in the magnetic field and the convection are in equipartition). However, the origin of the poloidal field from the toroidal field through the helical turbulence process is only possible if the toroidal field strength is not stronger than it's equipartition field strength. So the toroidal field cannot be twisted by helical turbulence and an alternate mechanism needs to be invoked for the regeneration of poloidal fields.

Following the discovery of the polar field reversal (Babcock, 1959), Babcock (1961) first proposed a mechanism for the poloidal field generation that is commonly known as the "Babcock and Leighton mechanism". This was further modified by a kinematic dynamo model by Leighton (1964, 1969). The tilt of sunspot pairs, in effect, causes one member of the sunspot pair to be leading and the other to be following (Figure 1.8). As the cycle advances the leading spots move towards the equator, and the following spots (of opposite polarity) move poleward (Figure 1.8). This generates a north-south poloidal field component. So in a solar magnetic cycle, toroidal fields are generated from poloidal fields by differential rotation, and re-generation of poloidal fields from toroidal fields occurs via the Babcock-Leighton mechanism. Such dynamo models, however, could only reproduce the poleward migration of toroidal fields, but failed

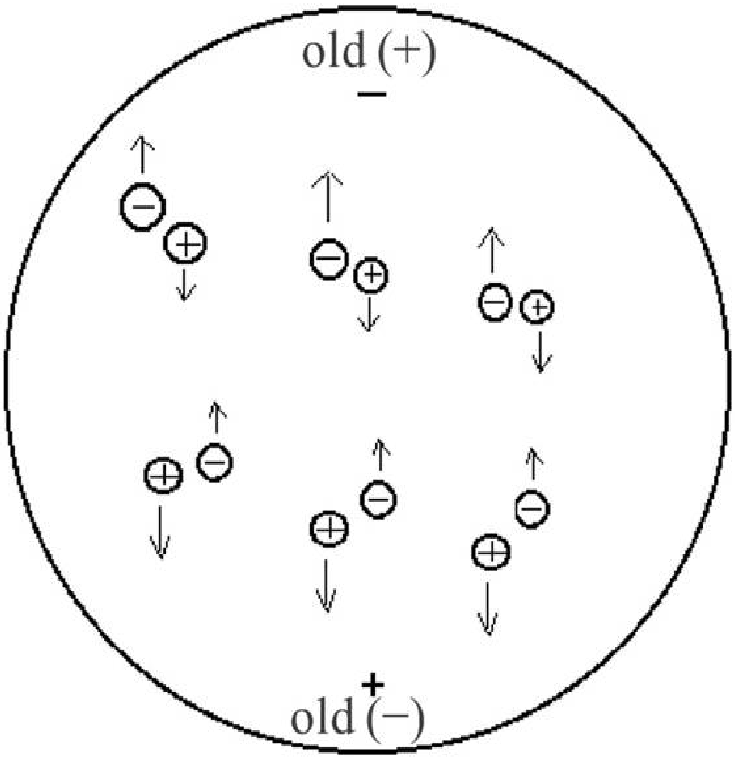

Figure 1.8: Shows sunspot pairs comprising of leading and following spots of opposite polarity. The arrow indicates that the leading spot moves equatorward while the following spot moves poleward. The net following polarity flux eventually cancels the old polar cap fields. Reproduced from http://www.iiap.res.in/meet/apspm/presentations/DibyenduNandy.pdf.

in reproducing the equatorward migration of the sunspot belt. So Choudhuri, Schussler and Dikpati (1995) proposed a meridional circulation model with a poleward directed flow on the surface and an equatorward flow in the convection zone below the surface. Such dynamo models are called as flux transport dynamo models (Choudhuri, Schussler and Dikpati, 1995; Dikpati and Charbonneau, 1999; Nandy and Choudhuri, 2002; Choudhuri, Chatterjee and Jiang, 2007). These models using the Babcock-Leighton mechanism and meridional circulation were fairly successful in reproducing the large-scale features of solar cycle and also in making predictions of the strength of future solar cycles (Dikpati, de Toma and Gilman, 2006; Choudhuri, Chatterjee and Jiang, 2007). In a nutshell, the solar dynamo action involves three basic processes− (1) the generation of toroidal fields by shearing pre-existing poloidal fields (the Ω effect), (2) the subsequent regeneration of poloidal fields of opposite polarities to that present earlier by twisting toroidal fields (Parker's α effect) and (3) transportation of poloidal fields from the equator to the poles on the surface and back to the equator at the base of the convection zone by "meridional circulation".

1.2 Solar Periodicities

The earlier sections talked mainly about two principal periodicities in solar activity, namely, the 11-year periodicity (sunspot cycle), and the 22-year periodicity (solar magnetic cycle). These two periodicities could be well explained by the $\alpha\omega-$dynamo that controls the dynamical evolution of magnetic field activity in the solar interior. Apart from these prominent periodicities, solar activity also shows other quasi-periodicities at both longer and shorter scales than the 11-year periodicity. Generally, quasi-periodicities refer to well-defined periodicities that are present only for limited intervals of time. It is believed that quasi-periodicities are also, in some way or the other, related to solar magnetic activity and are crucial in understanding the nature of solar magnetic fields.

At longer time scales, a 70-year periodicity of very low solar activity lasting from 1645 to 1715 has been reported (Maunder, 1890). This period of very low sunspot activity is known as the Maunder minimum. Gleissberg (1939) has also reported an 80 – 90-year periodicity in the cycle amplitudes from 1750 to 1928. In addition, a 205-year periodicity, determined using radiocarbon studies, has also been reported (Suess, 1980). At shorter time scales, the 27-day periodicity in the synodic rotation of the Sun is well known. A clear 154-day periodicity in the occurrence rate of high energy (0.3-100 MeV) flares has been reported (Rieger *et al.*, 1984) using data from the Gamma Ray Spectrometer (Forrest *et al.*, 1980) on board the Solar Maximum Mission. This 154-days periodicity in the solar flare occurrence was also confirmed at other wavelengths (Verma and Joshi, 1987; Droege *et al.*, 1990; Kile and Cliver, 1991), and for solar energetic particle events (Lean, 1990; Krivova and Solanki, 2002; Kiliç, 2008; Chowdhury, Khan and Ray, 2010; Chowdhury and Dwivedi, 2011).

In addition, a large number of other intermediate periodicities with periods (<1 year) have also been reported. These reported periodicities are: a 51-day periodicity in the comprehensive flare index (Bai, 1987), a 127-day periodicity in the 10 cm radio flux (Kile and Cliver, 1991), periodicities of 33.5 days, 51 days, 84 days, 129 days and 153 days in the solar flare occurrence during different phases of Solar Cycles 19 – 23 (Bai, 2003b), periodicities of 100 – 103 days, 124 – 129 days, 151 – 158 days, 177±2 days, 209 – 222 days, 232 – 249 days, 282±4 days, 307 – 349 days in the unsigned photospheric fluxes (Knaack, Stenflo and Berdyugina, 2005) and periodicities of 87 – 106 days, 159 – 175 days, 194 – 219 days, 292 – 318 days, and 69 – 95 days, 113 – 133 days, 160 – 187 days, 245 – 321 days, 348 – 406 days in sunspot areas at different phases of Cycle 22 and 23 respectively (Chowdhury, Khan and Ray, 2009).

A large number of periodicities, between 1 – 5 years have also been reported. These periodicities are: a 1.3-year periodicity in sunspot areas and numbers (Krivova and Solanki, 2002), 1-year and 1.7-year periodicity in solar total and open fluxes (Mendoza, Velasco and Valdés-Galicia, 2006), 1.3-year, 1.43-year, 1.5-year, 1.8-year, 2.4-year, 2.6-year, 3.5-year, 3.6-year, and 4.1-year periodicity in unsigned photospheric fluxes (Knaack, Stenflo and Berdyugina, 2004, 2005). Quasi-biennial oscillations (QBO) with period of ∼2 years have also been recognized in various types of solar activity (Krivova and Solanki, 2002; Bai, 2003b; Vecchio and Carbone, 2009; Fletcher *et al.*, 2010). Fletcher *et al.* (2010) proposed a second dynamo mechanism, other than the main 11-year dynamo mechanism, which operates these QBOs.

Studies of all these periodicities have shown the existence of an asymmetry, between the Northern and Southern hemispheres of the Sun, in solar activity phenomena. This North – South asymmetry, on different time scales and at different phases of the solar cycle, have been observed in various solar activity indicators, *viz.* photospheric magnetic flux (Howard, 1974; Knaack, Stenflo and Berdyugina, 2004, 2005), sunspot areas and sunspot numbers (Waldmeier, 1971; Oliver and Ballester, 1994; Temmer, Veronig and Hanslmeier, 2002; Knaack, Stenflo and Berdyugina, 2004; Joshi, Pant and Manoharan, 2006b), and solar flares occurrence (Reid, 1968; Roy, 1977; Verma, 1987; Bai, 2003b; Joshi, Pant and Manoharan, 2006a). These reported hemispheric asymmetries have been providing invaluable information about basic underlying physical processes on the Sun. Since processes such as differential rotation of the Sun and emergence of magnetic flux determine the strength and distribution of solar magnetic activity, investigation of solar-cycle related quasi-periodic variations are crucial in understanding the evolution of large-scale solar magnetic fields. In particular, the role of the North – South hemispheric asymmetry is important to study and understand the irregularities of solar cycles during solar minima conditions, and a study has been taken up in Chapter 4 to investigate the role of such North – South asymmetry in quasi-periodic variations of solar photospheric magnetic fields in the buildup to one of the deepest solar minima, experienced in the past 100 years, at the end of Solar Cycle 23.

1.3 Solar Wind

The Sun's outer atmosphere, namely the corona, has a very high temperature of nearly 10^6 °K. Such high temperature creates a huge pressure difference between the solar corona and the interstellar medium (ISM), and causes coronal plasma to flow out into interplanetary space, despite the restoring influence of solar gravity to form the solar wind. Parker (1958) first proposed a theoretical model for the continuous expansion of the corona, and termed it as "the solar wind". However, indirect observational evidences of this continuous outflow of solar wind plasma into the interplanetary medium (IPM) were already inferred from observations of aurorae (Chapman and Bartels, 1940), motions of cometary ion tails (Biermann, 1951) and the appearance of the zodiacal light (Behr and Siedentopf, 1953). Later, in the early 1960s, the long term *in situ* measurements from the spacecraft Mariner 2 (Neugebauer and Snyder, 1962) confirmed the existence of the solar wind, a continuous stream of charged particles in the IPM (Snyder, Neugebauer and Rao, 1963).

At the high temperature of the corona, hydrogen is completely ionized, and hence the coronal plasma consists largely of an electron-proton mixture along with a small admixture of helium ions and other heavier elements. The solar wind plasma, being a product of the expanding corona, is also a mixture of ions and electrons. It is known from Parker's solar wind model (Parker, 1958) that the solar wind undergoes acceleration close to the Sun, and thereafter attains a constant velocity of a few hundred km s^{-1}. In fact, spacecraft observations from the Mariner 2 to Venus mission, in the early 1960s, confirmed this aspect of the solar wind and reported the solar wind velocities, ranging from 250 km s^{-1} to 1,000 km s^{-1}, close to the values predicted by Parker (Parker, 1958). However, the typical speed of the solar wind near the Earth's orbit, at 1 AU (the distance between the Sun and the Earth) is approximately 400 km s^{-1}, and also the solar wind is highly super-Alfvénic (with Alfvénic Mach number of $\sim$5 – 20; Nishino *et al.* (2008)) and supersonic (Sonic Mach number

Table 1.1: Properties of the solar wind at 1 AU

Proton density	6.6 cm^{-3}
Electron density	7.1 cm^{-3}
He^{2+}	0.25 cm^{-3}
Flow Speed	450 km/s
Proton temperature	1.2×10^5 K
Electron temperature	1.4×10^5 K

of ∼8 − 9; Hietala *et al.* (2012)).

Furthermore, the solar wind undergoes a rapid and enormous change in the densities ranging from $\sim 10^{10}\, cm^{-3}$ at the base of the corona to $\sim 10\, cm^{-3}$ at 1 AU. It is also known that the solar wind density varies approximately as r^{-2}, where r is the heliocentric distance from the Sun. Some observed properties of the solar wind at 1 AU are given in Table 1.1. The solar wind plasma, due to these low densities in the IPM, becomes highly conducting, and thus, the charged particles in the solar wind move to very large distances, exceeding 100 AU, filling a region of space, called the heliosphere. The solar magnetic fields, which are frozen into the plasma, are continuously swept out into the heliosphere by the solar wind, and give rise to an interplanetary magnetic field (IMF). The outward-convected IMF, due to the rotation of the Sun with an angular rate of 2.7×10^{-6} rads^{-1}, follows the pattern of an Archimedian spiral, commonly referred to as a “Parker Spiral” or “Archimedes spiral”.

By the early 1970s, it was known that the solar wind was highly structured and dynamic, and the shape and structure of the solar corona changes with the level of solar activity. Solar wind flows were, principally, composed of two components, the fast wind (with solar wind speeds greater than 450 km/s) and the slow wind (with speeds lesser than 450 km/s). During the Skylab (Vaiana *et al.*, 1973) era, in the 1970s, coronal holes (CH) – the dark and relatively cool coronal regions of open magnetic field lines, were discovered, and regarded

Table 1.2: Solar wind parameters for the slow and fast wind adapted from Schwenn (1990).

	Slow wind	Fast wind
Flow speed v_p	$250-400$ kms^{-1}	$400-800$ kms^{-1}
Proton density n_p	10.7 cm^{-3}	3.0 cm^{-3}
Proton flux density $n_p\ v_p$	$3.7\times10^8\ cm^{-2}s^{-1}$	$2.0\times10^8\ cm^{-2}s^{-1}$
Proton temperature T_p	3.4×10^4 K	2.3×10^4 K
Electron temperature T_e	1.3×10^5 K	1×10^5 K
Momentum flux density	2.12×10^8 dyncm^{-2}	2.26×10^8 dyncm^{-2}
Total energy flux density	$1.55\times$ erg$cm^{-2}s^{-1}$	$1.43\times$ erg$cm^{-2}s^{-1}$
Helium content n_p/n_{He}	2.5%, variable	3.6%, stationary

as the source regions for the fast solar wind streams (Krieger, Timothy and Roelof, 1973; Timothy, Krieger and Vaiana, 1975). CH are prominently seen during the solar activity minima conditions, and often confined to the polar regions of the corona. Slow wind, on the other hand, originates from the hot regions of bipolar closed magnetic structures in the corona, namely the helmet streamers (Feldman *et al.*, 1976; Bame *et al.*, 1976), and usually seen near the equatorial zones of the corona. A comparison between the different solar wind parameters, adapted from Schwenn (1990), is given in Table 1.2. In addition to these source regions, sometimes highly transient and explosive coronal mass outflow from the Sun, commonly known as Coronal Mass Ejections (CMEs) (Brueckner, 1974; Gosling *et al.*, 1974), were observed. CMEs are considered as the other source regions for the solar wind, where the solar wind velocity abruptly increase many fold as compared to the average solar wind speed. These transient dynamic phenomena will be discussed at length in section 1.4.1.

The solar wind due to its expansion through the interplanetary space develops fluctuations (Parker, 1958, 1963) or turbulence (Bruno and Carbone,

2005) in velocity, magnetic field, and density. The scale sizes of such fluctuations often show a wide range of spatial scales, and the large-scale sizes in the solar wind, above 10^4 km, generally, follow a power-law spectrum (Intriligator and Wolfe, 1970). Fluctuations of scale sizes greater than 10^7 km also occur in the solar wind. These are principally developed due to stream structures in the solar wind, and cannot be explained by the turbulence spectrum. Studies of the turbulent fluctuations in the solar wind have been made using space-based satellite measurements as well as ground-based remote sensing radio observations. Earlier, *in situ* spacecraft observations were made for measuring these fluctuations at 1 AU and beyond. However, the launch of the twin space missions, Helios 1 and 2, in the early 1970s, successfully bridged the large observational gap between 0.3 and 1 AU in the inner heliosphere.

1.3.1 IPS as a Probe to Study the Solar Wind

Unlike velocity or velocity and magnetic field fluctuations, density fluctuations are ubiquitous in the solar wind. Further, density fluctuations are also believed to be a better tracer of solar wind flows as compared to the solar wind density (Ananthakrishnan, Coles and Kaufman, 1980; Woo *et al.*, 1995; Huddleston, Woo and Neugebauer, 1995). Density fluctuations/irregularities in the IPM cause scattering of the electromagnetic radiation, coming from distant point-like, extra-galactic radio sources, and produce amplitude fluctuations in the received intensity at ground-based radio telescopes. This phenomenon is commonly known as "Interplanetary scintillation (IPS)", and was first reported by Hewish, Scott and Wills (1964) during a series of observations carried out at 178 MHz between June 1962 and July 1963. The IPS phenomenon is similar to the twinkling of stars where the Earth's neutral atmosphere acts as an inhomogeneous media, that actually causes the twinkling of stars by scattering the incoming light. Excellent reviews by Jokipii (1973) and Coles (1978) cover the theoretical and observational aspects of the IPS phenomena. In Chapter

5, we have discussed IPS observations at length.

It is known that IPS is sensitive to density irregularities of scale sizes less than few hundred km (at a wavelength of ≈ 1 m) that are convected outwards by the solar wind (Little and Hewish, 1966). Using IPS measurements recorded either at a single IPS station or by a cross-correlation of intensity variations from a network of three or more IPS stations, one can determine the degree of scintillation and the solar wind velocity. IPS is an integrated measurement along the line of sight to the radio source being observed and can be quantified through a parameter, called the scintillation index (m), that is defined as the as ratio of the scintillating flux ΔS to the mean source flux $< S >$, $\mathsf{m} = \frac{\Delta \mathsf{S}}{<\mathsf{S}>}$. At 327 MHz, IPS can probe a large region of inner heliosphere, covering from 0.2 to 0.8 AU. So IPS measurements have been efficiently used for studying the large-scale changes of the solar wind in the inner heliosphere by deriving solar wind speed and intensity scintillations (Rickett, 1975; Ananthakrishnan, Coles and Kaufman, 1980; Hewish, 1989; Ananthakrishnan, Balasubramanian and Janardhan, 1995; Janardhan *et al.*, 1996; Hayashi *et al.*, 2003; Tokumaru, Kojima and Fujiki, 2010; Manoharan, 2012; Kojima *et al.*, 2013). Since radio sources with angular diameter less than 1 arcsec, generally, produce strong scintillation, IPS has been successfully used to estimate the angular diameter of radio sources in the range $0.1-1$ arcsec (Little and Hewish, 1968; Readhead and Hewish, 1974; Bhandari, Ananthakrishnan and Pramesh Rao, 1974; Janardhan and Alurkar, 1992, 1993). In Chapter 5 of this thesis, we have studied, using IPS measurements at 327 MHz, the solar cycle changes of the solar wind microturbulence levels in the inner heliosphere.

1.4 Space Weather Disturbances

1.4.1 CMEs and Flares

The continuous outflow of solar wind, carrying the energetic solar particles and the entrained IMF, drive space weather effects on the Earth and in the near-earth environment. Superimposed on the quasi-steady solar wind flow are transient solar wind flows, commonly referred to as CMEs. High speed CMEs (2000 km s^{-1}) cause intense interplanetary disturbances, and in the presence of a southward component of the IMF (IMF-Bz) lead to strong magnetic storms on the Earth. So CMEs have been extensively studied by several authors, and a large number of articles and reviews are available in the literature (Hildner, 1977; Wagner, 1984; Kahler, 1992; Hundhausen, 1997; Gopalswamy, 2004).

CMEs were first discovered in the early 1970s (Brueckner, 1974; Gosling *et al.*, 1974) by white light coronagraphs on board Skylab. Currently, the Large Angle Spectrometric Coronagraph (LASCO; (Brueckner *et al.*, 1995)) on board the Solar and Heliospheric Observatory (SoHO) has been regularly recording CMEs, and are available in the public domain at http://cdaw.gsfc.nasa.gov/CME_list. A huge amount of matter ($\sim 10^{10}$ kg) is typically ejected outwards into the interplanetary space, by each CMEs, at speeds of several hundreds of kms^{-1} in the range 100 – 3,000 kms^{-1} (Yashiro *et al.*, 2004), with an average speed of around 400 kms^{-1}. CMEs account for solar mass flux, roughly varying between 5×10^{12} and 5×10^{13} kg (Vourlidas *et al.*, 2002), or equivalent to about 5% of the total solar wind mass flux. CMEs are also highly energetic, carrying kinetic energy of 10^{23} to 10^{24} J (Vourlidas *et al.*, 2002) which is comparable to the energy carried by large solar flares. CME's are also characterized by their angular width ranging from 24° to 72° (Yashiro *et al.*, 2004). The basic characteristics of CMEs are given in Table 1.3. CMEs (of high speed) often drive shock waves as they travel faster than the speed of sound in the interplanetary medium. These shocks, upon reaching 1 AU,

Table 1.3: Basic properties of CMEs. Adapted from (Bothmer, 2006).

Speed	300 - 3000 km/s
Mass	$5 \times 10^{12} - 5 \times 10^{13}$ kg
Kinetic energy	$10^{23} - 10^{24}$ J
Angular width	$\sim 24° - 72°$

compress the Earth's magnetosphere, buildup the ram pressure in the solar wind, and cause major geomagnetic storms. Highly energetic solar flares, on the other hand, cause short-term interplanetary variations at the time of their observations.

Solar flares are processes of sudden energy releases occurring over a period of a few seconds to minutes. It emits flashes of electromagnetic radiation over a wider wavelength ranges, *viz.*, radio, infrared, visible, UV, X-ray, and even γ-ray. Unlike CMEs, solar flares rarely cause any large scale effects on the Earth's magnetic field. However, solar flares can give rise to instantaneous effects on the Earth's ionosphere owing to increased ionization. It has also been seen that ionospheric electron densities increase in response to flares. Although CMEs are largely associated with prominence eruptions, they also occur in association with flares, and such flare-associated CMEs sometimes cause sudden impulses in the Earth's magnetic field due to the interplanetary shocks driven by them. A description of one such event has been undertaken in Chapter 6.

1.4.2 Impact of Solar Wind on the Earth

From the earlier discussion, it is known that the frozen-in IMF is dragged into interplanetary space (by the radially flowing solar wind) along an Archimedian spiral pattern. Further, the bimodal structure of the solar wind with open magnetic field lines from the coronal holes and bipolar closed loop structures at the equatorial coronal region, showed that there are areas of alternate magnetic field sectors with the directions towards the Sun as well as the directions away from the Sun in the IMF. The existence of these inward and outward magnetic sectors, having magnetic fields antiparallel to each other, cause electric current to develop between them, as per Maxwell's law, $\nabla \times B = \mu_0 J$. The current sheet is known as "heliospheric current sheet". Wrapped in the heliospheric current sheet, the IMF near the Earth's orbit will be either inward or outward depending upon whether the Earth lies above or below the current sheet. Furthermore, the inclination of the ecliptic plane (the plane containing the Sun and the Earth) with the current sheet gives rise to either a northward or a southward component of the IMF. The IMF components are generally studied using the GSM (Geocentric Solar Magnetospheric) coordinate system (Russell and McPherron, 1973), where the X-axis points from the Earth towards the Sun, the Y-axis is perpendicular to the earth's magnetic dipole, and the Z-axis represents the direction of the Northern magnetic pole. Generally, the solar wind velocity acts as one of the key drivers of the geomagnetic activity, however, it is the magnetic field components of the IMF (northward and southward components) that plays a crucial role in the transfer of the solar wind energy into the Earth's magnetosphere, thereby causing major geomagnetic activity.

The solar wind, moving with the velocity V, and having a frozen-in IMF imposes an electric field, E = (-V $\times$ B), called the Interplanetary Electric Field (IEF), on the Earth's magnetosphere. The magnetosphere is a region of influence of the Earth's own magnetic field and it protects the Earth from the solar wind flows. However, the presence of a southward component of the IMF (IMF-Bz) causes or leads to magnetic reconnection between the IMF and magnetospheric fields (Dungey, 1961), which in turn, opens the path for the transmission of solar wind energy into the magnetosphere, and subsequently alters to the Earth's magnetospheric and ionospheric current systems (Burton, McPherron and Russell, 1975; McPherron, 1979; Gonzalez, 1990; Tsurutani and Gonzalez, 1997). Figure 1.9 shows a schematic representation of how an IMF is reconnected with the terrestrial magnetic field lines. The different stages of this solar wind interaction with the Earth's magnetosphere and ionosphere are labeled, in Figure 1.9, by the numbers 1 through 9. The currents developed include currents such as the ring current, the tail current, the auroral electrojets, and the field aligned currents. These currents are shown schematically in Figure 1.10.

Generally, when the Earth's magnetosphere is open, the IEF is transmitted without any time delay to the day side polar cap regions. Since the field lines are equipotential, these electric fields are mapped into the night side magnetosphere, and cause convection motion under the action of E $\times$ B drift. Therefore, these IEF are also referred to as convection electric fields. Further, due to the action of gradient and curvature drifts, the plasma convection driven by the electric field constitutes a ring current that flows in closed loops around the Earth. The current which flows in the cross tail regions of the night side magnetosphere is known as the tail current. The field aligned currents (FAC) generally connect the auroral ionosphere to the inner and outer magnetospheres, where the Region 1 FAC (R1 FAC) connects the boundary layer plasma with the poleward motions of auroral oval and the Region 2 FAC (R2 FAC) connects the inner edge of the ring current to the auroral oval near its equatorward edge. During periods of enhanced plasma convection, a part of the ring current closes through the auroral ionosphere in the dusk-midnight sector, and is known as partial ring current.

The electrojet currents in the auroral oval are referred to as the auroral electrojet current. Sudden changes in magnetospheric and ionospheric currents give rise to the geomagnetic disturbances. For example, during a geomagnetic storm the increase in the ring current cause a depression in the horizontal component (H-comp) of magnetic field. The strength of such magnetic disturbances are characterized in terms of geomagnetic activity indices, which will be discussed in the forthcoming section 1.4.3.

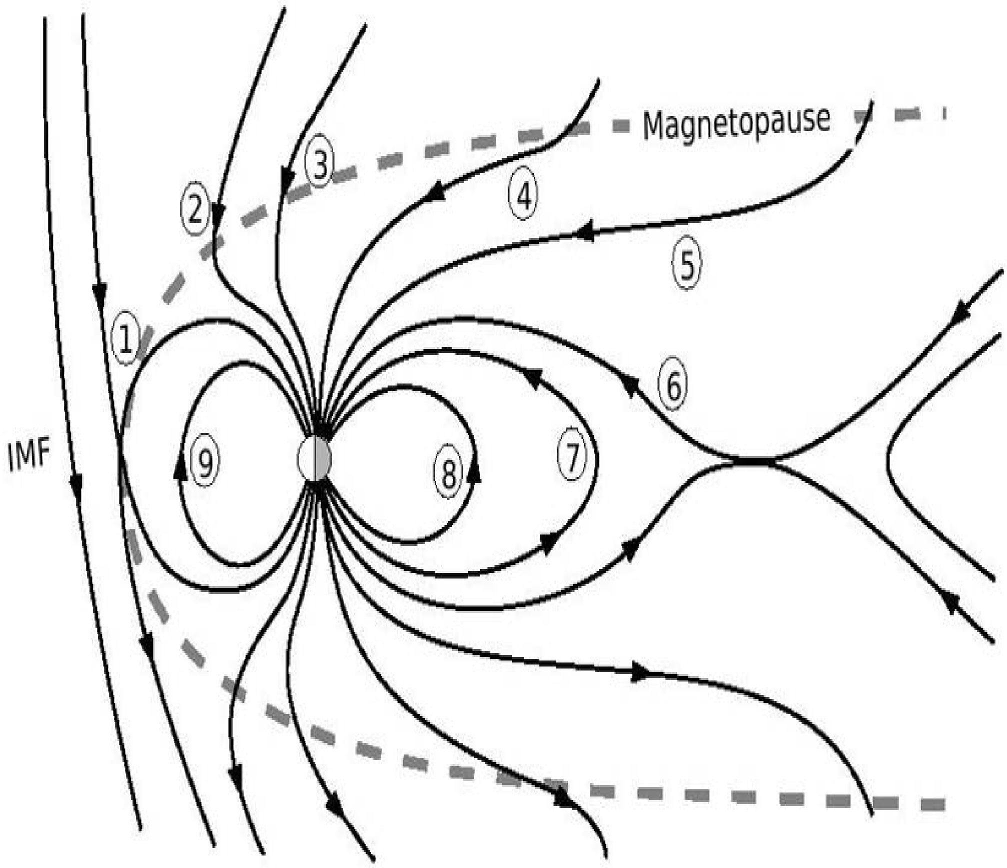

Figure 1.9: Shows a schematic representation of magnetic reconnection process of the IMF with the Earth's magnetospheric fields, and the subsequent solar wind energy transfer into the magnetosphere. The magnetopause, a boundary layer between the Earth's magnetopshere and the sourrounding solar plasma, is shown by a solid dotted line. The numbers 1 through 9 label different stages of this solar wind interaction with the Earth's magnetosphere and ionosphere. Credit: http://web.ift.uib.no/Romfysikk/RESEARCH/PROJECTS/CLUSTER/index.php.

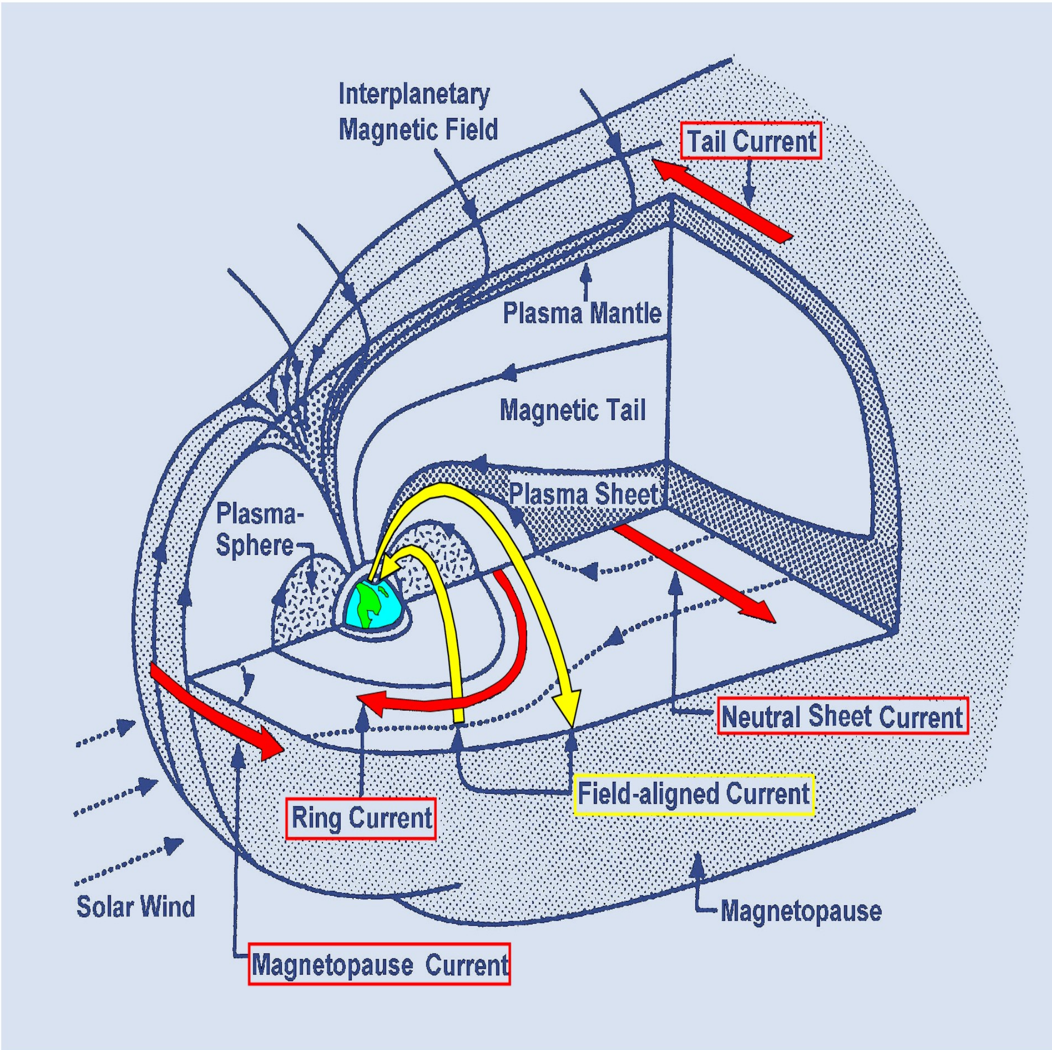

Figure 1.10: Shows a schematic representation of different currents systems developed in the magnetosphere and ionosphere of the Earth through interaction with the solar wind. Credit: http://geomag.org/info/magnetosphere.html.

1.4.3 Geomagnetic Activity Indices

The geomagnetic activity indices are created using geomagnetic records from global stations located from auroral to middle/low latitudes. The indicator of geo-magnetic disturbances at mid-latitude stations is the Dst (or Disturbance storm time) index, which acts as a proxy for the intensity of the ring current. While the Dst index is an hourly average value, a high-resolution SYM/H index is the minute by minute average value, representing the intensity of the ring current through mean variations of H over all mid-latitude stations. In addition to the symmetric part, the ring current also comprises an asymmetric part, called the asymmetric ring current, the ASY/H index.

On the other hand, the auroral zone activity is characterized by auroral electroject indices, like AU, AL, and AE (Davis and Sugiura, 1966), derived from magnetic stations located in auroral zones. The AL (or auroral lower) index represents the westward electrojet currents in the nightside auroral ionosphere and can capture the substorm expansion phase activity in the magnetosphere. The AU (or auroral upper) index represents the eastward flowing current in the dayside auroral ionosphere. The AE index (or auroral electrojet) is the difference between the AU and AL, and is a good indicator of substorm activity. The other geomagnetic indices are K_p and A_p, derived from 13 magnetic observatories in the sub-auroral latitude zones ($44-60°$) (Mayaud, 1980). Both K_p (ranges from 0 to 9) and A_p indices (0 to 32) characterize global geomagnetic disturbance.

1.4.4 Shielding of Convection Electric Field

The inner magnetosphere of the Earth is generally shielded from the effects of the IEF (V $\times$ Bz) or the convection electric field (Vasyliunas, 1970; Senior and Blanc, 1984; Wolf *et al.*, 2007). However, there are occasions when this shielding is weakened or broken due to rapid changes in the IMF-Bz. At such times convective electric fields penetrate instantaneously down to the low latitude and equatorial ionosphere. This is well known as prompt penetration, and has been extensively studied since 1970s (Nishida, 1968; Rastogi and Patel, 1975; Spiro, Wolf and Fejer, 1988; Wolf *et al.*, 2001; Goldstein *et al.*, 2002; Huang, Richmond and Chen, 2005; Wang *et al.*, 2008; Kikuchi *et al.*, 2010). In the next section 1.4.4.1, we will discuss briefly the current understanding of these events.

1.4.4.1 Prompt Penetration and Overshielding

We have already discussed earlier about convective plasma motions in the nightside magnetosphere. Generally, these convective motions in the night side magnetosphere bring ions and electrons towards the Earth. As the plasma approaches closer to the Earth it stops penetrating further at certain distance due to increase in the Earth's closed magnetic field lines which opposes the plasma motions. At this point the ions and electrons move in opposite directions due to the Lorentz force exerted by the Earth's magnetic field, and a westward current begins flowing around the earth, due to the net transport of charges. This current is known as the ring current. Under active geomagnetic conditions when convection increases, the ion pressure generally exceeds the electron pressure, and leads to a partial ring current (PRC). To make the total current divergenceless, the PRC connects to the auroral ionosphere via region 2 field aligned currents (R2 FAC) and closes via perpendicular current flows in the auroral oval.

The R2 FAC currents goes into the auroral ionosphere in the dusk sector and comes out from the auroral ionosphere in the dawn sector. These currents cause a zonal charging in such way that the dusk side becomes positively charged and the dawn side becomes negatively charged. This dusk-dawn polarization leads to a potential drop across the inner magnetosphere, and gives rise to an electric field which more or less, under steady state conditions, cancels the convective electric field in the dusk-dawn direction. Figure 1.11 shows the shielding of convective electric field through a sequence of diagrams. The

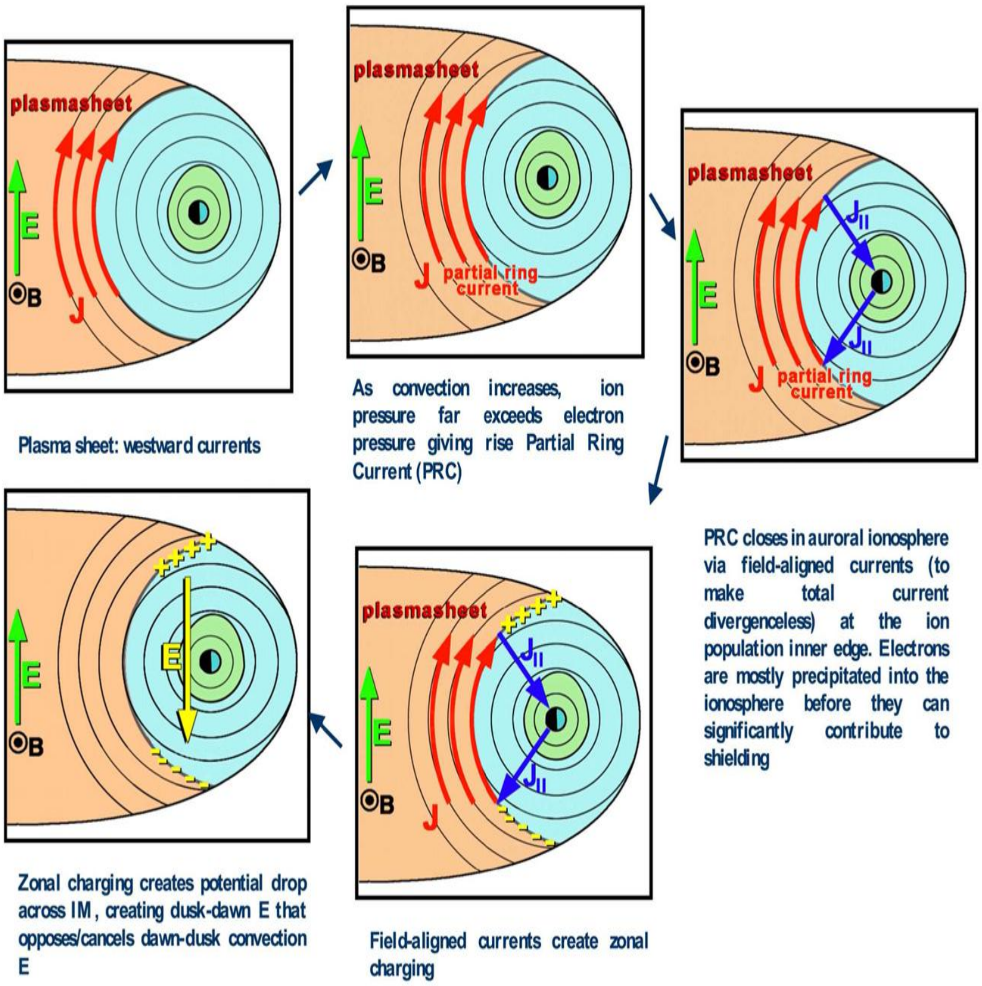

Figure 1.11: Shows the schematic sequence diagrams for shielding of convective electric field. Adapted from Chakrabarty (2007).

time scale of this process is generally around ∼30 minutes (Vasyliunas, 1970; Senior and Blanc, 1984) but can sometimes be much longer. During times of rapid increase in the convection electric field, – that is, when the IMF-Bz is southward, R2 FAC takes time to develop and the shielding is temporarily inactive or broken (Kelley *et al.*, 2003; Huang, Richmond and Chen, 2005). This causes prompt penetration of the IEF into the ionosphere over low latitudes. On the other hand, a sudden northward turning of the IMF-Bz after a period of steady southward IMF-Bz causes the convective electric field to decrease, and the R2 FAC takes a long time to readjust, and produce a residual electric field opposite to the prompt penetration electric field. This is known as the overshielding effect (Wolf *et al.*, 2007; Kikuchi *et al.*, 2010).

We have taken up a study in Chapter 6 to investigate sudden impulses in the Earth's magnetic field wherein, we have discussed prompt penetration and overshielding effects occurring during sudden impulses in H, the horizontal component of the Earth's magnetic field, caused by a sudden change in the southward and northward configuration of the IMF.

1.5 Organization of the Thesis

The work carried out in the thesis is organized as follows:

1.5.1 Chapter 1 – Introduction

Chapter 1 includes a brief introduction to solar cycle related studies of solar magnetic field activity, and investigation of different kinds of solar periodicities showing the North – South asymmetry. It also briefly discusses the properties of the solar wind and the interplanetary magnetic field, and describes how IPS has been used as an effective probe to study the solar wind in the IPM. In addition, this chapter brings out aspects of space weather disturbances due to solar and solar wind phenomena that cause geomagnetic variations through solar wind – magnetosphere – ionosphere interactions.

1.5.2 Chapter 2 – Observational Data and Analysis

Chapter 2 details briefly the ground-based and space-borne instruments used for solar and solar wind studies relevant to our work. The chapter covers the description of both the ground-based telescopes such as the Kitt Peak Vacuum telescope and the SOLIS tower telescope of the National Solar Observatory at Kitt Peak, in USA, and the space-based Magnetic Doppler Imager (MDI) instrument on board the Solar and Heliospheric Observatory (SoHO). Also, the IPS radio facility at the Solar Terrestrial Environment Laboratory (STEL), Japan has been thoroughly discussed along with a description of the ground-based magnetograms from the magnetic stations around the world and the solar wind interplanetary data at 1 AU from the OMNI database.

1.5.3 Chapter 3 – Solar Polar Fields During Solar Cycles 21, 22, and 23

In Chapter 3, we investigated the solar cycle related magnetic activity, using ground-based magnetograms from the NSO/Kitt Peak and space-borne magnetograms from the MDI/SoHO instruments, during the last three Solar Cycles, *viz.* Cycles 21, 22, and 23, and in particular during the extended solar minima, at the end of Cycle 23, which was the deepest minima experienced in the past 100 years. Specifically, the evolution of polar magnetic fields during Cycles 21 – 23 have been described. In addition, the Chapter also discussed the crucial role of the polar magnetic fields in determining the strength and amplitude at the maximum of the next Cycle 24, and the key role of polar fields in causing the prolonged and deep solar minimum at the end of Cycle 23.

1.5.4 Chapter 4 – Changes in Quasi-periodic Variations of Solar Photospheric Fields

In Chapter 4, we investigated the role of various quasi-periodicities observed in photospheric magnetic fields in the buildup to the deep solar minimum at the end of Cycle 23. The magnetic field measurements used were derived from the ground-based NSO/Kitt Peak observatory that spanned the period from 1975 to 2010. We employ a wavelet analysis to find the behavior of spectral power of periodicities both in the solar fields above a latitude of 45° (high-latitude fields) and those below latitudes of 45° (low-latitude fields). Similarly, we also studied using a Fourier analysis the behavior of periodicities obtained in the divided high- and low-latitude photospheric magnetic fields prior to 1996 and those after 1996. The results of these analyses were then used to show that the buildup to one of the deepest solar minima in the past 100 years actually started in mid-1990s.

1.5.5 Chapter 5 – Solar Cycle Changes of the Solar Wind Microturbulence Levels in the Inner Heliosphere Using IPS Observations

In Chapter 5, we investigated the consequences of the systematic decline of photospheric magnetic fields in the interplanetary medium through studies of the changes in the solar wind turbulence levels in the inner heliosphere, covering radial distances from 0.2 AU to 0.8 AU in the inner heliosphere. For the investigation of these changes, scintillation index measurements, derived from IPS radio observations from the STEL, Japan, at 327 MHz and covering the years from 1983 to 2009, were used.

1.5.6 Chapter 6 – Unique Observations of a Geomagnetic $SI^+ - SI^-$ Pair and Associated Solar Wind Fluctuations

In Chapter 6, we studied two oppositely directed sudden impulses (SI) in the geomagnetic field, referred to as $SI^+ - SI^-$ pair, observed at the ground stations between 1835 UT and 2300 UT on 23 – 24 April 1998. We verified the changes, if any, in the solar wind parameters like the solar wind magnetic field, velocity, and density, using the interplanetary solar wind data at 1 AU collected from the OMNI database, and the SYM/H data from the ground-based measurements of the Earth's horizontal magnetic field component. Further, we investigated the solar source locations of this geomagnetic event, and discussed how a rear side solar event can also propagate a shock towards the earth.

1.5.7 Chapter 7 – Conclusions and Future Scope

Chapter 7 briefly describes the future scope of the investigations carried out in this thesis, which are important and need to be carried forward through additional observations and analysis in the future.

Chapter 2

Observational Data and Analysis

2.1 Introduction

Significant advances in observations, made over the last few decades, using both ground-based telescopes and space-borne platforms, have made huge improvement in our understanding and established new frontiers in solar research. In particular, observations of the strength and distribution of the line-of-sight (LOS) component of solar photospheric magnetic fields have been made since the mid-seventies, at several ground-based facilities in the USA like, the Mount Wilson Observatory (MWO; Ulrich *et al.* (2002)), Wilcox Solar Observatory (WSO; Svalgaard, Duvall and Scherrer (1978)), National Solar Observatory, Kitt Peak (NSO/KP; Livingston *et al.* (1976a)), and the NSO Synoptic Optical Long-term Investigations of the Sun (NSO/SOLIS; Keller, Harvey and Giampapa (2003)) facility. Regular and systematic observations carried out at these facilities have provided one a unique opportunity to study the large-scale distributions of magnetic fields over the solar surface. However, in the last two decades, space-borne observations made at high spatial and temporal scales by spacecrafts like, the Michelson Doppler Interferometer on board the Solar and

Heliospheric Observatory (SoHO/MDI; Scherrer *et al.* (1995); Domingo, Fleck and Poland (1995)), and the Helioseismic and Magnetic Imager on board the Solar Dynamics Observatory (SDO/HMI; Pesnell, Thompson and Chamberlin (2012); Schou *et al.* (2012)), have vastly improved our understanding of the behavior of solar magnetic activity. In addition, observations spanning the region of space from just above the photosphere out to 1 AU and beyond by space-borne platforms like, Wind (Acuña *et al.*, 1995), Ulysses (Wenzel *et al.*, 1992), SoHO, Advanced Composition Explorer (ACE; Stone *et al.* (1998)), Solar TErrestrial RElations Observatory (STEREO; Kaiser *et al.* (2008)), Hinode (Kosugi *et al.*, 2007), and SDO, have contributed equally to our understanding of the solar wind and the changes in the frozen-in interplanetary magnetic fields (IMF). Another well-exploited ground-based method to study the large-scale structure of the solar wind is the technique of interplanetary scintillation (IPS) observations at meter wavelengths, using ground-based radio telescopes to probe the interplanetary medium, and study the solar wind in the inner heliosphere.

The data used in the thesis come from both ground- and space-based observations and this chapter has been divided into three parts. In the first part, a brief overview of the instruments and observations from the NSO/KP, NSO/SOLIS, and SOHO/MDI, which facilitate solar magnetogram data, are presented. We have also presented, in this chapter, a detailed description of the synoptic magnetograms used in our study. The IPS observations used in our study were made at 327 MHz from the four stations IPS observatory of the Solar Terrestrial Environment Laboratory (STEL; Asai *et al.* (1995); Tokumaru, Kojima and Fujiki (2012)), Japan. The last part of the Chapter describes the space-borne solar wind interplanetary data collected at 1 AU from the OMNI database. Lastly, this chapter describes geomagnetic field observations made at magnetic stations, located at low- and mid-latitudes.

2.2 Magnetic Field Data

Photospheric magnetic field data, used in the thesis, are mainly derived from synoptic maps available from the ground-based Vacuum telescope and SOLIS facility of the National Solar Observatory, Kitt Peak (NSO/KP), USA and from the space-based MDI instrument on-board SoHO. The synoptic maps are actually produced from daily observed full-disk magnetograms of the NSO/KP and SoHO/MDI.

2.2.1 Kitt Peak Vacuum Telescope

The Vacuum telescope, at Kitt Peak, is a dedicated solar facility for magnetic and velocity field measurements. The NSO/KP observatory is located atop the Kitt Peak mountain 3000 feet above the desert floor, about 56 miles southwest of Tucson, Arizona. The details of the telescope and associated instrumentation can be found in Livingston *et al.* (1976a). Figure 2.1 shows a cross-section of the Kitt Peak Vacuum telescope, which is a Zeiss type coelostat system, in contrast to the McMath Pierce Kitt Peak solar telescope (Pierce, 1964), that uses a heliostat system. The 104-cm coelostat feeds light into a 2.4-m diameter 60-feet vertical vacuum tank through an 86-cm diameter, 10-cm thick, fused silica entrance window. The image forming element is a 60-cm aperture, 36-m focal length silvered mirror whose light is folded through the tank to a vertical, underground Littrow spectrograph. Prior to entering the spectrograph, the light is channeled through an electronically modulated half-wave retarder (Kerr cell), a quarter wave plate, a linear polarizer, and broad-band blocking filters that alternately transmits left and right circular polarized components.

The Littrow spectrograph, having an air-spaced doublet lens with a diameter of 27-cm and focal length of 10.7-m, guides appropriate spectral lines to the two 512-element linear Reticon integrated diode array magnetograph (Livingston *et al.*, 1976b). The 512-channel solar magnetograph is the principal ancillary instrument associated with this spectrograph, and has been produc-

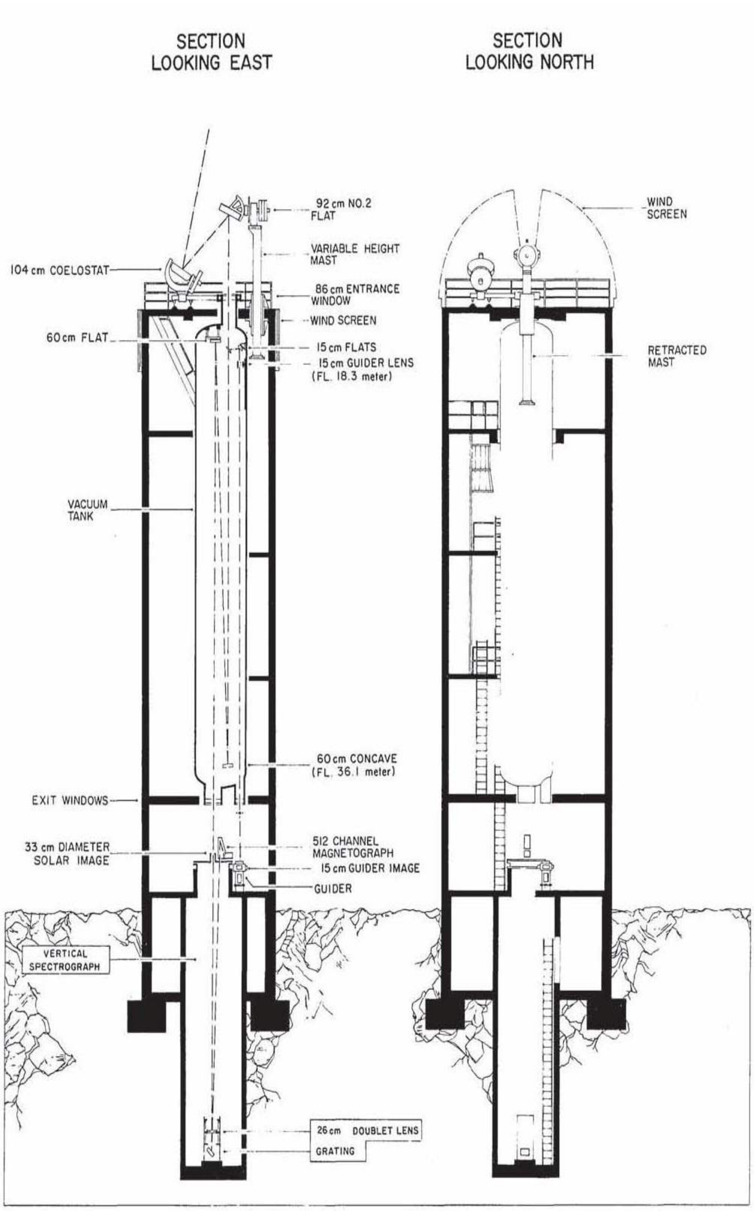

Figure 2.1: Shows cross-sections of the 60 cm Kitt-Peak Vacuum telescope (Adapted from Livingston *et al.* (1976a)).

ing daily full-disk magnetograms since its installment in 1974 through 1992. A schematic illustration of this 512-channel magnetograph is shown in Figure 2.2. The two sets of spatial elements of the double array are positioned on the blue and red wings of the spectral line (Fe I; 8688 Å). The sums and differences of paired pixel intensities in the two polarization states are combined appropriately to yield velocity, total intensity, and longitudinal magnetic flux at each position along the slit. In addition to the main image, a separate guide image is formed from the displaced light path by a guiding system, centrally located just below the entrance slit, with a 18-m focal length double lens, thus helps to keep the image fixed. Control and monitoring of telescope functions is entirely computer controlled. Daily high-resolution magnetograms taken through the magnetograph form a unique synoptic data set.

A new instrument, the NSO Spectromagneotgraph (SPMG), replaced the Diode array magnetograph after 1992 and was operational until 2003 (Jones *et al.*, 1992). It used a two dimensional CCD detector to sample both spectrally and spatially the spectral lines at the exit plane of the Littrow spectrograph. Synoptic map data set obtained from these two magnetographs are available in the public domain at `ftp://nsokp.nso.edu/kpvt/synoptic/mag/` and cover Carrington Rotations CR 1625 – 2006 corresponding to years 1975 to 2003.

2.2.2 SOLIS Facility

Synoptic map data set after 2003 were obtained from the Synoptic Long-term Investigation of the Sun (SOLIS) facility (Keller, Harvey and Giampapa, 2003), operated at the summit of Kitt Peak. The SOLIS facility has three instruments, *viz.* a 50-cm Vector Spectromagnetograph (VSM), a 14-cm Full-Disk Patrol (FDP), and a 8-mm Integrated Sunlight Spectrometer (ISS). Of the three, the VSM only provides photospheric and chromospheric full-disk longitudinal magnetograms along with photospheric full-disk vector magnetograms. A schematic, showing the details of the components of the VSM, is shown in

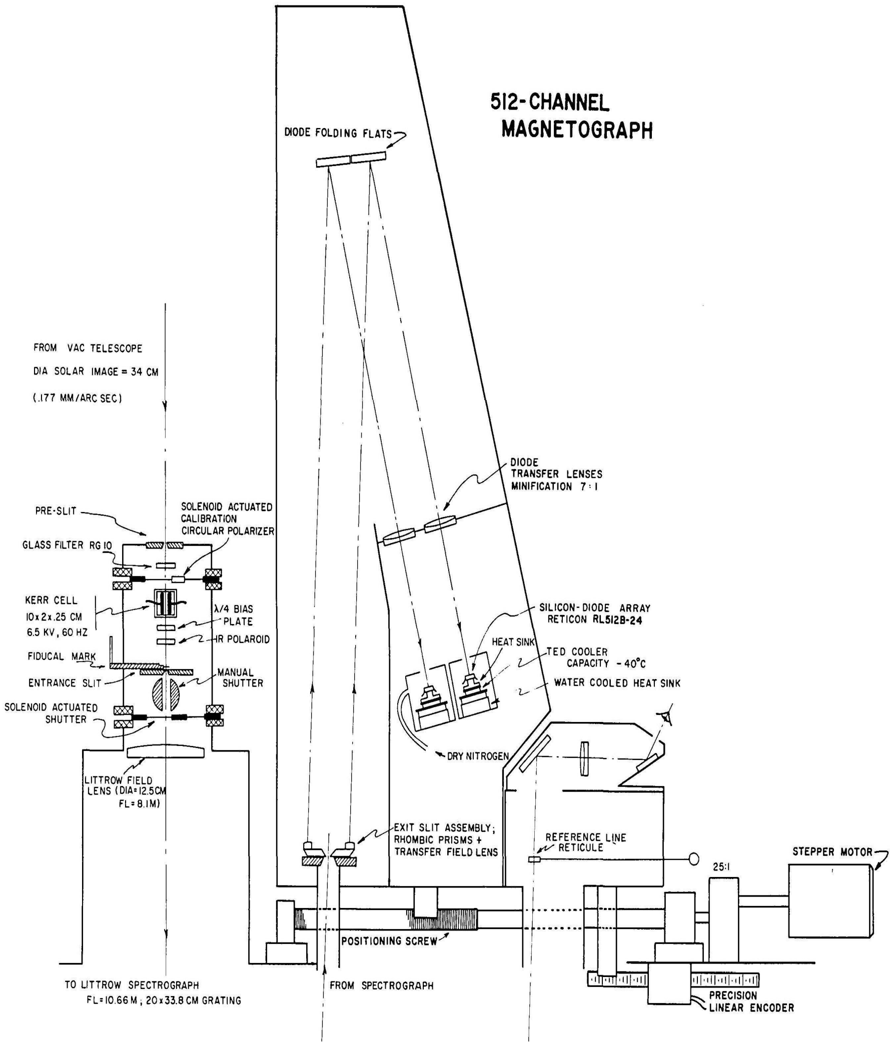

Figure 2.2: Shows schematic illustration of 512-channel magnetograph used in 60 cm Kitt-Peak Vacuum telescope (Adapted from Livingston *et al.* (1976b)).

Figure 2.3. Synoptic maps, used in the thesis, are constructed from photospheric longitudinal magnetograms, which record LOS magnetic fluxes from full stokes profiles of the Fe I 630.15 and 630.25 nm lines.

The VSM operates through a 50-cm aperture Ritchey-Chritien optical telescope with a two-lens field corrector. The entrance window of the telescope is a 6 mm fused silica window. The telescope is filled completely with helium gas to provide cooling to the system. The imaging system of the telescope comprises of a spectrograph and CCD cameras. The image is formed on the entrance slit of the spectrograph covering an area of 2048 arcseconds. On the frontside of the spectrograph slit, there are two calibration packages for selecting the appropriate Fe I and Ca II lines, while on the rear side are four modulator packages placed on a mechanical slide to observe and derive vector spectropolarimetry and LOS polarimetry in appropriate wavelength regions. The focal beam-splitter located in front of the CCD camera splits the image into two parts each of 1024 arseconds, which is reimaged by CCD cameras with image sizes of 1024 $\times$ 512 pixles. A full-disk magnetogram is constructed from the projected solar image, on the entrance slit of the Littrow spectrograph, by moving the telescope in declination. One scan takes 0.6 seconds in FeI 630.15-630.25 nm line, and about 1.2 seconds for the Ca II 854.2 nm line, and so a full disk magnetogram in the photospheric and chromospheric spectral lines takes about 20 and 40 minutes respectively. Synoptic maps produced from these full-disk magnetograms are available in the public domain at `ftp://solis.nso.edu/synoptic/level3/vsm/merged/carr-rot/` and cover CR2007 – CR2080 corresponding to years 2003 – 2009.

2.2.3 SoHO/MDI

The Solar and Heliospheric Observatory (SoHO; Domingo, Fleck and Poland (1995)) is a joint European Space Agency (ESA) and NASA space mission. It was launched on 02 December 1995 for studying the Sun all the way from

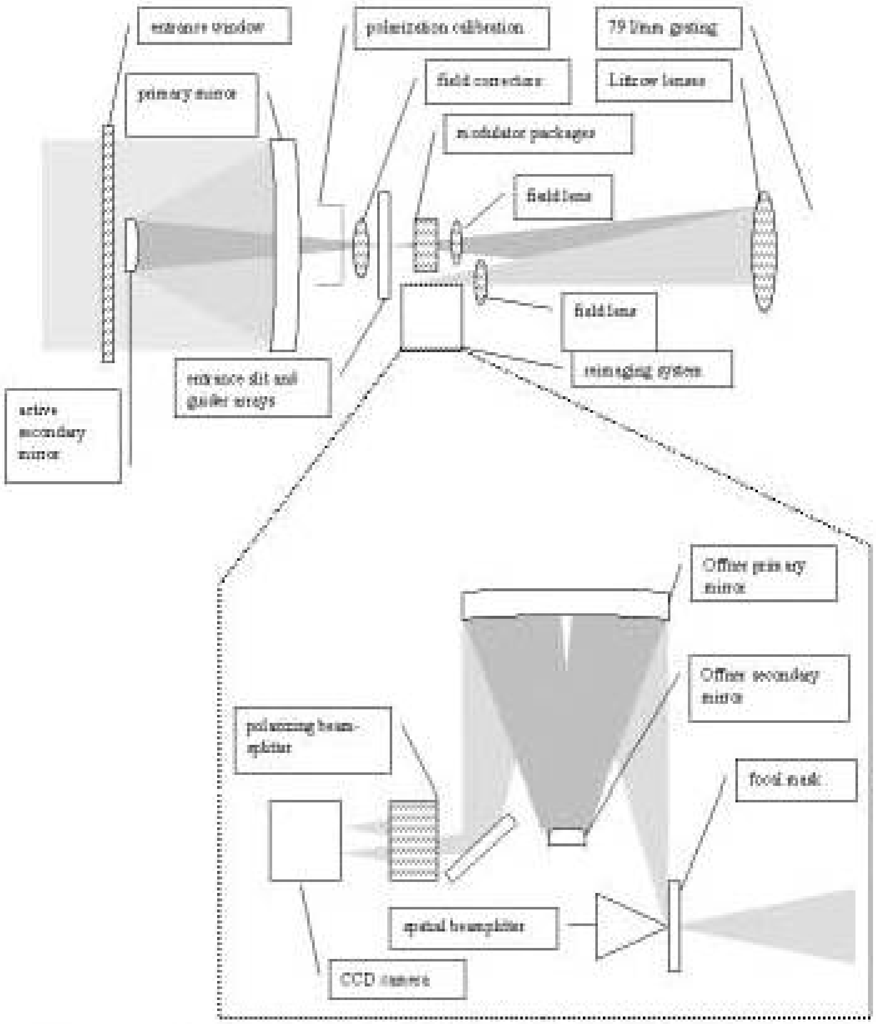

Figure 2.3: Schematic details of VSM components of the SOLIS telescope (Credit: http://solis.nso.edu/VSMOverview.html).

its deep interior out to its outer corona and the solar wind. However, regular operations by SoHO only began from May 1996. Although the mission was originally planned for only two years, the spacecraft is still operating and collecting data on the Sun. In this thesis, the synoptic data set of only one instrument, *viz.* the Michelson Doppler Imager (MDI; Scherrer *et al.* (1995)), on board the SoHO spacecraft is used for deriving photospheric magnetic fields.

The MDI instrument is a 1024 $\times$1024 pixel CCD camera, sitting behind a refracting telescope, which images the Sun through a series of narrow spectral filters. It has a pair of tunable Michelson interferometers with a full width half maximum (FWHM) bandwidth of 940 mÅ and can be tuned across the Ni I 6768 Å spectral absorption line for obtaining images. The MDI instrument is mainly divided into optical packages (OP) and electronic packages (EP). The OP comprises of the telescope, the image stabilization system, spectral and polarizing filters, the beam distribution system, the shutter, and the CCD camera, while the EP consists of the control and communication circuit, the image processor, and the power supply. Figure 2.4 shows the optical layout of the MDI on board SoHO. The green coloured part in Figure 2.4 represents the telescope, filter wheels, and image stabilization system, while all the filters and reimaging optics are colored in blue. The red portion of Figure shows the beam distribution system and the CCD camera. Full details of the MDI instrument can be found in Scherrer *et al.* (1995).

The MDI instrument records various data products, *viz.* LOS velocity (Dopplergrams), line and continuum intensity (Intensitygrams), and magnetic field (Magnetograms). However, only magnetograms have been used in this thesis. The magnetograms used are produced with a cadence of 96 minutes (15 times per day) and a spatial resolution of 1.98 arcseconds per pixel. The longitudinal magnetograms are computed from the Doppler shifts observed in the two left and right circularly polarized components of light. The difference between these two components is a measure of the line splitting due to the Zeeman effect (Electrons in the same energy level with different angular

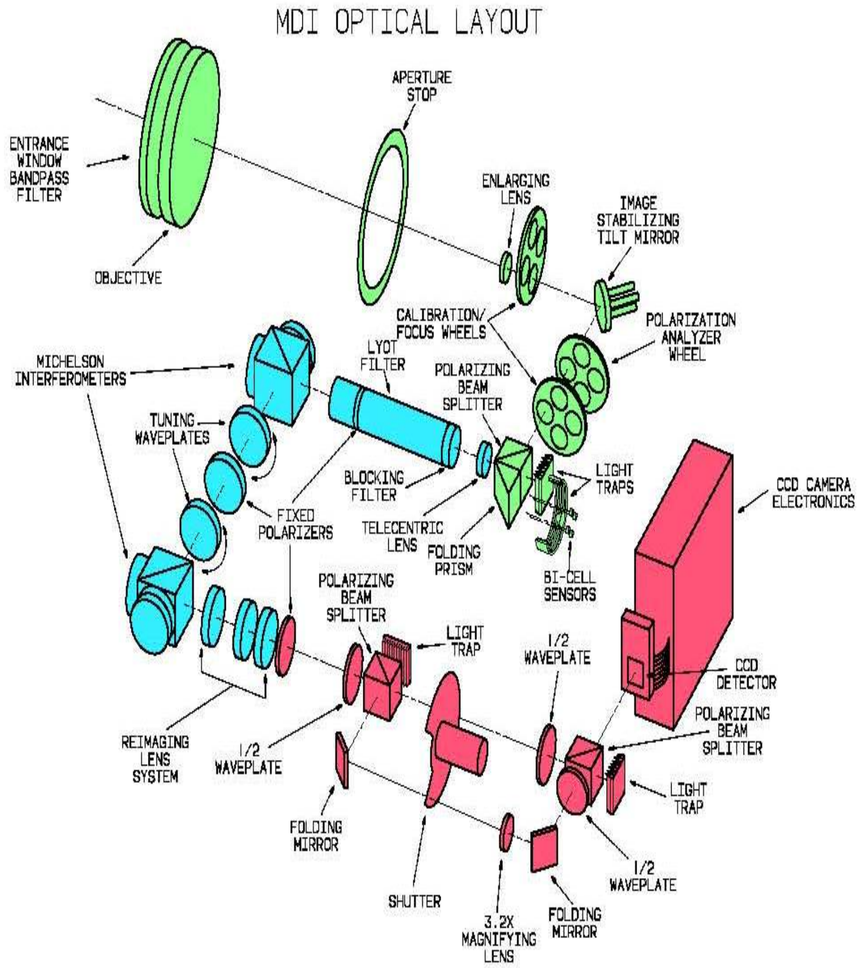

Figure 2.4: Shows the optical layout of MDI instrument on board SoHO spacecraft (Adapted from Scherrer *et al.* (1995)).

momenta have varied energies when magnetic field is applied) and provides the LOS component of the magnetic field. These measurements are generally presented as full-disk magnetograms which are then combined to produce synoptic maps. Each synoptic map covers one full rotation of the Sun of 27.2753 days and is numbered in terms of the Carrington rotation (CR) number with the first Carrington rotation being (by convention) on Julian Date 2398167.40193. We are currently in CR2141 spanning the period 04 August to 31 August 2013. MDI synoptic images are available in the public domain from http://soi.stanford.edu/magnetic/index6.html.

2.2.4 Synoptic Maps

A synoptic map, in the simplest form, gives a quick overview or (a synopsis) of the global distribution of solar photospheric magnetic activity. In the following section, we have described such synoptic maps from the NSO/KP and SoHO/MDI database.

2.2.4.1 NSO/KP

Each daily solar photospheric magnetic image is remapped onto a Carrington coordinate system (Hilton, 1992), which comprises of a Carrington longitude as the abscissa (the distance from the central meridian of the Sun) and either latitude or its sine as the ordinate. The sine latitude map represents an equal area projection of the solar surface. In remapping the disk data, the flux density estimates are conserved in the output map by the careful projection of the flux measured in the full disk image. In addition, the remapped images are weighted by appropriate functions and the strongest weight is applied to observations made near the central meridian. The remapping is done at three spatial resolutions: one-degree elements in latitude and longitude, one degree in longitude and 180 elements in sine latitude, and 0.2 degree in longitude and 900 elements in sine latitude. While the low-resolution map is weighted by a

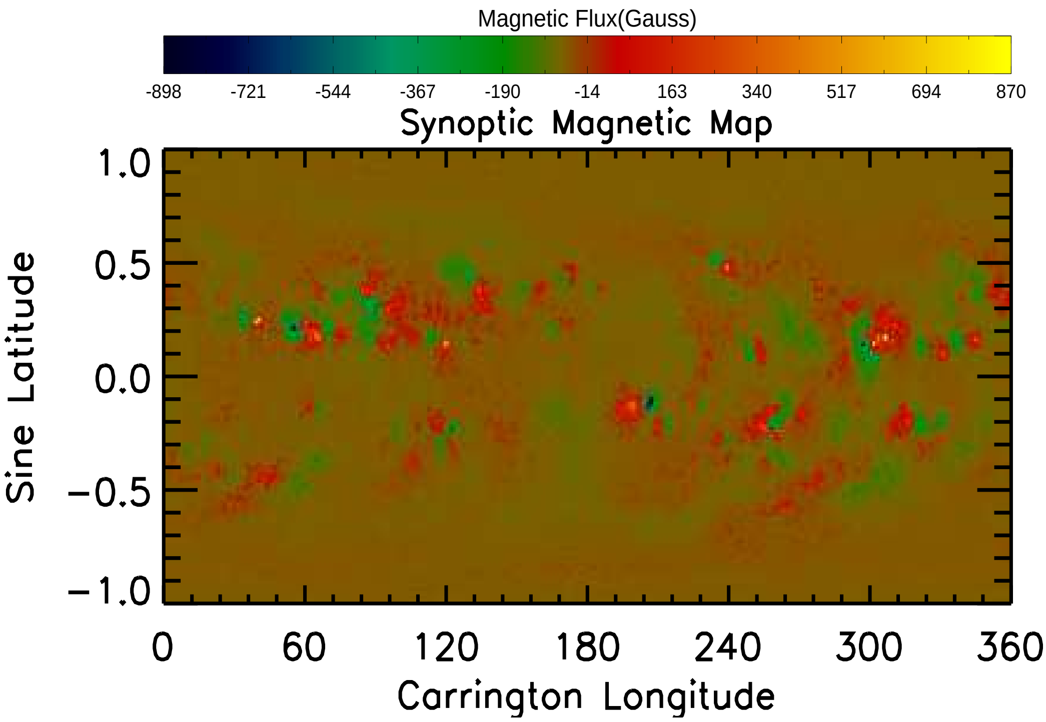

Figure 2.5: Shows a Carrington synoptic map for CR1971. It covers the period from 21 December 2000 to 17 January 2001.

factor of cosine central meridian distance to the fourth power, the high resolution map is weighted by a Gaussian function with a FWHM of 14 degrees. Finally, the weighted maps are merged with maps of other days to construct the final synoptic maps. So a synoptic magnetic map represents essentially the magnetic flux near the central meridian as function of time. Due to the tilt of the Sun's rotation axis relative to the ecliptic, the solar poles are either unobserved or partially observed. So the data gap at the poles, instead of being left missing or unpresented in the high-resolution maps, is filled with a fifth-order, two-dimensional, cubic-spline interpolated data for the low-resolution maps. In estimating photospheric magnetic fields, we have used the low-resolution NSO/KP synoptic maps. For more details about synoptic maps, one can refer Harvey and Worden (1998).

An example of NSO/KP synoptic map is shown in Figure 2.5. This map has 360 × 180 pixels in longitude and sine of latitude format respectively. The longitude increases from left to right (or increasing pixel number) in steps of 1 degree starting at 0 degrees. While there are 180 elements for each degree which represent equal steps in the sine of the latitude, ranging from -1 (South Pole) for row 1 to +1 for row 180 (North Pole). A color coded bar on the top of Figure 2.5 shows the magnetic flux density distribution in the map.

2.2.4.2 SoHO/MDI

MDI synoptic maps are produced from full-disk calibrated magnetograms with 96 minute cadence. The calibrated MDI magnetogram, like the NSO/KP magnetogram, is mapped from image coordinates to a high-resolution Carrington coordinate grid using a cubic–convolution interpolation method. The LOS fields are converted to radial fields under the assumption that the MDI instrument makes LOS measurements of a purely radial field. Such projection corrections, which also takes into account the differential solar rotation, actually remove projection effects due to the inclination of the equator (the solar B_0 angle). The field strength of each pixels, closest to the central meridian passage of the Sun, in a certain number of remapped magnetograms are then averaged to form a synoptic map representing the entire solar surface.

MDI full rotation synoptic magnetic maps, available in the public domain at http://soi.stanford.edu/magnetic/index6.html, have 3600 ×1080 pixels respectively in the longitude and sine latitude format. Both axes are linear in longitude (0.1 degree intervals) and sine latitude. The pixels near the poles, however, due to the inclination of the solar rotation axis relative to the ecliptic, have missing data. To fill these data gaps, a polar field correction is applied which is a multistep process. First, the best polar observations, above 62°, for the year is smoothed using a 7th order polynomial fit. In general, the best polar observations are available during September 8 (March 6) for the North (South) pole. Subsequently, the smoothed data for each map is interpolated using a temporal cubic spline technique to estimate the values above 75°.

Finally, this smoothed polar field above 75° is merged with full resolution observations between 62° and 75°. For more details about polar field correction for MDI data, one can see Sun *et al.* (2011). The polar field corrected MDI synoptic images are available in the public domain at `http://soi.stanford.edu/magnetic/index6.html`.

2.3 Solar Wind IPS Data

2.3.1 STEL

Solar wind observations have been carried out regularly at STEL, Nagoya University, Japan since the early 1970s (Kakinuma, Washimi and Kojima, 1973). The laboratory comprises of large antennas at the following locations, *viz.* Toyokawa, Fuji, and Sugadaira. Initially these telescopes worked at a frequency of 69 MHz, but was changed, after 1982 to work at a frequency of 327 MHz. The frequency of 327 MHz is a protected radio frequency and at this frequency one can carry out IPS observations in the distance range $0.2-0.9$ AU, spanning almost the entire inner heliosphere (Kojima *et al.*, 1982; Kojima and Kakinuma, 1990). One more antenna was commissioned at a fourth site called Kiso in 1993 forming a four–station dedicated IPS network that has been making systematic and reliable estimates for solar wind velocities (Asai *et al.*, 1995; Tokumaru, Kojima and Fujiki, 2012) from 1982 to the present. The location of the four antenna sites, showing the distances between them, are shown in Figure 2.6.

The antenna at each station is a large-aperture asymmetric parabolic cylinder reflector, similar to the Ooty Radio Telescope (Swarup *et al.*, 1971) in India. A picture of the antenna at the Kiso station is shown in Figure 2.7. The antennas at the other sites are identical. The antenna has a long axis of 100 m in east-west and short axis of 20 m in north-south. A low-noise phased array receiver installed on the antenna enables daily IPS observations of 30-

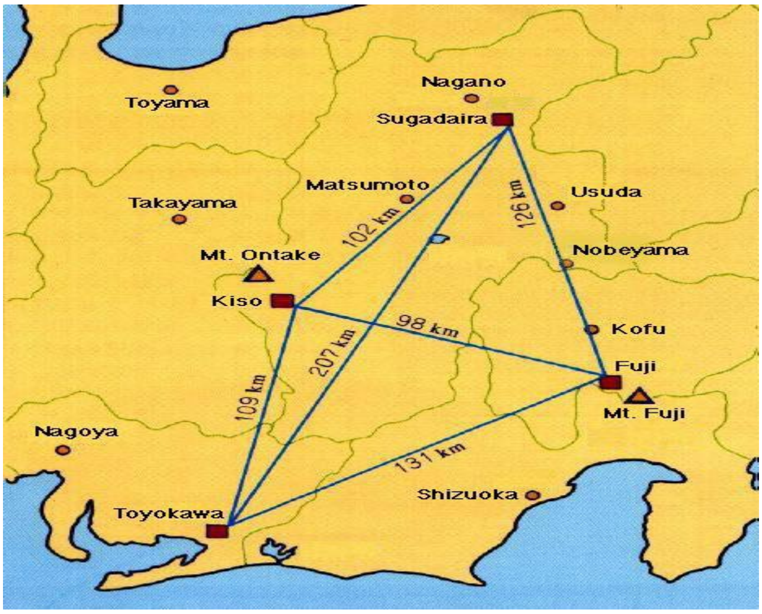

Figure 2.6: Shows locations of STEL IPS stations (Credit: STEL, Japan).

40 scintillating radio sources. Each station is fully automated, and connected to the host station at Toyokawa for data acquisition and system control via public telephone lines. The IPS observations are used to estimate solar wind speed using a cross-correlation analysis of the multi-station data, and also to measure the scintillation levels using a power spectral analysis of data at each station. For our study, we have only used the scintillation level data, available as daily values of scintillation index (m) from 1983 to 2009.

2.4 Solar Wind Interplanetary Data

2.4.1 OMNI

Data for solar wind parameters and geomagnetic indices used in this thesis were obtained from OMNI database, available in the public domain at `http://cdaweb.gsfc.nasa.gov/cgi-bin/eval2.cgi`. OMNI is a multi-source database, first created by National Space Science Data Center (NSSDC) in the mid-1970s and subsequent maintenance and evolution were taken over by the Space

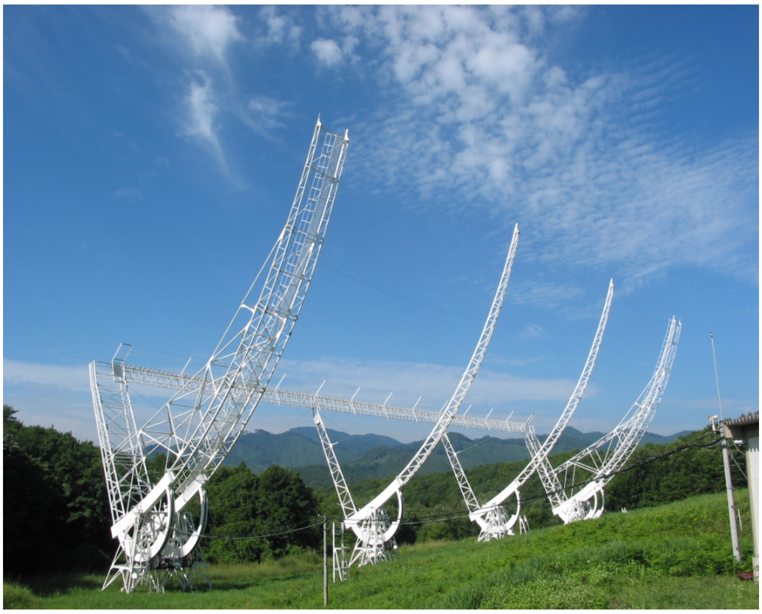

Figure 2.7: The 327 MHz radio telescope of Kiso Observatory (Credit: STEL, Japan).

Physics Data Facility at Goddard. OMNI data includes 1-min and 5-min resolution combined magnetic field and plasma data set, time-shifted to the nose of the Earth's bow shock. In this time-shift method, it is assumed that the values of solar wind variation, observed by a spacecraft at a given time and place, lie on a planar surface, known as “phase front”. Since the phase front is being convected outward with the solar wind, these observed values of solar wind variation will be same at a different place at the time when the phase front sweeps over that location. The OMNI database collects data from several spacecraft, *viz.* ACE, Wind, IMP 8, and Geotail.

The ACE spacecraft (Stone *et al.*, 1998) was launched on 25 August 1997, and carries a total of nine instruments, which has continued to provide magnetic field, plasma and energetic particle data since 5 February 1998. The ACE Level-2, 16 s IMF and 64 s plasma data, are available in the public domain at `http://www.srl.caltech.edu/ACE/ASC/level2/index.html`. Three of the ACE instruments, *viz.* the Magnetometer (MAG), the Electron, Proton and Alpha Monitor (EPAM), and the Solar wind Electron Proton Alpha Monitor

(SWEPAM), gather these data continuously (Stone *et al.*, 1998; Zwickl *et al.*, 1998).

The Wind spacecraft (Acuña *et al.*, 1995) was launched on 1 November 1994 and similar to ACE, it has also been continuously monitoring solar wind, magnetic fields, plasma, and energetic particle data since mid-2004. The Wind spacecraft data is available in the public domain at `http://wind.gsfc.nasa.gov/mfi/`. Two instruments, the Magnetic Field Experiment (MFI) and the Solar Wind Experiment (SWE), on board Wind, have been providing these magnetic field and plasma data.

The IMP 8 spacecraft was launched on 26 October 1973 into a low eccentricity Earth orbit. IMP 8 data has been acquired through the Massachusetts Institute of Technology (MIT) plasma instrument and three energetic particle detectors, and these data are available in the public domain at `http://wind.gsfc.nasa.gov/imp8/`.

The Geotail spacecraft was launched on 24 July 1992 to investigate the geomagnetic tail region of the magnetosphere and is a joint project between Institute of Space and Astronautical Science of Japan (ISAS) and the United States National Aeronautics and Space Administration (NASA). Geotail magnetic field and plasma data are available in the public domain at `http://www.stp.isas.jaxa.jp/geotail/`.

The geomagnetic activity indices, like, AE, AL, AU and SYM/D, SYS/H, ASYM/D, ASYS/H, already described in section 1.4.3, in the IP data have been obtained from the World Data Ceneter (WDC) for Geomagnetism at University of Kyoto. Details about the OMNI IP data and the time-shifting technique can be obtained from `http://omniweb.gsfc.nasa.gov/html/HROdocum.html`.

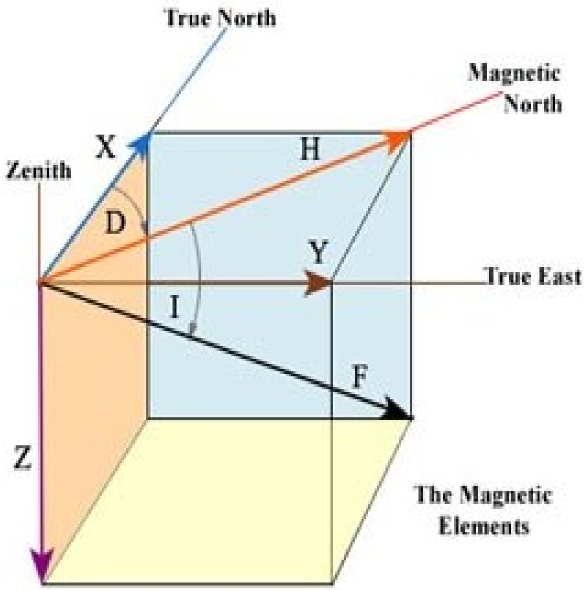

Figure 2.8: Shows the magnetic coordinate system with declination (D), Inclination (I), Horizontal intensity (H), Vertical intensity (Z), North-south intensity (X), East-west intensity (Y), and Total intensity (F) (Courtesy:IIG, Mumbai).

2.5 Ground-based Magnetogram Data

The strength and direction of the Earth's magnetic field have been continuously measured at ground-based magnetic observatories (Macmillan, 2007). These observatories are located at various locations worldwide and form a global network. However, in this thesis, we have used magnetic observations obtained from equatorial and low-latitude stations.

2.5.1 Magnetic Coordinates

The intensity of the Earth's magnetic field, a vector quantity having amplitude and direction, is denoted by F. The components of the Earth's magnetic field are shown in Figure 2.8. These are the horizontal intensity (H), the vertical intensity (Z), and the declination (D). The declination is the angle between the true north and magnetic north, while the inclination (I) is the angle between F, the total magnetic field intensity and the magnetic north. Magnetic observatories measure these components on a regular basis to study geomagnetic field variations. Besides these three components, the Earth's magnetic field is also expressed by vectors X, Y, and Z which represent respectively the geographic north, the geographic east, and the vertical.

2.5.2 Magnetogram

Geomagnetic field variations have been recorded, over the last few decades, in the form of magnetograms which are analogue recordings on sheets of photographic paper. However, magnetograms are now less common and magnetic field variations these days are measured using digital magnetometers (Reay *et al.*, 2011).

Several geographic locations in India have been used for measurements of ground magnetic field variations with magnetic observatories being established in Tirunelveli, Pondicherry, Alibag, Visakhapatnam, Nagpur, Rajkot, Jaipur, Silchar, Shilong, and Gulmarg. These observatories cover a wide range of latitudes extending from the dip equator up to the focus of the Solar-Quiet (Sq) current system. These currents generally flow in the E-region of the ionosphere. Although many of these observatories have been modernized and used Digital Fluxgate Magnetometers (DFM), normal analogue magnetograms are still in use and these magnetogram data have been used in the thesis for studying the sudden impulses in the Earth's geomagnetic field. In addition data from magnetic stations all over the world are collected and archived at the World Data Centres (WDC) for public access. These WDC centres are located at Edinburgh, Kyoto, Copenhagen, Mumbai, Moscow, Boulder, Sydney, and Beijing (Reay *et al.*, 2011). The geomagnetic field data at these centres include magnetograms, hourly digital values, one-minute digital values, and one-second digital values. Magnetograms from these data centres at low- and mid- latitudes are also used for geomagnetic field variation studies in this thesis.

2.6 Summary

The present chapter discusses instruments and observations from the ground-based and space-based observatories. Photospheric magnetic fields used in the thesis were derived from Carrington synoptic magnetic maps. These maps were compiled from data set of full-disk longitudinal magnetograms, accumulated from the Vacuum telescope and SOLIS facility of the ground-based NSO/KP observatory. The Vacuum telescope uses a 512 channel diode array magnetograph, for obtaining the full-disk magnetograms from 1975 to 1992, through the Fe I 8688 Å photospheric absorption line. A spectromagnetograph replaced this magnetograph after 1992 and collected full-disk images until 2003. A new synoptic program, at the SOLIS facility, was initiated at Kitt Peak after 2003 that used a vector spectormagnetograph for obtaining daily full-disk magnetograms. On the other hand, high-resolution full-disk magnetograms (15 maps per day with 96-min cadence) were simultaneously obtained through the MDI instrument on-board the SoHO spacecraft since 1996. The MDI images were taken in the Ni I 6768 Å spectral absorption line.

In addition to magnetic field measurements, the IPS data used were obtained from STEL, Japan. This is a multi-station IPS network comprising four large antennas and observations from each station were used to obtain the scintillation index by a power spectral analysis. The solar wind parameters used were obtained from 5-min resolution OMNI IP data at 1 AU. These IP data are magnetic field and plasma data from the spacecraft, like ACE, Wind, IMP 8, and Geotail. Ground-based magnetic field variation recorded as magnetogram, usually measures the H, D, and Z components of the Earth's magnetic field. These magnetograms used are obtained from magnetic observatories in India and from World Data Centres for geomagnetism.

Chapter 3

Solar Polar Fields During Solar Cycles 21, 22, and 23

3.1 Introduction

The Sun's magnetic field plays a key role in the evolution of solar activity by modulating heliospheric activity out to 1 AU (the distance between the Sun and the Earth), and beyond and driving space weather in near-Earth space environment. Measurements of the Sun's magnetic fields using ground-based magnetograph dates back to Babcock and Babcock (1955). The magnetograph, generally, measures the line-of-sight (LOS) magnetic fields at the photospheric level. Babcock, using his magnetograph observations, proposed that the Sun's magnetic field was mainly composed of a general magnetic field, bipolar magnetic regions (BMRs), and unipolar magnetic regions (UMRs). The BMRs like sunspots vary in steps with the solar cycle, and follow Hale's polarity law and Joy's law of magnetic polarity. Babcock (1959), using observations from 1953 to 1957, proposed that the General Magnetic Fields, reported by Babcock and Babcock (1955), reverse their polarity around the maximum of each solar cycle. While magnetic fields of the BMRs are very high, magnetic fields of the general magnetic fields are very weak and of the order of 10 G only. These weak and diffuse fields which reverses their polarity around the maximum of each solar cycle are referred to as "polar fields".

Following the discovery of polar field reversal (Babcock, 1959), Babcock (1961) proposed a dynamo model, using his magnetographic observations, to explain the observational findings, *viz.* Polar field reversal, Spörer's law, Hale's polarity law, and the decay and disappearance of BMRs during a solar magnetic activity cycle. This model was further modified by Leighton (1964) to develop a kinematic dynamo model for the expansion and transport of photospheric magnetic flux. As a result, the evolution of large-scale photospheric magnetic fields during any given solar cycle can be considered to control by three basic processes which operated through a solar dynamo located deep inside the Sun. These three processes are – (1) the generation of the toroidal fields by shearing of pre-existing poloidal fields (the Ω effect), (2) the subsequent regeneration of poloidal fields (of opposite polarities to that present earlier) by the twisting of toroidal fields (Parker's α effect) (Parker, 1955a,b; Babcock, 1961; Leighton, 1964; Steenbeck and Krause, 1969), and (3) transportation of poloidal fields from the equator to the poles on the solar surface (Wang, Nash and Sheeley, 1989), and back again to the equator at the base of the convection zone (Choudhuri, Schussler and Dikpati, 1995; Dikpati and Charbonneau, 1999) by a process called "meridional circulation".

Although it is hard to measure the meridional flow speed using observations, a few successful attempts have been made to measure meridional flows which transport flux to the solar polar regions with a poleward bulk flow speed of 10 – 20 m s^{-1} (Duvall, 1979; Hathaway, 1996). Such measurements have shown that close to sunspot minimum the flow speed was $\sim$ 20 m s^{-1}. Such flows produce giant polar surges, which in turn create large fluctuations in polar fields (Wang, Nash and Sheeley, 1989). Periodic variations in meridional flow speed were recently reported by Hathaway and Rightmire (2010) through a cross-correlation of data obtained using solar magnetograms. These authors reported that the meridional flow speed varied with solar cycle, being stronger at the sunspot minimum and weaker at the sunspot maximum. It is believed that polar fields are confined mostly to higher latitudes, ranging from $\pm 55^{\circ}$ all the way to the poles and are generated by the Babcock-Leighton mechanism, in which the BMRs decay and the remnant magnetic flux move polewards via meridional circulation. The Babcock-Leighton model was further modified by (Wang and Sheeley, 1991; Wang, Sheeley and Nash, 1991) to include the distribution of, and to correlate it with that of the observational poleward meridional flow and show that meridional flow was a primary agent for photospheric polar flux distribution. It is noteworthy that the temporal behavior of photospheric polar fields also follows the solar cycle, with the polar fields peaking during solar minima and being at their lowest during solar maxima. Furthermore, many investigations have been carried out to explore the relation between evolution of large-scale magnetic fields and their association with polar-field structures (Fox, McIntosh and Wilson, 1998; Benevolenskaya, Kosovichev and Scherrer, 2001, 2002; Gopalswamy *et al.*, 2003b).

The sunspot minimum at the end of Cycle 23 has been characterized with roughly 71%–73% of the days in 2008 and 2009 showing a complete absence of sunspots, and also showing continuously low magnetic activity. In addition, it was also observed that the areas covered by polar coronal holes were $\sim$ 15-20% smaller than those observed during the previous cycle minimum (Kirk *et al.*, 2009; Wang, Robbrecht and Sheeley, 2009). It will be shown later in this thesis that such an extended period of minimum has had its effect not only on solar activity, but was also in the heliosphere, thereby leaving its impact on the Sun, the inner-heliosphere and the near-earth environment. In addition, a rich variety of ground-based and satellite observations have revealed several other peculiarities in the last solar cycle, *viz*. Cycle 23.

Unlike other odd numbered solar cycles, Cycle 23 showed a second maximum during the declining phase and a very slowly rising phase approaching the maximum. Additionally, in Cycle 23, a significant asymmetry in polar reversal of the Northern and Southern hemispheres has been seen. This rather peculiar and unusual behavior in Cycle 23 had been explained by Dikpati *et al.* (2004) using a calibrated flux transport dynamo model. A number of space-based observatories and improved ground-based telescopes in past 35–37 years have provided a unique opportunity to explore the Sun's magnetic fields during the past three solar cycles as they are crucial for understanding the evolution of magnetic activity and space weather.

In this chapter, we have made use of the extensive and systematically obtained data set available from the ground-based National Solar Observatory, Kitt Peak, USA (NSO/KP) and from the Michelson Doppler Interferometer instrument on board the Solar and Heliospheric Observatory (SoHO/MDI). While we have used the ground-based data from 1975 upto 2009, spanning the last three solar cycles, *viz.* Cycle 21, 22, 23, the space-based data used covers the period from 1996 upto 2009. Both these ground- and space-based measurements are available as standard Carrington synoptic magnetograms, and are appropriately processed to extract the magnetic fields over the solar photosphere for each Carrington rotation. This chapter discusses in detail the temporal variability of these photospheric magnetic fields at low, mid and high latitudes. More specifically, the behavior of solar polar fields, in the latitude belt of $\pm78°$ to $\pm90°$, has been investigated using both NSO/KP and (SoHO/MDI) magnetograms.

It is believed that polar fields carry forward the memory of the quiet-sun from the previous cycle into the next cycle. This in turn influences the evolution of solar magnetic fields and determines the amplitude of the next cycle. This Chapter also discusses the role of solar polar fields in deciding the strength of the maximum in the following cycle.

3.2 Observations and Analysis

We have employed low-resolution Carrington synoptic magnetograms from the ground-based facilities at the NSO/KP, and high-resolution space-based magnetograms from the SoHO/MDI. Usually, a synoptic magnetogram is compiled from images obtained over a Carrington rotation (CR) period (27.2753 days). The data set include synoptic maps from the NSO/KP, covering CR1625 – CR2080, and from the SoHO/MDI, covering CR1911 to CR2080.

3.2.1 NSO/KP Data

Three data set of NSO/Kitt Peak synoptic magnetograms, available as standard FITS format files, are employed for this study. The first two sets include synoptic maps from the database (ftp://nsokp.nso.edu/kpvt/synoptic/mag/) of NSO at Kitt Peak starting from CR 1625 through CR 2006 corresponding to years 1975 to 2003. Between these two, the first data set comprises the 512-channel Diode array magnetographs from the NSO/Kitt Peak vacuum telescope (NSO/KPVT) from 1974 until 1992 (Livingston *et al.*, 1976b), and the second data set comprises the National Aeronautics and Space Administration (NASA) NSO spectromagneotgraph (SPMG) from the NSO/KPVT from 1992 until 2003 (Jones *et al.*, 1992). The third data set includes maps from the magnetic database (ftp://solis.nso.edu/synoptic/level3/vsm/merged/carr-rot/) from the Vector Spectro Magnetograph (VSM) of the NSO Synoptic Optical Long-term Investigations of the Sun (SOLIS) for CR2007 to CR2080 covering period from 2003 until 2009 (Keller, Harvey and Giampapa, 2003). In all, the three data set span for a period from 1975 to 2009, covering Solar Cycles 21, 22, and 23. A few data gaps were found in CR1640 – CR1644, CR1854, CR1890,CR2015, CR2016, CR2040 and CR2041 amounting to only 2.5% of the entire data set.

Each synoptic map is in the form of a 180×360 array corresponding to sine of latitude and Carrington longitude. The resolution of the synoptic maps is $1°$ in both longitude ($1°$ to $360°$) and latitude ($-90°$ to $90°$). The magnetic flux density in each unit pixel area is known as “field strength”, and in rest of the thesis, this will be used for flux density per unit area. A typical Carrington synoptic map is produced from full-disk magnetograms spanning an entire Carrington rotation period. Each individual magnetogram is first remapped into latitude and longitude coordinates and then added together to produce the final synoptic map for each CR. All synoptic magnetogram maps, represented as an $i \times j$ data array with i and j representing the latitude and longitude respectively, for any given CR number n, contain magnetic flux density $[\phi_{i,j,n}]$, in units of Gauss averaged over equal areas of the Sun. The actual flux units are then obtained by multiplying by the appropriate area.

Since we are interested in the variation of photospheric magnetic fields with latitude, data is processed by taking longitudinal averages for each latitude bin of 1° by converting the data to a one dimensional array of 1 × 180. Any latitude element i, for a given CR, $[n]$ will contain the averaged magnetic field represented by Equation (3.1).

$$\phi_{\mathsf{i,n}} = \frac{\sum_{\mathsf{j=1}}^{360} \phi_{\mathsf{i,j,n}}}{360} \tag{3.1}$$

Now, the averaged magnetic field for a range of latitudes in any CR is obtained by averaging $\phi_{i,n}$ as shown by Equation (3.2).

$$\phi_{\mathsf{n}} = \frac{\sum_{\mathsf{i=k}}^{\mathsf{p}} \phi_{\mathsf{i,n}}}{\mathsf{p} - \mathsf{k}} \tag{3.2}$$

Where k and p are the row numbers corresponding to a latitude bin. Using the above procedure, we have obtained average magnetic fields in each solar hemisphere for three different latitude bins between ranges:

- 0° and 45° – representing the equatorial or toroidal fields;
- 45° and 78° – representing the mid-latitude fields;
- and 78° and 90° – representing polar fields in each hemisphere.

The basic motive behind such a latitudinal division of the data is to enable the investigation of the temporal variation of magnetic fields over the whole range of latitudes. Again, it is to be borne in mind that photospheric magnetic fields constitute or represent radial poloidal magnetic fields, B_r, so the use of the term, *viz.* "toroidal fields" and "polar fields" to describe low and high-latitude fields are only for our convenience in denoting a range of low and high latitude fields. It may be noted that in general, in the solar community, the fields above a latitude range of $\pm 55°$ are commonly referred to as polar fields.

Due to the tilt of the solar rotation axis with respect to the ecliptic plane by 7.25°, the fields $> 75°$ cannot be measured accurately. This is because fields near the poles will either be observed with a large viewing angle or not observed at all for about six months in a year. Thus, the polar field measurements at latitudes $> 75°$ need to be corrected and we have used a cubic spline interpolation to the annual averages of the observed fields to correct for the inaccurately determined or missing polar fields. The cubic spline interpolation is carried out when the solar axis tilt angle (B_0) is $> 5°$ in the Northern hemisphere and is $< 5°$ in the Southern hemisphere.

3.2.2 SoHO/MDI Data

In addition to the low-resolution NSO/KP magnetograms, we have used synoptic magnetograms, from the MDI (Scherrer *et al.*, 1995) instrument on board SoHO (Domingo, Fleck and Poland, 1995), complied from high-cadence (96-mins, 15 maps per day), and high-resolution (1024 × 1024 pixels) LOS full-disk magnetograms acquired from 1996 onwards. These full-disk magnetograms are generated using Ni I 676.8 nm spectral absorption lines in the solar atmosphere. Like, NSO/KP synoptic images, each MDI synoptic image is constructed over a period of one CR, and our MDI magnetic data set cover images from CR1911 to CR2080 corresponding to years 1996 to 2009 with few data gaps for CR1938 – CR 1942, CR1945, and CR2073. In a manner similar to ground-based observations, the solar poles are only partially observable at small values of the angle B_0. We have, therefore, used polar field corrected MDI synoptic images available at http://soi.stanford.edu/magnetic/index6.html where the fields above 75° have been corrected using a cubic spline. A detailed description of the application of such polar field corrections to MDI synoptic images had been given in Sun *et al.* (2011).

Each MDI synoptic magnetogram represents a two dimensional array in longitude and latitude respectively, having 3600 × 1080 pixels with a resolution of 1″ per pixel in both longitude and latitude. Since MDI measurements are considered to be more reliable, as they are more frequent and stable as compared to Kitt-Peak observations, we have compared the two data sets for the period after 1996 to check if the results agree with each other. Also, data gaps when present, for example from CR1938 to CR1941, were dealt with by replacing them with interpolated values. Finally, the resolution of the MDI data was degraded (by averaging) to the resolution of the NSO/KP data so as to be able to compare the results. It may be noted that for the MDI data, only the latitude bin between 78° and 90° was considered.

3.3 Results

3.3.1 Magnetic Field Behavior

Figure 3.1 shows the measurements of the magnetic field in each solar hemisphere as a function of time in the two latitude ranges $0° - 45°$ and $45° - 78°$. While the upper two panels of Figure 3.1 show the absolute value (unsigned) of the magnetic field in the latitude range $0° - 45°$ for the Northern and Southern hemisphere respectively, the lower two panels show the absolute value of the magnetic field in the latitude range $45° - 78°$ for the Northern and Southern hemisphere respectively. The filled dots represent the actual measurements derived from the NSO/KP data base, while the solid line is a smoothed curve representing the data. The vertically oriented dashed parallel lines demarcate Cycles 21, 22, and 23. It can be seen from Figure 3.1 (upper two panels) that there is a strong solar cycle modulation present in the latitude range $0° - \pm 45°$

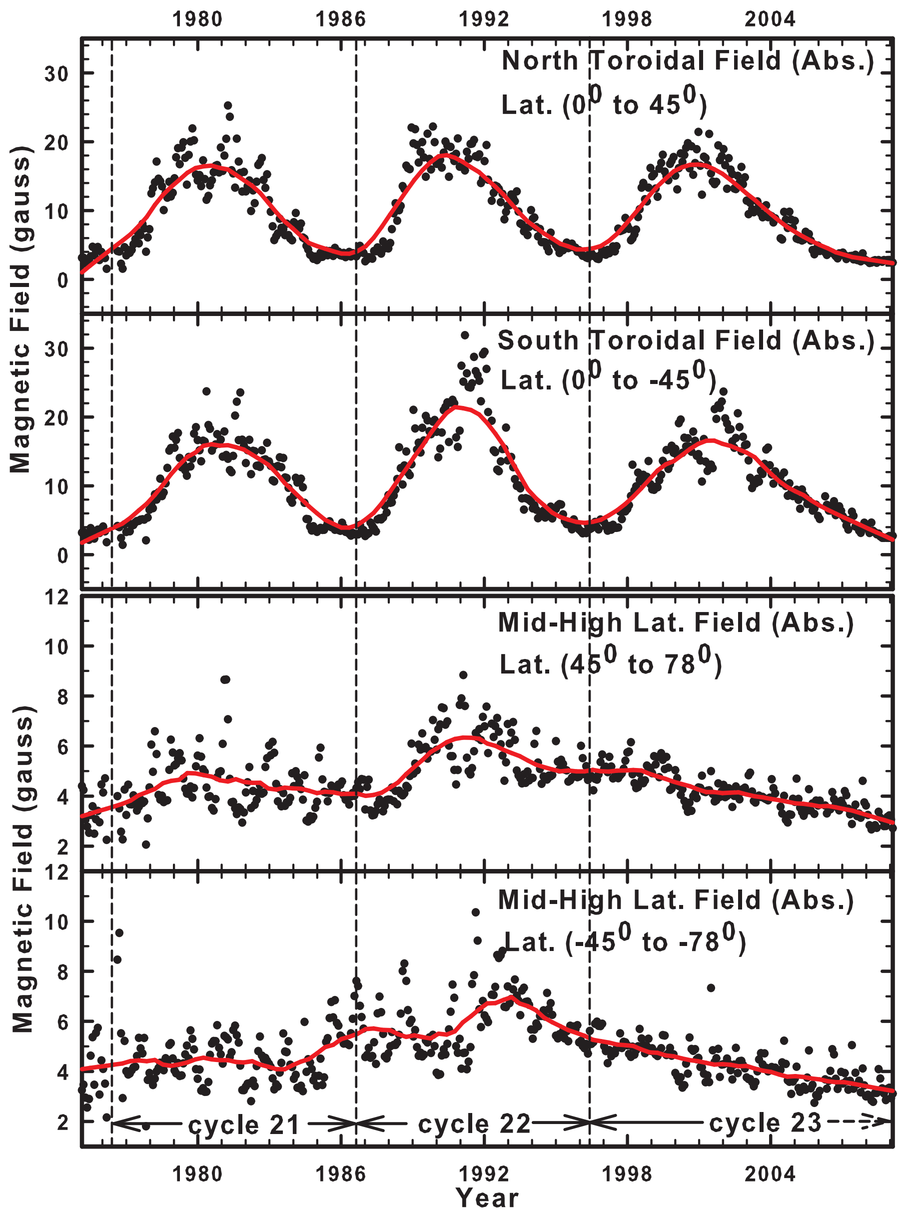

Figure 3.1: The four panels, in pairs starting from the top, show the variations in the magnetic field in the North and South solar hemisphere respectively, as a function of years for the Solar Cycles 21 – 23. The absolute value of the magnetic field in the latitude range $0° - \pm 45°$ is shown in the first pair of panels while the second pair of panels show the absolute value of magnetic field in the latitude range $45° - 78°$. The filled dots represent the actual measurements while the solid line is a smoothed curve. The vertically oriented dashed parallel lines demarcate Cycles 21, 22 and 23 respectively.

while the solar cycle modulation is much weaker and barely discernable in the latitude range $\pm 45° - \pm 78°$ for Cycles 21 and 22 while it is not seen for Cycle 23. Additionally, mid- to high-latitude fields show a steady decline starting from $\sim$1995 − 1996. This steady declining trend is seen to continue all the way to the end of the data set in 2009.

Figure 3.2 shows the actual (signed) measurements of magnetic field, in each solar hemisphere, as a function of time in years in the latitude range $78° - 90°$. While the upper panel of Figure 3.2 shows the magnetic field for the Northern hemisphere, the lower panel shows the value of the magnetic field for the Southern hemisphere. The filled dots, with 1 σ error bars, represent the measurements derived from the NSO/KP data, while the thick, solid, blue line is a smoothed curve. Points where data gaps were filled by interpolation are shown by red open circles. A comparison of the polar field during Cycles 22 and 23 from Figure 3.2 shows that the longitude-averaged polar magnetic field between $\pm 78° - \pm 90°$ during the current extended minimum leading up to the current Cycle 24 is weaker than the corresponding minimum period in Cycles 21 and 22. Also, a comparison of the fields in the two hemispheres in Cycle 23 shows that the South polar field is weaker than North polar field. In a detailed analysis of sunspot data and longitude-averaged photospheric magnetic flux (Dikpati *et al.*, 2004) has also pointed out several peculiarities during Cycle 23 such as the slow buildup of the polar field after the occurrence of the polar-field reversal, the asymmetry in polar reversal for the North and South, and the steady behaviour of the North polar field in comparison to South polar field from the late declining phase of Cycle 22 to early rising phase of Cycle 23. All of these features can also be clearly seen in Figure 3.2 for the period of Cycle 23. The temporal polar field variation in Fig 3.2 approximates the dipolar fields of the Sun, which alter polarity in each cycle at or around solar maximum. It is obvious from Figure 3.2 that the North and South polar fields reverse their polarity around solar maximum as stated in the epoch-making paper by Babcock (1959). However, the polar field reversals in the Northern and Southern hemispheres do not happen at the same time. The reversal of the Southern field precedes the Northern field in the Cycle 21 and 22, while the reversal of the Southern field lags behind the reversal of the Northern field in the Cycle 23.

The two panels of Figure 3.3 show the variation in the absolute value of the polar magnetic field in the latitude range $78° - 90°$ for the North and South solar hemisphere as a function of years for Solar Cycles $21-23$. Measurements from NSO/KP data are shown by filled dots while the thick, blue, solid line is a smoothed curve. MDI data for Cycle 23 is shown by red crosses to enable comparison between NSO/KP and MDI data. Marked by open black circles are points where MDI data gaps were filled in by interpolation. It may be noted that the resolution of the MDI data was reduced, by averaging, to match that of the NSO/KP data for comparison. A striking feature in Figure 3.3 is a steep and continuous drop of the average polar field (in both NSO and MDI data) from the late declining phase of Cycle 22 to the maximum of Cycle 23 in both the hemispheres. A slow continuous drop of ≈13 G from 1994 to 2001 is seen in the northern hemisphere while a sharp continuous drop of ≈9 G from 1995 to 2002 is seen in the Southern hemisphere. Cycles 21 and 22, however, showed no such drop. The recent and extended minimum at the end of Cycle 23 is also interesting in that the average polar-field behaviour showed no variation and remained steady from 2004 onwards in both hemispheres as seen from both NSO/KP and MDI data. The MDI data however, is systematically lower than the NSO/KP values throughout Cycle 23.

3.3.2 Correlation With Meridional Flows

As mentioned earlier (Section 3.1), it is well known that meridional circulation is the primary poloidal flux-transport agent in the Sun both on the surface and below. Unlike, other major surface flows, *viz.* granulation (~ 3000 m s^{-1}), super granulation (~ 300 m s^{-1}), and differential rotation (~ 170 m s^{-1}), these

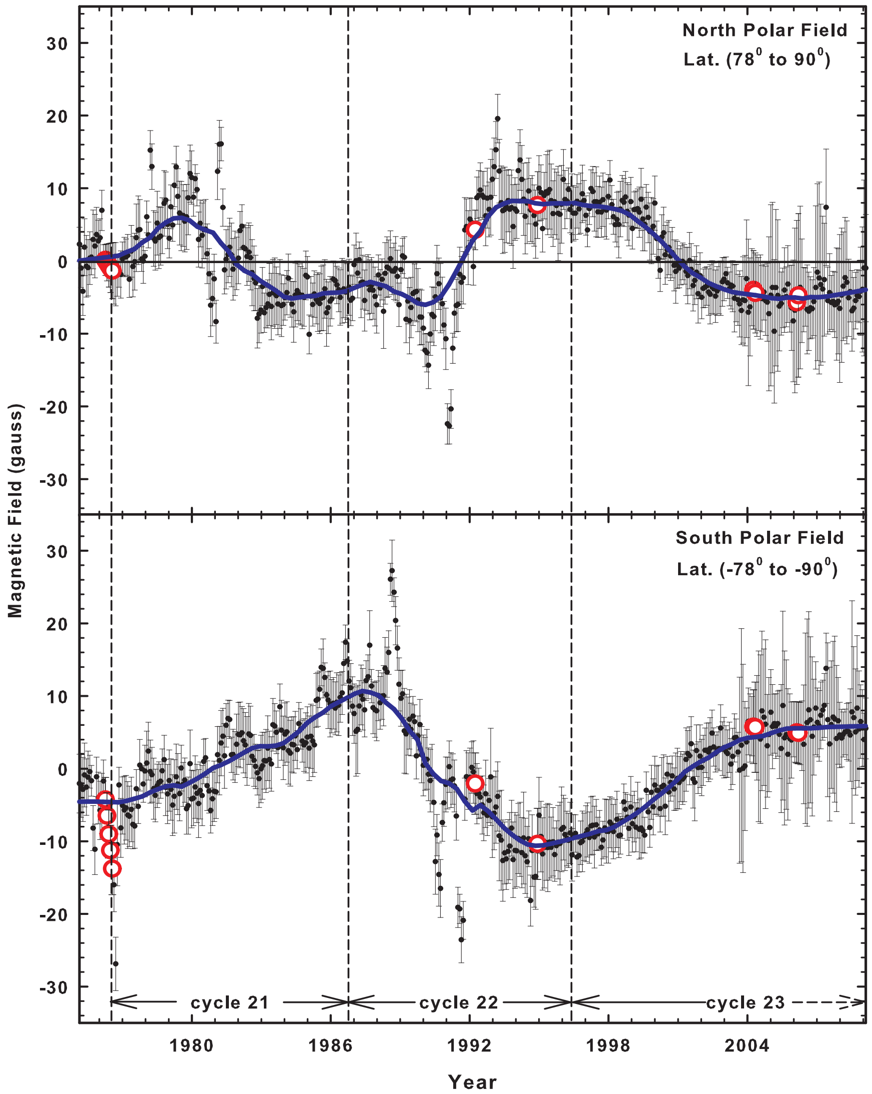

Figure 3.2: Shows the variations in the magnetic field in the North (upper panel) and South solar hemisphere (lower panel) as a function of years for the Solar Cycles 21 − 23. The actual (signed) magnetic field in the latitude range $78° - 90°$ is shown in the two panels. The filled dots, with 1σ error bars represent the actual measurements while the blue solid line is a smoothed curve. The vertically oriented dashed parallel lines demarcate Cycles 21, 22 and 23 respectively. Points where data gaps were filled by interpolation are shown by red open circles.

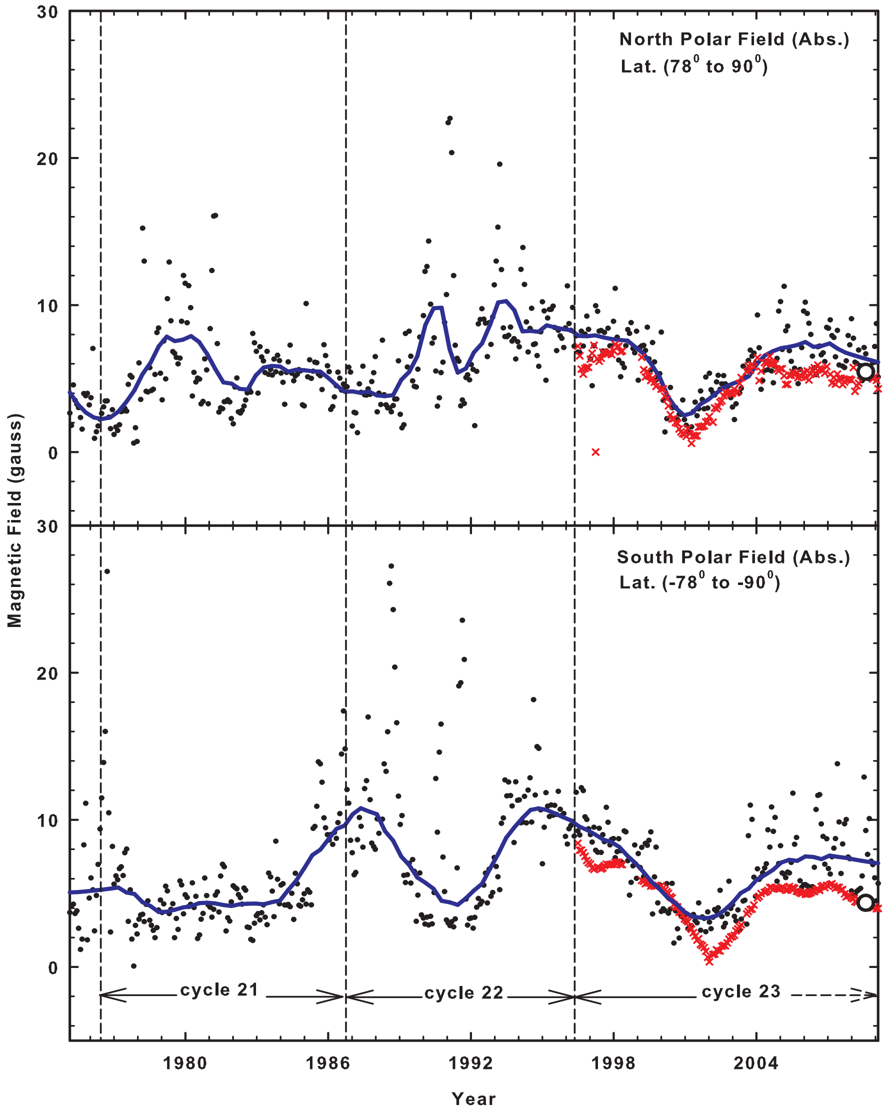

Figure 3.3: Shows the variation in the absolute value of the polar magnetic field in the latitude range $78° - 90°$ for the North and South solar hemisphere as a function of years for the Solar Cycles $21 - 23$. The actual measurements derived from the NSO/KP data base is shown by filled dots while the blue solid line is a smoothed curve. MDI data for Cycle 23 (for comparison) is shown by red crosses. The vertically oriented dashed parallel lines demarcate Cycles 21, 22 and 23 respectively. Points where MDI data gaps were filled by interpolation are shown by green open circles.

axis-symmetric meridional flows are generally weak ($\sim 10-20$ m s^{-1}) making their measurements difficult. However, a few techniques have been successful in measuring the meridional flow speed. These techniques include magnetic feature tracking, Doppler measurements, and helioseismology using ring-diagram or time-distance analysis. Employing the magnetic feature tracking method to the 628 NSO/KP magnetograms from 1975 to 1991, Komm, Howard and Harvey (1993b) measured the meridional flow variation and reported that the latitudinal profile for meridional flow was flatter at sunspot maximum than at sunspot minimum. Further, extending this work, Komm, Howard and Harvey (1993a) estimated a poleward meridional flow of nearly 13 m s^{-1}, and proposed that the flow was slower at sunspot maximum than at sunspot minimum. Also, Haber *et al.* (2002) made an attempt to measure meridional flows, using a helioseismic technique that employed ring diagram analysis to high-resolution MDI data from 1996 till 2001, and reported the large-scale meridional flows in the upper convection zone.

A recent and detailed study using MDI images of the LOS magnetic fields (Hathaway and Rightmire, 2010) has reported measurements of the surface meridional flow speed in the latitude range $\pm 75°$ in Cycle 23, covering the period 1996 – 2009. Employing a magnetic feature tracking method, and carefully correlating the latitudinal displacement of small magnetic elements in MDI magnetogram pairs, separated by 8 hours, Hathaway and Rightmire (2010) obtained the meridional flow profile by repeating these calculations for latitude positions between latitudes of $\pm 75°$ using 60,000 image pairs. These authors determined a meridional-flow speed of 11.5 m s^{-1} at minimum of Cycle 23 in 1996 – 1997 which then dropped to 8.5 m s^{-1} at the maximum in 2000 – 2001. It must be noted here that this drop in the flow speed coincides with the steep drop in the absolute value of the magnetic field that is seen in both the NSO/KP and MDI data (Figure 3.3) (Janardhan, Bisoi and Gosain, 2010). In fact, the MDI data in the Southern hemisphere continues to drop until 2002 after which it rises again. Between 2001 and 2004, the measured

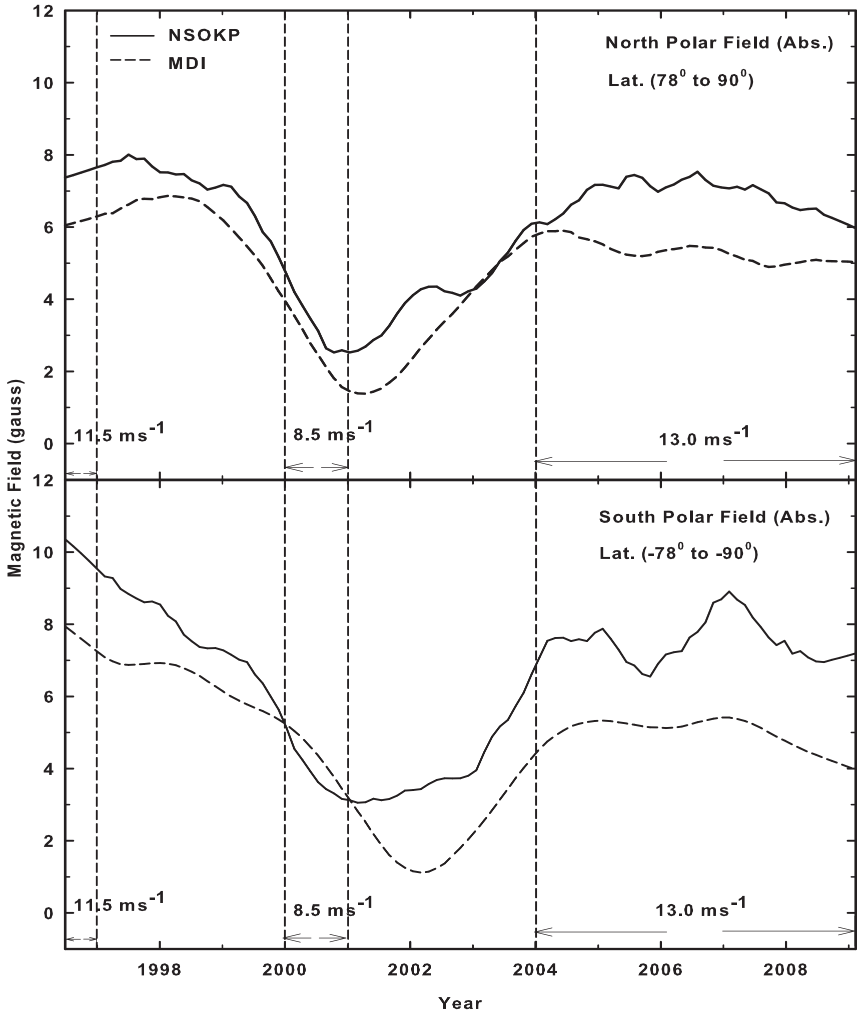

Figure 3.4: Shows a comparison between NSO/KP data and MDI data in Cycle 23 for the two solar hemispheres. The Northern hemisphere is shown in the upper panel while the Southern hemisphere is shown in the lower panel. The meridional flow speeds as reported by Hathaway and Rightmire (2010) have been indicated by vertically oriented dashed parallel lines.

meridional-flow speed by Hathaway and Rightmire (2010) again increased to 13.0 m s^{-1} and remained constant at this value thereafter. Again, from Figure 3.3 we can see a corresponding steep increase in the absolute value of the polar field between 2001 and 2004. After this, the absolute value of the magnetic field remains constant in both hemispheres until 2009. From Figure 3.3 it is clear that the polar field strength since 2004, as seen by both NSO/KP and MDI has remained constant.

Figure 3.4 shows a comparison between the averaged absolute magnetic fields determined from NSO/KP synoptic magnetogram maps and MDI synoptic magnetogram maps for the Northern (upper panel) and Southern (lower panel) hemispheres for Solar Cycle 23. While the solid line is a smoothed curve representing the NSO/KP data, the dashed line is a smoothed curve representing the MDI data. The meridional flow speeds, as reported by Hathaway and Rightmire (2010), are indicated at the bottom of each panel and demarcated by vertically oriented dashed parallel lines. The recent and extended minimum at the end of Cycle 23 is also interesting in that the average polar field behaviour showed no variation and remained steady from 2004 onwards in both hemispheres as seen from Figure 3.4. We could see also a systematically higher polar field strength for the NSO/KP than the MDI measurements, due possibly, because of the two sets of measurements being obtained from different instruments. It may be noted again that the MDI high-resolution data (3600×1080 pixels) was averaged and reduced to that of the NSO/KP data (360×180 pixels) for comparison. In spite of this degradation in MDI data, we still see a good correlation between the two data sets. Our detailed analysis of solar magnetic fields (Janardhan, Bisoi and Gosain, 2010) thus correlates well with the manner in which meridional flows varied in the Cycle 23

3.4 Prediction for Upcoming Cycle 24

Prediction of future solar magnetic activity, primarily the strength of the upcoming cycles, has become an important focus of research in solar-terrestrial physics. As a result, over the course of time, various methods have been proposed, using both observations and models, to address and understand the various issues and factors involved in making such predictions. It is known that the evolution of solar magnetic fields and the generation of polar fields are governed by what is known as Babcock-Leighton mechanism, wherein the advection of surplus amount of trailing polarity flux from the decayed active regions, cancels the old polar cap fields and builds up the fresh polar fields (Babcock, 1961; Leighton, 1964, 1969). Further, these polar fields in the declining phase of any given solar cycle act as seed fields for the generation of toroidal fields in the next cycle. The Sun's memory or magnetic persistence of the polar-field strength at minimum of the previous cycle have been used as a precursor or seed fields in the next cycle for models that predict the strength of the future solar cycle. Some authors have used this method to try and predict the strength of upcoming cycles through magnetic persistence or Sun's memory (Schatten *et al.*, 1978; Layden *et al.*, 1991; Schatten and Sofia, 1996; Sofia, Fox and Schatten, 1998). In a more recent study, Svalgaard, Cliver and Kamide (2005) made an attempt to predict the upcoming Cycle 24, using polar field measurements from the Mount Wilson Observatory (MWO) and Wilcox Solar Observatory (WSO) of the last four solar cycles. The author proposed that Cycle 24 would be the weakest cycle in the past 100 years with a peak monthly smoothed sunspot number (SSN) of $\sim 75 \pm 8$ at the maximum of Cycle 24.

In contrast to the above predictions based on observations, the model-based predictions that invoked magnetic persistence or the Sun's memory of polar fields from earlier cycles, for the strength or amplitude of Cycle 24 proposed two very divergent views. One forecasted the amplitude of the new Cycle 24 to be about 50% stronger than Cycle 23, and the other forecasted the amplitude to be about 35% weaker than Cycle 23. The first prediction was based on a highly "advection dominated" flux-transport dynamo model that employed sunspot area as a proxy for poloidal fields, and proposed that the poloidal fields from cycle n-3, n-2, and n-1 contribute to the toroidal fields of any given cycle n (Dikpati, de Toma and Gilman, 2006). The second prediction, on the other hand, invoked a highly "diffusion dominated" flux-transport dynamo model, which employed the dipole moment of the previous three cycles as a proxy for poloidal fields, and claimed that only the poloidal fields from cycle n-1 contributed measurably to the toroidal fields for cycle n (Choudhuri, Chatterjee and Jiang, 2007).

From our polar fields measurements (Janardhan, Bisoi and Gosain, 2010), we have seen much weaker polar fields in the Cycle 23 compared to the previous two Cycles 21 and 22. Since the Sun's memory of previous cycle polar fields influence the strength of the new toroidal fields, we believe that these weaker polar fields during Cycle 23 would lead to a weak Cycle 24, which supports the prediction by Choudhuri, Chatterjee and Jiang (2007). Also, it was postulated that magnetic persistence is itself governed by meridional flow speed (Hathaway, 1996; Haber *et al.*, 2002; Basu and Antia, 2003) with slower meridional flows resulting in longer memory. This would imply that a faster meridional flows seen during the extended minimum of the Cycle 23 gave rise a shorter memory which, in turn, would make Solar Cycle 24 a weaker cycle than Cycle 23.

3.5 Discussions

Although a great deal of progress has been made in our understanding of meridional flows and their role in determining the strength of the polar field and the amplitude of the following cycles, there seems to be a basic disagreement between flux-transport-dynamo models (Dikpati, de Toma and Gilman, 2006; Choudhuri, Chatterjee and Jiang, 2007) and surface-flux-transport models (DeVore, Sheeley and Boris, 1984; van Ballegooijen, Priest and Joy, 1998; Wang, Lean and Sheeley, 2005; Schrijver, 2008). Fast meridional flows, in the flux-transport-dynamo models, produce stronger polar fields and a short cycle, as compared to the observations of surface-flux-transport model which give rise to weak polar fields and a long solar cycle. While the dynamo models have fields of one polarity centred on the sunspot latitudes, surface-flux-transport models have bands of opposite magnetic polarity on either side of the sunspot latitudes. The cause of the difference in these two models arises mainly due to the above difference in the latitudinal distribution of magnetic polarities, and has been explained by Hathaway and Rightmire (2010) and references therein. In the flux-transport-dynamo models, one polarity is found on both sides of sunspot latitudes, so stronger meridional flows transport more of these opposite polarity fluxes to poles in short period of time producing stronger polar fields at sunspot minimum. While in the surface-flux-transport model, fast meridional flows inhibit opposite polarities from canceling each other across the Equator. Thus, elements of both polarities will be carried to the poles and a longer time would be required to reverse the old polar fields. This would in turn result in weaker polar fields of the new or reversed polarity. Such a mechanism would support the observations of faster meridional flows in Cycle 23 by Hathaway and Rightmire (2010). In addition, this mechanism would also support our observations of having a weaker polar fields at solar maximum.

We have seen from our data, a large and unusual drop in the absolute value of the polar fields during Cycle 23 compared to previous cycles (Section 3.3.1) and also its association with similar behaviour in meridional flow speed (Section 3.3.2). In addition, Hathaway and Rightmire (2010) have shown that the meridional flow generally shows a decrease from minimum to maximum as has also been reported for earlier solar cycles (Komm, Howard and Harvey, 1993a), although with greater uncertainty and poorer temporal resolution than for Cycle 23, where high-resolution MDI data are available. The minimum leading up to the start of Cycle 24 has been very deep and prolonged and we have seen that the corresponding polar fields have been at their lowest compared to Cycles 21 and 22. We believe that the "memory" of this very weak polar field in Cycle 23 is the cause of the extended solar minimum we have witnessed.

We have seen above that the absolute value of the polar magnetic field in the latitude range $78° - 90°$ virtually mirrors the change in the meridional flow speeds in Cycle 23, with meridional flow speeds dropping when the absolute value of the field drops. Unlike Cycles 21 and 22, the absolute values of the polar magnetic fields in Cycle 23 showed similar trends in both hemispheres. Since high-resolution MDI data are available only from 1996, it is not possible to compute meridional flow speeds during Cycles 21 and 22. However, it may be noted that in both Cycles 21 and 23, the behaviour of the absolute value of the polar fields is different in each hemisphere. If we assume that the correlation between the absolute value of the polar fields and the meridional flow velocities holds good for all solar cycles, then this would imply that the field reversals occurred at different times in the two hemispheres in Cycles 21, 22, and 23.

3.6 Summary and Conclusions

In this chapter, we have studied the temporal behaviors of solar magnetic fields during the last three solar cycles, *viz.* Cycles 21, 22 and 23 with an emphasis on polar fields variations during the unusually deep and extended solar minimum at the end of Solar Cycle 23. The main findings of this chapter have been enumerated below.

1. While temporal variations of unsigned toroidal fields, in the latitude range, $0° - 45°$, show a strong modulation (as expected) of the sunspot activity cycle, the temporal changes in unsigned mid-high latitude fields, in the latitude range, $45° - 78°$, show a weak modulation (as expected)

of sunspot activity cycles. In addition, we find a systematically and steady decline in mid-high latitude fields in both the hemispheres from $\sim$1995-1996 till the end of 2009.

2. The temporal changes in signed (without absolute value) polar fields, in the latitude range, $78° - 90°$, for the last three solar cycles $21 - 23$, showed an asymmetry in polar field reversal for the two solar hemispheres. In Cycle 21 and 22, the reversal of polar field in the the South precedes the North, while in Cycle 23, the reversal of polar field in the South lags the North. In addition, it has been observed that the polar field strength in Cycle 23 is weaker compared to Cycles 21 and 22 and an inspection of fields in the Cycle 23, clearly indicates a slow buildup of fields (after reversal) in the North while the buildup of fields in the South is faster.

3. The unsigned (the absolute value) polar fields, in the latitude range, $78° - 90°$, has shown a steady decline in both the hemispheres starting since $\sim$1995, and has continued until the maximum of the Cycle 23 ($\sim$2000). Subsequently the strength of these fields increased until 2004, and thereafter, the strength of these fields has become steady until the end of 2009. This behavior of unsigned polar fields has been verified with both NSO/KP and SoHO/MDI data, which show similar results in Cycle 23.

4. The unsigned polar fields in the latitude range, 78°–90°, virtually mirrors the change in the meridional flow speeds in Cycle 23 reported by Hathaway and Rightmire (2010) with meridional flow speeds dropping when the unsigned polar field drops.

5. From our observations of a very weak polar field (Janardhan, Bisoi and Gosain, 2010) in Cycle 23, we believe that the "memory" of these weak polar fields in Cycle 23 is the cause of the extended solar minimum at the end of Cycle 23 and would lead to a much weaker Cycle 24 compared to Cycle 23, which is in accordance with the prediction proposed by

Choudhuri, Chatterjee and Jiang (2007).

The study of polar magnetic fields can thus provide good clues to the nature of the meridional flows in each hemisphere. Such inputs would be important in predicting the behaviour of the future solar cycles. In addition to such measurements, other inputs from radio measurements of circular polarization that are sensitive to the LOS component of the coronal magnetic field, interplanetary scintillation measurements at high latitudes that can indicate the change in turbulence levels due to changes in polar fields (Ananthakrishnan, Balasubramanian and Janardhan, 1995) and high-resolution high dynamic range quiet Sun radio imaging (Mercier *et al.*, 2006a) of the Sun at low frequencies that can examine the changes in polar coronal hole boundaries, will also be very useful.

Chapter 4

Changes in Quasi-periodic Variations of Solar Photospheric Fields

4.1 Introduction

At the end of the Solar Cycle 23, the Sun went to an extended solar minimum, one of the deepest minima experienced in the past 100 years, when there was a complete absence of sunspots and solar polar fields were much weaker compared to the previous solar cycles (Figure 3.2). Using both high-quality observations from spacecrafts (Hathaway and Rightmire, 2010) and theoretical modeling (Dikpati *et al.*, 2010; Nandy, Muñoz-Jaramillo and Martens, 2011), there have been continuous efforts to explain and understand the cause of this deep minimum using meridional flow variations. However, these studies do not provide any direct insights into the onset of such a deep minimum and the basic physical processes that triggered this kind of unusual behaviour in the solar cycle. The well-known 11-year solar cycle (the Schwabe cycle; Schwabe (1843)) of solar magnetic activity, involving the generation of strong toroidal fields from weak poloidal fields ($\omega-$effect) and the subsequent regeneration of poloidal fields from toroidal fields ($\alpha-$effect), is attributed to a solar dynamo operating deep within the Sun. The departure from such cyclic activity, therefore, should be linked to the changes in the underlying basic processes, which can be understood by studying periodicities in various surface magnetic activity produced at different phases of different solar cycles.

Apart from the well-known solar cycle periodicity of 11 years and the synodic rotation periodicity of 27 days, the Sun also shows periodicities at longer and shorter scales than 11 years in various solar activity indicators, most of which have been described in detail in Section 1.2 of Chapter 1. Moreover, quasi-biennial oscillations (QBO) of period $\sim$2 years have also been recognized in different types of solar activity (Krivova and Solanki, 2002; Bai, 2003b; Vecchio and Carbone, 2009; Fletcher *et al.*, 2010). These periodic and quasi-periodic variations detected in various solar activity features have provided direct insights into the underlying basic processes that govern the nature and evolution of solar magnetic fields. For example, the 158-day Rieger periodicity first reported in the solar flare occurrence rates (Rieger *et al.*, 1984) has also been detected in the total sunspot area on the solar surface (Oliver, Ballester and Baudin, 1998) and the cause of this 158-day periodicity has been linked to the periodic emergence of magnetic flux through the photosphere (Oliver, Ballester and Baudin, 1998). Similarly, a 1.3-year periodicity reported, through a helioseismic study, in the rotation rate of the Sun at the tachocline (Howe *et al.*, 2000b), the presumed site for the initiation of the solar dynamo processes, is believed to play a significant role in the 22-year solar magnetic activity cycle. The same 1.3-year periodicity has also been detected in sunspot areas and sunspot numbers using wavelet transforms (Krivova and Solanki, 2002) and in fact, these authors have claimed that the 154$-$158-day Rieger period is a harmonic of the 1.3-year periodicity (3×156 days $=$ 1.28 years). Subsequently, they proposed that the rotation rate in the interior (that unexpectedly varies with a period of 1.3 years) has a bearing on the sunspot evolution and in the variations of the solar flare occurrence rates. Additionally, the QBO's detected, using helioseismic data from the Birmingham Solar Oscillation Network (BiSON), have been ascribed to a second dynamo mechanism, separate from the main dynamo which operates the 11-year solar cycle (Fletcher *et al.*, 2010).

In the previous Chapter, using NSO/KP synoptic magnetograms, covering Solar Cycles 21 – 23, we have reported a significant decline in the photospheric magnetic fields at latitudes of 78° – 90° in Cycle 23 unlike Cycles 21 and 22, which has shown a good correlation with the meridional flow speed reported by Hathaway and Rightmire (2010). Such weaker polar fields, produced due to faster meridional flows in the declining phase of Cycle 23, are believed to be the cause of the extended minimum at the end of Cycle 23. In addition, a steady decline in the photospheric magnetic fields, at latitudes of 45° – 78°, has also been noticed in both the Northern and Southern solar hemispheres which began since around the minimum of Solar Cycle 22, in ≈1995 – 1996 (Janardhan, Bisoi and Gosain, 2010). Such a steady decline in the photospheric magnetic fields at these high latitudes has provided the motivation to extend our study to investigate the periodicities of solar photospheric magnetic fields.

Subsequently, in this Chapter, we have undertaken a study of quasi-periodic variations in solar photospheric magnetic fields to investigate the possible precursor signatures, if any, to the build-up of the recent deep minimum at the end of Cycle 23. For this purpose, photospheric magnetic fields derived from the NSO/KP synoptic magnetic database, spanning the period from 19 February 1975 to 09 November 2009 (1975.14 – 2009.86) were subjected to a detailed spectral analyses using both Wavelet and Fourier techniques. The wavelet analysis, carried out for the photospheric fields in the latitude range, 0° – 45° and 45° – 78°, reveals a clear and unambiguous transition around 1996 in the spectral power and distribution of periodicities. Based on this wavelet result, the magnetic data was divided into two parts: one prior to 1996 and other after 1996, and were subjected to a Fourier spectral analysis. Further, in this Chapter, our finding of a significant North – South asymmetry, existing almost

12 years before the deep solar minimum period in 2008 – 2009, has also been discussed.

4.2 Decline in Mid-to High Latitude Solar Fields

In the bottom two panels of Figure 3.1, which has already been described in Section 3.3.1 of Chapter 3, we have shown a steady decline since ∼1995 – 1996 in the unsigned, or absolute, photospheric magnetic fields, in the latitude range 45° – 78°. This study of the variability in solar magnetic fields spanned over the period from 19 February 1975 (1975.14) to 10 February 2009 (2009.11). In this Chapter, we have studied again these photospheric fields using measurements of magnetic field strengths obtained from 466 individual Carrington rotations (CR) of NSO/KP synoptic magnetograms from CR 1625 through CR 2090 in the period from 19 February 1975 to 09 November 2009 (1975.14 – 2009.86). Each magnetogram, generated from daily ground-based full-disk magnetograms spanning over a Carrington rotation period (27.27 days), was longitudinally averaged to a 1° wide longitudinal strip covering the latitude range from -90° to +90°. Surface magnetic fields in both solar equatorial (-45° to +45°) and high-latitude zones (>45° in both hemispheres) of the Sun were then derived by averaging over appropriate latitude regions. Full details of the method can be found in Janardhan, Bisoi and Gosain (2010), and has also been described in Section 3.2.1. In the remainder of this Chapter, the fields obtained in the equatorial belt of -45° to +45° are referred to as low-latitude fields while the fields obtained at latitudes >45° in both solar hemispheres are referred to as high-latitude fields. However, it is to be kept in mind that these terms, coined for the above specified latitude ranges, are only a convenient description for our purposes in this Chapter and shouldn't be confused with those of toroidal fields and mid-high latitude fields, used in the Chapter 3 in a different context.

Figure 4.1 shows the temporal variation in the unsigned photospheric mag-

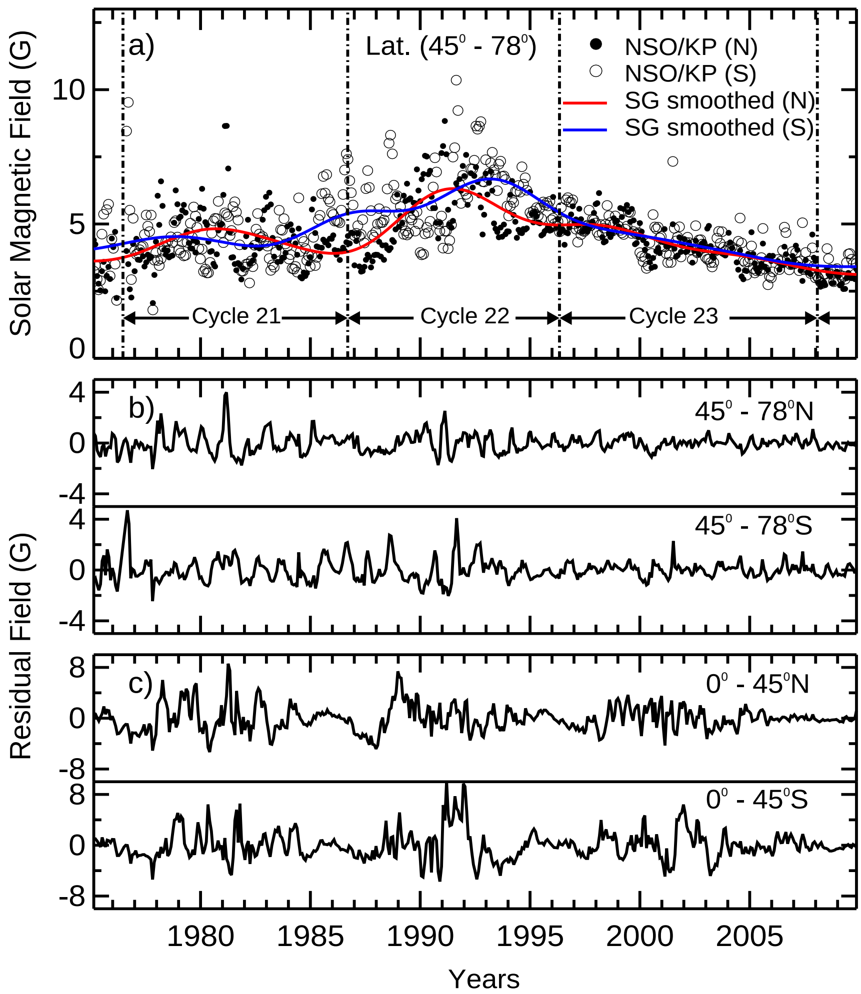

Figure 4.1: a) Shows measurements of solar photospheric magnetic fields in the latitude range, 45° to 78°. The filled dots and the open circles respectively represent the actual measurements for the Northern and Southern hemispheres while the fit obtained using the SG algorithm is shown by the solid red (North) and blue (South) lines. The vertically oriented dotted lines demarcate the periods of Solar Cycles 21, 22 and 23. b) The residuals obtained after subtracting the SG smoothed values from the magnetic fields in the latitude range, 45° to 78°, are shown for the North and South. c) Show the residual fields for both the Northern and Southern hemispheres obtained from the magnetic fields at latitudes below 45°.

netic fields in the latitude range $45° - 78°$ in both solar hemispheres for the period from February 1975 to November 2009 (panel (a)), covering Solar cycles 21, 22, and 23, which are demarcated by the vertically oriented dotted lines. The small, black filled dots and the open circles are the actual measurements for the Northern and Southern hemispheres respectively while the solid red (Northern hemisphere) and blue (Southern hemisphere) lines are smoothed curves derived using a robust Savitzky–Golay (SG) algorithm (Savitzky and Golay, 1964) that has the ability to preserve features of the input distribution like maxima and minima while effectively suppressing noise. Such features are generally flattened by other smoothing techniques. The decline in photospheric magnetic fields in both hemispheres, starting around the early to mid-1990s can be clearly seen in Figure 4.1. While the decline in photospheric fields had started in ≈1991 for the Northern hemisphere (solid red curve), for the Southern hemisphere the decline started in ≈1995 (solid blue curve). Beyond ≈1996, a steady decline in the photospheric fields for both hemispheres can be clearly seen. A similar decline in the sunspot umbral magnetic field strength since ≈1998 has also been reported (Livingston, 2002; Penn and Livingston, 2006; Livingston, Penn and Svalgaard, 2012). Although temporal variations in the low-latitude fields are not described here, but one can refer to the upper two panels of Figure 1 in Janardhan, Bisoi and Gosain (2010) for measurements of the magnetic field in the range $\pm 45°$, which show a strong solar-cycle modulation in the data, as expected.

Also shown in the bottom two panels of Figure 4.1 are the magnetic residuals, obtained by subtracting the SG fit from the actual measurements, for both the hemispheres in the latitude range $45° - 78°$ (panel (b)) and $0° - 45°$ (panel (c)) respectively. Such a detrending of the data, in general, removes large periodic variations like for example the 11-year solar cycle periodicity and facilitates the detection, if any, of smaller periodic variations. In addition, these time series of the residual fields obtained are made stationary *i.e.*, the mean of time series is or approaches zero. This condition of achieving stationarity in the time series can be achieved by an appropriate choice of SG smoothing of the input data. These stationary residual time series thus obtained are then subjected to both a Wavelet and a Fourier spectral analysis to study temporal quasi-periodic variations in the photospheric magnetic fields.

4.3 Transition in Wavelet Periodicities

A wavelet transform is the convolution of a time series with the scaled and translated version of a chosen mother wavelet function. Wavelet analysis is now frequently used in the analysis of time series data since it yields information in both time and frequency domains (Torrence and Compo, 1998; Oliver, Ballester and Baudin, 1998; Krivova and Solanki, 2002; Knaack, Stenflo and Berdyugina, 2005). On contrary, the Fourier analysis provides information only in frequency domain. The chosen mother wavelet function consists of a normalized wavelet basis function which can be of different kinds, *viz.* Morlet, Paul, and DOG (Torrence and Compo, 1998). Using a Morlet wavelet as the mother wavelet and based on the algorithm by Torrence and Compo (1998), the magnetic residuals obtained for both the high-latitude and low-latitude fields in the period from 19 February 1975 to 09 November 2009 (1975.14–2009.86) were subjected to a wavelet analysis. Scattered data gaps amounting to $\approx 2.5\%$ of the data were replaced with values obtained using a cubic-spline interpolation. The Morlet wavelet function $\psi_0(\eta)$, represented in Equation (4.1) below, is a plane wave modulated by a Gaussian.

$$\psi_0(\eta) = \pi^{-1/4} e^{i\omega_0 \eta} e^{-\eta^2/2} \tag{4.1}$$

Here, ω_0 is a non-dimensional frequency that determines the number of oscillations in the wavelet, and η is a non-dimensional time parameter. The choice of different non-dimensional frequencies defines the frequency resolution. However, by varying the frequency resolution, one has to compromise with temporal resolution. In this case, we have chosen ω_0 to be six for obtaining a better frequency resolution. This value is left unchanged and is not tuned to different values as our interest is to look for changes in the frequency components rather than to find precisely the low- and high- frequency components.

Figure 4.2 shows the wavelet spectrum for the high-latitude fields in the Northern (upper panel) and Southern hemisphere (lower panel), while Figure 4.3 shows the wavelet spectrum for the low-latitude fields in the Northern (upper panel) and Southern hemispheres (lower panel). The green-cross hatched regions in both figures represent the cone of influence (COI). In a wavelet analysis, the length of the time series is made equal to the next higher power of two by introducing zeroes. This zero-padding in turn yields discontinuities and thus reduces the power at the edges by a factor of e^2 in the COI and hence this region is not reliable. The white contours in Figure 4.2 and 4.3 are drawn at a significance level of 95%. The significance levels in the wavelet power spectrum are determined by assuming a white noise background spectrum modeled via a univariate lag-1 autoregressive process. A color coded bar on the right of each panel indicates the power level and a dashed vertical line in each panel is drawn at 1996.

For the high−latitude fields (Figure 4.2), in both the North and South, significant wavelet power is only seen at lower periods (≈one to three years) prior to 1985, while significant wavelet power is observable both at lower and higher periods (≈three to five years) for the interval between 1985 and 1996. Strong power noticed in the 1-year periodicity prior to 1985 as well as during 1985 − 1996 indicates it as a prominent periodicity during these periods. For the low-latitude fields (Figure 4.3), we don't see significant changes in the power levels between 1975 and 1996.

It is important to note here that there is a clear transition in both periodicities and power levels in both hemispheres around 1996 for both high-latitude and low-latitude fields. We stress here that we have taken care to check that the selection of different colors or changes in the color intensity in the wavelet plots makes no difference in the transition noticed in the wavelet power spec-

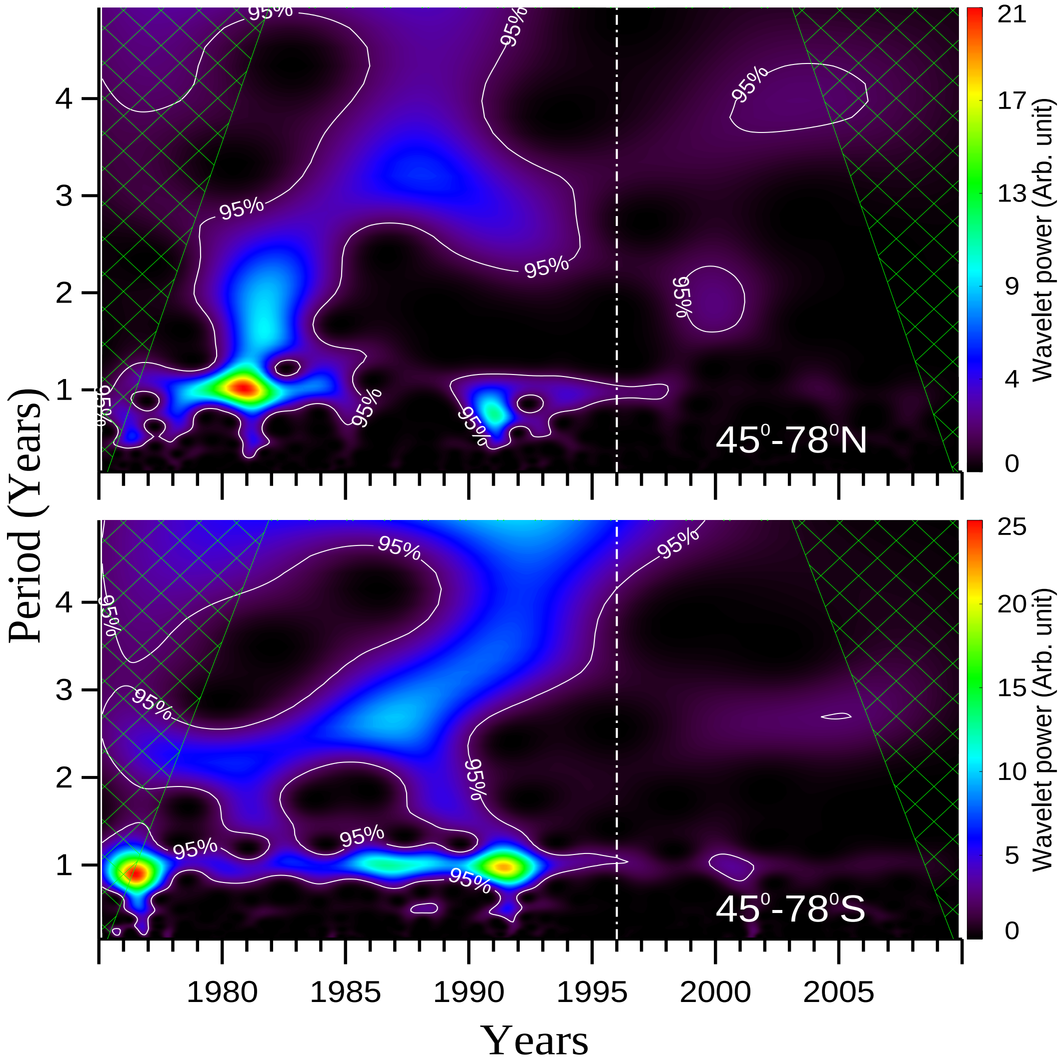

Figure 4.2: Shows the wavelet power distribution of solar periodicity over years for high-latitude fields for the Northern hemisphere (upper panel) and Southern hemisphere (lower panel) in the latitude range, 45° to 78°. The green cross hatched regions are the cone of influence (COI) while the white contours indicate a significance level at 95%. The dashed vertical lines are marked at 1996 when a clear transition has observed in wavelet power of periodicities for both the North and South high-latitude fields.

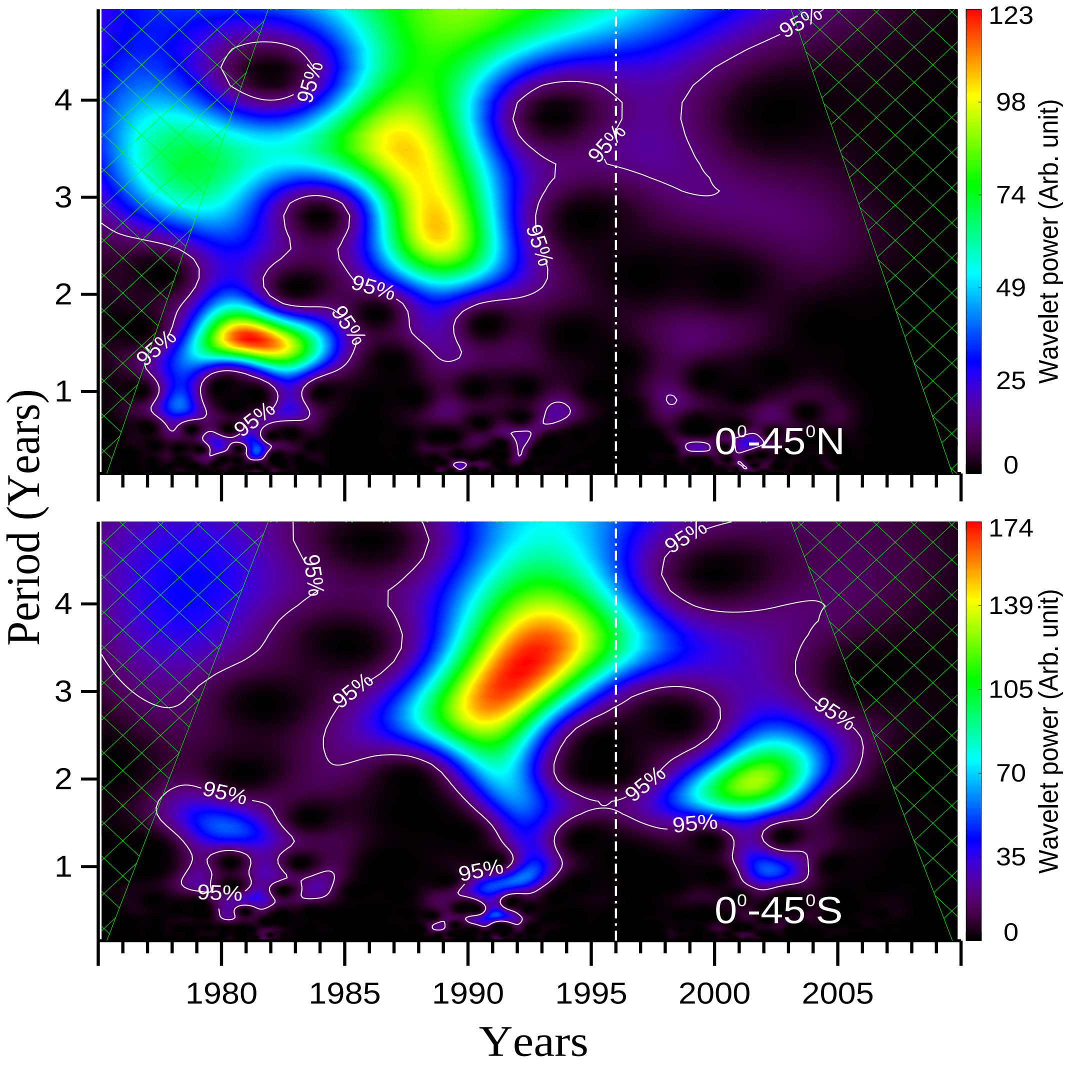

Figure 4.3: The wavelet power distribution of solar periodicity over time for low-latitude fields for the Northern hemisphere (upper panel) and Southern hemisphere (lower panel) in the latitude range, 0° to 45°. The green cross hatched region is the cone of influence (COI) while the white contours indicate a significance level at 95%. The dashed vertical line demarcates the sharp transition around 1996 in the wavelet power and periodicities for both the hemispheres.

tra. Although the decline in the fields has started in the early to mid-1990, as seen from Figure 4.1, we see from the wavelet spectra that there is an unambiguous transition in the quasi-periodic variations of fields in both the hemispheres at ≈1996. We have therefore chosen, in the rest of the analysis, to divide the residuals into two sets based on this transition seen in the wavelet spectra around 1996 in order to study the changes, if any, in the periodicities before and after the transition seen in the wavelet spectra. A Fourier time-series analysis was then carried out separately on the residuals used in the wavelet analysis, for the period prior to 1996 and the period after 1996 for both high-latitude and low-latitude fields, which has been discussed in Section 4.4.

It is important to bear in mind here that the transition in wavelet power spectra, around 1995 – 1996, corresponds to the time when the photospheric magnetic field at high-latitudes above $\pm 45^\circ$ had started to steadily decline (Janardhan, Bisoi and Gosain, 2010).

4.4 Fourier Periodicities - Asymmetries and Symmetries

Based on the unambiguous transition seen in the wavelet spectra at ≈ 1996 (see Section 4.3), the residuals obtained from the SG fits were divided into two parts, one prior to 1996 and other after 1996. These data were then separately subjected to a Fourier spectral analysis. Since these magnetic residuals were not evenly spaced, due to the presence of data gaps amounting to ≈2.5% of the total magnetic field data, an algorithm based on the Lomb-Scargle Fourier Transform for unevenly spaced data (Lomb, 1976; Scargle, 1982, 1989; Schultz and Stattegger, 1997) was used. The Lomb-Scargle Fourier analysis works in combination with the Welch-Overlapped-Segment-Averaging (WOSA) procedure (Welch, 1967) and generates periodograms (the spectral power as function of frequencies). The spectral power derived from such an analysis is generally normalized with respect to the total power contained in all the Fourier components taken together. This procedure makes the relative distribution of the spectral power independent of the spectral windowing used in the algorithm. Such normalized power spectra are referred to as normalized Fourier periodograms, or simply normalized periodograms. The following Sections 4.4.1 and 4.4.2 respectively, discuss these normalized periodograms for high− and low−latitude fields, obtained prior to 1996 and after 1996 in both the Northern and Southern hemispheres.

4.4.1 High-latitude Fields

Figure 4.4 shows the resultant normalized periodograms, for photospheric fields at high and low latitudes, obtained from the Lomb-Scargle Fourier analysis. It is important to note here that although the Fourier components obtained from the analysis, range in periods from 54 days to 12 years corresponding to 214 nHz to 2.6 nHz in frequency, Figure 4.4 only shows those components with periods lying in the range 300 days to 12 years *i.e.* the low-frequency range. Normalized periodograms containing Fourier components with periods shorter than 300 days are discussed later.

Normalized periodograms obtained from the Fourier analysis are shown in Figure 4.4. Figure 4.4 (a) – (d) represent the high-latitude fields while Figure 4.4 (e) – (h) represent the low-latitude fields. The upper four panels (high-latitude fields) show normalized periodograms before and after 1996 in the North (panels (a) and (b) respectively), and before and after 1996 in the South (panels (c) and (d) respectively). In a similar fashion, the lower four panels (low-latitude fields) show normalized periodograms in the North before and after 1996 (panels (e) and (f) respectively) and in the South before and after 1996 (panels (g) and (h) respectively). The significant periodic components were determined using the Siegel test statistics (Seigel, 1980) and are those

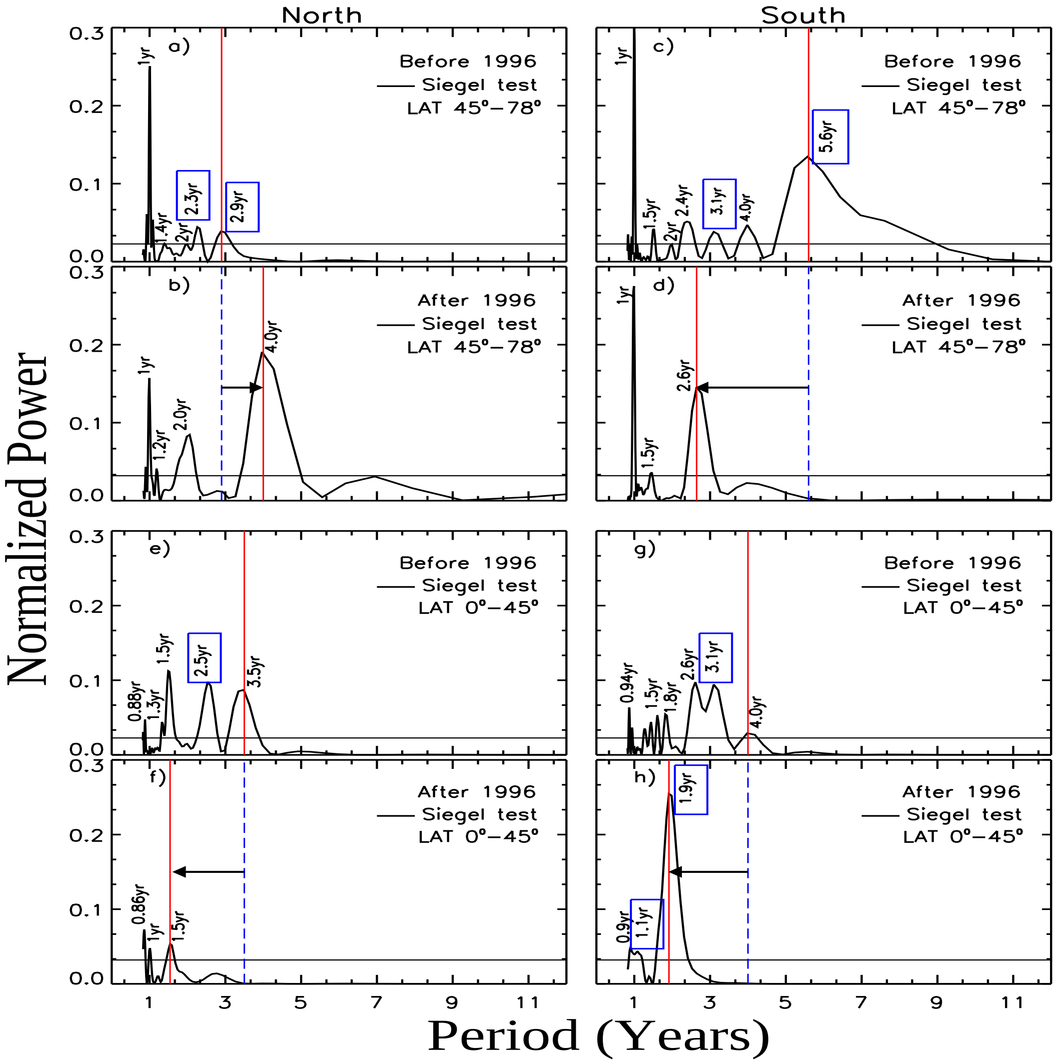

Figure 4.4: Normalized Fourier power distribution with periodicity for photospheric fields in the North (left column) and South (right column) before 1996 [(a), (c), (e), (g)] and after [(b), (d), (f), (h)] 1996. The solid-red vertical lines demarcate the highest period in each of the four panels while the dotted-blue vertical line and direction of the black arrow in each panel are used to show the shift in the periodicity of the longest periods. The solid-horizontal lines depict significance levels as determined by the Siegel test. The new periodicities from our analysis have been boxed in blue.

components having power levels above the black horizontal line drawn in each panel of Figure 4.4. The Siegel test is an extension of Fisher test (Fisher, 1929). The Fisher test attempts to spot the single dominant periodicity in a time series that has maximum power in the periodogram and is above the critical level defined by Fisher test statistics, the Siegel test relaxes this stringent condition a little and considers two to three dominant periodic components above the critical level. Both the aforementioned test statistics and the process of determining the confidence/significance level are discussed by Percival and Walden (1993) and also briefly by Schultz and Stattegger (1997). In the present analysis, 95% confidence level (or 5% significance level) is chosen. This is equivalent to the $\pm 2\sigma$ level in the FFT method. It is to be noted that the choice of this confidence level decides the critical level of the Siegel test statistics (Schultz and Stattegger, 1997).

The red vertical lines in each panel of Figure 4.4 are drawn through the peak of the component with the longest significant period. It can be seen that the component with the longest period before and after 1996 shows a shift in periodicity either in forward towards longer periods or backward towards shorter periods. The direction of this shift is shown by a dotted blue vertical line and a solid black arrow. It must be emphasized that our interest here is not in the individual periods themselves, but in the manner in which the component with the longest period shifts or changes before and after 1996. In addition to the shift in the component with the longest periodicity, it has also noticed that the Fourier spectral power in each panel of Fig. 4.4 differs significantly from each other before and after 1996. If we denote the longest periods before and after 1996 in the North as T_1 and T_2 respectively, we find that $T_2 > T_1$. This indicates a shift in periodicity in the forward direction, as shown in panel b of Figure 4.4. Also the spectral power for the longest periods after 1996 is higher than those before 1996 (panel a and b).

For the Southern hemisphere, the direction of the shift in the component with the longest period, as indicated by the black arrow in Figure 4.4, is in the opposite direction as compared to the Northern hemisphere. Thus, if we denote the longest periods in the South before 1996 and after 1996 as T_3 and T_4 respectively, we find that $T_4 < T_3$. Also, the spectral power of the longest periods after 1996 is significantly lower than the power level before 1996 (panel c and d).

Thus, it is noteworthy that the distribution of power in the components with the longest periodicities in the normalized periodograms clearly demonstrate a North – South asymmetry for the high-latitude fields. Since the normalized periodograms are generated from a time series of residual photospheric magnetic fields, their behavior is a good proxy for photospheric magnetic fields. A North – South asymmetry in periodicities would thus reflect a similar asymmetry in the high-latitude photospheric fields before 1996 and after 1996.

4.4.2 Low-latitude Fields

In contrast to the behavior of the high-latitude fields, the low-latitude fields shown in Figure 4.4 (e) – (h) show no asymmetry in the manner in which the longest periods shift when one compares the periodograms prior to and after 1996. The shift in the longest periods in both the North and South low-latitude fields before and after 1996 has been depicted in the lower four panels of Figure 4.4 in a manner similar to that of the upper four panels. The vertical solid-red line is drawn through the peak of the component with the longest period and the dotted-blue line and a black arrow in each panel indicate the direction of the shift.

Denoting the longest period for the low-latitude fields in the North before and after 1996 as T_5 and T_6 respectively, we find that $T_5 > T_6$. In the Southern hemisphere, denoting the longest period for the low-latitude fields prior to 1996 and after 1996 as T_7 and T_8 respectively, it is clear that $T_7 > T_8$. Hence, the longest periods show a shift in the same direction as shown by the forward direction of arrows in the North (panel e and f) as well as in the South (panel g and h). This indicates that there is no asymmetry in the distribution of periodicities for low-latitude fields before and after 1996.

4.5 Latitudinal Profile for Fourier Power Spectrum

In the previous section, we have seen a North – South asymmetry in Fourier periodicities for high-latitude fields, while we don't see the same for low-latitude fields. So it is of interest to see how the Fourier spectrum for photospheric fields varies with a higher latitudinal resolution in the range of latitude bins used. To examine this aspect, we have further subdivided the fields into smaller latitude bins of width 15° each. A Fourier analysis was carried out in a manner similar to that described earlier. It is known that the distribution of photospheric fields varies with latitude. So such an examination of the latitudinal profile of the Fourier spectrum can reveal whether a similar kind of North – South asymmetry persists across other latitude bins or not. The latitudinal variation for Fourier spectrum has been shown in Figure 4.5 and Figure 4.6.

Figure 4.5 and Figure 4.6 show normalized Fourier periodograms for photospheric fields in two latitude range, *viz*. 0° to 30° and 30° to 75°, in the latitude steps of 15°. In Figure 4.5 (a) – (d), and (e) – (h) represent, respectively, normalized periodograms showing the distribution of Fourier periodicities in the latitude ranges, 0° − 15° and 15° − 30°. While in Figure 4.6 (a) – (d), (e) – (h), and (i) – (k) represent, respectively, normalized periodograms showing the distribution of Fourier periodicities in the latitude ranges 30° − 45°, 45° − 60° and 60° − 75°. The latitude ranges are indicated at the top-right hand corner of each panel. Starting from the top, each of the left-hand panels of Figure 4.6 represent, in pairs before 1996 and after 1996 respectively, the power spectra for the Northern hemisphere in each latitude bin. Similarly, the right-hand panels of Figure 4.6 represent, in pairs before 1996 and after 1996 respectively,

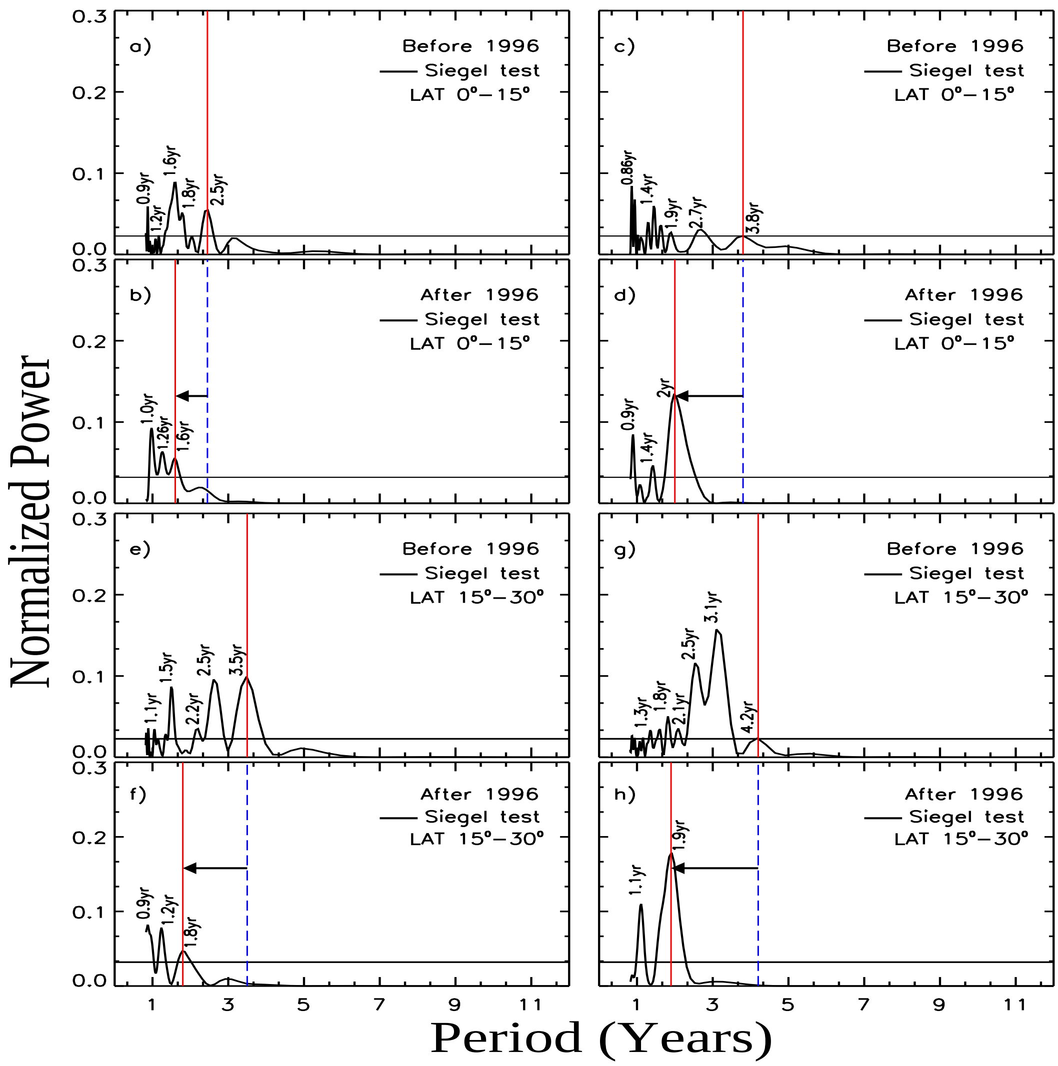

Figure 4.5: Normalized Fourier periodograms in the North (left column) and South (right column) before [(a), (c), (e), (g)] and after [(b), (d), (f), (h)] 1996 for the photospheric fields in the latitude ranges, $0°-15°$, and $15°-30°$. The solid-red vertical line, the dotted-blue vertical line and the black arrow in each panel are used to show the shift in periodicity and the spectral power of the fields before and after 1996 both in the Northern and Southern hemisphere. The solid horizontal lines depict significance levels as determined by the Siegel test.

the power spectra obtained for each latitude bin in the Southern hemisphere. In a manner similar to that shown in Figure 4.4, the red vertical lines in each panel of Figure 4.5 and 4.6 are drawn through the peak of the component with the longest period and the dotted blue line and a black arrow indicate the direction in which the longest periodicities shift. We can clearly see from Figure 4.5 the absence of North − South asymmetry for fields in the latitude ranges, $0° - 15°$ and $15° - 30°$ as indicated by the direction (backward) of the arrow for the shift in longest periodicities. The Fourier periodograms in Figure 4.6 also demonstrate a similar situation for the fields in the latitude ranges, $30° - 45°$ and $60° - 75°$, where the North − South asymmetry has also not been detected. It is important to note here that the North − South asymmetry is only present in the latitude range, $45° - 60°$, as seen in Figure 4.6 (e) − (h). It is also noteworthy that in the $60° - 75°$ bin (bottom four panels of the Figure 4.6), the shift of the longest periods before and after 1996 shows no North − South asymmetry. However, the spectral powers in the longest periods are significantly different before and after 1996. The spectral power in the longest period component increases significantly after 1996 for the Northern hemisphere while it decreases for the Southern hemisphere.

It is important to note here that the latitude band $45° - 60°$ in both hemispheres is dominated by surges or tongues of magnetic flux being carried polewards by the meridional flow. These surges are a direct surface manifestation of the meridional flow which is in turn governed by an internal solar dynamo. Beyond 60° in latitude, the high-latitude flux in both hemispheres saturates and can be best seen along with the magnetic surges in the $45° - 60°$ latitude band in a magnetic butterfly diagram, which will be described in the following section.

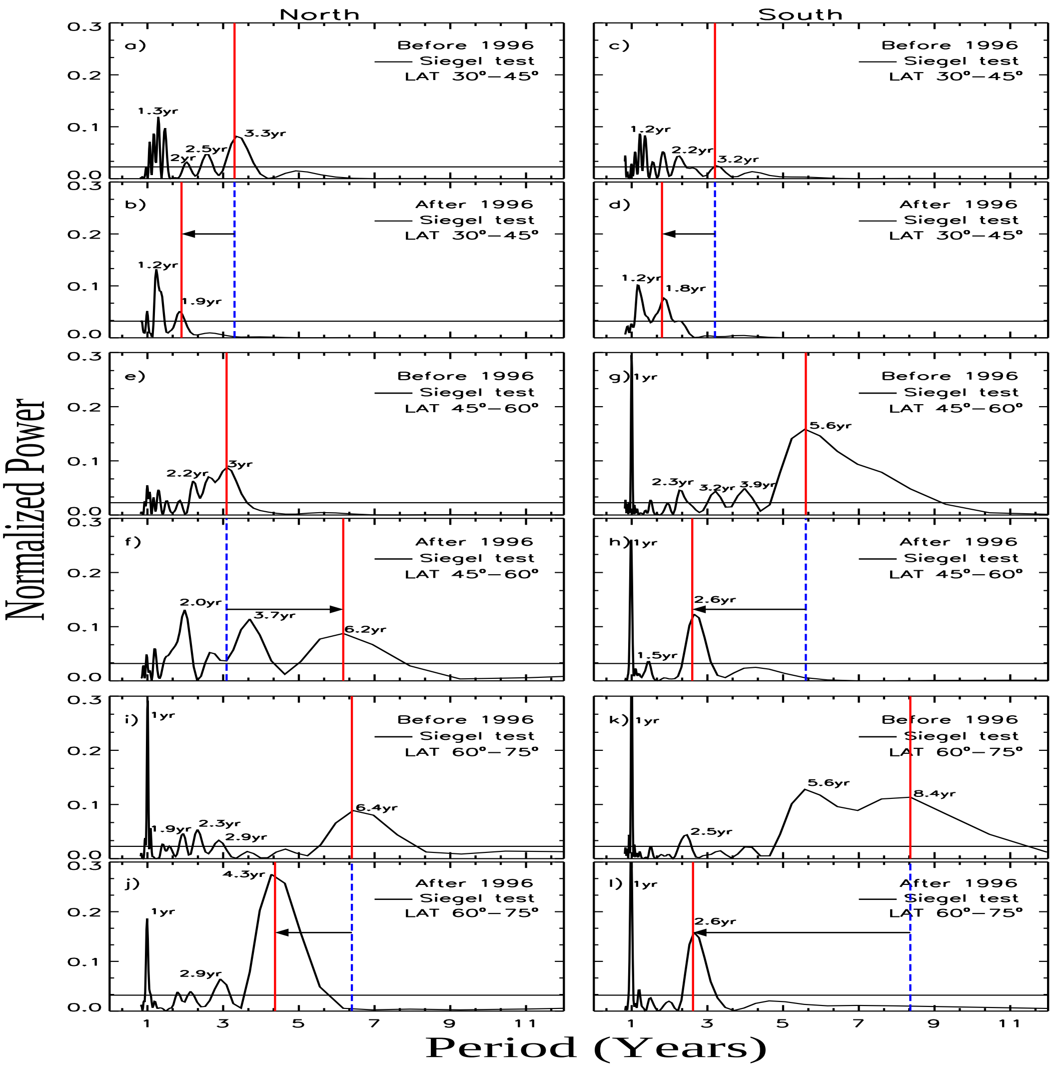

Figure 4.6: Normalized Fourier periodograms in the North (left column) and South (right column) before 1996 [(a), (c), (e), (g), (i), (k)] and after 1996 [(b), (d), (f), (h), (j), (l)] for the photospheric fields in the latitude ranges, 30°−45°, 45°−60°, and 60°−75°. The solid-red vertical line, the dotted-blue vertical line and the black arrow in each panel are used to show the shift in periodicity and the spectral power of the fields before and after 1996 both in the Northern and Southern hemisphere. The solid horizontal lines depict significance levels as determined by the Siegel test.

4.5.1 The Magnetic Butterfly Diagram and Polar Surges

Detailed observations of sunspots since many decades have shown that sunspots first appear at mid-latitude bands around both sides of the solar equator, and subsequently widen and disperse towards the equator as the solar cycle progresses. This motion of sunspots produces, when plotted as longitudinally averaged magnetic fields in time, a butterfly like appearance, well known as the "butterfly diagram". It is believed that the emergence and evolution of magnetic fields are governed by an internal solar dynamo, and the current understanding of the solar dynamo comes through mathematical models which explains the evolution of magnetic fields using the coupled action of toroidal and poloidal fields. The toroidal field component is generated by the shearing of a pre-existing poloidal fields caused as a result of solar differential rotation (ω effect) on the solar plasma. These toroidal magnetic fields form magnetic flux tubes which become buoyant and erupt through the solar surface forming sunspots or bipolar magnetic regions (BMRs). Subsequently, these BMRs decay and disperse over the solar surface mediated by diffusion, differential rotation and meridional circulation to generate the poloidal fields (Babcock-Leighton type α-effect). The decay of BMRs or sunspots cause migration of magnetic flux toward the equator as the solar cycle progresses. It is this migration which gives rise to a magnetic butterfly diagram, which is basically a map of longitudinally averaged magnetic fields in time. Figure 4.7 shows such a magnetic butterfly diagram.

The magnetic butterfly diagram shown in Figure 4.7 has been generated using NSO/KP synoptic maps from CR1625 to CR2090, covering the period from 19 February 1975 to 09 November 2009 (1975.86 – 2009.86). Each synoptic map, ranging over longitudes from (1° to 360°) and over latitudes from (-90° to 90°), represents the distribution photospheric magnetic flux distribution for a period of 27.27 days. Each map is averaged in longitude (1° to 360°) for each latitude bin starting from -90° to 90°. The longitudinal averaged

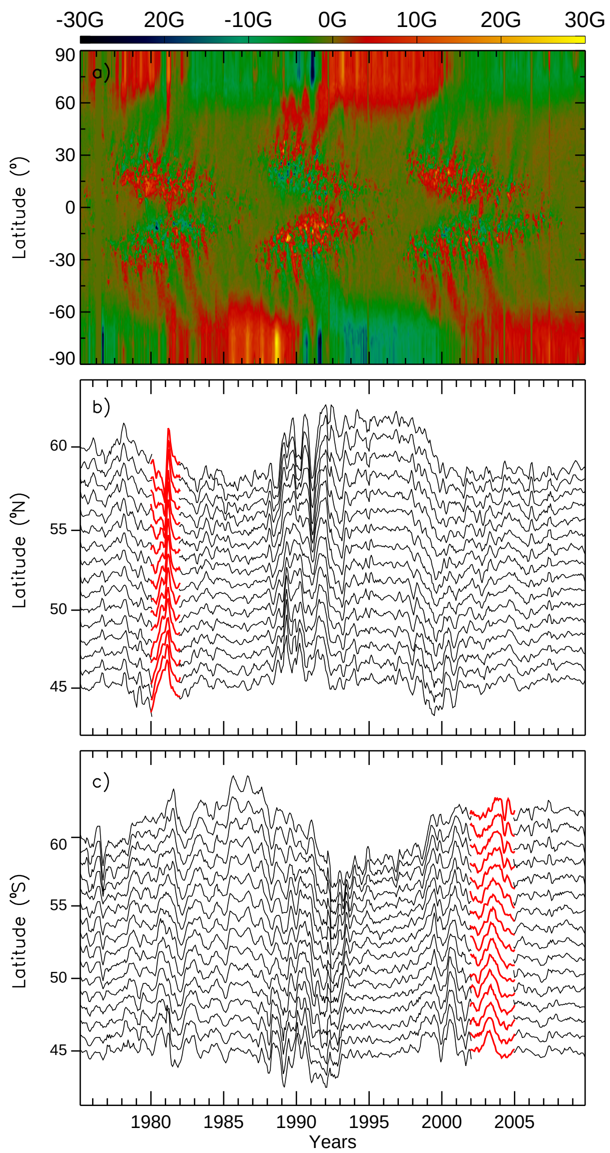

Figure 4.7: The top panel labeled a shows a magnetic butterfly diagram generated using NSO/Kitt Peak magnetograms and depicts the net photospheric magnetic flux distribution on the Sun for Solar Cycles 21, 22 and 23. For better contrast the magnetic flux has been limited to ±30 Gauss. The positive and negative polarities are shown in red and green respectively. Polar surges or lateral motions of magnetic flux moving polewards above latitudes of ±45° are seen as tongues of red and green bands. The lower two panels labeled b and c show the variation of magnetic field, after smoothing over three Carrington rotations, for each degree of latitude in the range 45° to 60°. An example of a surge is highlighted in red in the bottom two panels representing the Northern and Southern hemisphere respectively.

photospheric fields when plotted as a function of time gives rise to a magnetic butterfly diagram. The distribution of magnetic flux is shown in red and green corresponding to either the leading or following polarity. It must be pointed out that in a given cycle, if the leading polarity in one hemisphere is positive, then the leading polarity in the other hemisphere of the same cycle will be negative and the pattern will flip from cycle to cycle and hemisphere to hemisphere. Leading and following polarity fluxes in the Northern hemisphere for Cycle 21 are shown in red and green respectively in Figure 4.7. A color coded bar on the top of Figure 4.7 indicates the magnetic flux level.

In order to achieve a better contrast in Figure 4.7, the magnetic fluxes in the diagram have been limited to the range ±30G. The diagram clearly depicts that the leading polarity fluxes move equatorward while the following polarity fluxes move poleward. The polewards motions of magnetic flux is not a smooth steady flow, but actually happens in fits and starts called polar surges, which are episodic (Wang, Nash and Sheeley, 1989) and can be best seen as red (positive polarity) and green (negative polarity) tongues of poleward moving flux in the latitude band, $45° - 60°$, as depicted in panel - a of Fig. 4.7. For a better view of the polar surges, the magnetic field intensity has been shown as a function of time in each $1°$ strip of latitude in the latitude range $45° - 60°$ in the middle (panel - b) of Figure 4.7 for the Northern hemisphere and lower panels (panel - c) for the Southern hemisphere respectively. The magnetic field for each degree of latitude has been shown after smoothing over three Carrington rotations. An example of a surge in the North and South has been highlighted in red.

Knaack, Stenflo and Berdyugina (2005) reported a periodicity of 1.3 years in the photospheric fields that has been correlated with these polar surge motions. We see an approximate periodicity of one year in the polar surge flows in the lower two panels of Figure 4.7. This agrees with the strong one year periodicity seen in Figure 4.4, 4.5, and 4.6. Further, a variation in the strength and occurrence rate of surges prior to and after 1996 can be seen from a careful inspection of Figure 4.7. In the latitude bin $\pm45° - \pm60°$, we find that the frequency of these surges is greater during the years $1996-2009$ while it is less during the years $1986-1995$.

4.6 Fourier Periodicity - Low and High Frequency Periods

The harmonic analysis yielded Fourier components with periods ranging from 54 days to 12 years corresponding to a frequency range of 2.6 nHz to 214 nHz. The significant periodic components, as determined by the Siegel test, were grouped into low-frequency periods in the frequency range 38.5 nHz (300 days) to 2.6 nHz (12 years) and high-frequency periods in the frequency range 214 nHz (54 days) to 38.5 nHz (300 days). These periods have been listed in Table 4.1 (long periods) and Table 4.2 (short periods) respectively. Many of these periodicities have already been reported by other workers and a few new periodicities have also been seen in our analysis. These new periodicities have been listed in bold face in Tables 4.1 and 4.2 and boxed in blue in Figures 4.4 and 4.8.

4.6.1 The Low-frequency Periods

In the low-frequency range, 38.5 nHz (300 days) to 2.6 nHz (12 years), we restrict our analysis to periodicities in the range, 305 days to 5.6 years. Periods longer than 5.6 years are not taken into account because of their inaccurate determination as a consequence of division of time series. The periodicities are listed in Table 4.1 where the upper half lists periodicities for high-latitude fields in the North and South grouped before and after 1996 while the lower half lists periodicities for low-latitude fields in a similar fashion.

For photospheric fields in the high-latitude range we find periodicities of 305 days (0.84 years), 325 days (0.89 years), 339 days (0.92years), 341 days

North high-latitude Field				South high-latitude Field			
Before 1996		After 1996		Before 1996		After 1996	
Period[yr]	Power	Period[yr]	Power	Period[yr]	Power	Period[yr]	Power
2.9	**0.04**	4.0	0.19	**5.6**	**0.13**	2.6	0.15
2.3	**0.04**	2.0	0.08	4.0	0.05	1.5	0.04
2.0	0.02	1.2	0.04	**3.1**	**0.04**	1.0	0.28
1.4	0.02	1.0	0.16	2.4	0.05	—	—
1.0	0.25	0.89	0.04	2.0	0.02	—	—
0.93	0.06	—	—	1.5	0.04	—	—
—	—	—	—	1.0	0.02	—	—
—	—	—	—	0.92	0.03	—	—
—	—	—	—	0.89	0.02	—	—
—	—	—	—	0.84	0.04	—	—
—	—	—	—	—	—	—	—
North low-latitude Field				South low-latitude Field			
Before 1996		After 1996		Before 1996		After 1996	
Period[yr]	Power	Period[yr]	Power	Period[yr]	Power	Period[yr]	Power
3.5	0.09	1.5	0.05	4.0	0.03	**1.9**	**0.25**
2.5	**0.10**	1.0	0.04	**3.1**	**0.09**	**1.1**	**0.04**
1.5	0.11	0.86	0.07	2.6	0.1	0.90	0.05
1.3	0.04	—	—	1.8	0.05	—	—
0.88	0.04	—	—	1.5	0.05	—	—
—	—	—	—	1.44	0.04	—	—
—	—	—	—	1.27	0.04	—	—
—	—	—	—	0.94	0.04	—	—
—	—	—	—	0.87	0.06	—	—

Table 4.1: The Fourier periods in the frequency range, 38.5 nHz to 2.6 nHz (low-frequency zone), are listed with their Fourier power respectively in the upper and lower half of the table for high-latitude fields and low-latitude fields in both the North and South prior to 1996 and after 1996.

(0.93 years), 1 years, 1.2 years, 1.4 years, 1.5 years, 2 years, 2.4 years, 2.6 years, and 4 years while for photospheric fields in the low-latitude range we find periods of 312 days (0.86 years), 318 days (0.87 years), 321 days (0.88 years), 327 days (0.9 years), and 343 days (0.94 years), 1 years, 1.27 years, 1.3 years, 1.44 years, 1.5 years, 1.8 years, 2.6 years, 3.5 years, and 4 years. All of these quasi-periodicities in various types of solar activity have been reported earlier by other researchers (Howe *et al.*, 2000b; Krivova and Solanki, 2002; Knaack, Stenflo and Berdyugina, 2005; Mendoza, Velasco and Valdés-Galicia, 2006; Chowdhury, Khan and Ray, 2009). Knaack, Stenflo and Berdyugina (2005) had discussed a North − South asymmetry in quasi-periodic variations in unsigned photospheric flux with periods of 1.3 years, 1.5 years, and 2.6 years.

In addition to these known periodicities, we have found some new periodicities in the high-latitude fields with periods of 2.3 years, 2.9 years, 3.1 years, and 5.6 years and in the low-latitude fields with periods 1.1 years, 1.9 years, 2.5 years, and 3.1 years (Bisoi *et al.*, 2013). These new periodicities have been shown in boldface in Tables 4.1 and 4.2. Though the periodicity of one year has already been reported, we find this periodicity to be the prominent periodicity observed in both the North and South high-latitude fields before and after 1996. The Fourier power in the one year period is comparatively more both in the North and South prior to 1996 than after 1996. On the other hand, although the one year period is present in the low-latitude fields both in the North and South, it is only present after 1996. Besides these, periods of 1.2 − 1.6 years are common to both the North and South low-latitude fields and have significant power.

Among these periodicities, the most discussed and reported periodicity is the 1.3-year periodicity (Krivova and Solanki, 2002; Knaack, Stenflo and Berdyugina, 2004, 2005) which has been linked to polar surges that can be seen most clearly in the latitude band 45° to 60° (Wang, Nash and Sheeley, 1989; Knaack, Stenflo and Berdyugina, 2005) in magnetic butterfly diagrams as depicted in Figure 4.7. Also, the 1.3-year periodicity has been linked to the variation of the rotation rate near the base of the convection zone (Howe *et al.*, 2000b).

4.6.2 The High Frequency Periods

In the high-frequency range we have frequencies ranging from 214 nHz (54 days) to 38.5 nHz (300 days). These periodicities for both the high-latitude and low-latitude fields are listed in the Table 4.2. The upper half of Table 4.2 lists periodicities for the high-latitude fields with periods ranging between 157 days to 294 days. Few of these periodicities with their Fourier spectral power are shown in the top four panels a, b, c, d in Figure 4.8. Similarly, the lower half of Table 4.2 lists significant periodicities for the low-latitude fields with periods ranging in between 134 days to 288 days. The bottom four panels e, f, g, h in Figure 4.8 show a few of these periodicities with their spectral power. As stated earlier the significant periodic components were determined using the Siegel test statistics and are those periodic components having power levels above the black horizontal line drawn in each panel of Figure 4.8.

The known periodicities in the high-latitude zone include those with periods 157 days, 183 days, 184 days, 240 days, 263 days, 278 days, and 288 days and the new periodicities, *viz*. with period 253 days and 294 days, not reported in the literature earlier, are shown in boldface in the upper part of Table 4.2.

The Rieger periodicity of 157 days is a well known fundamental periodicity that we find only in the high-latitude fields in the Northern hemisphere prior to 1996. In addition, the periodicity of 182 – 184 days is seen to be always present and the Fourier power corresponding to this periodicity does not vary much in both the North and South fields at high latitudes both before and after 1996. These high-frequency periods, in the high-latitude fields, do not show much variation in their normalized Fourier power and we do not see any North – South asymmetry in these high-latitude fields.

North high-latitude Field				South high-latitude Field			
Before 1996		After 1996		Before 1996		After 1996	
Period[day]	Power	Period[day]	Power	Period[day]	Power	Period[day]	Power
294	**0.02**	**253**	**0.04**	288	0.037	184	0.07
278	0.06	183	0.061	184	0.06	—	—
263	0.04	—	—	—	—	—	—
240	0.02	—	—	—	—	—	—
183	0.04	—	—	—	—	—	—
157	0.04	—	—	—	—	—	—
North low-latitude Field				South low-latitude Field			
Before 1996		After 1996		Before 1996		After 1996	
Period[day]	Power	Period[day]	Power	Period[day]	Power	Period[day]	Power
288	0.02	**257**	**0.04**	283	0.04	—	—
278	0.03	181	0.08	248	0.02	—	—
261	0.03	172	0.11	228	0.03	—	—
—	—	147	0.04	157	0.03	—	—
—	—	—	—	151	0.03	—	—
—	—	—	—	145	0.03	—	—
—	—	—	—	—	—	—	—
—	—	—	—	—	—	—	—

Table 4.2: The Fourier periods with their Fourier spectral power in the frequency range, 214 nHz to 38.5 nHz (high-frequency zone) are listed respectively in the upper and lower half of the table for high-latitude fields and low-latitude fields both in the North and South prior to 1996 and after 1996.

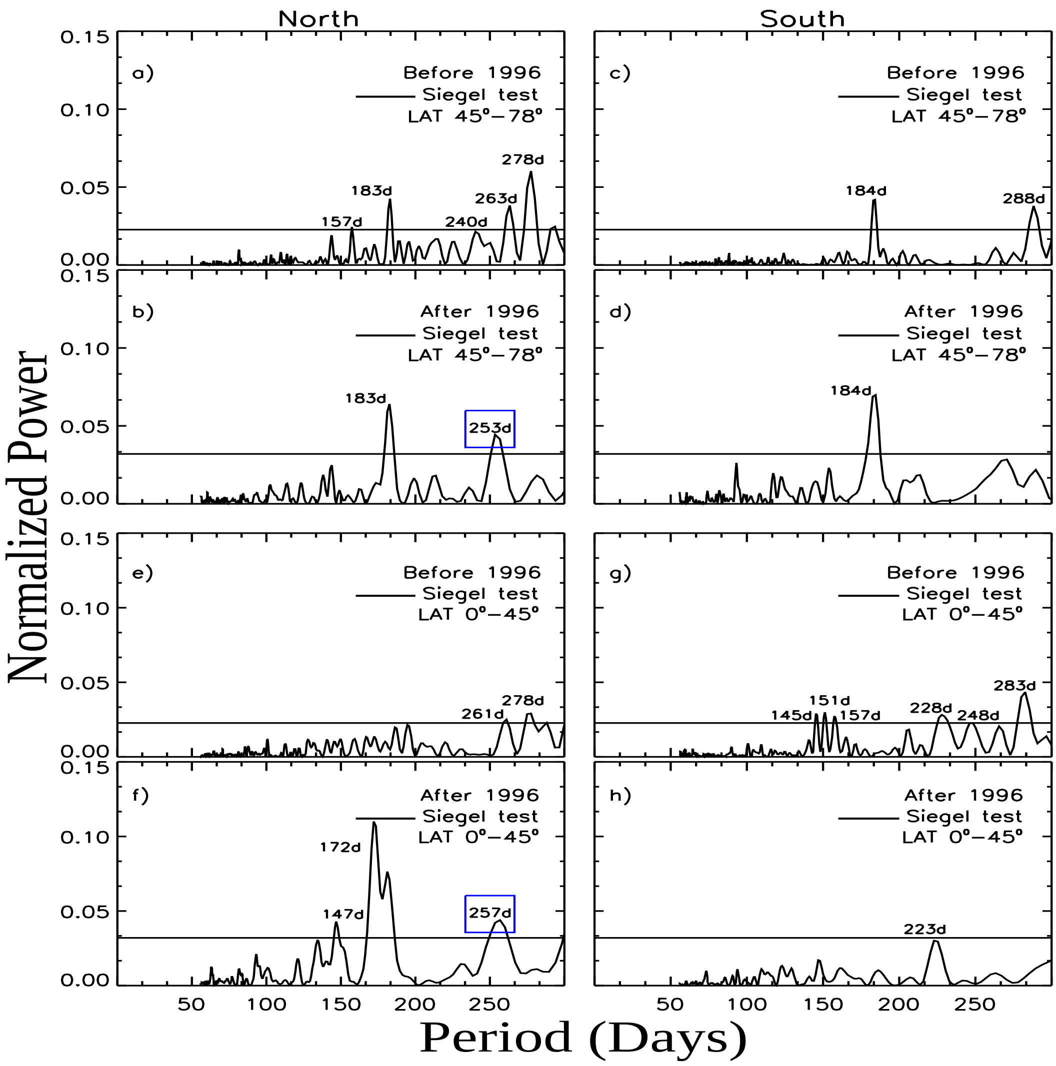

Figure 4.8: Normalized Fourier periodograms in the North (left column) and South (right column) before 1996 [(a), (c), (e), (g)] and after 1996 [(b), (d), (f), (h)] for high-latitude fields (top panel) and low-latitude fields (bottom panel) for the high-frequency periods in the frequency range 214 nHz to 38.5 nHz. The new periodicities in our analysis have been boxed in blue.

On the other hand, in the low-latitude zone, shown in the lower part of Table 4.2, we report periodicities of 145 days, 147 days, 151 days, 157 days, 172 days, 228 days, 248 days, 261 days, 278 days, 283 days and 288 days, which have already been reported in earlier work (Oliver, Ballester and Baudin, 1998; Krivova and Solanki, 2002; Knaack, Stenflo and Berdyugina, 2005; Chowdhury, Khan and Ray, 2009). The new periodicity from our analysis was 257 days and is shown in boldface in the lower half of Table 4.2. The Rieger periodicity of 157 days is only seen in the South low-latitude field before 1996. Also, the semi-annual variation of period 181 days is observed only in North low-latitude fields.

4.7 Discussions

The wavelet analysis carried out by us has shown a transition around 1996 in the distribution of power and periodicities for photospheric fields (Bisoi *et al.*, 2013). It is important to note that this unambiguous transition corresponds in time to the period, starting around 1995 – 1996, when solar photospheric fields began to show a steady declining trend (Janardhan, Bisoi and Gosain, 2010). It is based on this sharp transition seen in the distribution of power in the wavelet analysis that the data, comprising the residuals of photospheric fields, were divided into two parts, one before and one after 1996. These two data sets were then subjected to a Fourier analysis that revealed a hemispheric asymmetry in the distribution of Fourier periodicities in high-latitude photospheric fields that were confined only to the latitude band, $45° - 60°$. It is to be borne in mind that the $45° - 60°$ latitude band is dominated by polar surges carrying magnetic flux polewards in both hemispheres. Polar surges above latitudes $\pm 45°$ show significant changes in their occurrence rates and strength in each cycle. Therefore, it is expected these changes will be reflected, as corresponding variations in the distribution of power and periods in the Fourier analysis. This is clear when we compare these polar surges in the last three cycles, *viz.* Cycle

21, 22 and 23. We actually find an asymmetrical distribution in the occurrence rate of these surges in the latitude band, $45° - 60°$. This would contribute to the hemispheric asymmetry that we have reported (Bisoi *et al.*, 2013) in the Fourier periodicities of photospheric fields prior to 1996 and after 1996.

It has been reported that the frequency in the occurrence rate of polar surges is $\sim$ 1 year (Knaack, Stenflo and Berdyugina, 2005). Our analysis has also shown an approximate periodicity of 1 year for fields confined to the latitude band of $45° - 60°$. Polar surges are the direct surface manifestation of meridional flow variations and are thus linked to the changes taking place in the internal solar dynamo. So these variations around 1996 in Wavelet and Fourier periodicities of surface magnetic fields, coupled with the steady decline in the high-latitude surface fields since 1996 suggest that active changes occurred around this time in the solar dynamo. These changes in turn probably initiated, in our opinion, the build-up to one of the deepest solar minima experienced in recent times that occurred, between the Solar Cycles 23 and 24. The last time that such a deep minimum had been recorded was 100 years ago in 1913.

We have also detected some other significant mid-term periodicities ($1-2$ years) showing significant spectral power changes before and after 1996. It is believed that these prominent periods in the lower solar latitudes, below $45°$, are a result of stochastic process caused by the periodic emergence of magnetic flux with the progress of solar cycle (Wang and Sheeley, 2003). Howe *et al.* (2000b) reported a 1.3-year periodicity in the rotation rate of the Sun at the tachocline, the presumed site for the interior solar dynamo. The same periodicity of 1.3 years has also been reported in sunspot areas and numbers (Krivova and Solanki, 2002; Chowdhury and Dwivedi, 2011). This suggests that variations detected in photospheric magnetic fields are manifestations of the changes in the solar interior.

It is known that the trailing polarity fluxes, moving polewards, cancel old pre-existing polar fields and produce new opposite polarity polar fields

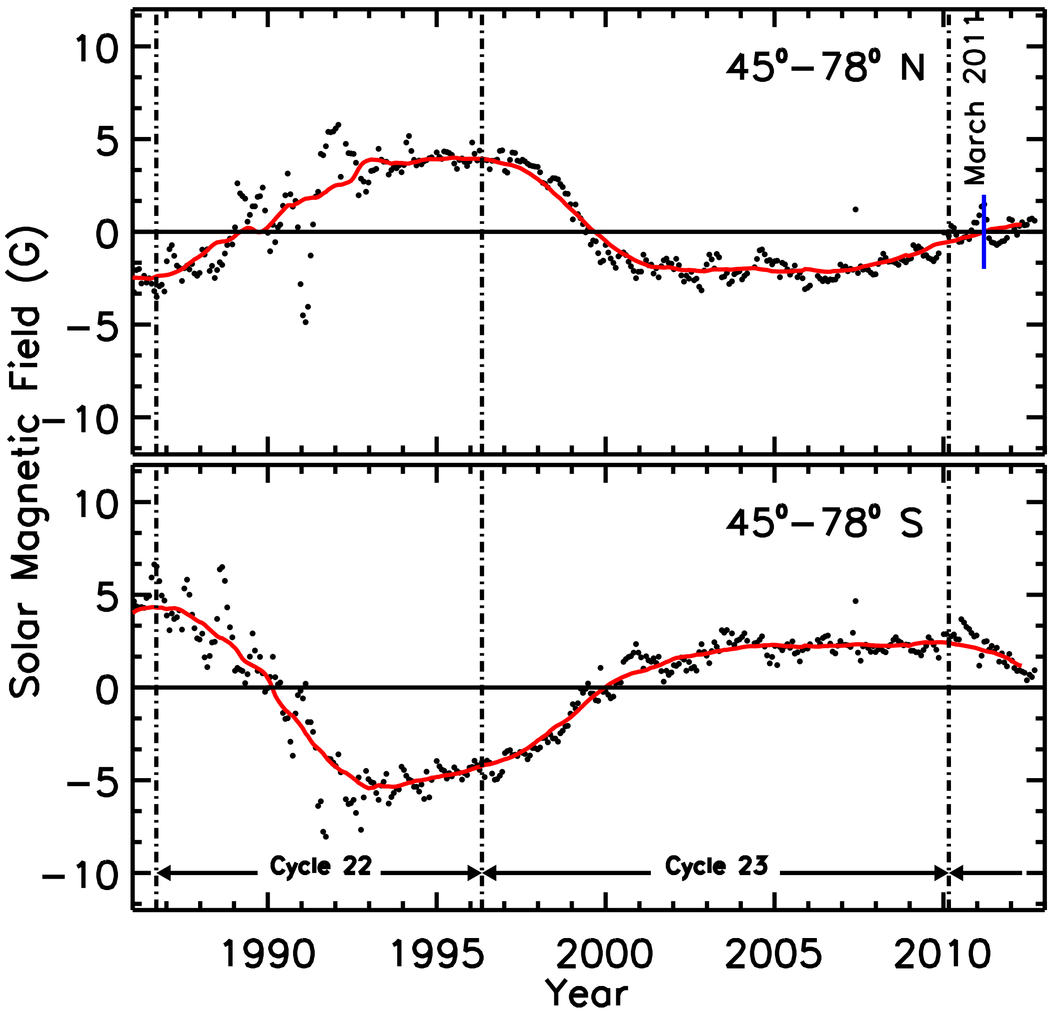

Figure 4.9: Shows the solar magnetic field in the Northern (top) and Southern (bottom) solar hemispheres in the latitude range 45° to 78° for Solar Cycles 22 and 23. It is clear that the North solar field has reversed in March 2011 while the South solar field is still to do so. The time of reversal of the North solar field is indicated by a small blue arrow.

at around the maximum of each sunspot cycle. This is known as the polar field reversal which was first reported by Babcock (1961) for solar cycle 19 while studying magnetic fields using solar magnetographic observations. Babcock (1961) reported an asymmetry in the polar field reversal with the Southern hemisphere reversing first followed by than the Northern hemisphere. We have discussed, in the previous Chapter (Section 3.3.1, Figure 3.2) the polar field reversal for Solar Cycles 21, 22 and 23, using photospheric magnetic field observations covering the period from 1975.14 to 2009.11. While examining the magnetic field data beyond 2009 and upto March 2012, we find an asymmetry in polar field reversal for solar cycle 24. Figure 4.9 shows the reversal in field at high-latitudes for the Northern hemisphere in Cycle 24 in March 2011 while the reversal in the Southern hemisphere has just taken place in August 2013.

In Figure 4.9, the small black filled dots represent actual signed magnetic fields in the latitude band, $45°-78°$ while the solid red curve is for the smoothed magnetic fields. The upper and lower panel respectively, represents the fields for the Northern and Southern solar hemisphere. The small blue vertical line in the upper panel marks the time of polar field reversal period in the Northern hemisphere. Polar field reversals in the earlier cycles too did not occur simultaneously and had a time gap between them, but in the Cycle 24 time lag between the reversal for the Northern hemisphere and Southern hemisphere is really large compared to the earlier cycles.

The poleward motions of surface magnetic fluxes are attributed to the cumulative actions of surface-meridional flow, diffusion and differential solar rotation. A poleward meridional flow of $\sim 10-20$ m s^{-1} has been reported in the last few years using helioseismic study (Haber *et al.*, 2002) and Doppler shift technique (Hathaway, 1996). A counter meridional flow from the poles towards the equator has also been reported near the base of the convection zone. The poleward surface meridional flow and the interior equatorward flow thus forms the Sun's conveyer belt (Dikpati *et al.*, 2010; Dikpati, 2011). Using a flux-transport dynamo simulation, Dikpati *et al.* (2010) found a difference between the latitudinal extents of the poleward meridional flow for the Cycles 22 and 23. In the Cycle 23, the flow approached closer to the poles while in the Cycle 22 it reached only to the latitude 60°. As a result, the period of the Sun's conveyer belt was longer in the Cycle 23 than that in the Cycle 22 thereby causing a slower return flow in Cycle 22 which in turn leads to an extended solar minimum at the end of Cycle 23. We believe that this asymmetry in the sub-surface meridional flows may cause an asymmetry in the distribution of magnetic flux that erupts out on to the solar surface.

In a more recent work, Basu *et al.* (2012) has reported the difference in behavior of solar oscillation frequencies in the sub-surface magnetic layers during the descending phase of Cycle 22 and 23. They used helioseismic data from the Birmingham Solar Oscillation Network (BiSON), an instrument that is very sensitive in probing the solar interior close to the solar surface. These authors then went on to propose that the long solar minimum prior to the Cycle 24 could have been predicted. The North−South asymmetry noticed in periodicities of photospheric fields before and after 1996, from our analysis, leads us to the conclusion that the changes initiated around this period of time in the meridional flow rates and flux emergence was the cause behind. That in turn causes the initiation of one of the deepest solar minima in 100 years that took place at the end of Cycle 23 (Bisoi *et al.*, 2013).

In the solar dynamo process, the toroidal field is generated from the pre-existing poloidal fields by the action of solar differential rotation forming magnetic flux tubes. These magnetic flux tubes are buoyant and rise to the solar surface to form tilted bipolar active regions with the tilt being imparted by the action of the coriolis force. The decay of these tilted bipolar regions regenerates the poloidal field through the Babcock−Leighton mechanism (Choudhuri, Chatterjee and Jiang, 2007; Jiang, Chatterjee and Choudhuri, 2007). While the generation of toroidal fields and meridional circulation processes are deterministic, the generation of poloidal fields involves randomness. This is because of the dependence of the eventual strength of polar field on the tilt angle of bipolar active regions, which in turn is determined by the action of Coriolis force on magnetic flux tubes that rise to the surface from the turbulent convection zone (D'Silva and Choudhuri, 1993). Consequently, this process imparts a large scatter in the average tilt angle thereby causing the polar field to be randomly weaker or stronger than the previous cycle (Longcope and Choudhuri, 2002). We have seen that the high-latitude fields, above latitude 45°, have shown a steady decline for ∼15 years from mid-1990s to the end of 2009 implying continuous weaker polar fields for the last two solar cycles, *viz.* Cycles 22 and 23. A continuation of this declining trend beyond 22 years would imply a third successive weak polar field imparted by the Babcock-Leighton mechanism. This is probably unlikely as the polar field is imparted by a random process and if it happens, it would have serious implications on our present understanding of the solar dynamo.

4.8 Summary and Conclusions

In this Chapter, we have undertaken a study of quasi-periodic variations of photospheric fields in order to investigate their role in the buildup to the deepest solar minima experienced in the past 100 years that took place, at the end of the Solar cycle 23. For studying these quasi-periodic changes, we have employed both a Wavelet and a Fourier method to the magnetic time series derived from the NSO/KP magnetograms in the period from 19 February 1975 to 09 November 2009 (1975.14 – 2009.86). The important findings of this Chapter have been summarized below.

1. We have extended the magnetic field data, used in the previous Chapter, which now covers the period from 1975 to the end of 2009 (1975.14 – 2009.86). In a manner that is similar to that carried out in the previous Chapter, we have computed the magnetic fields from the NSO/KP synoptic magnetograms in the latitude ranges, $0° - 45°$ and $45° - 78°$, that are referred as low-latitude and high-latitude fields respectively. We found

that the magnetic field variations for high-latitude fields both in the Northern and Southern hemispheres have shown a steady decline since around 1995 – 1996.

2. The time series comprising magnetic residuals obtained by subtracting a smoothed SG fit from the actual data were subjected to a Wavelet analysis based on Torrence and Compo (1998) algorithm. The resultant wavelet power spectrum of periodicities for both high- and low-latitude fields showed an unambiguous transition in the distribution of power at 1996.

3. Based on the clear transition seen, around 1996, in the wavelet spectrum, the magnetic time series was grouped into two sets: one before 1996 and other after 1996. These two data sets for both high- and low-latitude fields were then subjected to a special Fourier analysis that could handle unevenly spaced data. The Fourier periodicities obtained for high-latitude fields before and after 1996 have shown a North – South asymmetry in the distribution of the longest periodic component while the low-latitude fields don't show the same asymmetry.

4. Additionally, this North – South asymmetry for fields before and after 1996 is seen to be confined to the latitude range, $45^\circ - 60^\circ$, a latitude belt that is dominated by polar surges. Further examination of these surges for the last three solar cycles have shown an asymmetrical distribution in their occurrence rate and strength indicating similar kind of changes in meridional flow rates. This asymmetry, confined to the latitude range, $45^\circ - 60^\circ$, coupled with the decline in high-latitude fields from the mid-nineties suggests that active changes occurred in the solar dynamo in the interior around this time which in turn initiated the buildup to one of the deepest solar minima in the past 100 years, at the end of the Solar Cycle 23.

5. Besides the study of the distribution of periodicities before and after 1996, we have also detected a number of new periodicities both in high- and low-latitude fields. The new periodicities detected in our analysis are: 1.1 years, 1.9 years, 2.3 years, 2.5 years, 2.9 years, and 3.1 years in the low-frequency periods and 253 days, 257days, and 294 days in the high frequency periods. In contrast to the low-frequency Fourier components, the high frequency Fourier components for both high- and low-latitude fields do not show any asymmetry.

Chapter 5

Solar Cycle Changes of the Solar Wind Microturbulence Levels in the Inner Heliosphere Using IPS Observations

5.1 Introduction

The previous two Chapters discussed solar cycle changes of photospheric magnetic fields and their quasi-periodic variations using ground-based and space-borne magnetograph measurements. Our new findings, namely a correlation between variations of high-latitude photospheric fields and meridional flow rates in Cycle 23 (Janardhan, Bisoi and Gosain, 2010) and a North – South asymmetry in the quasi-periodic variations of photospheric fields at high-latitudes (Bisoi *et al.*, 2013) have given insights into the existing link between photospheric field activity and dynamic changes taking place below the solar surface. It is known that photospheric magnetic fields extend out into the corona and are subsequently dragged into the interplanetary medium by hot, tenuous, and continuous outflow of solar wind plasma to form the heliospheric or interplanetary magnetic fields (IMF). It is therefore obvious to expect similar variations in the IMF in response to the solar cycle dependent changes of solar photospheric magnetic field activity. Such changes could be detected through studies of solar wind turbulence because the IMF could vary in keeping with the variations in photospheric magnetic fields and heliospheric open flux. It has also been shown that the solar wind turbulence is related to both the rms electron density fluctuations (ΔN_e) and large scale magnetic field fluctuations in fast solar wind streams (Ananthakrishnan, Coles and Kaufman, 1980). So the long-term changes in the solar wind turbulence level could manifest themselves as corresponding changes in the rms electron density fluctuations which can be inferred by the technique of interplanetary scintillation (IPS). We have, in the present Chapter, taken up a study to investigate this aspect by studying the long-term changes in the solar wind scintillation or microturbulence levels using IPS observations at 327 MHz. Moreover, it is important to study and understand how the solar wind plasma responds to the steadily declining solar photospheric fields since ∼1996 that we have discussed in the previous two Chapters.

We have already discussed, in the previous two Chapters, the extremely deep solar minimum at the end of Cycle 23 during which the number of spotless days experienced in the years 2008 and 2009 were over 70%. Apart from this, solar polar fields during Cycle 23 were found to be weaker than those during the earlier Cycles, 21 and 22 (Janardhan, Bisoi and Gosain, 2010; Jiang *et al.*, 2011). This has far reaching consequences in the heliosphere with a global reduction of open magnetic flux, as revealed by the unprecedented solar wind measurements from the complete 17 years of operation of the *Ulysses* spacecraft (Wenzel *et al.*, 1992), which has been in space since October of 1990. Although other very successful and dedicated solar and solar wind space-missions, *viz.* Wind (Acuña *et al.*, 1995), Advanced Composition Explorer (ACE; Stone *et al.* (1998)), Solar and Heliospheric Observatory (SoHO; Domingo, Fleck and Poland (1995)), Solar TErrestrial RElations Observatory

(STEREO; (Kaiser *et al.*, 2008)), and the Hinode spacecraft (Kosugi *et al.*, 2007), have contributed significantly to our understanding of the solar wind in the heliosphere, the *Ulysses* spacecraft was the first and only out-of-ecliptic mission, to-date, that has explored the mid- and high-latitude heliosphere, during it's three solar passages. *Ulysses*, for the first time, has studied the dependence of $|B_r|$, the radial component of the IMF, as a function of the heliographic distance (r), and showed that product $|B_r|\, r^2$ is independent of the heliographic latitude (Smith *et al.*, 2003; Lockwood, Owens and Rouillard, 2009). This result implies that the magnetic field and solar wind expand radially from the high to low latitudes, and essentially enables one to use the measurements of $|B_r|$ to quantify the heliospheric open flux (Smith and Balogh, 2008). However, during the second Ulysses orbit (1999 – 2004), the solar wind dynamic pressure (momentum flux) was found to be significantly lower in the post maximum phase of Cycle 23 than during its earlier orbit, spanning the declining phase of Cycle 22 (Richardson, Wang and Paularena, 2001; McComas *et al.*, 2003). The third Ulysses orbit (2004 – 2008) showed an $\sim 20\%$ reduction in both solar wind mass flux and dynamic pressure in Cycle 23 as compared to the earlier two cycles (McComas *et al.*, 2008). While the measurements of heliospheric open magnetic flux ($|B_r|\, r^2$) have shown a decrease by 0.64 (Smith and Balogh, 2008) from the solar minimum of Cycle 22 to 23. *In situ* plasma data and magnetic field observations between 1995 – 2009 from the Wind and ACE, have shown that the solar minimum in 2008 – 2009 has experienced the weakest solar wind dynamic pressure and magnetic field as compared to the earlier three solar cycles (Jian, Russell and Luhmann, 2011).

In addition to the *in situ Ulysses* measurements, interplanetary scintillation (IPS) observations have been the only ground-based technique that is effective in studying the large-scale structure of the solar wind both in and out of ecliptic and over a large range of heliocentric distances. At 327 MHz, IPS observations can probe the inner heliosphere from ≈ 0.2 AU to 0.8 AU and over a wide range of heliolatitudes, and provide reliable estimates for the solar wind

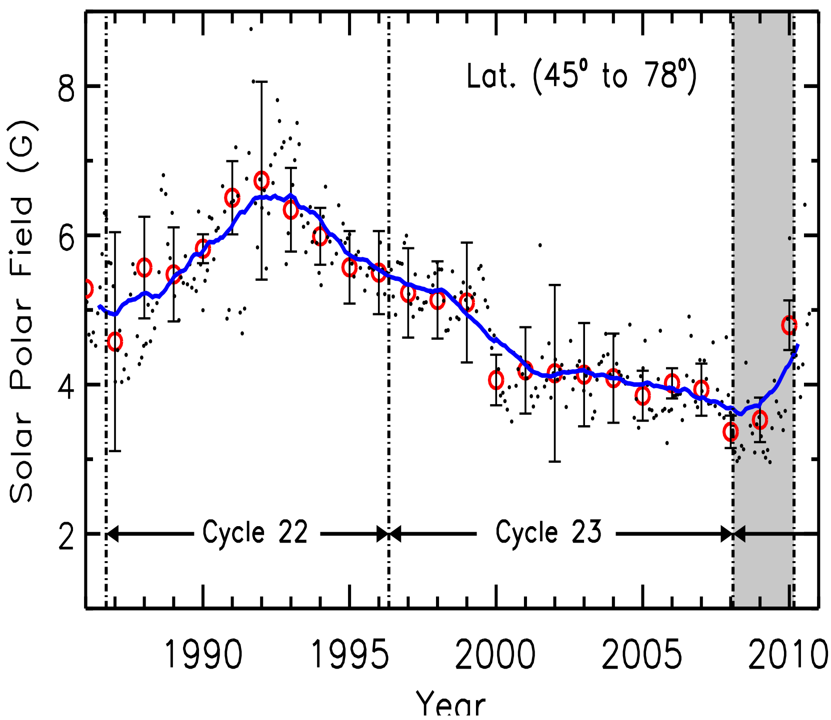

Figure 5.1: Shows the absolute value of the solar polar field, in the latitude range $45-78°$, as a function of time in years for Solar Cycles 22 and 23. The filled dots represent the actual measurements of solar polar magnetic fields, derived from the NSO/Kitt Peak data while the open red circles are the annual means with 1σ error bars. The solid blue line is a smoothed curve depicting the magnetic field variation during Cycles 22 and 23. The vertical lines demarcate respective, Cycle 22 and 23 while the grey shaded area indicates the period between the expected beginning of Cycle 24 and the actual time when Cycle 24 began.

speed and rms electron density fluctuations ΔN_e. The IPS technique has therefore been successfully used to study the large-scale structure of solar wind as function of heliolatitudes and distances over several solar cycles (Rickett, 1975; Ananthakrishnan, Coles and Kaufman, 1980; Hewish, 1989; Ananthakrishnan, Balasubramanian and Janardhan, 1995; Janardhan *et al.*, 1996; Hayashi *et al.*, 2003; Tokumaru, Kojima and Fujiki, 2010; Manoharan, 2012; Kojima *et al.*, 2013). In the present Chapter, we have exploited the IPS methodology to study solar cycle changes in solar wind microturbulence. Moreover, IPS is a very useful and cost-effective method (compared to *in-situ* spacecraft measurements) that has been efficiently used in the last few decades for probing the solar wind and in determining the angular diameter of radio sources in the range $0.1-1$ arcsec (Little and Hewish, 1968; Readhead and Hewish, 1974; Bhandari, Ananthakrishnan and Pramesh Rao, 1974; Janardhan and Alurkar, 1992, 1993).

In Chapter 3, we have discussed solar photospheric magnetic fields, computed from the ground-based magnetograms, spanning the last three Solar Cycles, *viz.* Cycles 21, 22, and 23. Figure 5.1 shows the variations of solar photospheric fields in the latitude range $45°-78°$ for Cycles 22 and 23. The filled dots represent the actual magnetic field measurements while the open circles are the yearly means with 1σ error bars. The solid line is a smoothed curve and the vertically oriented dashed parallel lines demarcate Cycles 22 and 23, respectively. The shaded gray area in the Figure indicates the time between the expected minimum in Cycle 23 and the time when Cycle 24 actually began. From Figure 5.1, a discernible and steady decline in the magnetic field is clearly seen since around 1995. As stated earlier, it is expected that these changes in magnetic field will be reflected in the solar wind plasma. In this present Chapter, employing IPS measurements from the Solar Terrestrial Environment Laboratory (STEL), Japan, covering the period $1983-2009$, we have thus undertaken a study to investigate the long-term changes in the microturbulence levels of the solar wind in the inner heliosphere. Although there have been many studies to try and understand the reasons behind this long and deep solar minimum, using both observations (Hathaway and Rightmire, 2010) and theoretical modeling (Dikpati *et al.*, 2010; Nandy, Muñoz-Jaramillo and Martens, 2011), none of these studies have provided any direct insights into the onset of this deep minimum. Using IPS observations of 27 extra-galactic radio sources, we have found a continuous decline since around 1995 in the turbulence levels of the solar wind in the inner heliosphere. In the following sections, the observations and the implication of this result in the buildup to one of the deepest solar minima, experienced in the past 100 years, at the end of Cycle 23, will be discussed.

5.2 Interplanetary Scintillation

IPS is a phenomenon similar to the twinkling of stars. The Earth's neutral atmosphere acts as an inhomogeneous media that actually causes the twinkling of stars by scattering of incoming light. In IPS, the electromagnetic radiation, coming from distant extra-galactic radio sources, suffer scattering on passing through the interplanetary medium and develop into a diffraction pattern which can be detected by ground-based radio telescopes (Hewish, Scott and Wills, 1964). The typical geometry during an IPS observation is shown in Figure 5.2. The broken lines in Figure 5.2 lie in the ecliptic plane, while the solid lines lie out of the ecliptic plane. The long-dashed line is the orbit of the earth around the Sun. The Line-of-sight (LOS) to a distant compact radio source with respect to the Sun ('S') and the Earth ('E') is shown by a solid line from E passing through the 'P', the point of closest approach of the LOS to the Sun. The angles ϵ and γ are respectively, the solar elongation and heliographic latitude of the source while 'A' is the foot point of a perpendicular from P to the ecliptic plane. The radial distance from the Sun, 'r' of the LOS to the radio source is given by $\sin(\epsilon)$.

Using the power spectrum of temporal intensity variations, recorded by

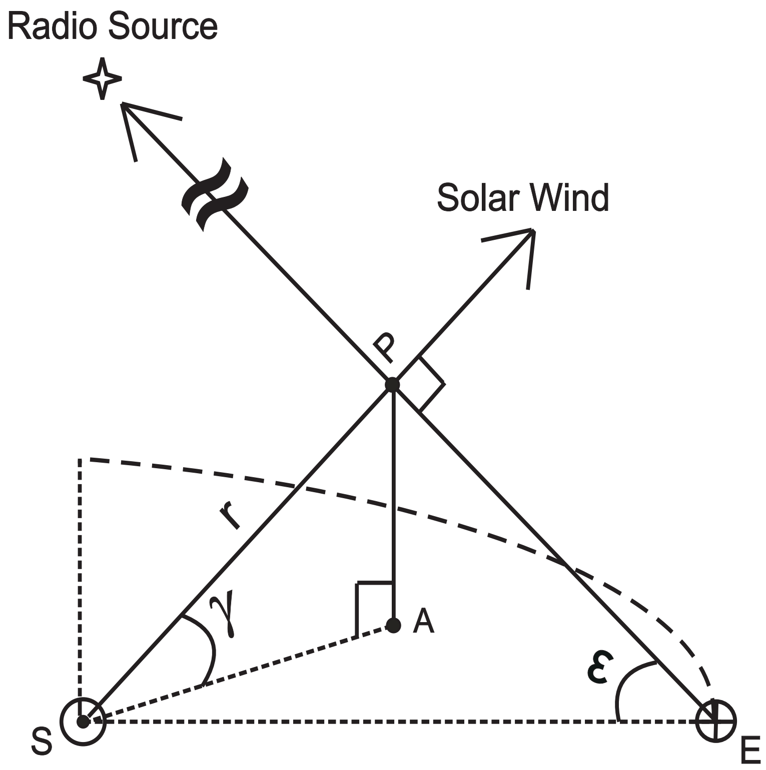

Figure 5.2: A schematic of the IPS observing geometry. The Earth, the Sun, the point of closest approach of the LOS to the Sun, and the foot point of a perpendicular from P to the ecliptic plane are shown by points E, S, P and A while the angles ϵ and γ are the solar elongation and heliographic latitude of the observed source. The radial distance from the Sun, 'r' of the LOS to the radio source is generally given by $\sin(\epsilon)$.

a single radio telescopes or by employing a cross-correlation analysis of the intensity variations using a network of three or more telescopes, one can find the solar wind speed and quantify the amount of scintillation along the LOS to a given source through a quantity called the scintillation index, m which is a measure of the rms electron density fluctuations, ΔN_e in solar wind along the LOS. The scintillation index, m is defined as ratio of the scintillating flux ΔS to the mean source flux $\langle S \rangle$.

$$m = \Delta S / \langle S \rangle \tag{5.1}$$

Thus, an ideal point source, whose scintillating flux is equal to the mean source flux, will have a scintillation index, m, of unity at some fixed distance from the Sun. In fact m increases with decreasing r or ϵ, until a certain ϵ. This region is known as weak scattering region. Beyond this point m falls off sharply as it approaches closer to the near-Sun region, called as strong scattering region. The ϵ at which m turns over is dependent on frequency and at 327 MHz it lies between 10° and 14° or ~40 $R_\odot$, where, $R_\odot$ is the solar radius.

It is important to note that IPS measures only fluctuations, and not the bulk density itself. However, any enhancement or decrease in IPS level in solar wind has been shown to be associated with corresponding variations in density. The relation between the scintillation level and the density (Hewish, Tappin and Gapper, 1985) is as given by equation 5.2.

$$g = (Ncm^{-3}/9)^{0.52 \pm 0.05} \tag{5.2}$$

where 'g' is the scintillation index normalized in a manner so as to make it independent of both distance from the Sun and the angular diameter of the extragalactic radio source and 'N' is the density.

Thus, whenever interplanetary disturbances (IPDs) travel in the IPM, containing either enhanced or depleted rms electron density fluctuations (ΔN_e) as compared to the background solar wind, they exhibit themselves as changes in the levels of scintillation (m), *i.e.* higher or lower than expected m. It implies that whenever solar wind turbulence levels change, they will be reflected in IPS measurements as changes in m. In other sense, identification of enhanced (g $>$ 1) or depleted (g $<$ 1) g-value indicates the presence of IPDs in the solar wind.

It is known from earlier studies that the IPS is extremely sensitive to small changes in ΔN_e. Therefore, IPS has been used to study such density fluctuations in tenuous cometary ion tails well downstream of the nucleus (Janardhan *et al.*, 1992) and also for solar wind disappearance events wherein average solar wind densities at 1 AU drop to values below 0.1 cm^{-3} for well over 24 hours (Balasubramanian *et al.*, 2003; Janardhan *et al.*, 2005, 2008b).

It is known that the solar wind density beyond $\sim$0.2 AU varies as r^{-2} (Bird *et al.*, 1994), where r = sin(ϵ). Thus as described earlier m also varies as function of r or ϵ from the Sun. The scattering for the region at ϵ larger than the turnover has been explained through a thin-screen approximation (Salpeter, 1967), where the scattering power, β of the medium falls rapidly with r ($\beta\ \alpha\ r^{-4}$ (Readhead, Kemp and Hewish, 1978). Therefore, the maximum contribution to the scattering occurs at the point 'P' on the LOS that is closest to the Sun. For an ideal point source (angular sizes of zero milli arcsec (mas)), m varies between unity at turn over distance to below unity at r greater than turn over distance. For sources, with finite compact component sizes ($>$ 0 mas), m will be $<$ unity at the turnover. Figure 5.3 shows how m for the source 1148-001 varies with r in a weak scattering regime where r is expressed in units of AU. These m values are derived from IPS observations regularly carried out at the STEL, Nagoya University, Japan. The source 1148-001 has an angular size of $\leq$10 mas at 327 MHz and is regarded as a nearly ideal point source (Venugopal *et al.*, 1985). It can be seen from Figure 5.3 that m decreases from unity as r increases, and thus m decreases as ϵ increases.

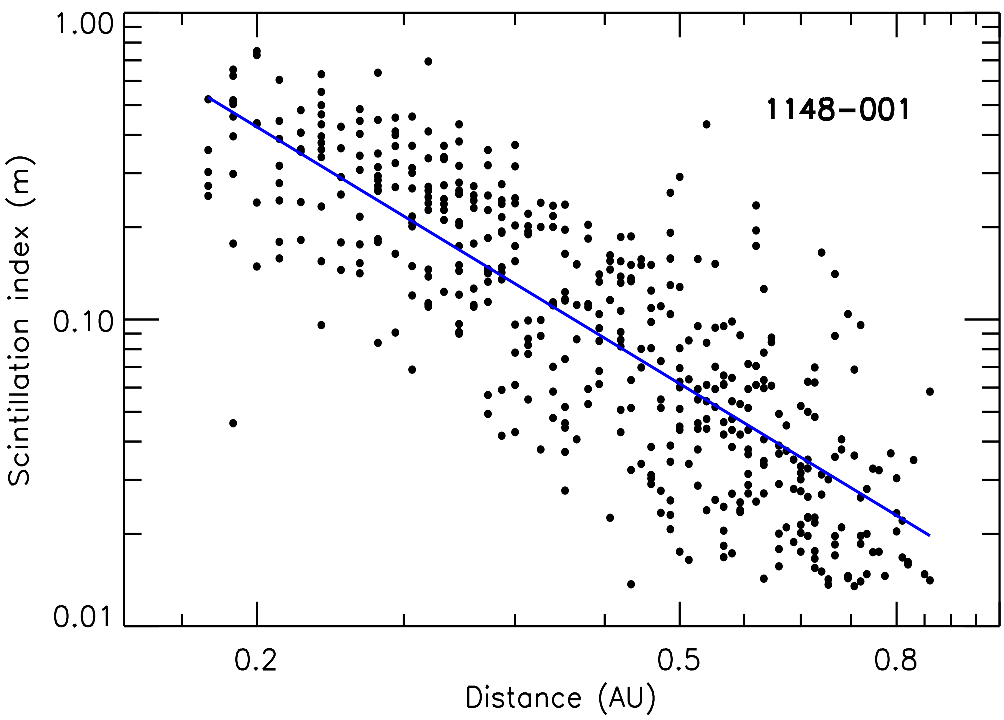

Figure 5.3: Shows variation of m as function of heliodistance, expressed in units of AU, in a weak scattering regime at 327 MHz, for a nearly ideal point radio source 1148-001 whose angular diameter is known to be 10 mas. The solid blue line is a least square fit to the data.

5.2.1 Distance Independence of Scintillation Index

For the steady state solar wind, values of m can be computed by obtaining theoretical temporal power spectra using a solar wind model assuming weak scattering and a power law distribution of density irregularities in the IP medium for any given source size and distance r of the LOS from the Sun (Marians, 1975).

The set of six curves (labeled 'A') in Figure 5.4 show the theoretically expected m as a function of ϵ for various source sizes in mas, assuming weak scattering at 327 MHz. To remove the ϵ or distance dependence of m, each observation of m has to be normalized by that of a point source at the corresponding ϵ. It has been shown that the source 1148-001 is $\leq$10 mas in angular extent at 327 MHz. Thus, 1148-001 can be treated as a nearly ideal point source, with most of its flux contained in a scintillating compact component of angular size $\sim$10 mas (Venugopal *et al.*, 1985). Normalizing all observations of m in this manner will yield an ϵ or distance independent value of m as shown for three source sizes (labeled 'B') in Figure 5.4. It must be noted that the curves in Figure 5.4 imply that the radial fall off rate is slightly different for different source sizes. Thus, the m for the larger source sizes will be overcorrected at large distances. However, most of the observed IPS sources are strong scintillators at 327 MHz with sizes $\leq$250 mas and will not suffer from this normalization.

5.3 Observations and Data Reduction

The Japanese multi-station IPS facility consists of three antennas at Toyokawa, Fuji and Sugadaria, operated by the STEL, Nagoya University, Japan, and are used for the observations described in this Chapter. This three-station IPS facility has carried out IPS observations at 327 MHz on about 200 compact extragalactic radio sources on a regular basis to derive solar wind velocities and

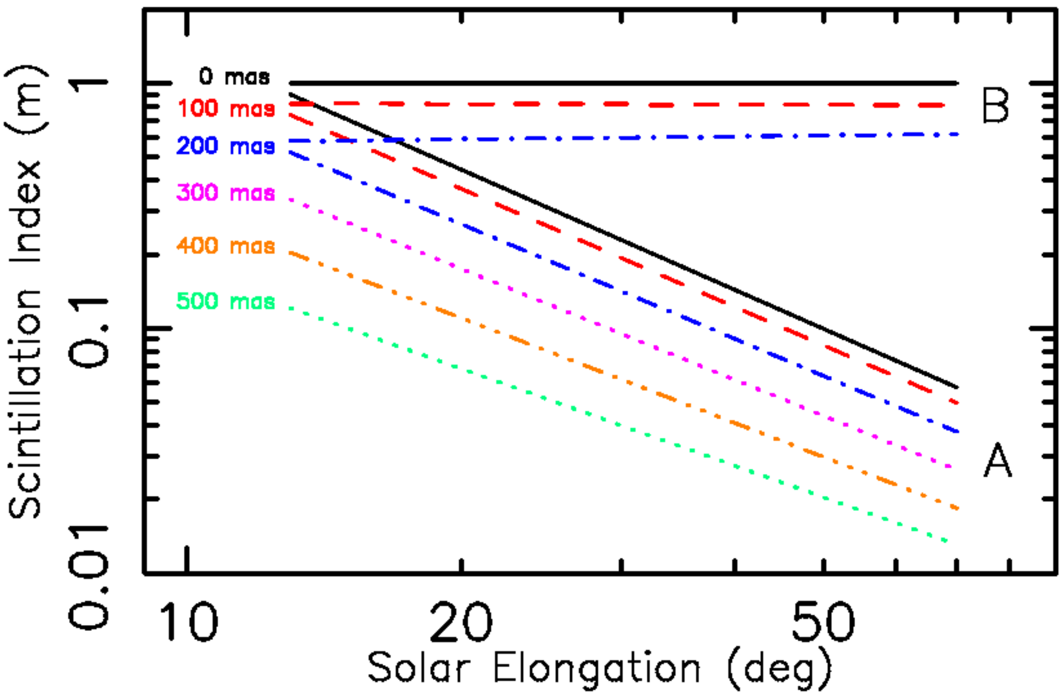

Figure 5.4: Curves (labeled 'A') of theoretically expected m as a function of ϵ for various source sizes. Curves (labeled 'B') corresponding to source sizes of 0 mas, 100 mas, and 200 mas, have been normalized by the point source m at the corresponding ϵ and have hence made independent of the distance from the Sun.

scintillation index (Kojima and Kakinuma, 1990; Asai *et al.*, 1998; Tokumaru, Kojima and Fujiki, 2012). In 1994, a fourth antenna at Kiso was added to the system to form a four-station network that could provide more robust estimates of the solar wind speed owing to the redundancy in the baseline geometry obtained by having an additional station.

We have used data from 1983 to 2009, which had a one year data gap in 1994 owing to the development of the fourth IPS station, and have chosen sources which had at least 400 individual observations over this period of 27 years. We also ensured that there were no significant data gaps in any given year, apart from the one year gap in 1994. Of the total of 215 sources observed, we were finally left with 26 sources covering the entire 24 hour range of source right ascensions (RA) and a wide range of source declinations (Dec). The point source 1148-001 was included as the 27th source even though it had some data gaps and therefore did not fully comply with our selection criteria. Figure 5.5 shows positions of all these 27 sources with respect to the Sun, while Table 5.1 lists the RA and Dec of these sources. Both from Figure 5.5 and Table 5.1, it is again clear that the 27 selected sources actually cover a wide range of declinations, which gives a broad range for studying solar wind turbulence levels in the inner heliosphere.

As stated earlier, we made the IPS observations distance independent by normalizing every individual observation for each source by the value of m for the source 1148-001 at the corresponding ϵ.

Table 5.1: Lists source right ascensions and declinations for all 27 sources.

IAU Name	Common Name	Coordinates (J2000)
0003−003	3C2	00 06 22.6 −00 04 25
0056−001	-	00 59 05.5 +00 06 52
0127+233	3C43	01 29 59.8 +23 38 20

Continued on next page

Table 5.1 – *Continued from previous page*

IAU Name	**Common Name**	**Coordinates (J2000)**
0134+329	3C48	01 37 41.3 +33 09 35
0316+162	CTA21	03 18 57.8 +16 28 33
0320+053	-	03 23 20.3 +05 34 12
0429+415	3C119	04 32 36.5 +41 38 28
0518+165	3C138	05 21 09.9 +16 38 22
0538+498	3C147	05 42 36.1 +49 51 07
0624−058	3C161	06 27 10.1 −05 53 05
0741−063	-	07 44 21.6 −06 29 36
0809+483	3C196	08 13 36.0 +48 13 03
0949+002	3C230	09 51 58.8 −00 01 27
1005+077	3C237	10 08 00.0 +07 30 16
1116−027	3C255	11 19 25.2 −03 02 52
1140+223	3C263.1	11 43 25.1 +22 06 56
1148−001	-	11 50 43.9 −00 23 54.2
1226+023	3C273	12 29 06.7 +02 03 09
1245−197	-	12 48 23.9 −19 59 19
1253−055	3C279	12 56 11.1 −05 47 22
1416+067	3C298	14 19 08.2 +06 28 35
1428−033	-	14 30 49.0 −03 34 46
1524−136	-	15 26 59.4 −13 51 00
1730−130	-	17 33 02.7 −13 04 50
2251+158	3C454.3	22 53 57.7 +16 08 54
2347−026	-	23 50 25.4 −02 24 43

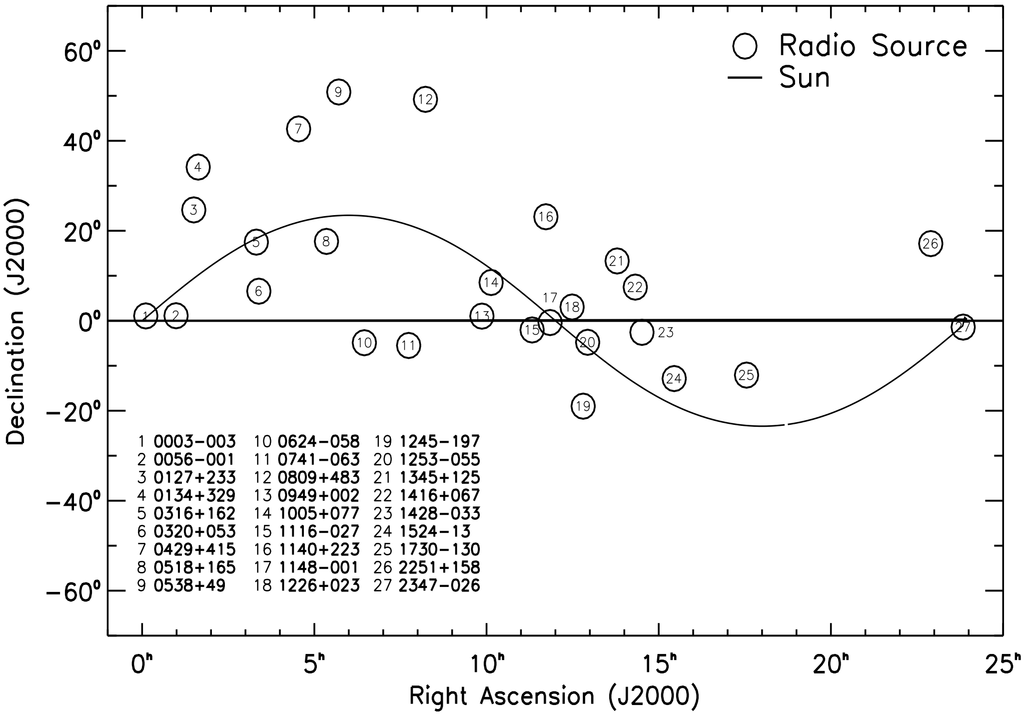

Figure 5.5: Shows position of all 27 radio sources. The open circles represent radio source positions while the solid line shows the path of the Sun. The IAU name of all 27 sources are indicated at the bottom left.

5.4 Results

Figure 5.6 shows plots of m as a function of time in years for the 27 chosen sources lying in the distance range 0.26 to 0.82 AU. The grey crosses are measurements when the source heliolatitude is $\leq 45°$ while the fine red dots are measurements when the source heliolatitude is $>45°$. The large, blue, open circles are yearly averages taken without the high latitude observations. The reason for dropping the high latitude observations from the yearly averages is because IPS observations have shown (Tokumaru *et al.*, 2000) that the solar wind structure changes with the solar cycle, being more or less symmetric at solar maximum and considerably asymmetric during solar minimum. This asymmetry could change the way m falls off with radial distance. Since our IPS observations contain measurements distant from the Sun near the solar equator and measurements at small ϵ at high solar latitude, we drop the high latitude observations from the yearly averages in order not to affect the yearly means. In addition, long term and gradual changes in the antenna sensitivity caused by degradation in the efficiency of the system, could cause some changes in the IPS measurements over time. Such changes are very difficult to quantify, but every effort has been made to maintain the system stability and we believe that these changes cannot account for or explain the systematic drop in m, seen in Figure 5.6, starting from around 1995.

It can be seen from Figure 5.6 that all the sources show a steady decline in m starting from around $\sim$1995 implying a reduction in solar wind turbulence levels. The drop in m ranges between 10% and 25% when the annual means are taken considering all observations and it ranges between 10% and 22% when the annual means are taken without including the high latitude observations. The average drop is, therefore, around 16%. One must note, however, that only 16 of the 27 sources go to latitudes above 45° while the remaining 11 sources have all observations at heliolatitudes $\leq 45°$. In order to achieve greater clarity and to avoid any confusion caused by showing a large number of panels

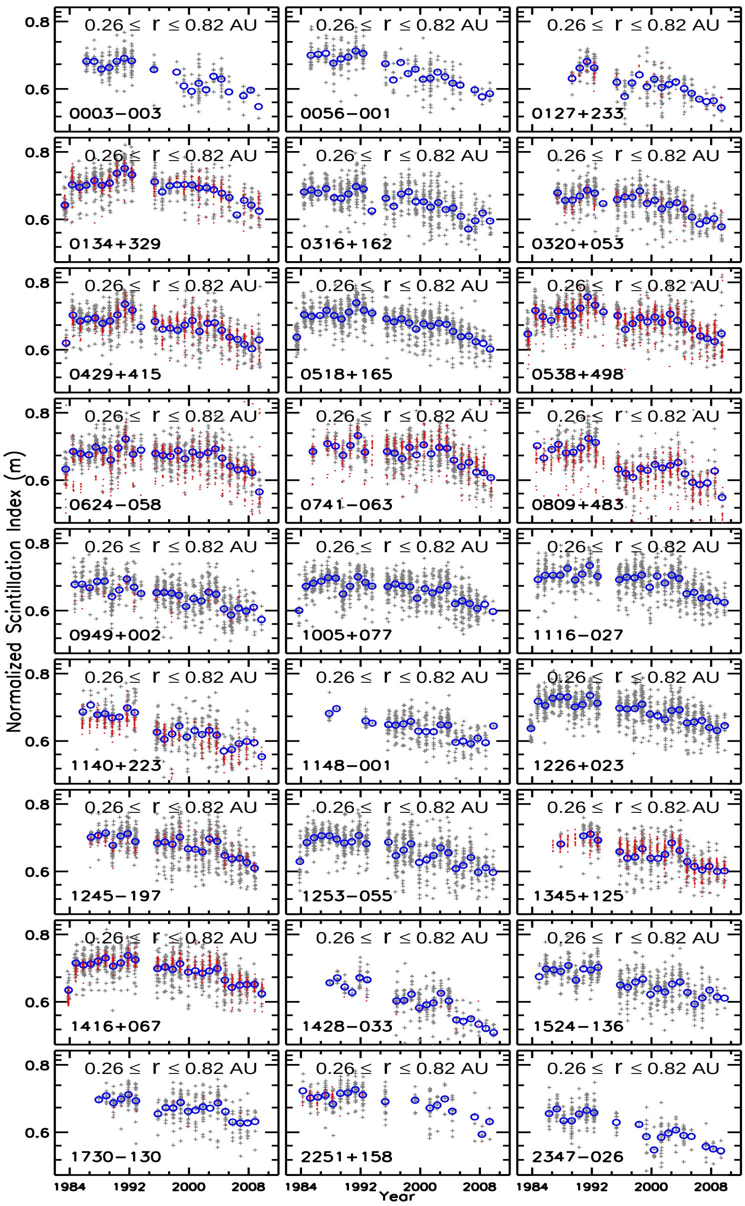

Figure 5.6: Plots m as a function of time in years for 27 sources, in the distance range 0.26 – 0.82 AU corresponding to an elongation range 12° –55°, after m has been made independent of distance from the Sun by normalizing each observation by the value of m for the source 1148-001. The grey crosses are observations at source helio latitudes ≤45° while the fine red dots are observations at source heliolatitudes >45°. The open circles are yearly averages by excluding the high latitude observations. The IAU name of each source is indicated at the bottom left in each panel.

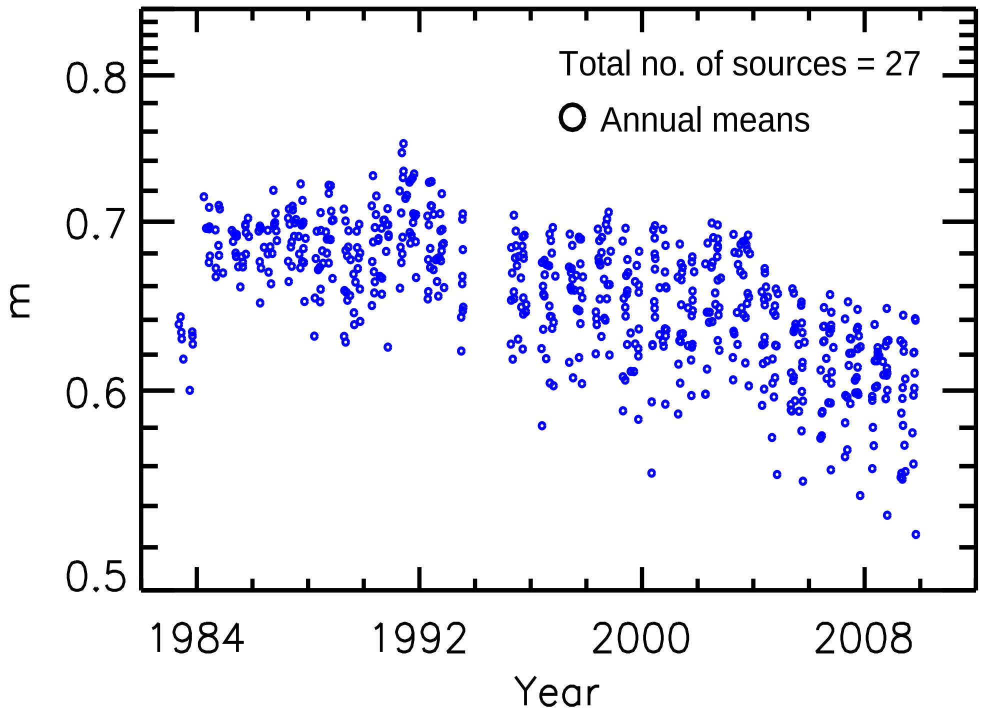

Figure 5.7: Shows the annual means of m as a function of time, covering the period between 1983 − 2009, for each of the the 27 sources shown in Figure 5.6.

in Figure 5.6 the yearly means of each source (blue open circles) are shown again, in Figure 5.7, as a composite plot of m as a function of time in years. The steady drop in m from ∼1995 can be unambiguously seen again in Figure 5.7.

5.5 Discussions

From our results, we have thus noticed that the turbulence levels, as indicated by reduced scintillation levels in the IP medium, have dropped steadily since ∼ 1995. Also, we have found that solar polar fields have shown a steep decline since ∼1995. Since solar polar fields supply most of the heliospheric magnetic flux during solar minimum conditions (Svalgaard, Cliver and Kamide, 2005), the long-term decline in polar field strength imply that the IMF would also be significantly lower. In fact, $|B_r|$ has been found to be lower during this long deep solar minima, at the end of Cycle 23, than in the past three minima (Smith and Balogh, 2008) indicating much lower heliospheric open flux. Moreover, this decline in polar fields and heliospheric open flux have affected magnetic field fluctuations or the solar wind turbulence in fast solar wind at high-latitudes resulting a decrease by a factor of 0.75 (Smith and Balogh, 2008). A causal relationship between stronger magnetic fields and turbulence in the high-latitude region implies a decrease in turbulence levels over the solar poles since ∼1995. It has been shown that the solar wind turbulence is related to both the rms electron density fluctuations (ΔN_e) and large scale magnetic field fluctuations in fast solar wind streams (Ananthakrishnan, Coles and Kaufman, 1980). Similarly, it is possible that a global reduction in the IMF is being reflected as a large scale global reduction in m (or microturbulence) as shown by our observations.

As opposed to our method, IPS observations of the change in the turnover distance of m, which defines the minimum distance (from the Sun) at which the weak scattering regime starts, have shown a steady decrease in the scattering diameter of the corona since 2003 (Manoharan, 2010). It must be noted, however, that the turnover distance is not sharply peaked, but is a rather broad turnover, so the method is not as sensitive as the one that we have used. Our method can thus detect the decline in solar wind turbulence as early as ∼1996.

A great deal of work has been done in modeling the solar dynamo and predicting the strength of future solar cycles. It has been argued (Dikpati, de Toma and Gilman, 2006) that since the meridional circulation period is between 17–21 years in length, the strength of the polar fields during the on-going cycle minimum and the preceding two solar minima will influence the strength of the next cycle. Another viewpoint is that of Choudhuri, Chatterjee and Jiang (2007) who claim that only the value of the polar field strength in the ongoing cycle minimum is important in predicting the next cycle. Nandy, Muñoz-Jaramillo and Martens (2011) used a kinematic dynamo simulation model that adjusted the flow speeds in each half of the cycle to reproduce the extended minimum in Cycle 23. Their model showed that the changes in the meridional flow speeds that led to the extended minimum began as early as the mid to late 1990s and also predicted that very deep minima are generally associated with weak polar fields. Furthermore, Dikpati (2011) compared the last two minima in Cycle 22 and 23, and using the theory of meridional circulation, they found a difference in the latitudinal extent of meridional flow speeds in Cycle 22 and 23. Based on the finding that meridional flows, in Cycle 23, extended to the poles while in Cycle 22 it extended only to latitudes $\pm 60°$, they went on to propose that the longer conveyer belt of the Sun in Cycle 23 actually caused the extended solar minimum of Solar Cycle 23.

However, none of these studies provide any insights into the onset of this deep minimum. The fact that the change in the meridional flow that regulates the solar dynamo began in the mid 1990s coupled with the fact that solar polar fields have been declining since ∼1995 and our IPS observations all provide a consistent result showing that the buildup to the long solar minimum, prior to

Solar Cycle 24, actually began around 1996 ≈ 13 years ago when our analysis stopped in 2009. Additionally, a North – South asymmetry, in quasi-periodic distribution of photospheric fields grouped prior to and after 1996, has also shown that the buildup to this deep solar minimum was initiated at ≈ 1995 – 1996, almost 12 years before the minimum period in 2008 – 2009.

It is important to state here that observations beyond 2009 have shown that the declining trend is continuing to the present date (until 2012) and Figure 5.8 shows this updated annual means of m as function of time, covering a period of 1983 – 2012, for the 27 selected sources.

On the other hand, solar maximum has been predicted through the drift of coronal Fe XIV emission features over time at high latitudes, referred to as "rush-to-the-poles (RttP)" (Altrock, 2003). The RttP began to appear approximately 3 or 4 years prior to solar maximum and then rush to the poles. Using observations of these coronal emission features from ground-based intensity synoptic maps, Altrock (2011) was able to show that the solar maximum, for Cycles 21, 22 and 23, occurs approximately 1.5 years prior to the RttP reaching the solar poles.

5.6 Summary and Conclusion

In the present Chapter, we have investigated solar cycle changes of solar wind micro-turbulence levels in the inner heliosphere through measurements of scintillation levels obtained from the STEL, IPS facility, Japan, covering the period from 1983 to 2009. For carrying out the study of temporal changes in m, we prepared a sample of m for 27 radio sources selected from around 200 radio sources. The selection criterion was made based on the ground that each of radio sources should have at least 400 measurements of m spreading from 1983 to 2009 without any data gap except for the year 1994. Each of these m values then were made distance independent by normalizing individual m for each source by the value of m for the source 1148-001 at the corresponding ϵ. Af-

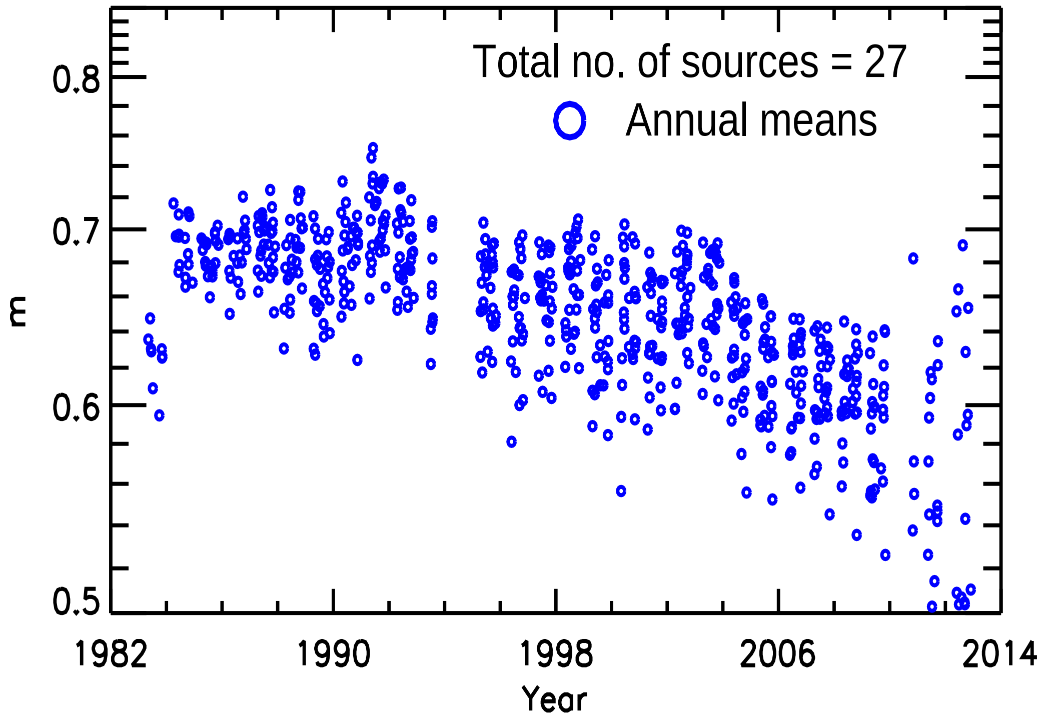

Figure 5.8: Shows the new annual means of m as a function of time for each of the 27 selected radio sources. Scintillation index measurements used here were extended, from those used in Figure 5.7, covering the period between 1983 − 2012.

ter removal of the distance dependence, the temporal variations of m for each of the 27 sources at helio-latitudes $\leq 45°$ were studied in the distance range $0.26 - 0.82$ AU in the entire inner heliosphere.

The temporal changes of m in our observations have shown a steady decline of m since mid-1990s for each of the selected 27 sources. A global reduction in m since mid-1990s implies a global reduction of microturbulence levels in the inner heliosphere since mid-1990s too. Also, a similar decrease in solar polar fields have been noticed since around 1995. In addition, a numerical simulation model of solar dynamo has shown that meridional flow changes also began in the mid-1990s (Nandy, Muñoz-Jaramillo and Martens, 2011).

In conclusion, our IPS observations coupled with the fact that solar polar fields have been declining since $\approx 1995 - 1996$ provide a consistent result that the buildup to one of the deepest solar minima in the past 100 years, that occurred at the end of Cycle 23, began well over a decade earlier.

Chapter 6

Unique Observations of a Geomagnetic SI^{+} – SI^{-} Pair and Associated Solar Wind Fluctuations

6.1 Introduction

It is well known that dynamic evolution of photospheric solar magnetic fields and changing conditions in the solar wind drive space weather at 1 AU and in near-space environment. Specifically, events on the Sun that cause perturbations in the Earth's coupled magnetosphere-ionosphere system are usually called geo-effective and are primarily responsible for geomagnetic activity on the Earth. In the previous Chapter, using the ground-based magnetograph observations, we have shown a systematic decline in the solar wind microturbulence levels in the entire inner heliosphere since ∼1995 – 1996 as the causal effect of the steady decline in solar photospheric magnetic field activity (Janardhan, Bisoi and Gosain, 2010; Janardhan *et al.*, 2011). In the present Chapter, we have undertaken a detailed study of one ground-based magnetic event to show the observational link between the specific solar events and space weather effects at 1 AU.

Generally, solar wind plasma moving with the velocity, V and having a frozen-in interplanetary magnetic field (IMF), normal to the ecliptic, imposes an electric field, E = (-V $\times$ B), called the interplanetary electric field, continuously on the Earth's magnetosphere. However, a southward pointing IMF (IMF-Bz), if present, causes or leads to magnetic reconnection between the IMF and magnetospheric fields (Dungey, 1961), which in turn, opens up the path for transmission of solar wind energy into the magnetosphere resulting in magnetic disturbances on the Earth (Burton, McPherron and Russell, 1975; McPherron, 1979; Gonzalez, 1990; Tsurutani and Gonzalez, 1997). Geomagnetic disturbances are thus, outcomes of the complex interactions of solar and magnetospheric processes at various time scales ranging from solar cycle time scales and longer (long-term solar cycle variations) to 27 days (recurrent solar activity), days (magnetic storms) and hours (magnetospheric substorms). Solar sources of these geomagnetic disturbances can range from fast and slow solar wind streams, solar flares, filament eruptions, co-rotating interaction regions (CIR), coronal mass ejections (CMEs), interplanetary CMEs (ICMEs), and solar energetic particle events (SEPs). Although a majority of space weather events at 1 AU are caused by explosive and energetic solar events, such as CMEs and solar flares, some recent studies have unambiguously associated large space weather events at 1 AU, like "solar wind disappearance events", to small transient mid-latitude coronal holes butting up against large active regions at central meridian (Janardhan *et al.*, 2005, 2008b; Janardhan, Tripathi and Mason, 2008a). These studies have provided the first observational link between the Sun and space weather effects at 1 AU, arising entirely from non-explosive solar events.

There have been substantial observations and discussions on the close correspondence between solar wind parameters at 1 AU and ground-based geomagnetic field variations (Dungey, 1961; Heppner and Maynard, 1987; Goodrich *et al.*, 1998; Lu *et al.*, 1998). However, it is not straightforward, under this broad framework, to pinpoint either the solar origins of specific space weather events or find specific correlations between solar wind parameters at 1 AU and ground-based magnetic observations. This is because such signatures are generally weak and are usually washed out or masked by the large variety of interactions that can take place both in the interplanetary medium and within the Earth's magnetosphere. Space weather events are, however, often preceded by the arrival at 1 AU of strong interplanetary (IP) shocks that shows strong discontinuities in solar wind plasma parameters and an abrupt increase in the magnetic field intensity (Gosling *et al.*, 1968). Therefore the studies of IP shocks are crucial and provide important inputs in understanding the propagation of solar-initiated IP disturbances out to 1 AU and beyond. In this Chapter, we have studied the role of such IP shocks that caused a ground-based magnetic event of a sudden impulse or $SI^+ - SI^-$ pair observed on April 23 – 24, 1998 (Rastogi *et al.*, 2010). This study deals with the unique correspondence between solar wind density fluctuations at 1 AU and geomagnetic field variations at low-/mid-latitudes.

The very first observations, by the Mariner 2 spacecraft (Neugebauer and Snyder, 1962) in 1962, of interplanetary shock waves showed the possibility of the existence of double shock ensembles in the interplanetary medium (Sonett *et al.*, 1964). However, the very unusual plasma and field variations associated with these structures prompted Sonett and Colburn (1965) to suggest that the first or '*forward*' shock would give rise to a positive H-component at ground based observatories while the second or '*reverse*' shock would cause an oppositely directed or negative change in the H-component of the Earth's horizontal field, as measured along the local geomagnetic meridian (H). These impulses, known as sudden impulse or $SI^+ - SI^-$ pairs, were typically separated by a few hours in time and were hypothesized to be caused by the arrival at 1 AU of the forward and reverse shock pair convected towards the Earth by the solar wind. Razdan, Colburn and Sonett (1965) described worldwide occurrences of such

SI pairs and suggested that they were associated with solar disturbances driving interplanetary shocks at highly oblique angles to the solar wind streaming direction. They however, did not find any solar activity or associated occurrences of solar radio emission during the period of SI pairs. The existence of forward and reverse shock pairs was finally established by the careful analysis of plasma and magnetic field measurements associated with shocks by Burlaga (1970) and Lazarus, Ogilvie and Burlaga (1970). However, in a study of a number of $SI^+ - SI^-$ pairs covering the period 1995–1999, Takeuchi *et al.* (2002) concluded that the observed SI^- or negative impulses in their sample were not associated with reverse shocks and showed no preferential association to any particular kind of solar wind structure, like high- and low-speed stream interface discontinuities or front boundaries of interplanetary magnetic clouds.

Early theoretical support came from Dryer (1970, 1972) who introduced the physics of finite electrical conductivity within the forward and reverse shock pairs, to derive reasonable first order predictions for the observed distribution of solar wind speed, density, and temperature. This was followed up by several other early papers on similar lines by (Eviatar and Dryer, 1970; Shen and Dryer, 1972; Dryer *et al.*, 1975). In more recent times, there have been a number of theoretical models that use inputs from solar data to predict the arrival of IP shocks and IP CMEs at Earth (Odstrcil, 2003; Vandegriff *et al.*, 2005; Tóth *et al.*, 2005; Detman *et al.*, 2006), including the well-known Hakamada-Akasofu-Fry (HAFV2) model, described in detail by Fry *et al.* (2003). It may be noted that the HAFV2 is the only model to have been substantially validated in an operational forecasting environment during Solar Cycle 23 (Smith *et al.*, 2009a,b).

It is occasionally noticed that the y-component (dawn-to-dusk) of interplanetary electric field (IEF_y), which when imposed onto the nightside magnetosphere causes a convection of plasma towards the Earth. Under normal circumstances, the effects of IEF does not reach directly to low-latitude ionosphere owing to a process called "shielding" (Nishida, 1968; Vasyliunas, 1970;

Spiro, Wolf and Fejer, 1988; Wolf *et al.*, 2001; Goldstein *et al.*, 2002), that occurs at the inner edge of the ring current. The shielding, however, in the presence of a fast fluctuating southward IMF-Bz, is temporarily weakened or broken. This leads to prompt penetration of the IEF. During period of sudden northward turning of the IMF-Bz, from a steady southward configuration, the convection electric field decreases abruptly while the shielding electric field takes a longer time to decay and produces a residual electric field, that is opposite to the direction of the IEF. This process is commonly known as the overshielding effect. The present Chapter describes these events of prompt penetration and overshielding occurred due to sudden changes (southward or northward turning) of the IMF between the time interval of $SI^+ - SI^-$ pair observed on April 23-24, 1998. In addition, we have also discussed, in this Chapter, how the changes in the geomagnetic fields are caused by the arrival at 1 AU of a forward-reverse shock pair associated with a rear side fast (~1850 kms^{-1}) partial halo CME and an optically occulted GOES M1.4 class flare which took place just behind the limb at S43W90 on April 20, 1998.

6.2 The $SI^+ - SI^-$ Pair of 23 April 1998

An $SI^+ - SI^-$ pair was identified at the three Indian geomagnetic observatories, Gulmarg, Alibag, and Trivandrum, between 1835 and 2300 UT on 23-24 April 1998. The SI pair recorded as a sudden positive impulse in H at 1835 UT (2335 LT) followed by a sudden negative impulse at 2300 UT (24 Apr. 0430 LT). Figure 6.1 (bottom-most panel) shows the tracings of H magnetograms (projected onto the x-direction and marked ΔX in Figure 6.1 at Gulmarg, Alibag and Trivandrum. During the time interval between the SI^+ and the SI^- impulse, the amplitude of H first decreased and then attained a peak of 44 nT at Trivandrum that progressively increased to 54 nT at Alibag and 76 nT at Gulmarg. Between 2100-2300 UT large fluctuations were recorded at all stations. The fluctuations in H, at all stations, were remarkably similar to each other with the amplitude increasing from Trivandrum to Gulmarg.

Figure 6.1 shows (starting from the top and going down) the corresponding variations of the solar wind velocity, IMF-Bz, the interplanetary electric field, the solar wind flow pressure, the solar wind density and the symmetrical H Field on 23-24 April 1998 respectively. These solar wind parameters are obtained from combined IMF and solar wind data at 1 AU, recorded by instruments on board the Advanced Composition Explorer (ACE; Stone *et al.* (1998)) and Wind (Acuña *et al.*, 1995) spacecrafts, available in the public domain from `http://cdaweb.gsfc.nasa.gov/cgi-bin/eval2.cgi`. The curve for the solar wind density, as observed by the spacecraft ACE has been shaded grey, in Figure 6.1, in the region between the $SI^+ - SI^-$ pair. The vertically oriented dashed parallel lines demarcate the time interval between the SI^+ impulse and the SI^- impulse. It is to be noted that the symmetric H field (SYM/H), characterizing the mean variation of H at the mid-latitude stations around the world, too had remarkably similar variations as the H at Indian stations. This therefore implies that the SI pair was a global event. SYM/H components used here are average values of symmetric H components at each minute for six stations collected from the World Data Center (WDC) for Geomagnetism at the University of Kyoto.

It can be seen from Fig. 6.1 that ΔX at Indian stations just after the SI^+ at 1835 UT (around local midnight) had gradually decreased until 2000 UT. This effect is due to the prompt penetration of the electric field when the IMF-Bz is negative during the period. At around 2000 UT, ΔX again increased suddenly to values much above the first impulse level. Correspondingly, it can be seen that IMF-Bz turned from southward to northward at this instant, implying that it is due to the overshielding condition. After this, the level of ΔX went down, with some oscillations, and finally came down to normal level at 2300 UT. It is interesting to note that the fluctuations in ΔX between 2130-2200 UT were correlated with the solar wind density rather than with the IMF-Bz or the solar wind speed. The SI^+ at 1835 UT was associated with a sudden

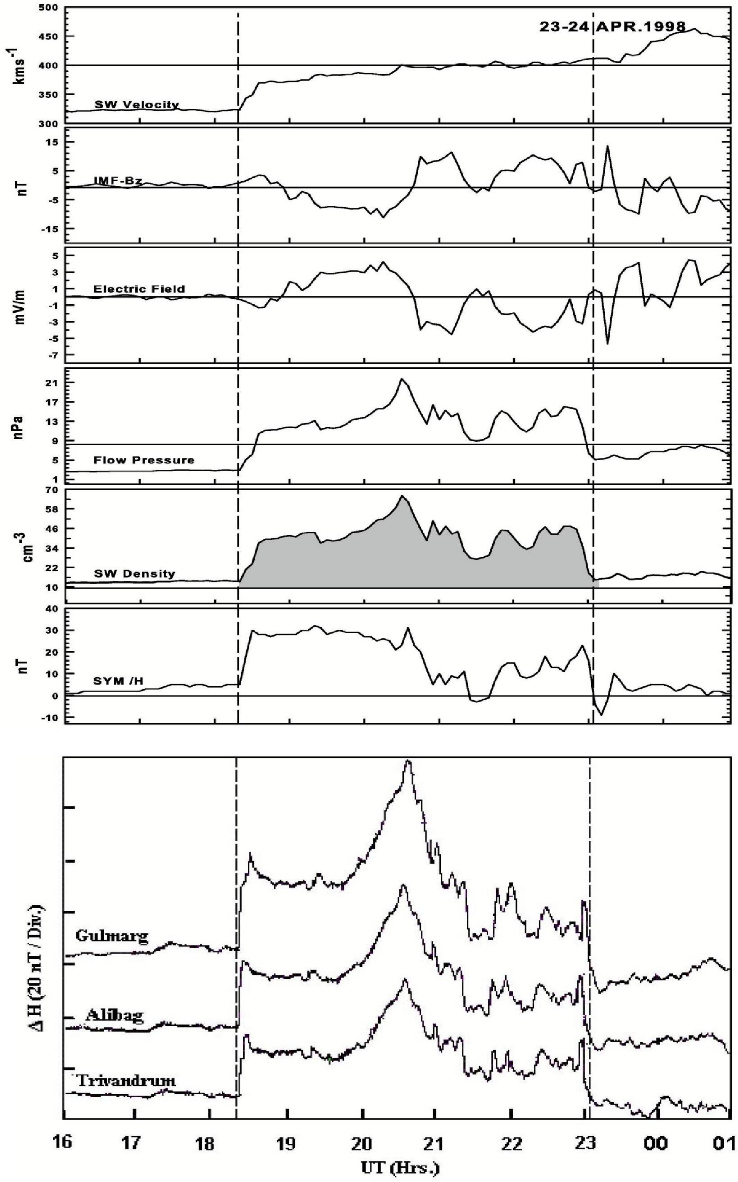

Figure 6.1: The first six panels starting from the top show the variations as a function of time in UT on 23–24 April 1998 of the solar wind velocity, Bz, the Electric field, the solar wind flow pressure, the solar wind density (shaded grey) and the symmetrical H Field respectively. Observations of the H field at Indian geomagnetic stations Gulmarg, Alibag and Trivandrum are shown in the bottom most panel. The pair of dashed vertically oriented parallel lines in all panels demarcate the times 1835 UT and 2300 UT. These times correspond respectively to the times of the SI$^+$ impulse and the SI$^-$ impulse in the H field, that were observed at Indian stations.

increase of both the solar wind density and speed causing a sudden pressure or impulse on the magnetosphere, as first suggested by Gold (1959), on the other hand, the SI^- at 2300 UT was associated with the sudden decrease of solar wind density.

6.2.1 Global Geomagnetic Fields

Figure 6.2 shows the variation of the horizontal component of the geomagnetic field projected onto the X direction (ΔX) from eleven low latitude stations around the world on 23–24 April 1998. The stations, starting from Alibag (ABG – Lat. 18.64; Long.72.87), India (uppermost curve) and arranged in increasing order of geographic longitude are respectively, Gnangara (GNA – Lat. -31.78; Long. 115.95), Esashi (ESA – Lat. 39.24; Long. 141.35), Honululu (HON – Lat. 21.32; Long. 202.00), Frenso (FRN – 37.10; Long. 240.30), Del Rio (DLR – Lat. 29.49; Long. 259.08), Kourou (KOU – Lat. 2.21; Long. 307.27), Ascension Island (ASC – Lat. -7.95; Long. 345.62), Hermanus (HER – Lat. -34.42; Long. 19.23), Addis Ababa (AAE – Lat. 9.02; 38.77) and Tanan- anarive (TAN – Lat. -18.92; Long. 47.55). The geographic longitudes of the ground stations are indicated at the left of each curve. Also, indicated to the right of the vertical dashed line (marked at 20.5 Hrs UT in Fig. 6.2) for each curve is the local time at 20.5 hrs UT. The stations chosen range from geographic longitudes of 19° to 346° corresponding to local times of ~22 hours through the midnight, dawn, noon to dusk (20 hours).

The negative IMF-Bz between 1835 – 2000 UT caused a decrease of ΔX at stations in the night sectors (HER, AAE, and TAN) and an increase at stations in the mid day sector (FRN, DLR, KOU and ASC). ΔX around 20.50 UT showed strong positive peaks at AAE, TAN and ABG, no change at ESA and HON and negative peaks at FRN, DLR and KOU. These data conform very well with the hypothesis of Rastogi and Patel (1975) wherein, a southward IMF-Bz (between 1835 and 2000 UT) would cause a decrease of ΔX at night

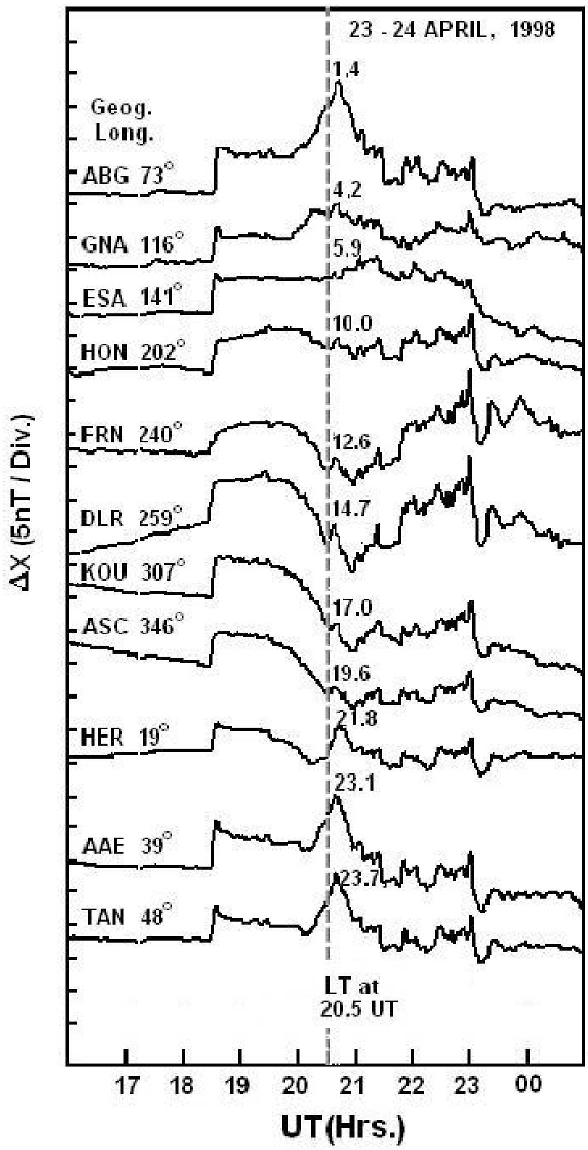

Figure 6.2: Variation of the horizontal component of the geomagnetic field projected on to the x-direction at eleven low latitude stations around the world on 23 – 24 April 1998. The vertical dashed line is marked at 20.5 UT and shown alongside it, for each curve, is the corresponding local time at each station. Also indicated on the left of each curve is the geographic longitude of the station.

side stations and a increase of ΔX at day side stations of the earth while a northward turning of IMF-Bz would produce a strong positive ΔX at stations in the night side sector and negative ΔX at stations in the day side sector due to the imposition of either a dusk-to-dawn or dawn-to-dusk electric field. The fluctuations in ΔX between $2130-2300$ UT are synchronous at all stations in the day as well as in the night sectors, suggesting the effect to be due to solar wind flow pressure and not due to the IMF-Bz. It is important to note here that the solar wind density fluctuations virtually mirrors those seen in ΔX at ground stations, thereby implying that the solar wind density was the main key or the driver for this event. Qualitatively, the fluctuations seem to be independent of the latitude. The dominant parameter is the solar wind pressure that makes the magnetosphere shrink and expand self similarly, with some scaling factor depending on the pressure. This is reflected in the magnetic field data at all latitudes and longitudes in a configuration where the IMF appears to have no role to play.

Thus, this was a unique space weather event in which one could unambiguously associate solar wind density variations with variations in ΔX at ground stations while no such changes were seen in the solar wind speed or magnetic field. Furthermore, it is, in general, noticed that compression of the dayside magnetosphere, due to sudden changes in the solar wind density or speed, causes a sudden increase in geomagnetic fields. However, as stated earlier, we found the compression of magnetosphere has been occurred on dayside as well as nightside, which is unlikely for this kind of geomagnetic events.

6.3 Solar Source Locations

Since all geomagnetic events are triggered by activity on the solar surface it is of interest to see if the solar source regions of such events can be identified. During periods of intense solar activity, such as around the maximum phase of the solar cycle, locating or pinpointing the solar sources of geomagnetic activity becomes extremely difficult as a large amount of activity takes place all over the solar sunspot belt between ±35°. However, during quieter solar conditions, one familiar method of finding or pinpointing solar source locations, of geomagnetic activity observed at 1 AU, is the trace back technique where solar wind outflows are traced back to the surface of the Sun. It is well known that owing to the rotation of the Sun ($\Omega = 1.642\times10^{-4}$ deg s^{-1}), a radially directed outflow of solar wind and the IMF will trace out an Archimedean spiral through the interplanetary medium (Parker, 1958).

For a steady state solar wind with a velocity of 430 km s^{-1}, the tangent to this spiral, at 1 AU, will make an angle of 45° with the radial vector from the Sun (Schwenn, 1990). As a consequence, the longitudinal offset (ϕ_R) of a solar wind stream with a velocity V, when traced backwards from a distance R_1 (say 1 AU) to a distance R_2, will be $\phi_R = \Omega(R_1 - R_2)/V$. The observed solar wind velocities, thus, can be projected back to the Sun to determine the sources of the solar wind flows on the Sun.

Rickett (1975) has used such a technique for the first time to trace solar wind outflows at 1 AU back to the Sun. For the present geomagnetic event, we have followed the same technique and back-projected the observed ACE velocities along Archimedean spirals to the source surface at 2.5 $R_\odot$ to determine its solar source location. Though this method is generally applicable to a steady-state flow of the solar wind, it has also been applied in cases when the solar wind outflows were not steady-state and highly non-radial. For example, during the well-known disappearance event of 11 May 1999, the work by Janardhan *et al.* (2005) and Janardhan (2006) has shown that solar source locations determined by the traceback technique, using constant velocities along Archimedean spirals, do not have significant errors even though the solar wind flows were known to be highly non-radial during that period. In the present case under discussion the solar wind flows would have been highly kinked and non-radial due to the propagating forward and reverse shocks arising from the optically occulted flare and the rear side CME. Therefore, if the $SI^+ - SI^-$ pair had a source on the solar disk, the ambiguity about the location of the source region would be within reasonable errors as shown by Janardhan *et al.* (2005) and Janardhan (2006).

Figure 6.3 shows a map of the solar photosphere indicating the locations of the active regions. The back projected region of the solar wind flows go back to the vicinity of the large active region AR8205 located at N21W25, to the west of central meridian on 20 April 1998, and indicated by a solid arrow in Fig. 6.3. Typically, the solar disk shows a large number of active regions during the rising phase of the solar cycle. A detailed theoretical study by Schrijver and DeRosa (2003), has shown that solar wind outflows from active regions comprise $\leq$10% during solar minimum and up to $30-50$% during solar maximum. However, the visible solar disk on 20 April 1998 showed no activity in terms of flares or CMEs and had only two active regions AR8206 and AR8205 as shown in Figure 6.3. The Active region AR8206 was smaller than AR8205 being around 245 millionth of the solar disk in size as compared to 312 millionth of the solar disk for AR8205. Also, AR8205 was less than 30° west of central meridian as compared to over 40° east of central meridian for AR8206.

The central meridian location implies that any activity like a large CME or flare would be earth directed. However, there was no flare or CME on the visible solar disk on 20 April. Images from the Extreme-ultraviolet Imaging Telescope (EIT; Delaboudinière *et al.* (1995)) and the Michelson Doppler Imager (MDI, Scherrer *et al.* (1995)) on board the Solar and Heliospheric Observatory (SoHO;Domingo, Fleck and Poland (1995)) were also examined carefully to confirm that there was no other possible source regions on the solar disk on 20 April 1998.

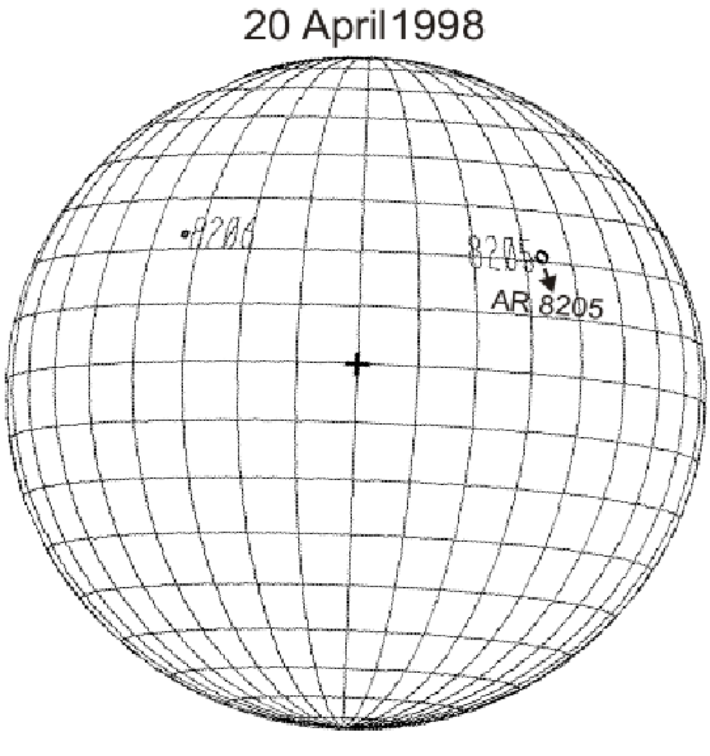

Figure 6.3: Map of the solar photosphere on 20 April 1998 showing the locations of the large active regions. The active region AR8205 has been indicated by an arrow for convenience.

6.3.1 The Rearside CME and Optically Occulted Flare of 20 April 1998

As stated earlier, a rearside, fast ($\sim$1850 km s^{-1}) partial halo CME occurred in association with an optically occulted GOES M1.4 class flare which took place just behind the limb at S43W90 on 20 April 1998. A partial (P) halo CME is one class of halo CMEs (Howard *et al.*, 1982, 1985) while the other classes of halo CMEs are Full (F) and Asymmetric (A) types. This CME classification is based on the width of the halos, which they create surrounding the occulting disk of the coronagraph on radial expansion from their source locations on the Sun. The Large Angle and Spectrometric Coronagraph (LASCO; (Brueckner *et al.*, 1995)) on board the SoHO routinely observes halo CMEs. The F- and A- halo CMEs have angular width of 360° whereas the P-halo CMEs have width $\geq$ 120° (Gopalswamy *et al.*, 2003a). While CME's can take place on both the front and rear side of the sun, as observed from the earth, it is the front-side solar events that are, often, found to be geo-effective as the rear side events propagate away from the earth. It must be pointed out here that most forecasters of space weather events generally ignore the possibility that a limb or backside solar explosive event could propagate a disturbance towards the earth. However, there have been some instances where such cases have been studied and reported in recent times (McKenna-Lawlor *et al.*, 2006; Smith *et al.*, 2009b,a).

A GOES M1.4 flare at S43W90 was first detected in 1-8 Å band at 09:15 UT on 20 April 1998 and reached its maximum at 10:21 UT. The rear side partial halo CME was first seen in the LASCO coronagraph C2, at 10:04:51 UT on 20 April 1998, as a bright, sharply defined loop structure spanning $\sim$80° in latitude and extending to $\sim$3.1 $R_\odot$. The same was first observed by the LASCO C3 coronagraph at 10:45:22 UT. Both the CME and the flare have been extensively studied and reported (Bastian *et al.*, 2001; Simnett, 2000, 2002) and it has been shown that the CME, which was radio loud (Gopalswamy, 2000), actually pushed aside pre-existing streamers while moving beyond the LASCO C3 field of view. Since this was a rear-side CME, the shock front that it drove ahead of it would have been in a direction away from the earth.

In a study of the arrival time of flare driven shocks at 1 AU and beyond (Smart and Shea, 1985; Janardhan *et al.*, 1996) it has been assumed that the trailing edges of flare driven shock waves travel at roughly half the velocity of the shock in the flare radial direction. It is, therefore, not unreasonable to assume that the trailing edges of CME driven reverse shock would be much slower and could be convected outwards towards the earth by the solar wind. The flare and the rear-side CME would thus provide the forward and reverse shocks to cause the SI^+ and SI^- pair.

Figure 6.4 shows the hourly averaged value of the absolute magnitude of the magnetic field, as recorded by the Magnetometer Experiment (MAG; (Zwickl *et al.*, 1998)) on the ACE spacecraft, as a function of time in UT. It is expected that the strength of the magnetic field would increase at the forward shock or SI^+ impulse and decrease at the reverse shock or SI^- impulse. It can be easily seen from Figure 6.4 that there is a sharp increase in the magnetic field at around 1835 UT, corresponding to the arrival of the forward shock associated with the SI^+ impulse and a decrease in the magnetic field at 2300 UT corresponding to the arrival of the reverse shock associated with the SI^- impulse. The vertically oriented dashed parallel lines in Figure 6.4 are marked at 1835 UT and 2300 UT, the time corresponding to the SI^+ and SI^- impulse respectively.

6.4 Discussion

The solar event lasting only for some 4 to 5 hours showed signatures of all mechanisms involving solar – magnetosphere – ionosphere relationships. The arrival at 1 AU of the forward and reverse shock pair associated with the SI^+ and SI^- respectively is clearly seen in the behaviour of the hourly averaged

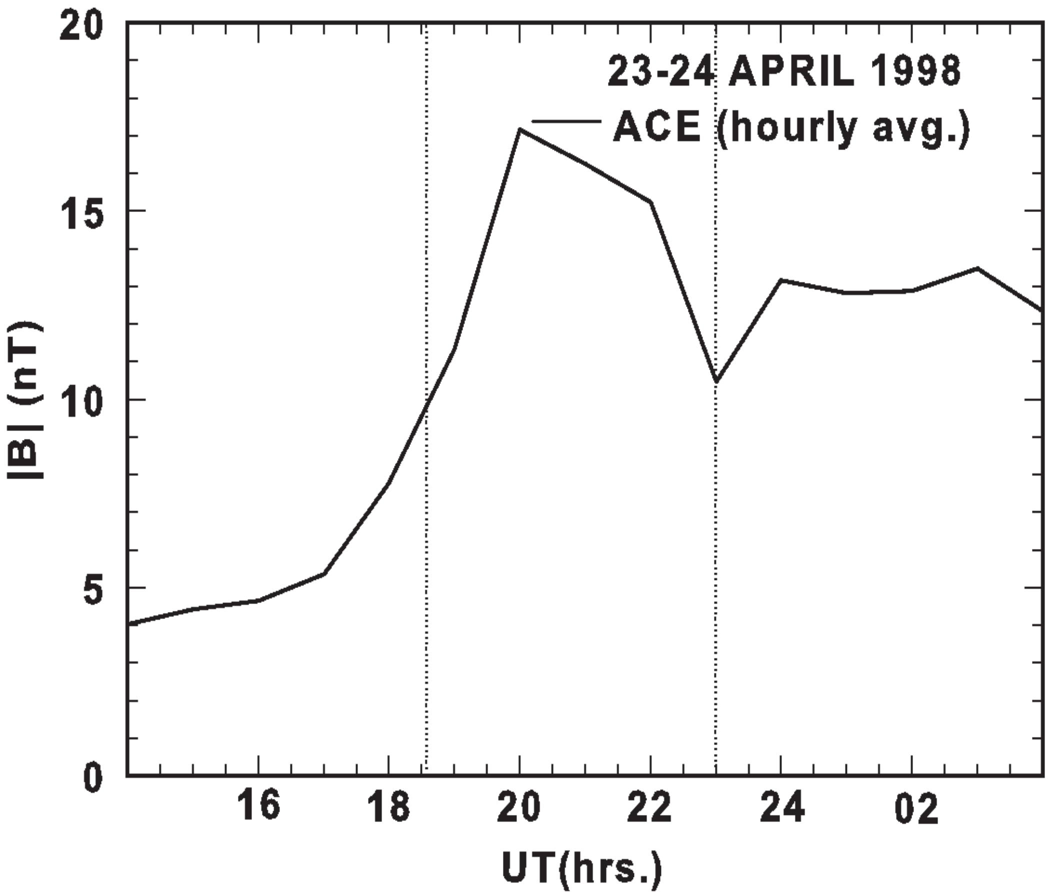

Figure 6.4: Hourly averaged total magnetic field as a function of time in UT as observed by the ACE spacecraft located at the L1 Lagrangian point at 1 AU. The vertically oriented dashed parallel lines at 1835 UT and 2300 UT correspond to the time of the SI^{+} and SI^{-} impulse respectively.

values of the total magnetic field, which shows a sharp increase at ∼1835UT and a decrease at ∼2300 UT. The SI^+ impulse at 1835 UT was associated with a sudden increase of both the solar wind density and speed causing a sudden pressure on the Earth's magnetosphere. On the other hand, the SI^- at 2300 UT was associated with the sudden decrease of solar wind density. Moreover, it is important to note that the IMF-Bz plays a significant role in the H-field variations as the southward IMF-Bz between 1835 – 2000 UT resulted in a decrease of ΔX at night side stations and an increase of ΔX at day side stations of the earth due to the prompt penetration of electric field into the low latitude ionosphere. Similarly, at 2000 UT, a northward turning of IMF-Bz produces a strong positive ΔX at stations in the night sector and negative ΔX at stations in the day side sector due to the imposition of a dawn-to-dusk overshielding electric field.

Between 2015 – 2300 UT the fluctuation in ΔX were similar at all stations in the day or night sectors and were well correlated with the fluctuation of solar wind flow pressure. The solar wind flow pressure nevertheless represents fluctuations in the solar wind density, and thus the magnetic variations between 2015 – 2300 UT correspond to the solar wind density fluctuations. It is noteworthy, therefore, to see the effect of sudden changes in the solar flow pressure due to change of solar wind density clearly identified during the period of 2015 – 2300 UT.

Although theoretical first order predictions for the observed distribution of solar wind speed, density, and temperature during the propagation of forward and reverse shock pairs were already derived four decades ago (Dryer, 1970, 1972), the analysis of this geomagnetic event has been rewarding due to the relative quiet solar conditions. This situation allowed us to identify specific solar sources as the possible drivers of the SI^+ and SI^- pair. The only activity on Sun, at this time, was the rear side CME and the associated solar flare. This is thus a very unique observation wherein, a pair of SI events have been shown to be associated with corresponding changes in the solar wind density while no such changes are seen in the solar wind speed or magnetic field.

6.5 Summary and Conclusions

The observations of an SI^+-SI^- pair, presented in this Chapter, has been able to establish the link between the interplanetary magnetic structure and worldwide magnetospheric response, using observations of the Indian magnetic stations to provide the first clue. The use of the solar wind traceback technique helped in locating the solar sources of this particular event to a rearside solar event involving the occurrence of a solar flare in association with a partial halo CME. We summarize the results of this Chapter:

1. The arrival at 1 AU of the forward and reverse shock pair at 1835 UT and 2300 UT respectively have caused the SI^+ and SI^- pair at 1835 UT and 2300 UT.

2. The effect of sudden changes in the solar wind flow pressure due to a change of only solar wind density have been clearly identified between 2015 and 2300 UT.

3. The effect of the slowly varying IMF-Bz has been shown to impose dusk-to-dawn or dawn-to-dusk electric field globally, depending on the southward or northward turning of the IMF-Bz, that cause either decrease or increase in the H-field variations.

4. The solar sources of the event, a flare and a partial halo CME on the rear-side of the Sun, would have provided the forward and the reverse shock causing the SI^+ and SI^-.

Although there has been a large body of work, over the past four decades, that have addressed the issues concerned with forward/reverse shock pairs, their manifestation at 1 AU and their relation to specific solar events, this work, however, presents empirical evidence, which to our knowledge, is the best convincing evidence for the association of specific solar events to the observations of an $SI^+ - SI^-$ pair. In addition, this work shows that it is possible for a rearside solar flare to propagate a shock towards the earth. Many more such events need to be observed, retrieved and studied, both from archival records and future observations, before a clearer understanding of the exact nature and physics behind such events is obtained. High resolution and high dynamic range radio imaging techniques (Mercier *et al.*, 2006b) can also provide useful information in this regard.

Chapter 7

Conclusions and Future Scope

In this thesis, solar cycle related changes in photospheric magnetic activity are addressed, through investigation of temporal variation of solar magnetic fields, and through a study of the changes in quasi-periodic variations of solar magnetic fields, during the last three Solar Cycles, *viz.* 21, 22 and 23, spanning 1975 – 2009. In addition, the consequences of the variation in photospheric magnetic fields on corresponding variation in the interplanetary space are dealt with by studying the long-term solar cycle changes of the solar wind microturbulence levels in the inner heliosphere. In particular, the above studies are used to address the solar cycle changes that led to the buildup of one of the deepest solar minima experienced in the past 100 years, which occurred between the end of last Solar Cycle 23 in 2008 – 2009 and the present Solar Cycle 24 which started in 2012. In addition, space weather effects of solar and solar wind events leading to the magnetic disturbances on the Earth are also addressed through a study of a sudden impulse pair on 23 – 24 April 1998.

The results and conclusions of the work described in Chapters 3, 4, 5, and 6 are summarized respectively in sections 7.1, 7.2, 7.3, and 7.4. Finally, the future scope for such studies of the solar magnetic fields, the solar wind microturbulence levels, and space weather events has been briefly described in section 7.5.

7.1 Solar Polar Fields During Solar Cycles 21, 22, and 23

We have examined solar polar magnetic fields, using ground-based NSO/KP low-resolution magnetograms for the last three Solar Cycles, *viz.*, 21, 22 and 23 and space-based SoHO/MDI high-resolution magnetograms for the Cycle 23. Our investigation of the temporal variations of unsigned polar fields (Janardhan, Bisoi and Gosain, 2010), reported in this thesis, have shown a clear and steady decline in both the Northern and Southern hemispheres since ∼ 1995. This decline has continued until the maximum of the Cycle 23. Subsequently, the polar field strength has started to increase till 2004, and then became constant till the end of 2009. We found that the long-term changes in the unsigned polar fields, in the Cycle 23, are very well correlated with the changes in the meridional flow speed reported by Hathaway and Rightmire (2010). Further, we believe that the observed weak polar fields at the end of Cycle 23 is the cause of the prolonged solar minimum that occurred between Cycle 23 and 24. The continuously weaker polar fields, at the minimum of Cycle 23, we believe, would in turn lead to a weak Cycle 24. This supports the prediction made by Choudhuri, Chatterjee and Jiang (2007) for Cycle 24 who have claimed that Cycle 24 would be a very weak one contrary to the prediction for a strong Cycle 24 by Dikpati, de Toma and Gilman (2006).

7.2 Changes in Quasi-periodic Variations of Solar Photospheric Fields

For finding periodicities of solar photospheric fields, we have used magnetic field residuals derived from the NSO/KP magnetic measurements and these residuals were further subjected to both a Wavelet and a Fourier analysis. We have reported a clear transition occurring around 1996 (Bisoi *et al.*, 2013) in the distribution of wavelet spectral power and periodicities for high-latitude ($> 45°$) and low-latitude ($< 45°$) fields in both the Northern and Southern solar hemispheres. This period corresponds to the decline of photospheric fields that began around 1995−1996 (Janardhan, Bisoi and Gosain, 2010; Janardhan *et al.*, 2011). When the photospheric fields were divided, based on a wavelet analysis, into fields before and after 1996, a hemispheric asymmetry was noticed in the periodicities of photospheric fields. However, such an asymmetry has not seen in periodicities for low-latitude fields. Subsequent analysis at greater latitudinal resolution showed that this hemispheric asymmetry is confined to the latitude band, 45°−60°.

Polar surges above latitudes of ±45°, as seen in a magnetic butterfly diagram, show significant changes in their occurrence rates and strength in each cycle. These surges are regarded as surface manifestations of meridional flow variation, and thus are linked to the internal solar dynamo. Hence, the hemispheric asymmetry coupled with the steady decline in the high-latitude fields since around 1996 suggest that active changes occurred around this time in the solar dynamo, which in turn probably initiated the buildup of one of the deepest solar minima experienced in the past 100 years that occurred between Solar Cycles 23 and 24.

7.3 Solar Cycle Changes of the Solar Wind Microturbulence Levels in the Inner Heliosphere Using IPS Observations

Our investigations of the solar polar fields, in the latitude range 45° − 78°, have shown a steady decline in the fields since ∼1995 − 1996 (Janardhan, Bisoi and Gosain, 2010; Janardhan *et al.*, 2011). To investigate how the decline in solar polar fields affect the solar wind in the inner heliosphere, we have used IPS measurements at 327 MHz from the Japanese four station IPS observatory covering the period 1983 – 2009. It was found that the temporal variations in scintillation index (m) also showed a steady and significant decline since ∼1995 in the scintillation levels, a good proxy for microturbulence, in the solar wind for all 27 selected radio sources observed. We believe that this large-scale IPS signature in the inner heliosphere, coupled with the fact that solar polar fields have also been declining since ∼1995, provide a consistent result showing the buildup to the deepest solar minima, in the last 100 years, actually began in the mid-1990s.

7.4 Unique observations of a Geomagnetic SI^+ – SI^- Pair and Associated Solar Wind Fluctuations

A sudden impulse pair (SI^+ – SI^-) was identified at three Indian geomagnetic stations, Gulmarg, Alibag, and Trivandrum, on 23 – 24 April 1998. By definition an SI^+ – SI^- pair occurs when one observes a sudden positive impulse in the horizontal component of the Earth's magnetic field (H) followed some time later by a sudden negative impulse in H. Such an SI^+ – SI^- pair was recorded on 23 – 24 April 1998 when there was a sudden positive impulse at 1835 UT followed by a sudden negative impulse at 2300 UT. It is to be noted that the symmetric variation of H (SYM/H) at all middle latitude stations around the world too had remarkably similar variations as the H at the three Indian stations thereby implying that the SI pair was a global event. The ΔX (projection of H in x-direction) at Indian stations just after the SI^+ impulse at 1835 UT (around local midnight) gradually decreased until 2000 UT. This effect was interpreted as due to the prompt penetration of the electric field when the IMF-Bz was negative during the period. At around 2000 UT, ΔX again increased suddenly to values much above the first impulse level. Correspondingly, it was seen that IMF-Bz turned from southward to northward at this instant, implying that this was due to the well known overshielding condition. After this, the level of ΔX went down, with some oscillations, and finally came down to normal level at 2300 UT. It is interesting to note that the fluctuations in ΔX between 2130 – 2200 UT were correlated with the solar wind density rather than with the IMF-Bz or the solar wind speed.

The magnetic field variations at all latitudes and longitudes around the globe have also showed the same magnetic configuration where the IMF appears to have no role to play while the solar wind density was the main key or driver for this event. A search for the solar source locations of this event yielded a rear side, fast partial halo CME that occurred in association with an optically occulted GOES M1.4 class flares just behind the south west limb. The flare and the rear side CME would thus provide a forward and reverse shock to cause the SI^+ and SI^- pair. Thus, our investigation (Rastogi *et al.*, 2010) has shown that the solar event lasting only for some 4 to 5 hours showed signatures of all mechanisms involving solar – magnetosphere – ionosphere relationships, and also showed that it is possible for a rearside solar flare to propagate a shock towards the earth. In addition, this event showed unique signatures of sudden impulse on the nightside magnetosphere, which is extremely unusual, as most such sudden impulses signatures are seen on the dayside due to compression of the magnetosphere by the solar wind ram pressure.

7.5 Future Scope

We have, in the thesis, used high-quality, high-resolution ground-based and space-borne observations, however, recent developments in instrumentation and techniques have substantially enhanced the quality and resolution of telescopic and spacecraft observations. Such superior goldmines of data are available in the public domain through the world wide web and can therefore be efficiently used for future studies of the solar cycle changes of solar magnetic fields and solar wind, and their consequences on the Earth and near-space environment.

The Solar Dynamic Observatory (SDO; Pesnell, Thompson and Chamberlin (2012)), launched in 2012, has been producing high-dynamic-range, high-resolution images of the Sun, and the Helioseismic Magnetic Imager (HMI; Schou *et al.* (2012)) instrument on board SDO can be used to study the solar interior in much greater detail than ever before through its high quality line-of-sight magnetic field measurements. Additionally, the techniques and methods employed in the thesis can be used in future studies of a similar nature. Described briefly below are some other aspects of the work carried out in this thesis which need to be followed up.

7.5.1 Probing for Active Longitudes

Contrary to the well-known latitudinal distribution of solar activity, as explained in butterfly diagrams and works reported in this thesis (Janardhan, Bisoi and Gosain, 2010; Bisoi *et al.*, 2013), the longitudinal distribution of solar activity is not fully understood. A lot of work has been carried to investigate these longitudinal distribution of solar activity by finding active longitudes (Gaizauskas, 1993; Bai, 2003a; Vernova *et al.*, 2004). An important characteristic of these active longitudes is the tendency of solar activity to appear preferentially at these longitudes. The stability and lifetime of these longitudes were reported to vary ranging from a few solar rotations to approximately $20-40$ consecutive solar rotations, and sometimes even ranging from one to three solar cycles (Vernova, Tyasto and Baranov (2007) and references therein). Vernova, Tyasto and Baranov (2007) postulated the presence of active longitudes ($180°$ and $0°$ or $360°$) from the longitudinal distribution of photospheric magnetic fields, derived from the NSO/KP data, covering the period of $1976-2003$. However, the authors only selected the latitude interval of $\pm 45°$ for finding these active longitudes. So the longitudinal distribution of the photospheric magnetic fields can be further examined to probe active longitudes making use of the new high resolution NSO/KP magnetic measurements obtained after 2003. In addition, the presence of active longitudes can also be verified for solar polar fields above latitude of $\pm 45°$.

7.5.2 Investigation of Multipulse Geomagnetic Events

In the thesis, we have reported a sudden impulse pair causing magnetic disturbances on the Earth and its correspondence with solar wind density fluctuations. More such sudden impulse pair events can be picked from the archival records, and can be studied to understand the processes of solar – magnetosphere – ionosphere coupling. Sometimes multipulse events have also been noticed in the geomagnetic field variations as well as in the solar wind density fluctuations with no corresponding changes in the solar wind velocity and the IMF. We have started to investigate many more of these rare geomagnetic events to fully understand the physical mechanism involved.

7.5.3 Synthesis Imaging of the Quiet-sun

Investigation of the boundary of polar coronal holes during the declining phase of Cycle 23 has shown $\sim$15% decease in coronal hole area as compared to those at the beginning of Cycle 23 (Kirk *et al.*, 2009). In this thesis, we have reported weaker polar fields during Cycle 23. So an investigation of the boundary of polar coronal holes would be useful in studying the evolution of polar magnetic fields. High-resolution and high-dynamic-range radio images of the quiet-sun (Mercier *et al.*, 2006b) provide a unique opportunity to carry out such investigations of the polar coronal hole boundaries. Using combined observations from the Giant Meterwave Radio Telescope (GMRT) in India and the Nancay Radio Heliograph (NRH) in France, we can produce the high-dynamic-range and high-spatial-resolution synthesis images of the quiet-sun at the low frequencies, *viz.* 150, 235 and 327 MHz, by combining the two sets of visibilities (Mercier *et al.*, 2006b). Thus, one needs to follow up on these initial measurements and carry out systematic observations over several years to understand and address these issues.

References

Acuña, M.H., Ogilvie, K.W., Baker, D.N., Curtis, S.A., Fairfield, D.H., Mish, W.H.: 1995, The Global Geospace Science Program and Its Investigations. *Space Sci. Rev.* **71**, 5 – 21. 44, 59, 122, 150

Alfvén, H.: 1943, On the Existence of Electromagnetic-Hydrodynamic Waves. *Arkiv for Astronomi* **29**, 1 – 7. 14

Altrock, R.C.: 2003, Use of ground-based coronal data to predict the date of solar-cycle maximum. *Solar Phys.* **216**, 343 – 352. 141

Altrock, R.C.: 2011, Coronal Fe xiv Emission During the Whole Heliosphere Interval Campaign. *Solar Phys.* **274**, 251 – 257. 141

Ananthakrishnan, S., Balasubramanian, V., Janardhan, P.: 1995, Latitudinal Variation of Solar Wind Velocity. *Space Sci. Rev.* **72**, 229 – 232. 29, 84, 125

Ananthakrishnan, S., Coles, W.A., Kaufman, J.J.: 1980, Microturbulence in solar wind streams. *J. Geophys. Res.* **85**, 6025 – 6030. 28, 29, 122, 125, 139

Asai, K., Ishida, Y., Kojima, M., Maruyama, K., Misawa, H., Yoshimi, N.: 1995, Multi-station system for solar wind observations using the interplanetary scintillation method. *J. Geomag. Geoelectr.* **47**, 1107 – 1112. 44, 56

Asai, K., Kojima, M., Tokumaru, M., Yokobe, A., Jackson, B.V., Hick, P.L., Manoharan, P.K.: 1998, Heliospheric tomography using interplanetary scintillation observations. III - Correlation between speed and electron density fluctuations in the solar wind. *J. Geophys. Res.* **103**, 1991. 133

Babcock, H.D.: 1959, The Sun's Polar Magnetic Field. *Astrophys. J.* **130**, 364. 10, 20, 63, 64, 72

Babcock, H.W.: 1961, The Topology of the Sun's Magnetic Field and the 22-YEAR Cycle. *Astrophys. J.* **133**, 572. 20, 64, 79, 116

Babcock, H.W., Babcock, H.D.: 1955, The Sun's Magnetic Field, 1952-1954. *Astrophys. J.* **121**, 349. 8, 10, 63

Bai, T.: 1987, Periodicities of the flare occurrence rate in solar cycle 19. *Astrophys. J. Lett.* **318**, L85 – L91. 23

Bai, T.: 2003a, Hot Spots for Solar Flares Persisting for Decades: Longitude Distributions of Flares of Cycles 19-23. *Astrophys. J.* **585**, 1114 – 1123. 170

Bai, T.: 2003b, Periodicities in Solar Flare Occurrence: Analysis of Cycles 19-23. *Astrophys. J.* **591**, 406 – 415. 23, 24, 86

Balasubramanian, V., Janardhan, P., Srinivasan, S., Ananthakrishnan, S.: 2003, Interplanetary scintillation observations of the solar wind disappearance event of May 1999. *J. Geophys. Res.* **108**, 1121. 129

Bame, S.J., Asbridge, J.R., Feldman, W.C., Gosling, J.T.: 1976, Solar cycle evolution of high-speed solar wind streams. *Astrophys. J.* **207**, 977 – 980. 27

Bastian, T.S., Pick, M., Kerdraon, A., Maia, D., Vourlidas, A.: 2001, The Coronal Mass Ejection of 1998 April 20: Direct Imaging at Radio Wavelengths. *Astrophys. J. Lett.* **558**, L65 – L69. 158

Basu, S., Antia, H.M.: 2003, Changes in Solar Dynamics from 1995 to 2002. *Astrophys. J.* **585**, 553 – 565. 80

Basu, S., Broomhall, A.M., Chaplin, W.J., Elsworth, Y.: 2012, Thinning of the Sun's Magnetic Layer: The Peculiar Solar Minimum Could Have Been Predicted. *Astrophys. J.* **758**, 43. 117

Behr, A., Siedentopf, H.: 1953, Untersuchungen über Zodiakallicht und Gegenschein nach lichtelektrischen Messungen auf dem Jungfraujoch. Mit 20 Textabbildungen. *Z. Astrophys.* **32**, 19. 25

Benevolenskaya, E.E., Kosovichev, A.G., Scherrer, P.H.: 2001, Detection of High-Latitude Waves of Solar Coronal Activity in Extreme-Ultraviolet Data from the Solar and Heliospheric Observatory EUV Imaging Telescope. *Astrophys. J. Lett.* **554**, L107 – L110. 65

Benevolenskaya, E.E., Kosovichev, A.G., Scherrer, P.H.: 2002, Evolution of Large-scale Coronal Structure with the Solar Cycle from EUV Data. In: F. Favata & J. J. Drake (ed.) *Stellar Coronae in the Chandra and XMM-NEWTON Era*, *Astronomical Society of the Pacific Conference Series* **277**, 419. 65

Bhandari, S.M., Ananthakrishnan, S., Pramesh Rao, A.: 1974, Structure of 194 southern declination radio sources from interplanetary scintillations. *Australian Journal of Physics* **27**, 121. 29, 125

Biermann, L.: 1951, Kometenschweife und solare Korpuskularstrahlung. *Z. Astrophys.* **29**, 274. 25

Bird, M.K., Volland, H., Paetzold, M., Edenhofer, P., Asmar, S.W., Brenkle, J.P.: 1994, The coronal electron density distribution determined from dual-frequency ranging measurements during the 1991 solar conjunction of the ULYSSES spacecraft. *Astrophys. J.* **426**, 373 – 381. 129

Bisoi, S.K., Janardhan, P., Chakrabarty, D., Ananthakrishnan, S., Divekar, A.: 2013, Changes in Quasi-periodic Variations of Solar Photospheric Fields:

Precursor to the Deep Solar Minimum in Cycle 23? *Solar Phys.*. 109, 113, 114, 117, 121, 166, 170

Bothmer, V.: 2006, In: Blondel, P., Mason, J.W. (eds.) *The Solar Atmosphere and Space Weather*, 1. 31

Brueckner, G.E.: 1974, The Behaviour of the Outer Solar Corona (3 R_{sun} to 10 R_{sun} during a Large Solar Flare Observed from OSO-7 in White Light. In: Newkirk, G.A. (ed.) *Coronal Disturbances*, *IAU Symposium* **57**, 333. 27, 30

Brueckner, G.E., Howard, R.A., Koomen, M.J., Korendyke, C.M., Michels, D.J., Moses, J.D., Socker, D.G., Dere, K.P., Lamy, P.L., Llebaria, A., Bout, M.V., Schwenn, R., Simnett, G.M., Bedford, D.K., Eyles, C.J.: 1995, The Large Angle Spectroscopic Coronagraph (LASCO). *Solar Phys.* **162**, 357–402. 30, 158

Bruno, R., Carbone, V.: 2005, The Solar Wind as a Turbulence Laboratory. *Living Reviews in Solar Physics* **2**, 4. 27

Burlaga, L.F.: 1970, A reverse hydromagnetic shock in the solar wind. *Cosmic Electrodynamics* **1**, 233–238. 148

Burton, R.K., McPherron, R.L., Russell, C.T.: 1975, An empirical relationship between interplanetary conditions and Dst. *J. Geophys. Res.* **80**, 4204–4214. 32, 146

Carrington, R.C.: 1858, On the Distribution of the Solar Spots in Latitudes since the Beginning of the Year 1854, with a Map. *Mon. Not. Roy. Astron. Soc.* **19**, 1–3. 4

Chakrabarty, D.: 2007, Investigations on the F region of the ionosphere over low latitudes using optical, radio and simulation techniques. PhD thesis. 38

Chapman, S., Bartels, J.: 1940, *Geomagnetic and Related Phenomena* **1**, 449. 25

Charbonneau, P.: 2010, Dynamo Models of the Solar Cycle. *Living Reviews in Solar Physics* **7**, 3. 13

Choudhuri, A.R.: 2003, In: Dwivedi, B.N., Parker, F.b.E.N. (eds.) *The solar dynamo as a model of the solar cycle*, 103 – 127. 17

Choudhuri, A.R., Chatterjee, P., Jiang, J.: 2007, Predicting Solar Cycle 24 With a Solar Dynamo Model. *Physical Review Letters* **98**(13), 131103. 22, 80, 81, 84, 117, 140, 166

Choudhuri, A.R., Schussler, M., Dikpati, M.: 1995, The solar dynamo with meridional circulation. *Astron. Astrophys.* **303**, L29. 22, 64

Chowdhury, P., Dwivedi, B.N.: 2011, Periodicities of Sunspot Number and Coronal Index Time Series During Solar Cycle 23. *Solar Phys.* **270**, 365 – 383. 23, 114

Chowdhury, P., Khan, M., Ray, P.C.: 2009, Intermediate-term periodicities in sunspot areas during solar cycles 22 and 23. *Mon. Not. Roy. Astron. Soc.* **392**, 1159 – 1180. 23, 109, 113

Chowdhury, P., Khan, M., Ray, P.C.: 2010, Short-Term Periodicities in Sunspot Activities During the Descending Phase of Solar Cycle 23. *Solar Phys.* **261**, 173 – 191. 23

Coles, W.A.: 1978, Interplanetary scintillation. *Space Sci. Rev.* **21**, 411 – 425. 28

Davis, T.N., Sugiura, M.: 1966, Auroral electrojet activity index AE and its universal time variations. *J. Geophys. Res.* **71**, 785 – 801. 36

Delaboudinière, J.P., Artzner, G.E., Brunaud, J., Gabriel, A.H., Hochedez, J.F., Millier, F., Song, X.Y., Au, B., Dere, K.P., Howard, R.A., Kreplin, R., Michels, D.J., Moses, J.D., Defise, J.M., Jamar, C., Rochus, P., Chauvineau, J.P., Marioge, J.P., Catura, R.C., Lemen, J.R., Shing, L., Stern, R.A., Gurman, J.B., Neupert, W.M., Maucherat, A., Clette, F., Cugnon, P., van Dessel, E.L.: 1995, EIT: Extreme-Ultraviolet Imaging Telescope for the SOHO Mission. *Solar Phys.* **162**, 291 – 312. 156

Detman, T., Smith, Z., Dryer, M., Fry, C.D., Arge, C.N., Pizzo, V.: 2006, A hybrid heliospheric modeling system: Background solar wind. *J. Geophys. Res.* **111**, 7102. 148

DeVore, C.R., Sheeley, N.R.J., Boris, J.P.: 1984,. *Solar Phys.* **92**, 1. 81

Dikpati, M.: 2011, Comparison of the Past Two Solar Minima from the Perspective of the Interior Dynamics and Dynamo of the Sun. *Space Sci. Rev.*, 143. 116, 140

Dikpati, M., Charbonneau, P.: 1999, A Babcock-Leighton Flux Transport Dynamo with Solar-like Differential Rotation. *Astrophys. J.* **518**, 508 – 520. 22, 64

Dikpati, M., de Toma, G., Gilman, P.A.: 2006, Predicting the strength of solar cycle 24 using a flux-transport dynamo-based tool. *Geophys. Res. Lett.* **33**, 5102. 22, 80, 140, 166

Dikpati, M., de Toma, G., Gilman, P.A., Arge, C.N., White, O.R.: 2004, Diagnostics of Polar Field Reversal in Solar Cycle 23 Using a Flux Transport Dynamo Model. *Astrophys. J.* **601**, 1136 – 1151. 66, 72

Dikpati, M., Gilman, P.A., de Toma, G., Ulrich, R.K.: 2010, Impact of changes in the Sun's conveyor-belt on recent solar cycles. *Geophys. Res. Lett.* **37**, 14107. 85, 116, 126

Domingo, V., Fleck, B., Poland, A.I.: 1995, The SOHO Mission: an Overview. *Solar Phys.* **162**, 1 – 2. 8, 44, 49, 69, 122, 156

Droege, W., Gibbs, K., Grunsfeld, J.M., Meyer, P., Newport, B.J., Evenson, P., Moses, D.: 1990, A 153 day periodicity in the occurrence of solar flares producing energetic interplanetary electrons. *Astrophys. J. Supplement.* **73**, 279 – 283. 23

Dryer, M.: 1970, Some effects of finite electrical conductivity on solar flare-induced interplanetary shock waves. *Cosmic Electrodynamics* **1**, 348 – 370. 148, 161

Dryer, M.: 1972, Interplanetary Double-Shock Ensembles with Anomalous Electrical Conductivity. *Solar Wind 2., NASA SP-308, (C. P. Sonett, P. J. Coleman Jr., and J. M. Wilcox, Eds.)* **2**, 453. 148, 161

Dryer, M., Smith, Z.K., Unti, T., Mihalov, J.D., Smith, B.F., Wolfe, J.H., Colburn, D.S., Sonett, C.P.: 1975, Pioneer 9 and OGO 5 observations of an interplanetary multiple shock ensemble on February 2, 1969. *J. Geophys. Res.* **80**, 3225 – 3234. 148

D'Silva, S., Choudhuri, A.R.: 1993, A theoretical model for tilts of bipolar magnetic regions. *Astron. Astrophys.* **272**, 621. 20, 118

Dungey, J.W.: 1961, Interplanetary Magnetic Field and the Auroral Zones. *Physical Review Letters* **6**, 47 – 48. 32, 146

Duvall, T.L. Jr.: 1979, Large-scale solar velocity fields. *Solar Phys.* **63**, 3 – 15. 10, 12, 64

Eviatar, A., Dryer, M.: 1970, Finite conductivity and interplanetary piston-driven shock waves. *Cosmic Electrodynamics* **1**, 371 – 379. 148

Fan, Y., Fisher, G.H., Deluca, E.E.: 1993, The origin of morphological asymmetries in bipolar active regions. *Astrophys. J.* **405**, 390 – 401. 20

Feldman, W.C., Asbridge, J.R., Bame, S.J., Gosling, J.T.: 1976, High-speed solar wind flow parameters at 1 AU. *J. Geophys. Res.* **81**, 5054 – 5060. 27

Fisher, R.A.: 1929, Tests of Significance in Harmonic Analysis. *Royal Society of London Proceedings Series A* **125**, 54 – 59. 98

Fletcher, S.T., Broomhall, A.M., Salabert, D., Basu, S., Chaplin, W.J., Elsworth, Y., Garcia, R.A., New, R.: 2010, A Seismic Signature of a Second Dynamo? *Astrophys. J. Lett.* **718**, L19 – L22. 24, 86, 87

Forrest, D.J., Chupp, E.L., Ryan, J.M., Cherry, M.L., Gleske, I.U., Reppin, C., Pinkau, K., Rieger, E., Kanbach, G., Kinzer, R.L.: 1980, The gamma ray spectrometer for the Solar Maximum Mission. *Solar Phys.* **65**, 15 – 23. 23

Fox, P., McIntosh, P., Wilson, P.R.: 1998, Coronal Holes and the Polar Field Reversals. *Solar Phys.* **177**, 375 – 393. 65

Fry, C.D., Dryer, M., Smith, Z., Sun, W., Deehr, C.S., Akasofu, S.: 2003, Forecasting solar wind structures and shock arrival times using an ensemble of models. *J. Geophys. Res.* **108**, 1070. 148

Gaizauskas, V.: 1993, On Recurrent Solar Activity (Invited). In: Zirin, H., Ai, G., Wang, H. (eds.) *IAU Colloq. 141: The Magnetic and Velocity Fields of Solar Active Regions*, *Astronomical Society of the Pacific Conference Series* **46**, 479. 170

Giles, P.M., Duvall, T.L., Scherrer, P.H., Bogart, R.S.: 1997, A subsurface flow of material from the Sun's equator to its poles. *Nature* **390**, 52 – 54. 13

Gleissberg, M.N.: 1939, A long-periodic Fluctuation of the Sun-spot Numbers. *Observatory* **62**, 158 – 159. 23

Gold, T.: 1959, Motions in the Magnetosphere of the Earth. *J. Geophys. Res.* **64**, 1219 – 1224. 152

Goldstein, J., Spiro, R.W., Reiff, P.H., Wolf, R.A., Sandel, B.R., Freeman, J.W., Lambour, R.L.: 2002, IMF-driven overshielding electric field and the origin of the plasmaspheric shoulder of May 24, 2000. *Geophys. Res. Lett.* **29**(16), 1819. 37, 149

Gonzalez, W.D.: 1990, A unified view of solar wind - Magnetosphere coupling functions. *Planet. Space Sci.* **38**, 627 – 632. 32, 146

Goodrich, C.C., Lyon, J.G., Wiltberger, M., Lopez, R.E., Papadopoulos, K.: 1998, An overview of the impact of the January 10-11, 1997 magnetic cloud on the magnetosphere via global MHD simulation. *Geophys. Res. Lett.* **25**, 2537 – 2540. 146

Gopalswamy, N.: 2000, Type II Solar Radio Bursts. In: R. G. Stone, K. W. Weiler, M. L. Goldstein, & J.-L. Bougeret (ed.) *Radio Astronomy at Long Wavelengths*, 123. 158

Gopalswamy, N.: 2004, A Global Picture of CMEs in the Inner Heliosphere. In: Poletto, G., Suess, S.T. (eds.) *The Sun and the Heliosphere as an Integrated System*, *Astrophysics and Space Science Library* **317**, 201. 30

Gopalswamy, N., Lara, A., Yashiro, S., Nunes, S., Howard, R.A.: 2003a, Coronal mass ejection activity during solar cycle 23. In: Wilson, A. (ed.) *Solar Variability as an Input to the Earth's Environment*, *ESA Special Publication* **535**, 403 – 414. 158

Gopalswamy, N., Lara, A., Yashiro, S., Howard, R.A.: 2003b, Coronal Mass Ejections and Solar Polarity Reversal. *Astrophys. J. Lett.* **598**, L63 – L66. 65

Gosling, J.T., Asbridge, J.R., Bame, S.J., Hundhausen, A.J., Strong, I.B.: 1968, Satellite observations of interplanetary shock waves. *J. Geophys. Res.* **73**, 43. 147

Gosling, J.T., Hildner, E., MacQueen, R.M., Munro, R.H., Poland, A.I., Ross, C.L.: 1974, Mass ejections from the sun - A view from SKYLAB. *J. Geophys. Res.* **79**, 4581 – 4587. 27, 30

Haber, D.A., Hindman, B.W., Toomre, J., Bogart, R.S., Larsen, R.M., Hill, F.: 2002, Evolving Submerged Meridional Circulation Cells within the Upper

Convection Zone Revealed by Ring-Diagram Analysis. *Astrophys. J.* **570**, 855 – 864. 13, 76, 80, 116

Hale, a.E.F. G. E., Nicholson, S.B., Joy, A.H.: 1919,. *Astrophys. J.* **49**, 153. 8

Hale, G.E.: 1908, On the Probable Existence of a Magnetic Field in Sun-Spots. *Astrophys. J.* **28**, 315. 6

Harvey, J., Worden, J.: 1998, New Types and Uses of Synoptic Maps. In: Balasubramaniam, K.S., Harvey, J., Rabin, D. (eds.) *Synoptic Solar Physics*, *Astronomical Society of the Pacific Conference Series* **140**, 155. 54

Hathaway, D.H.: 1996, Doppler Measurements of the Sun's Meridional Flow. *Astrophys. J.* **460**, 1027. 12, 64, 80, 116

Hathaway, D.H.: 2012, Supergranules as Probes of the Sun's Meridional Circulation. *Astrophys. J.* **760**, 84. 10

Hathaway, D.H., Rightmire, L.: 2010, Variations in the Suns Meridional Flow over a Solar Cycle. *Science* **327**, 1350. 12, 64, 76, 77, 78, 81, 83, 85, 87, 126, 166

Hayashi, K., Kojima, M., Tokumaru, M., Fujiki, K.: 2003, MHD tomography using interplanetary scintillation measurement. *Journal of Geophysical Research (Space Physics)* **108**, 1102. 29, 125

Heppner, J.P., Maynard, N.C.: 1987, Empirical high-latitude electric field models. *J. Geophys. Res.* **92**, 4467 – 4489. 146

Hewish, A.: 1989, IPS-imaging of heliospheric transients. *Advances in Space Research* **9**, 59 – 62. 29, 125

Hewish, A., Scott, P.F., Wills, D.: 1964, Interplanetary Scintillation of Small Diameter Radio Sources. *Nature* **203**, 1214 – 1217. 28, 126

Hewish, A., Tappin, S.J., Gapper, G.R.: 1985, Origin of strong interplanetary shocks. *Nature* **314**, 137 – 140. 128

Hietala, H., Partamies, N., Laitinen, T.V., Clausen, L.B.N., Facskó, G., Vaivads, A., Koskinen, H.E.J., Dandouras, I., Rème, H., Lucek, E.A.: 2012, Supermagnetosonic subsolar magnetosheath jets and their effects: from the solar wind to the ionospheric convection. *Annales Geophysicae* **30**, 33 – 48. 26

Hildner, E.: 1977, Mass ejections from the solar corona into interplanetary space. In: Shea, M.A., Smart, D.F., Wu, S.T. (eds.) *Study of Travelling Interplanetary Phenomena*, *Astrophysics and Space Science Library* **71**, 3 – 20. 30

Hilton, J.: 1992, *Explanatory Supplement to the Astronomical Almanac*, 383. 53

Howard, R.: 1974, Studies of solar magnetic fields. II - The magnetic fluxes. *Solar Phys.* **38**, 59 – 67. 24

Howard, R., Labonte, B.J.: 1980, The sun is observed to be a torsional oscillator with a period of 11 years. *Astrophys. J. Lett.* **239**, L33 – L36. 12

Howard, R.A., Michels, D.J., Sheeley, N.R. Jr., Koomen, M.J.: 1982, The observation of a coronal transient directed at earth. *Astrophys. J. Lett.* **263**, L101 – L104. 158

Howard, R.A., Sheeley, N.R. Jr., Michels, D.J., Koomen, M.J.: 1985, Coronal mass ejections - 1979-1981. *J. Geophys. Res.* **90**, 8173 – 8191. 158

Howe, R., Christensen-Dalsgaard, J., Hill, F., Komm, R.W., Larsen, R.M., Schou, J., Thompson, M.J., Toomre, J.: 2000a, Deeply Penetrating Banded Zonal Flows in the Solar Convection Zone. *Astrophys. J. Lett.* **533**, L163 – L166. 12

Howe, R., Christensen-Dalsgaard, J., Hill, F., Komm, R.W., Larsen, R.M., Schou, J., Thompson, M.J., Toomre, J.: 2000b, Dynamic Variations at the Base of the Solar Convection Zone. *Science* **287**, 2456 – 2460. 86, 109, 110, 114

Huang, C.M., Richmond, A.D., Chen, M.Q.: 2005, Theoretical effects of geomagnetic activity on low-latitude ionospheric electric fields. *Journal of Geophysical Research (Space Physics)* **110**, 5312. 37, 39

Huddleston, D.E., Woo, R., Neugebauer, M.: 1995, Density fluctuations in different types of solar wind flow at 1 AU and comparison with results from Doppler scintillation measurement near the Sun. *J. Geophys. Res.* **100**, 19951 – 19956. 28

Hundhausen, A.J.: 1997, Coronal Mass Ejections. In: Jokipii, J.R., Sonett, C.P., Giampapa, M.S. (eds.) *Cosmic Winds and the Heliosphere*, 259. 30

Intriligator, D.S., Wolfe, J.H.: 1970, Preliminary Power Spectra of the Interplanetary Plasma. *Astrophys. J. Lett.* **162**, L187. 28

Janardhan, P.: 2006, Enigmatic Solar Wind Disappearance Events - Do We Understand Them? *Jou. of Astrophys. & Astron.* **27**, 193. 155, 156

Janardhan, P., Alurkar, S.K.: 1992, Possible contribution of a solar transient to enhanced scintillation of a quasar. *Earth Moon and Planets* **58**, 31 – 38. 29, 125

Janardhan, P., Alurkar, S.K.: 1993, Angular source size measurements and interstellar scattering at 103 MHz using interplanetary scintillation. *Astron. Astrophys.* **269**, 119 – 127. 29, 125

Janardhan, P., Bisoi, S.K., Gosain, S.: 2010, Solar Polar Fields During Cycles 21 - 23: Correlation with Meridional Flows. *Solar Phys.* **267**, 267 – 277. 76, 78, 80, 83, 87, 88, 90, 95, 113, 121, 122, 145, 166, 167, 170

Janardhan, P., Tripathi, D., Mason, H.E.: 2008a, The solar wind disappearance event of 11 May 1999: source region evolution. *Astron. & Astrophys. Lett.* **488**, L1 – L4. 146

Janardhan, P., Alurkar, S.K., Bobra, A.D., Slee, O.B., Waldron, D.: 1992, Power spectral analysis of enhanced scintillation of quasar 3C459 due to Comet Halley. *Australian Journal of Physics* **45**, 115 – 126. 129

Janardhan, P., Balasubramanian, V., Ananthakrishnan, S., Dryer, M., Bhatnagar, A., McIntosh, P.S.: 1996, Travelling Interplanetary Disturbances Detected Using Interplanetary Scintillation at 327 MHz. *Solar Phys.* **166**, 379 – 401. 29, 125, 159

Janardhan, P., Fujiki, K., Kojima, M., Tokumaru, M., Hakamada, K.: 2005, Resolving the enigmatic solar wind disappearance event of 11 May 1999. *J. Geophys. Res.* **110**, 8101. 129, 146, 155, 156

Janardhan, P., Fujiki, K., Sawant, H.S., Kojima, M., Hakamada, K., Krishnan, R.: 2008b, Source regions of solar wind disappearance events. *J. Geophys. Res.* **113**, 3102. 129, 146

Janardhan, P., Bisoi, S.K., Ananthakrishnan, S., Tokumaru, M., Fujiki, K.: 2011, The prelude to the deep minimum between solar cycles 23 and 24: Interplanetary scintillation signatures in the inner heliosphere. *Geophys. Res. Lett.* **382**, 20108. 145, 167

Jian, L.K., Russell, C.T., Luhmann, J.G.: 2011, Comparing Solar Minimum 23/24 with Historical Solar Wind Records at 1 AU. *Solar Phys.*, 69. 123

Jiang, J., Chatterjee, P., Choudhuri, A.R.: 2007, Solar activity forecast with a dynamo model. *Mon. Not. Roy. Astron. Soc.* **381**, 1527 – 1542. 117

Jiang, J., Cameron, R.H., Schmitt, D., Schussler, M.: 2011, Can Surface Flux Transport Account for the Weak Polar Field in Cycle 23? *Space Sci. Rev.*, 136. 122

Jokipii, J.R.: 1973, Turbulence and Scintillations in the Interplanetary Plasma. *Annual Review of Astronomy and Astrophysics* **11**, 1. 28

Jones, H.P., Duvall, T.L. Jr., Harvey, J.W., Mahaffey, C.T., Schwitters, J.D., Simmons, J.E.: 1992, The NASA/NSO spectromagnetograph. *Solar Phys.* **139**, 211 – 232. 47, 67

Joshi, B., Pant, P., Manoharan, P.K.: 2006a, North-South Distribution of Solar Flares during Cycle 23. *Journal of Astrophysics and Astronomy* **27**, 151 – 157. 24

Joshi, B., Pant, P., Manoharan, P.K.: 2006b, Periodicities in sunspot activity during solar cycle 23. *Astron. Astrophys.* **452**, 647 – 650. 24

Kahler, S.W.: 1992, Solar flares and coronal mass ejections. *Annual Review of Astronomy and Astrophysics* **30**, 113 – 141. 30

Kaiser, M.L., Kucera, T.A., Davila, J.M., St. Cyr, O.C., Guhathakurta, M., Christian, E.: 2008, The STEREO Mission: An Introduction. *Space Sci. Rev.* **136**, 5 – 16. 44, 123

Kakinuma, T., Washimi, H., Kojima, M.: 1973, On the Analysis of the Observations of Interplanetary Scintillations Obtained with Three Spaced Receivers. *Pub. Astron. Soc. Japan* **25**, 271. 56

Keller, C.U., Harvey, J.W., Giampapa, M.S.: 2003, SOLIS: an innovative suite of synoptic instruments. In: Keil, S.L., Avakyan, S.V. (eds.) *Society of Photo-Optical Instrumentation Engineers (SPIE) Conference Series*, *Society of Photo-Optical Instrumentation Engineers (SPIE) Conference Series* **4853**, 194 – 204. 43, 47, 67

Kelley, M.C., Makela, J.J., Chau, J.L., Nicolls, M.J.: 2003, Penetration of the solar wind electric field into the magnetosphere/ionosphere system. *Geophys. Res. Lett.* **30**(4), 1158. 39

Kikuchi, T., Ebihara, Y., Hashimoto, K.K., Kataoka, R., Hori, T., Watari, S., Nishitani, N.: 2010, Penetration of the convection and overshielding electric fields to the equatorial ionosphere during a quasiperiodic DP 2 geomagnetic fluctuation event. *Journal of Geophysical Research (Space Physics)* **115**, 5209. 37, 39

Kile, J.N., Cliver, E.W.: 1991, A search for the 154 day periodicity in the occurrence rate of solar flares using Ottawa 2.8 GHz burst data, 1955-1990. *Astrophys. J.* **370**, 442 – 448. 23

Kiliç, H.: 2008, Midrange periodicities in sunspot numbers and flare index during solar cycle 23. *Astron. Astrophys.* **481**, 235 – 238. 23

Kirk, M.S., Pesnell, W.D., Young, C.A., Hess Webber, S.A.: 2009, Automated detection of EUV Polar Coronal Holes during Solar Cycle 23. *Solar Phys.* **257**, 99 – 112. 65, 171

Knaack, R., Stenflo, J.O., Berdyugina, S.V.: 2004, Periodic oscillations in the north-south asymmetry of the solar magnetic field. *Astron. Astrophys.* **418**, L17 – L20. 24, 109

Knaack, R., Stenflo, J.O., Berdyugina, S.V.: 2005, Evolution and rotation of large-scale photospheric magnetic fields of the Sun during cycles 21-23. Periodicities, north-south asymmetries and r-mode signatures. *Astron. Astrophys.* **438**, 1067 – 1082. 23, 24, 91, 106, 109, 113, 114

Kojima, M., Kakinuma, T.: 1990, Solar cycle dependence of global distribution of solar wind speed. *Space Sci. Rev.* **53**, 173 – 222. 56, 133

Kojima, M., Ishida, Y., Maruyama, K., Kakinuma, T.: 1982, An observation system of interplanetary scintillation at UHF. *Nagoya University Research Institute of Atmospherics Proceedings* **29**, 61 – 83. 56

Kojima, M., Coles, W.A., Tokumaru, M., Fujiki, K.: 2013, Scintillation Measurements of the Solar Wind Velocity in Strong Scattering near the Sun. *Solar Phys.* **283**, 519 – 540. 29, 125

Komm, R.W., Howard, R.F., Harvey, J.W.: 1993a, Meridional Flow of Small Photospheric Magnetic Features. *Solar Phys.* **147**, 207 – 223. 12, 76, 81

Komm, R.W., Howard, R.F., Harvey, J.W.: 1993b, Rotation rates of small magnetic features from two- and one-dimensional cross-correlation analyses. *Solar Phys.* **145**, 1 – 10. 76

Kosovichev, A.G., Schou, J.: 1997, Detection of Zonal Shear Flows beneath the Sun's Surface from f-Mode Frequency Splitting. *Astrophys. J. Lett.* **482**, L207. 12

Kosovichev, A.G., Schou, J., Scherrer, P.H., Bogart, R.S., Bush, R.I., Hoeksema, J.T., Aloise, J., Bacon, L., Burnette, A., de Forest, C., Giles, P.M., Leibrand, K., Nigam, R., Rubin, M., Scott, K., Williams, S.D., Basu, S., Christensen-Dalsgaard, J., Dappen, W., Rhodes, E.J. Jr., Duvall, T.L. Jr., Howe, R., Thompson, M.J., Gough, D.O., Sekii, T., Toomre, J., Tarbell, T.D., Title, A.M., Mathur, D., Morrison, M., Saba, J.L.R., Wolfson, C.J., Zayer, I., Milford, P.N.: 1997, Structure and Rotation of the Solar Interior: Initial Results from the MDI Medium-L Program. *Solar Phys.* **170**, 43 – 61. 12

Kosugi, T., Matsuzaki, K., Sakao, T., Shimizu, T., Sone, Y., Tachikawa, S., Hashimoto, T., Minesugi, K., Ohnishi, A., Yamada, T., Tsuneta, S., Hara, H., Ichimoto, K., Suematsu, Y., Shimojo, M., Watanabe, T., Shimada, S., Davis, J.M., Hill, L.D., Owens, J.K., Title, A.M., Culhane, J.L., Harra, L.K., Doschek, G.A., Golub, L.: 2007, The Hinode (Solar-B) Mission: An Overview. *Solar Phys.* **243**, 3 – 17. 44, 123

Krieger, A.S., Timothy, A.F., Roelof, E.C.: 1973, A Coronal Hole and Its Identification as the Source of a High Velocity Solar Wind Stream. *Solar Phys.* **29**, 505 – 525. 27

Krivova, N.A., Solanki, S.K.: 2002, The 1.3-year and 156-day periodicities in sunspot data: Wavelet analysis suggests a common origin. *Astron. Astrophys.* **394**, 701 – 706. 23, 24, 86, 91, 109, 113, 114

Layden, A.C., Fox, P.A., Howard, J.M., Sarajedini, A., Schatten, K.H.: 1991, Dynamo-based scheme for forecasting the magnitude of solar activity cycles. *Solar Phys.* **132**, 1 – 40. 79

Lazarus, A.J., Ogilvie, K.W., Burlaga, L.F.: 1970, Interplanetary Shock Observations by Mariner 5 and Explorer 34. *Solar Phys.* **13**, 232 – 239. 148

Lean, J.: 1990, Evolution of the 155 day periodicity in sunspot areas during solar cycles 12 to 21. *Astrophys. J.* **363**, 718 – 727. 23

Leighton, R.B.: 1964, Transport of Magnetic Fields on the Sun. *Astrophys. J.* **140**, 1547. 20, 64, 79

Leighton, R.B.: 1969, A Magneto-Kinematic Model of the Solar Cycle. *Astrophys. J.* **156**, 1. 20, 79

Little, L.T., Hewish, A.: 1966, Interplanetary scintillation and its relation to the angular structure of radio sources. *Mon. Not. Roy. Astron. Soc.* **134**, 221. 29

Little, L.T., Hewish, E.: 1968, Radio source structure derived from interplanarary scintillation. *Mon. Not. Roy. Astron. Soc.* **138**, 393. 29, 125

Livingston, W.: 2002, Sunspots Observed to Physically Weaken in 2000-2001. *Solar Phys.* **207**, 41 – 45. 90

Livingston, W., Penn, M.J., Svalgaard, L.: 2012, Decreasing Sunspot Magnetic Fields Explain Unique 10.7 cm Radio Flux. *Astrophys. J. Lett.* **757**, L8. 90

Livingston, W.C., Harvey, J., Pierce, A.K., Schrage, D., Gillespie, B., Simmons, J., Slaughter, C.: 1976a, Kitt Peak 60-cm vacuum telescope. *Appl. Opt.* **15**, 33 – 39. 43, 45, 46

Livingston, W.C., Harvey, J., Slaughter, C., Trumbo, D.: 1976b, Solar magnetograph employing integrated diode arrays. *Appl. Opt.* **15**, 40 – 52. 45, 48, 67

Lockwood, M., Owens, M., Rouillard, A.P.: 2009, Excess open solar magnetic flux from satellite data: 1. Analysis of the third perihelion Ulysses pass. *Journal of Geophysical Research (Space Physics)* **114**, A11103. 123

Lomb, N.R.: 1976, Least-squares frequency analysis of unequally spaced data. *Astrophys. Space Sci.* **39**, 447 – 462. 95

Longcope, D., Choudhuri, A.R.: 2002, The Orientational Relaxation of Bipolar Active Regions. *Solar Phys.* **205**, 63 – 92. 118

Lu, G., Baker, D.N., McPherron, R.L., Farrugia, C.J., Lummerzheim, D., Ruohoniemi, J.M., Rich, F.J., Evans, D.S., Lepping, R.P., Brittnacher, M., Li, X., Greenwald, R., Sofko, G., Villain, J., Lester, M., Thayer, J., Moretto, T., Milling, D., Troshichev, O., Zaitzev, A., Odintzov, V., Makarov, G., Hayashi, K.: 1998, Global energy deposition during the January 1997 magnetic cloud event. *J. Geophys. Res.* **103**, 11685 – 11694. 147

Macmillan, S.: 2007, *Observatories: an overview*, 708 – 711. 60

Manoharan, P.K.: 2010, Peculiar Current Solar-Minimum Structure of the Heliosphere. *Highlights of Astronomy* **15**, 484 – 487. 140

Manoharan, P.K.: 2012, Three-dimensional Evolution of Solar Wind during Solar Cycles 22-24. *Astrophys. J.* **751**, 128. 29, 125

Marians, M.: 1975, Computed scintillation spectra for strong turbulence. *Radio Science* **10**, 115 – 119. 131

Maunder, E.W.: 1890, Professor Spoerer's Researches on Sun-spots. *Mon. Not. Roy. Astron. Soc.* **50**, 251 – 252. 23

Maunder, E.W.: 1903, Spoerer's law of zones. *The Observatory* **26**, 329 – 330. 6

Maunder, E.W.: 1904, Note on the distribution of sun-spots in heliographic latitude, 1874-1902. *Mon. Not. Roy. Astron. Soc.* **64**, 747 – 761. 6

Mayaud, P.N.: 1980, Derivation, Meaning, and Use of Geomagnetic Indices. *Washington DC American Geophysical Union Geophysical Monograph Series* **22**, 607. 36

McComas, D.J., Elliott, H.A., Schwadron, N.A., Gosling, J.T., Skoug, R.M., Goldstein, B.E.: 2003, The three-dimensional solar wind around solar maximum. *Geophys. Res. Lett.* **30**(10), 1517. 123

McComas, D.J., Ebert, R.W., Elliott, H.A., Goldstein, B.E., Gosling, J.T., Schwadron, N.A., Skoug, R.M.: 2008, Weaker solar wind from the polar coronal holes and the whole Sun. *Geophys. Res. Lett.* **35**, L18103. 123

McKenna-Lawlor, S.M.P., Dryer, M., Kartalev, M.D., Smith, Z., Fry, C.D., Sun, W., Deehr, C.S., Kecskemety, K., Kudela, K.: 2006, Near real-time predictions of the arrival at Earth of flare-related shocks during Solar Cycle 23. *J. Geophys. Res.* **111**, 11103. 158

McPherron, R.L.: 1979, Magnetospheric substorms. *Reviews of Geophysics and Space Physics* **17**, 657 – 681. 32, 146

Mendoza, B., Velasco, V.M., Valdés-Galicia, J.F.: 2006, Mid-Term Periodicities in the Solar Magnetic Flux. *Solar Phys.* **233**, 319 – 330. 24, 109

Mercier, C., Subramanian, P., Kerdraon, A., Pick, M., Ananthakrishnan, S., Janardhan, P.: 2006a, Combining visibilities from the giant meterwave radio telescope and the Nancay radio heliograph. High dynamic range snapshot images of the solar corona at 327 MHz. *Astron. Astrophys.* **447**, 1189 – 1201. 84

Mercier, C., Subramanian, P., Kerdraon, A., Pick, M., Ananthakrishnan, S., Janardhan, P.: 2006b, Combining visibilities from the giant meterwave radio telescope and the Nancay radio heliograph. High dynamic range snapshot images of the solar corona at 327 MHz. *Astron. Astrophys.* **447**, 1189 – 1201. 163, 171

Nandy, D., Choudhuri, A.R.: 2002, Explaining the Latitudinal Distribution of Sunspots with Deep Meridional Flow. *Science* **296**, 1671 – 1673. 22

Nandy, D., Muñoz-Jaramillo, A., Martens, P.C.H.: 2011, The unusual minimumof sunspot cycle 23 caused by meridional plasma flow variations. *Nature*. 85, 126, 140, 143

Neugebauer, M., Snyder, C.W.: 1962, Solar Plasma Experiment. *Science* **138**, 1095 – 1097. 25, 147

Newton, H.W., Nunn, M.L.: 1951, The Sun's rotation derived from sunspots 1934-1944 and additional results. *Mon. Not. Roy. Astron. Soc.* **111**, 413. 12

Nishida, A.: 1968, Coherence of Geomagnetic DP 2 Fluctuations with Interplanetary Magnetic Variations. *J. Geophys. Res.* **73**, 5549 – 5559. 37, 148

Nishino, M.N., Fujimoto, M., Phan, T.D., Mukai, T., Saito, Y., Kuznetsova, M.M., Rastätter, L.: 2008, Anomalous Flow Deflection at Earth's Low-Alfvén-Mach-Number Bow Shock. *Physical Review Letters* **101**(6), 065003. 25

Odstrcil, D.: 2003, Modeling 3-D solar wind structure. *Adv. Space Res.* **32**, 497 – 506. 148

Oliver, R., Ballester, J.L.: 1994, The north-south asymmetry of sunspot areas during solar cycle 22. *Solar Phys.* **152**, 481 – 485. 24

Oliver, R., Ballester, J.L., Baudin, F.: 1998, Emergence of magnetic flux on the Sun as the cause of a 158-day periodicity in sunspot areas. *Nature* **394**, 552 – 553. 86, 91, 113

Ossendrijver, M.: 2003, The solar dynamo. *Astron. Astrophys. Rev.* **11**, 287 – 367. 13

Parker, E.N.: 1955a, Hydromagnetic Dynamo Models. *Astrophys. J.* **122**, 293. 15, 64

Parker, E.N.: 1955b, The Formation of Sunspots from the Solar Toroidal Field. *Astrophys. J.* **121**, 491. 18, 20, 64

Parker, E.N.: 1958, Dynamics of the Interplanetary Gas and Magnetic Fields. *Astrophys. J.* **128**, 664. 25, 27, 155

Parker, E.N.: 1963, A Kinematical Theory of Turbulent Hydromagnetic Fields. *Astrophys. J.* **138**, 226. 27

Penn, M.J., Livingston, W.: 2006, Temporal Changes in Sunspot Umbral Magnetic Fields and Temperatures. *Astrophys. J. Lett.* **649**, L45 – L48. 90

Percival, D.B., Walden, A.T.: 1993, *Spectral Analysis for Physical Applications.*, 583. 98

Pesnell, W.D., Thompson, B.J., Chamberlin, P.C.: 2012, The Solar Dynamics Observatory (SDO). *Solar Phys.* **275**, 3 – 15. 13, 44, 170

Pierce, A.K.: 1964, The McMath solar telescope of Kitt Peak National Observatory. *Appl. Opt.* **3**, 1337. 45

Rastogi, R.G., Patel, V.L.: 1975, Effect of the interplanetary magnetic field on the ionosphere over the magnetic equator. *Proceedings of the Indian National Science Academy Part A* **82**, 121 – 141. 37, 152

Rastogi, R.G., Janardhan, P., Ahmed, K., Das, A.C., Bisoi, S.K.: 2010, Unique observations of a geomagnetic $SI^+ - SI^-$ pair: Solar sources and associated solar wind fluctuations. *Journal of Geophysical Research (Space Physics)* **115**, 12110. 147, 169

Razdan, H., Colburn, D.S., Sonett, C.P.: 1965, Recurrent SI^+–SI^- impulse pairs and shock structure in M-region beams. *Planet. Space Sci.* **13**, 1111. 147

Readhead, A.C.S., Hewish, A.: 1974, Fine structure in radio sources at 8 1 -5 MHz-111. The survey. *Mon. Not. Roy. Astron. Soc.* **167**, 663. 29, 125

Readhead, A.C.S., Kemp, M.C., Hewish, A.: 1978, The spectrum of small-scale density fluctuations in the solar wind. *Mon. Not. Roy. Astron. Soc.* **185**, 207 – 226. 129

Reay, S., Herzog, D.C., Alex, S., Kharin, E., McLean, S., Nose, M., Sergeyeva, N.: 2011, *Magnetic Observatory Data and Metadata: Types and Availability*, 149. 61

Reid, J.H.: 1968, Cape Lyot H&alpha-Heliograph Results. An Analysis of Flare Activity 1958-65. *Solar Phys.* **5**, 207 – 235. 24

Richardson, J.D., Wang, C., Paularena, K.I.: 2001, The solar wind: from solar minimum to solar maximum. *Advances in Space Research* **27**, 471 – 479. 123

Rickett, B.J.: 1975, Disturbances in the solar wind from IPS measurements in August 1972. *Solar Phys.* **43**, 237 – 247. 29, 125, 155

Rieger, E., Kanbach, G., Reppin, C., Share, G.H., Forrest, D.J., Chupp, E.L.: 1984, A 154-day periodicity in the occurrence of hard solar flares? *Nature* **312**, 623 – 625. 23, 86

Rieutord, M., Rincon, F.: 2010, The Sun's Supergranulation. *Living Reviews in Solar Physics* **7**, 2. 10

Roy, J.R.: 1977, The north-south distribution of major solar flare events, sunspot magnetic classes and sunspot areas /1955-1974/. *Solar Phys.* **52**, 53 – 61. 24

Russell, C.T., McPherron, R.L.: 1973, The Magnetotail and Substorms. *Space Sci. Rev.* **15**, 205 – 266. 32

Salpeter, E.E.: 1967, Interplanetary Scintillations. I. Theory. *Astrophys. J.* **147**, 433. 129

Savitzky, A., Golay, M.J.E.: 1964, Smoothing and differentiation of data by simplified least squares procedures. *Analytical Chemistry* **36**, 1627 – 1639. 90

Scargle, J.D.: 1982, Studies in astronomical time series analysis. II - Statistical aspects of spectral analysis of unevenly spaced data. *Astrophys. J.* **263**, 835 – 853. 95

Scargle, J.D.: 1989, Studies in astronomical time series analysis. III - Fourier transforms, autocorrelation functions, and cross-correlation functions of unevenly spaced data. *Astrophys. J.* **343**, 874 – 887. 95

Schatten, K., Sofia, S.: 1996, Forecasting Solar Activity and Cycle 23 Outlook. In: *Bulletin of the American Astronomical Society*, *Bulletin of the American Astronomical Society* **28**, 1347. 79

Schatten, K.H., Scherrer, P.H., Svalgaard, L., Wilcox, J.M.: 1978, Using dynamo theory to predict the sunspot number during solar cycle 21. *Geophys. Res. Lett.* **5**, 411 – 414. 79

Scherrer, P.H., Bogart, R.S., Bush, R.I., Hoeksema, J.T., Kosovichev, A.G., Schou, J., Rosenberg, W., Springer, L., Tarbell, T.D., Title, A., Wolfson, C.J., Zayer, I., MDI Engineering Team: 1995, The Solar Oscillations Investigation - Michelson Doppler Imager. *Solar Phys.* **162**, 129 – 188. 8, 44, 51, 52, 69, 156

Schou, J., Scherrer, P.H., Bush, R.I., Wachter, R., Couvidat, S., Rabello-Soares, M.C., Bogart, R.S., Hoeksema, J.T., Liu, Y., Duvall, T.L., Akin, D.J., Allard, B.A., Miles, J.W., Rairden, R., Shine, R.A., Tarbell, T.D., Title, A.M., Wolfson, C.J., Elmore, D.F., Norton, A.A., Tomczyk, S.: 2012, Design and Ground Calibration of the Helioseismic and Magnetic Imager (HMI) Instrument on the Solar Dynamics Observatory (SDO). *Solar Phys.* **275**, 229 – 259. 13, 44, 170

Schrijver, a.L.Y. C. J.: 2008,. *Solar Phys.* **252**, 19. 81

Schrijver, C.J., DeRosa, M.L.: 2003, Photospheric and heliospheric magnetic fields. *Solar Phys.* **212**, 165 – 200. 156

Schultz, M., Stattegger, K.: 1997, Spectrum: Spectral analysis of unevenly spaced paleoclimatic time series. *Comput. Geosci.* **23**, 929 – 945. 95, 98

Schwabe, S.H.: 1843,. *Astron. Nachr.* **20**, 234. 4, 85

Schwenn, R.: 1990, In: Schwenn, R. & Marsch, E. (ed.) *Large-Scale Structure of the Interplanetary Medium*, 99 – 181. 27, 155

Seigel, A.F.: 1980, Testing for periodicity in a time series. *Journal of the American Statistical Association* **75**, 345 – 348. 96

Senior, C., Blanc, M.: 1984, On the control of magnetospheric convection by the spatial distribution of ionospheric conductivities. *J. Geophys. Res.* **89**, 261 – 284. 36, 39

Shen, W.W., Dryer, M.: 1972, Magnetohydrodynamic theory for the interaction of an interplanetary double-shock ensemble with the earth's bow shock. *J. Geophys. Res.* **77**, 4627 – 4644. 148

Simnett, G.M.: 2000, The Relationship between CMEs and Prominence Eruptions. *J. Atmos. Solar Terr. Phys.* **62**, 1479 – 1487. 158

Simnett, G.M.: 2002, The acceleration and release of solar energetic particles in events from April 20 - May 9, 1998. *Adv. Space Res.* **29**, 1493 – 1500. 158

Smart, D.F., Shea, M.A.: 1985, A simplified model for timing the arrival of solar flare-initiated shocks. *J. Geophys. Res.* **90**, 183 – 190. 159

Smith, E.J., Balogh, A.: 2008, Decrease in heliospheric magnetic flux in this solar minimum: Recent Ulysses magnetic field observations. *Geophys. Res. Lett.* **35**, L22103. 123, 139

Smith, E.J., Marsden, R.G., Balogh, A., Gloeckler, G., Geiss, J., McComas, D.J., McKibben, R.B., MacDowall, R.J., Lanzerotti, L.J., Krupp, N., Krueger, H., Landgraf, M.: 2003, The Sun and Heliosphere at Solar Maximum. *Science* **302**, 1165 – 1169. 123

Smith, Z.K., Dryer, M., McKenna-Lawlor, S.M.P., Fry, C.D., Deehr, C.S., Sun, W.: 2009a, Operational validation of HAFv2's predictions of interplanetary shock arrivals at Earth: Declining phase of Solar Cycle 23. *J. Geophys. Res.* **114**, 5106. 148, 158

Smith, Z.K., Steenburgh, R., Fry, C.D., Dryer, M.: 2009b, Predictions of Interplanetary Shock Arrivals at Earth: Dependence of Forecast Outcome on the Input Parameters. *Space Weather* **7**, 5106. 148, 158

Snodgrass, H.B.: 1983, Magnetic rotation of the solar photosphere. *Astrophys. J.* **270**, 288 – 299. 10

Snyder, C.W., Neugebauer, M., Rao, U.R.: 1963, The Solar Wind Velocity and Its Correlation with Cosmic-Ray Variations and with Solar and Geomagnetic Activity. *J. Geophys. Res.* **68**, 6361. 25

Sofia, S., Fox, P., Schatten, K.: 1998, Forecast update for activity cycle 23 from a dynamo-based method. *Geophys. Res. Lett.* **25**, 4149 – 4152. 79

Sonett, C.P., Colburn, D.S.: 1965, The SI^{+}-SI^{-} pair and interplanetary forward-reverse shock ensembles. *Planet. Space Sci.* **13**, 675. 147

Sonett, C.P., Colburn, D.S., Davis, L., Smith, E.J., Coleman, P.J.: 1964, Evidence for a Collision-Free Magnetohydrodynamic Shock in Interplanetary Space. *Physical Review Letters* **13**, 153 – 156. 147

Spiegel, E.A., Weiss, N.O.: 1980, Magnetic activity and variations in solar luminosity. *Nature* **287**, 616. 20

Spiegel, E.A., Zahn, J.P.: 1992, The solar tachocline. *Astron. Astrophys.* **265**, 106 – 114. 18

Spiro, R.W., Wolf, R.A., Fejer, B.G.: 1988, Penetrating of high-latitude-electric-field effects to low latitudes during SUNDIAL 1984. *Annales Geophysicae* **6**, 39 – 49. 37, 149

Spruit, H.C., van Ballegooijen, A.A.: 1982, Stability of toroidal flux tubes in stars. *Astron. Astrophys.* **106**, 58 – 66. 18

Steenbeck, M., Krause, F.: 1969, On the Dynamo Theory of Stellar and Planetary Magnetic Fields. I. AC Dynamos of Solar Type. *Astronomische Nachrichten* **291**, 49 – 84. 16, 64

Stone, E.C., Frandsen, A.M., Mewaldt, R.A., Christian, E.R., Margolies, D., Ormes, J.F., Snow, F.: 1998, The Advanced Composition Explorer. *Space Sci. Rev.* **86**, 1 – 22. 44, 58, 59, 122, 150

Suess, H.E.: 1980, The radiocarbon record in tree rings of the last 8000 years. *Radiocarbon* **22**, 200 – 209. 23

Sun, X., Liu, Y., Hoeksema, J.T., Hayashi, K., Zhao, X.: 2011, A New Method for Polar Field Interpolation. *Solar Phys.* **270**, 9 – 22. 56, 70

Svalgaard, L., Cliver, E.W., Kamide, Y.: 2005, Sunspot cycle 24: Smallest cycle in 100 years? *Geophys. Res. Lett.* **32**, 1104. 79, 139

Svalgaard, L., Duvall, T.L. Jr., Scherrer, P.H.: 1978, The strength of the sun's polar fields. *Solar Phys.* **58**, 225 – 239. 43

Swarup, G., Sarma, N.V.G., Joshi, M.N., Kapahi, V.K., Bagri, D.S., Damle, S.H., Ananthakrishnan, S., Balasubramanian, V., Bhave, S.S., Sinha, R.P.: 1971, Large Steerable Radio Telescope at Ootacamund, India. *Nature Physical Science* **230**, 185 – 188. 56

Takeuchi, T., Araki, T., Viljanen, A., Watermann, J.: 2002, Geomagnetic negative sudden impulses: Interplanetary causes and polarization distribution. *J. Geophys. Res.* **107**, 1096. 148

Temmer, M., Veronig, A., Hanslmeier, A.: 2002, Hemispheric Sunspot Numbers R_n and R_s: Catalogue and N-S asymmetry analysis. *Astron. Astrophys.* **390**, 707 – 715. 24

Timothy, A.F., Krieger, A.S., Vaiana, G.S.: 1975, The structure and evolution of coronal holes. *Solar Phys.* **42**, 135 – 156. 27

Tokumaru, M., Kojima, M., Fujiki, K.: 2010, Solar cycle evolution of the solar wind speed distribution from 1985 to 2008. *Journal of Geophysical Research (Space Physics)* **115**, A04102. 29, 125

Tokumaru, M., Kojima, M., Fujiki, K.: 2012, Long-term evolution in the global distribution of solar wind speed and density fluctuations during 1997-2009. *Journal of Geophysical Research (Space Physics)* **117**, 6108. 44, 56, 133

Tokumaru, M., Kojima, M., Ishida, Y., Yokobe, A., Ohmi, T.: 2000, Large-Scale Structure of Solar Wind Turbulence Near Solar Activity Minimum. *Advances in Space Research* **25**, 1943 – 1946. 136

Torrence, C., Compo, G.P.: 1998, A Practical Guide to Wavelet Analysis. *Bulletin of the American Meteorological Society* **79**, 61 – 78. 91, 119

Tóth, G., Sokolov, I.V., Gombosi, T.I., Chesney, D.R., Clauer, C.R., De Zeeuw, D.L., Hansen, K.C., Kane, K.J., Manchester, W.B., Oehmke, R.C., Powell, K.G., Ridley, A.J., Roussev, I.I., Stout, Q.F., Volberg, O., Wolf, R.A., Sazykin, S., Chan, A., Yu, B., Kóta, J.: 2005, Space Weather Modeling Framework: A new tool for the space science community. *J. Geophys. Res.* **110**, 12226. 148

Tsurutani, B.T., Gonzalez, W.D.: 1997, The Interplanetary causes of magnetic storms: A review. *Washington DC American Geophysical Union Geophysical Monograph Series* **98**, 77 – 89. 32, 146

Ulrich, R.K., Evans, S., Boyden, J.E., Webster, L.: 2002, Mount Wilson Synoptic Magnetic Fields: Improved Instrumentation, Calibration, and Analysis Applied to the 2000 July 14 Flare and to the Evolution of the Dipole Field. *Astrophys. J. Supplement.* **139**, 259 – 279. 43

Vaiana, G.S., Davis, J.M., Giacconi, R., Krieger, A.S., Silk, J.K., Timothy, A.F., Zombeck, M.: 1973, X-Ray Observations of Characteristic Structures and Time Variations from the Solar Corona: Preliminary Results from SKYLAB. *Astrophys. J. Lett.* **185**, L47. 26

van Ballegooijen, A.A.: 1982, The overshoot layer at the base of the solar convective zone and the problem of magnetic flux storage. *Astron. Astrophys.* **113**, 99 – 112. 20

van Ballegooijen, a.C.N.P. A. A., Priest, E.R., Joy, A.H.: 1998,. *Astrophys. J.* **501**, 866. 81

Vandegriff, J., Wagstaff, K., Ho, G., Plauger, J.: 2005, Forecasting Space Weather: Predicting interplanetary shocks using neural networks. *Adv. Space Res.* **36**, 2323 – 2327. 148

Vasyliunas, V.M.: 1970, Mathematical Models of Magnetospheric Convection and Its Coupling to the Ionosphere. In: McCormack, B.M., Renzini, A. (eds.)

Particles and Field in the Magnetosphere, *Astrophysics and Space Science Library* **17**, 60. 36, 39, 148

Vecchio, A., Carbone, V.: 2009, Spatio-temporal analysis of solar activity: main periodicities and period length variations. *Astron. Astrophys.* **502**, 981 – 987. 24, 86

Venugopal, V.R., Ananthakrishnan, S., Swarup, G., Pynzar, A.V., Udaltsov, V.A.: 1985, Structure of PKS 1148-001. *Mon. Not. Roy. Astron. Soc.* **215**, 685 – 689. 129, 131

Verma, V.K.: 1987, On the increase of solar activity in the Southern Hemisphere during solar cycle 21. *Solar Phys.* **114**, 185 – 188. 24

Verma, V.K., Joshi, G.C.: 1987, On the Periodicities of Sunspots and Solar Strong Hard X-Ray Bursts. *Solar Phys.* **114**, 415 – 418. 23

Vernova, E.S., Tyasto, M.I., Baranov, D.G.: 2007, Photospheric Magnetic Field of the Sun: Two Patterns of the Longitudinal Distribution. *Solar Phys.* **245**, 177 – 190. 170

Vernova, E.S., Mursula, K., Tyasto, M.I., Baranov, D.G.: 2004, Long-term longitudinal asymmetries in sunspot activity: Difference between the ascending and descending phase of the solar cycle. *Solar Phys.* **221**, 151 – 165. 170

Vourlidas, A., Buzasi, D., Howard, R.A., Esfandiari, E.: 2002, Mass and energy properties of LASCO CMEs. In: Wilson, A. (ed.) *Solar Variability: From Core to Outer Frontiers*, *ESA Special Publication* **506**, 91 – 94. 30

Wagner, W.J.: 1984, Coronal Mass Ejections. *Annual Review of Astronomy and Astrophysics* **22**, 267 – 289. 30

Waldmeier, M.: 1971, The asymmetry of solar activity in the years 1959 1969. *Solar Phys.* **20**, 332 – 344. 24

Wang, W., Lei, J., Burns, A.G., Wiltberger, M., Richmond, A.D., Solomon, S.C., Killeen, T.L., Talaat, E.R., Anderson, D.N.: 2008, Ionospheric electric field variations during a geomagnetic storm simulated by a coupled magnetosphere ionosphere thermosphere (CMIT) model. *Geophys. Res. Lett.* **35**, 18105. 37

Wang, Y.M., Sheeley, N.R. Jr.: 1991, Magnetic flux transport and the sun's dipole moment - New twists to the Babcock-Leighton model. *Astrophys. J.* **375**, 761 – 770. 65

Wang, Y.M., Sheeley, N.R. Jr.: 2003, On the Fluctuating Component of the Sun's Large-Scale Magnetic Field. *Astrophys. J.* **590**, 1111 – 1120. 114

Wang, Y.M., Lean, J.L., Sheeley, N.R. Jr.: 2005, Modeling the Sun's Magnetic Field and Irradiance since 1713. *Astrophys. J.* **625**, 522 – 538. 81

Wang, Y.M., Nash, A.G., Sheeley, N.R. Jr.: 1989, Evolution of the sun's polar fields during sunspot cycle 21 - Poleward surges and long-term behavior. *Astrophys. J.* **347**, 529 – 539. 64, 106, 109

Wang, Y.M., Robbrecht, E., Sheeley, N.R. Jr.: 2009, On the Weakening of the Polar Magnetic Fields during Solar Cycle 23. *Astrophys. J.* **707**, 1372 – 1386. 65

Wang, Y., Sheeley, N.R. Jr., Nash, A.G.: 1991, A new solar cycle model including meridional circulation. *Astrophys. J.* **383**, 431 – 442. 65

Welch, P.D.: 1967, The Use of Fast Fourier Transform for the Estimation of Power Spectra: A Method Based on Time Averaging Over Short, Modified Periodograms. *IEEE Transactions on Audio and Electroacoustics* **15**, 70 – 73. 95

Wenzel, K.P., Marsden, R.G., Page, D.E., Smith, E.J.: 1992, The ULYSSES Mission. *Astron. Astrophys. Suppl.* **92**, 207. 44, 122

Wolf, R.: 1861, Abstract of his latest Results. *Mon. Not. Roy. Astron. Soc.* **21**, 77. 4

Wolf, R.A., Garner, T.W., Goldstein, J., Sazykin, S., Spiro, R.W.: 2001, Storm-time Magnetospheric Effects on Electric Fields in the Subauroral Ionosphere. *AGU Fall Meeting Abstracts*, A12. 37, 149

Wolf, R.A., Spiro, R.W., Sazykin, S., Toffoletto, F.R.: 2007, How the Earth's inner magnetosphere works: An evolving picture. *Journal of Atmospheric and Solar-Terrestrial Physics* **69**, 288 – 302. 36, 39

Woo, R., Armstrong, J.W., Bird, M.K., Patzold, M.: 1995, Variation of fractional electron density fluctuations inside 40 R_0 observed by ULYSSES ranging measurements. *Geophys. Res. Lett.* **22**, 329 – 332. 28

Yashiro, S., Gopalswamy, N., Michalek, G., St. Cyr, O.C., Plunkett, S.P., Rich, N.B., Howard, R.A.: 2004, A catalog of white light coronal mass ejections observed by the SOHO spacecraft. *Journal of Geophysical Research (Space Physics)* **109**, 7105. 30

Zhao, J., Bogart, R.S., Kosovichev, A.G., Duvall, T.L., Hartlep, T.: 2013, Solar Interior Meridional Flow from SDO/HMI. In: *AAS/Solar Physics Division Meeting, AAS/Solar Physics Division Meeting* **44**, 204 – 02. 13

Zwickl, R.D., Doggett, K.A., Sahm, S., Barrett, W.P., Grubb, R.N., Detman, T.R., Raben, V.J., Smith, C.W., Riley, P., Gold, R.E., Mewaldt, R.A., Maruyama, T.: 1998, The NOAA Real-Time Solar-Wind (RTSW) System using ACE Data. *Space Sci. Rev.* **86**, 633 – 648. 59, 159

Solar Phys
DOI 10.1007/s11207-013-0335-3

Changes in Quasi-periodic Variations of Solar Photospheric Fields: Precursor to the Deep Solar Minimum in Cycle 23?

Susanta Kumar Bisoi · P. Janardhan · D. Chakrabarty · S. Ananthakrishnan · Ankur Divekar

Received: 15 November 2012 / Accepted: 20 May 2013

Abstract Possible precursor signatures in the quasi-periodic variations of solar photospheric fields were investigated in the build-up to one of the deepest solar minima experienced in the past 100 years. This unusual and deep solar minimum occurred between Solar Cycles 23 and 24. We used both wavelet and Fourier analysis to study the changes in the quasi-periodic variations of solar photospheric fields. Photospheric fields were derived using ground-based synoptic magnetograms spanning the period 1975.14 to 2009.86 and covering Solar Cycles 21, 22, and 23. A hemispheric asymmetry in the periodicities of the photospheric fields was seen only at latitudes above $\pm 45°$ when the data were divided into two parts based on a wavelet analysis: one prior to 1996 and the other after 1996. Furthermore, the hemispheric asymmetry was observed to be confined to the latitude range of 45° to 60°. This can be attributed to the variations in polar surges that primarily depend on both the emergence of surface magnetic flux and varying solar-surface flows. The observed asymmetry along with the fact that both solar fields above $\pm 45°$ and micro-turbulence levels in the

S.K. Bisoi (✉) · P. Janardhan
Astronomy & Astrophysics Division, Physical Research Laboratory, Navrangpura, Ahmedabad 380009, India
e-mail: susanta@prl.res.in

P. Janardhan
e-mail: jerry@prl.res.in

D. Chakrabarty
Space & Atmospheric Sciences Division, Physical Research Laboratory, Navrangpura, Ahmedabad 380009, India
e-mail: dipu@prl.res.in

S. Ananthakrishnan · A. Divekar
Department of Electronic Science, University of Pune, Pune, Maharasthra 411007, India

S. Ananthakrishnan
e-mail: subra.anan@gmail.com

A. Divekar
e-mail: wiztronix@gmail.com

Published online: 13 July 2013

inner-heliosphere have been decreasing since the early- to mid-nineties (Janardhan *et al.* in *Geophys. Res. Lett.* **382**, 20108, 2011) suggest that around this time active changes occurred in the solar dynamo that governs the underlying basic processes in the Sun. These changes in turn probably initiated the build-up to the very deep solar minimum at the end of Cycle 23. The decline in fields above $\pm 45°$, for well over a solar cycle, would imply that weak polar fields have been generated in the past two successive solar cycles, *viz.* Cycles 22 and 23. A continuation of this declining trend beyond 22 years, if it occurs, will have serious implications for our current understanding of the solar dynamo.

Keywords Magnetic fields, photosphere · Solar cycle, observations · Solar periodicity · Surges

1. Introduction

The delayed onset of Solar Cycle 24, after one of the deepest solar minima experienced in the past 100 years, has had significant solar and heliospheric consequences. Solar Cycle 23 has been characterized by a steady decline in solar activity (McComas *et al.*, 2008; Jian, Russell, and Luhmann, 2011), a continuous weakening of polar fields (Jiang *et al.*, 2011), and a decline in micro-turbulence levels in the inner heliosphere since ≈ 1995 (Janardhan *et al.*, 2011). Investigations of the boundary of polar coronal holes during the declining phase of Solar Cycle 23 using images from the *Extreme Ultraviolet Imaging Telescope* (EIT) onboard the *Solar and Heliospheric Observatory* (SoHO) have found a decrease in coronal hole area by ≈ 15 % in comparison to that observed at the beginning of Solar Cycle 23 (Kirk *et al.*, 2009). Using both ground-based and space-borne observations of photospheric magnetic fields (Janardhan, Bisoi, and Gosain, 2010; Hathaway and Rightmire, 2010) and theoretical modeling (Dikpati *et al.*, 2010; Nandy, Muñoz-Jaramillo, and Martens, 2011), there have been continuous efforts to investigate and understand the behavior of solar photospheric fields and their correlation with meridional flows to try to explain the delayed onset of Cycle 24 and the cause of the deep minimum at the end of Cycle 23.

Magnetic-field measurements using data from the National Solar Observatory, Kitt Peak (NSO/KP) synoptic magnetogram database, have shown that a decline in solar photospheric fields in the latitude range of 45° to 78° began around the minimum of Solar Cycle 22, in ≈ 1995 – 1996 (Janardhan, Bisoi, and Gosain, 2010). However, the dipole field of the Sun behaved differently. It was at its strongest in 1995, weakened at solar maximum around 2000, and then increased between ≈ 2000 and 2004 (Wang, Robbrecht, and Sheeley, 2009; Janardhan, Bisoi, and Gosain, 2010). Signatures of this decline in solar fields above latitude $\pm 45°$ have also been observed in the inner heliosphere as a corresponding decline in micro-turbulence levels, which in turn correspond to small-scale interplanetary magnetic fields (Ananthakrishnan, Coles, and Kaufman, 1980; Ananthakrishnan, Balasubramanian, and Janardhan, 1995). The decline in micro-turbulence levels was inferred from extensive interplanetary scintillation (IPS) observations at 327 MHz in the period 1983 – 2009 (Janardhan *et al.*, 2011). Because both solar magnetic fields and micro-turbulence levels in the inner-heliosphere have been declining since mid-1990, Janardhan *et al.* (2011) have argued that the build-up to the deep and extended solar minimum at the end of Cycle 23 was initiated as early as the mid-1990.

One method of gaining insights into underlying basic processes in the solar interior that govern the nature and evolution of solar photospheric magnetic fields is studying the periodicities produced by various surface-activity features at different times in the solar cycle. For example, the 158-day Rieger periodicity reported in the solar-flare occurrence rates (Oliver, Ballester, and Baudin, 1998) has been linked to the periodic emergence of magnetic flux through the photosphere, which in turn gives rise to a periodic variation of the total sunspot area on the solar surface. Similarly, a strong 1.3-year periodicity detected at the base of the solar convection zone in a helioseismic study (Howe *et al.*, 2000) has also been detected in sunspot areas and sunspot number time series studied using wavelet transforms (Krivova and Solanki, 2002). Krivova and Solanki have proposed that the 154 – 158-day Rieger period is a harmonic of the 1.3-year periodicity (3×156 days $= 1.28$ years) and that variations in the rotation rate have a strong influence on the workings of the solar dynamo (Krivova and Solanki, 2002).

To understand the role of periodic changes, if any, in the solar photospheric fields that led to the build-up of the recent deep minimum at the end of Cycle 23, data from the NSO/KP synoptic magnetic database during the period 1975.14 – 2009.86 were subjected to detailed spectral analyses using both wavelet and Fourier techniques. It has been shown that a significant North – South asymmetry in the quasi-periodic variations of the photospheric magnetic fields exist prior to and after 1996 (with 1996 being a clear transition period) almost 12 years before the deep minimum period in 2008 – 2009.

1.1. Solar Periodicities

Prominent periodicities related to the solar cycle, in addition to the well-known synodic rotation period of ≈ 27 days and the sunspot activity cycle of ≈ 11 years, have been a topic of interest for over two decades now. Using data from the *Gamma Ray Spectrometer* (Forrest *et al.*, 1980) onboard the *Solar Maximum Mission*, a clear 154-day periodicity in the occurrence rate of high-energy (0.3 – 100 MeV) flares has been reported (Rieger *et al.*, 1984). This was also confirmed at other wavelengths (Verma and Joshi, 1987; Droege *et al.*, 1990; Kile and Cliver, 1991; Chowdhury and Ray, 2006), and for solar energetic-particle events (Lean, 1990; Krivova and Solanki, 2002; Kiliç, 2008; Chowdhury, Khan, and Ray, 2010; Chowdhury and Dwivedi, 2011).

In addition, other intermediate periodicities with periods ($<$ one year) have also been reported, *viz.* a 51-day periodicity in the comprehensive flare index (Bai, 1987), a 127-day periodicity in the 10-cm radio flux (Kile and Cliver, 1991), periodicities of 33.5 days, 51 days, 84 days, 129 days, and 153 days in the solar-flare occurrence during different phases of Solar Cycles 19 – 23 (Bai, 2003), periodicities of 100 – 103 days, 124 – 129 days, 151 – 158 days, 177 ± 2 days, 209 – 222 days, 232 – 249 days, 282 ± 4 days, 307 – 349 days in the unsigned photospheric fluxes (Knaack, Stenflo, and Berdyugina, 2004, 2005) and periodicities of 87 – 106 days, 159 – 175 days, 194 – 219 days, 292 – 318 days for Cycle 22, and 69 – 95 days, 113 – 133 days, 160 – 187 days, 245 – 321 days, 348 – 406 days in sunspot areas at different phases of Cycle 23 (Chowdhury, Khan, and Ray, 2009).

For periodicities, between one and five years, a 1.3-year periodicity in sunspot areas and numbers (Krivova and Solanki, 2002), a 1-year and 1.7-year periodicity in solar total and open fluxes (Mendoza, Velasco, and Valdés-Galicia, 2006), a 1.3-year, 1.43-year, 1.5-year, 1.8-year, 2.4-year, 2.6-year, 3.5-year, 3.6-year, and 4.1-year periodicity in unsigned photospheric fluxes (Knaack, Stenflo, and Berdyugina, 2004, 2005) have been reported. Studies of all these periodicities have shown an asymmetry in solar-activity phenomena between the northern and southern hemispheres of the Sun. This hemispheric asymmetry, on different time scales and at different phases of different solar cycles, has been observed in various types of solar activity (Howard, 1974; Verma, 1987; Oliver and Ballester, 1994; Knaack, Stenflo, and Berdyugina, 2005) and has been providing invaluable information about basic underlying physical processes on the Sun. Since processes such as differential rotation of the Sun and emergence of magnetic flux determine the strength and distribution of solar magnetic activity, investigating solar-cycle-related periodic or quasi-periodic variations is crucial for understanding the behavior and nature of solar magnetic fields.

2. Decline in Mid- to High-Latitude Solar Fields

Figure 1 shows temporal variation in the unsigned, or absolute, solar photospheric magnetic fields in the latitude range of $45° - 78°$ in both solar hemispheres for the period from February 1975 to November 2009 (panel (a)) covering Solar Cycles 21, 22, and 23. The vertically oriented dotted lines demarcate the period of solar minimum of these three solar cycles. The small, black filled dots and the open circles are the actual measurements for the northern and southern hemispheres, while the solid red (northern hemisphere) and blue (southern hemisphere) lines are smoothed curves derived using a robust Savitzky–Golay (SG) algorithm (Savitzky and Golay, 1964) that can preserve features of the input distribution such as maxima and minima while effectively suppressing noise. These features are generally flattened by other smoothing techniques. The decline in photospheric magnetic fields in both hemispheres, starting around the early- to mid-1990s, can be clearly seen in Figure 1. While the decline in photospheric fields had started in ≈ 1991 for the northern hemisphere (solid red curve), for the southern hemisphere the decline started in ≈ 1995 (solid blue curve). Beyond ≈ 1996, a steady decline in the photospheric fields for both hemispheres can be clearly seen. A similar decline in the sunspot umbral magnetic field strength since ≈ 1998 has been reported as well (Livingston, 2002; Penn and Livingston, 2006). Also shown in the bottom two panels of Figure 1 are the magnetic residuals, obtained by subtracting the SG fit from the actual measurements for the two hemispheres in the latitude range of $45° - 78°$ (panel (b)) and $0° - 45°$ (panel (c)) respectively. See the upper two panels of Figure 1 in Janardhan, Bisoi, and Gosain (2010) for measurements of the magnetic field in the range of $\pm 45°$, which show a strong solar-cycle modulation in the data, as expected.

The main details of the method for deriving the magnetic fields are given below. We used measurements of magnetic-field strengths obtained from 466 individual Carrington rotations (CR) of NSO/KP synoptic magnetograms from CR 1625 through CR 2090 in the period from 19 February 1975 to 09 November 2009 (1975.14 – 2009.86). Each magnetogram, generated from daily ground-based full-disk magnetograms spanning a Carrington rotation period (27.27 days), was longitudinally averaged to a 1°-wide longitudinal strip covering the latitude range from $-90°$ to $+90°$. Surface magnetic fields in both equatorial ($-45°$ to $+45°$) and high-latitude zones ($> 45°$ in both hemispheres) of the Sun were then derived by averaging over appropriate latitude regions. Full details of the method are described by Janardhan, Bisoi, and Gosain (2010).

The SG smoothing was performed so that the resulting residual time-series is stationary: *i.e.* the mean of time series is or approaches zero. This detrending of the data removes strong periodic variations (≈ 11 years). The residuals were then subjected to a wavelet and a Fourier time-series analysis to study temporal periodic variations in the photospheric magnetic fields. In the remainder of the text the fields obtained in the equatorial belt of $-45°$ to $+45°$ are referred to as low-latitude fields, while the fields obtained at latitudes $> 45°$ in the two hemispheres are referred to as high-latitude fields.

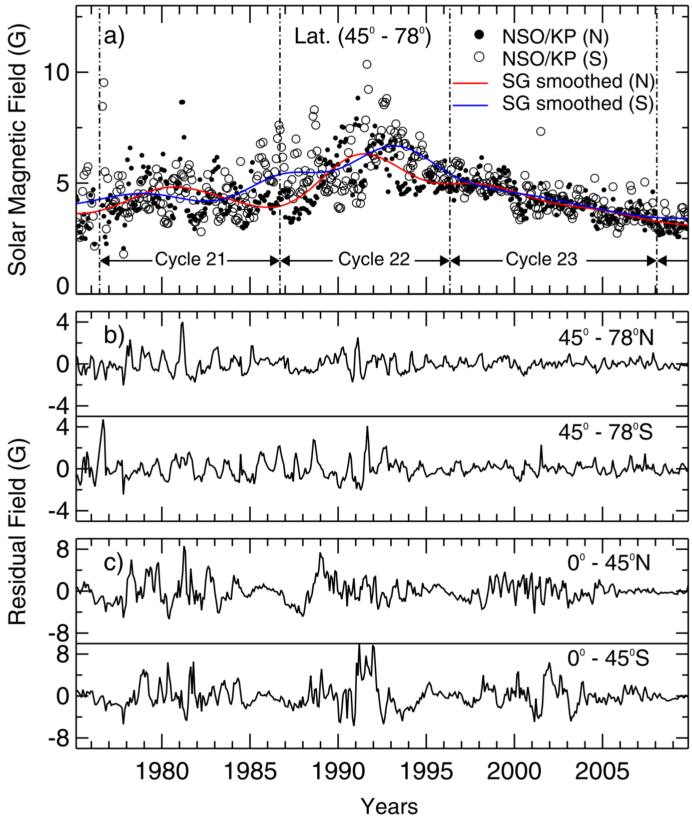

Figure 1 (a) Measurements of solar photospheric magnetic fields in the latitude range of 45° to 78°. The filled dots and the open circles represent the measurements for the northern and southern hemispheres while the fit obtained using the SG algorithm is shown by the solid red (North) and blue (South) lines. The vertically oriented dotted lines demarcate the periods of Solar Cycles 21, 22, and 23. (b) The residuals obtained after subtracting the SG-smoothed values from the magnetic fields in the latitude range 45° to 78° are shown for the North and South. (c) The residual fields for the northern and southern hemispheres obtained from the magnetic fields at latitudes below 45°.

2.1. Transition in Wavelet Periodicities

A wavelet transform is basically the convolution of a time series with the scaled and translated version of a chosen mother wavelet function. Wavelet analysis now is frequent used in the analysis of time-series data since it yields information in both time and frequency domains (Torrence and Compo, 1998). Using a Morlet wavelet as the mother wavelet and based on the algorithm by Torrence and Compo (1998), the magnetic residuals obtained for the high- and low-latitude fields in the period from 19 February 1975 to 09 November 2009 (1975.14 – 2009.86) were subjected to a wavelet analysis. Scattered data gaps amounting to ≈ 2.5 % of the data were replaced with values obtained using a cubic-spline interpolation. The Morlet wavelet function $\psi_0(\eta)$, represented in Equation (1) below, is a plane wave modulated by a Gaussian,

$$\psi_0(\eta) = \pi^{-1/4} e^{i\omega_0\eta} e^{-\eta^2/2}. \tag{1}$$

Here, ω_0 is a non-dimensional frequency that determines the number of oscillations in the wavelet, and η is a non-dimensional time parameter. The choice of different non-dimensional frequencies defines the frequency resolution. However, by varying the frequency resolution, one has to compromise with temporal resolution. In this case, we chose ω_0 to be six to obtain a better frequency resolution. This value was left unchanged and was not tuned to different values because our interest is to look for changes in the frequency components rather than to find precisely the low- and high-frequency components. However, in the following sections, we employed a Fourier-analysis technique to find the various frequency components.

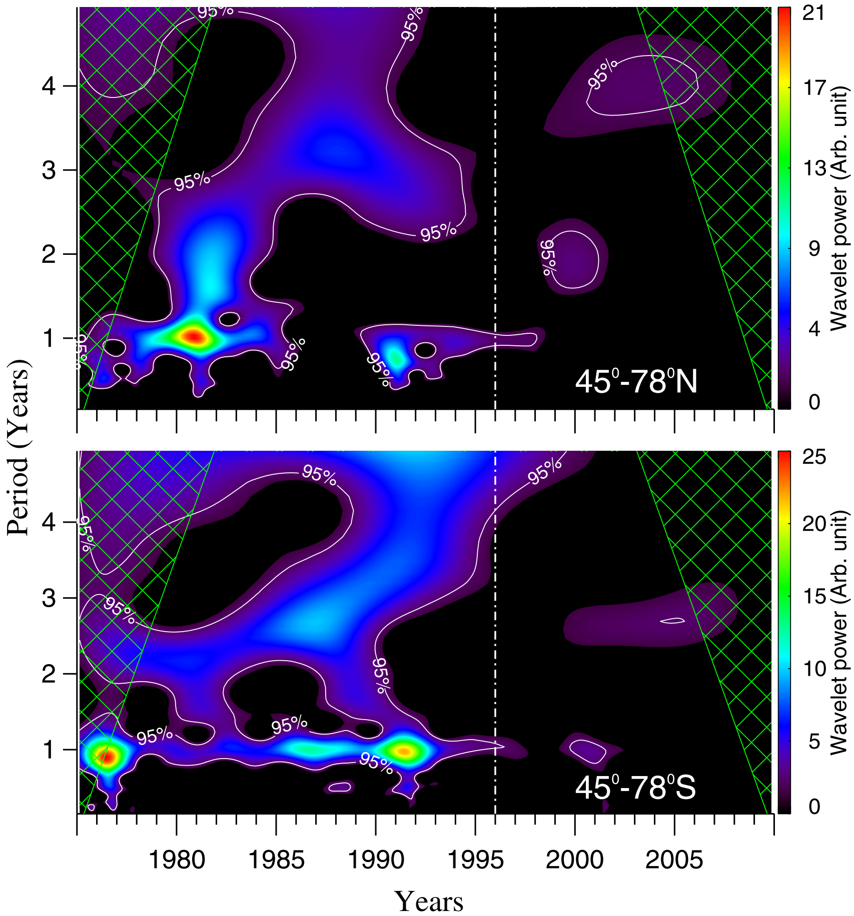

Figure 2 The wavelet-power distribution of the solar periodicity over years for high-latitude fields for the northern (upper panel) and southern hemisphere (lower panel) in the latitude range of 45° to 78°. The green cross-hatched regions are the cone of influence (COI), the white contours indicate a significance level at 95 %. The dashed vertical lines are marked at 1996 when a clear transition has been observed in the wavelet power of the periodicities for the North and South high-latitude fields.

Figure 2 shows the wavelet spectrum for the high-latitude fields in the northern (upper panel) and southern hemisphere (lower panel), while Figure 3 shows the wavelet spectrum for the low-latitude fields in the northern (upper panel) and southern hemispheres (lower panel). For the high-latitude fields (Figure 2) in the North and South, significant wavelet power is only seen at lower periods ($\approx$ one to three years) prior to 1985, while significant wavelet power is seen at lower and higher periods ($\approx$ three to five years) for the interval between 1985 and 1996. For the low-latitude fields (Figure 3), we see no significant changes in the power levels between 1975 and 1996.

It is important to note here that there is a clear transition in periodicities and power levels in the two hemispheres around 1996 for high- and low-latitude fields. We stress here that we carefully checked that selecting different colors or changes in the color intensity in the wavelet plots does not change the transition noticed in the wavelet-power spectra. Although the decline in the fields has started in the early- to mid-1990, as seen from Figure 1, the wavelet spectra show that there is an unambiguous transition in the quasi-periodic variations of fields in the two hemispheres at $\approx$ 1996. We therefore divided in the remaining analysis the residuals into two sets based on this transition in the wavelet spectra around 1996 to

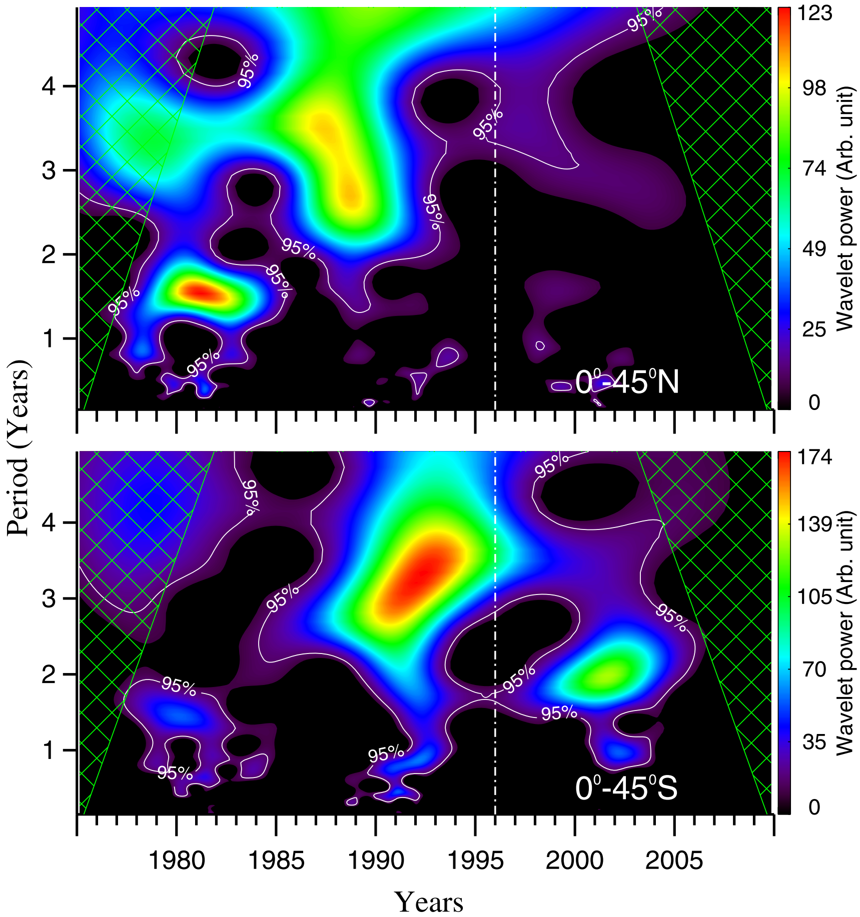

Figure 3 The wavelet-power distribution of the solar periodicity over years for low-latitude fields for the northern (upper panel) and southern hemisphere (lower panel) in the latitude range of 0° to 45°. The green cross-hatched regions are the cone of influence (COI), the white contours indicate a significance level at 95 %. The dashed vertical line demarcates the period of transition in wavelet power of the periodicities for the two hemispheres around 1996.

study the changes, if any, in the periodicities before and after this transition. A Fourier time-series analysis was then carried out separately on the residuals used in the wavelet analysis for the period prior to 1996 and the period after 1996 for the high- and low-latitude fields.

It is important to bear in mind here that the transition in the wavelet spectra around 1995 – 1996 corresponds to the time when the solar high-latitude fields above ±45° and solar wind turbulence levels in the entire inner heliosphere began to decline (Janardhan, Bisoi, and Gosain, 2010; Janardhan *et al.*, 2011).

3. Fourier Periodicities – Asymmetries and Symmetries

Based on the transition seen in the wavelet spectra at ≈ 1996, we subjected the residuals obtained from the SG fits to a Fourier analysis after dividing the time series of the residuals, spanning years 1975.14 to 2009.86, into two parts, one prior to 1996 and the other after 1996. Since the time series of the residual field has some data gaps amounting to ≈ 2.5 % of the data, the algorithm used for this purpose was based on the Lomb–Scargle Fourier transform for unevenly spaced data (Lomb, 1976; Scargle, 1982, 1989; Schultz and Stattegger, 1997) in

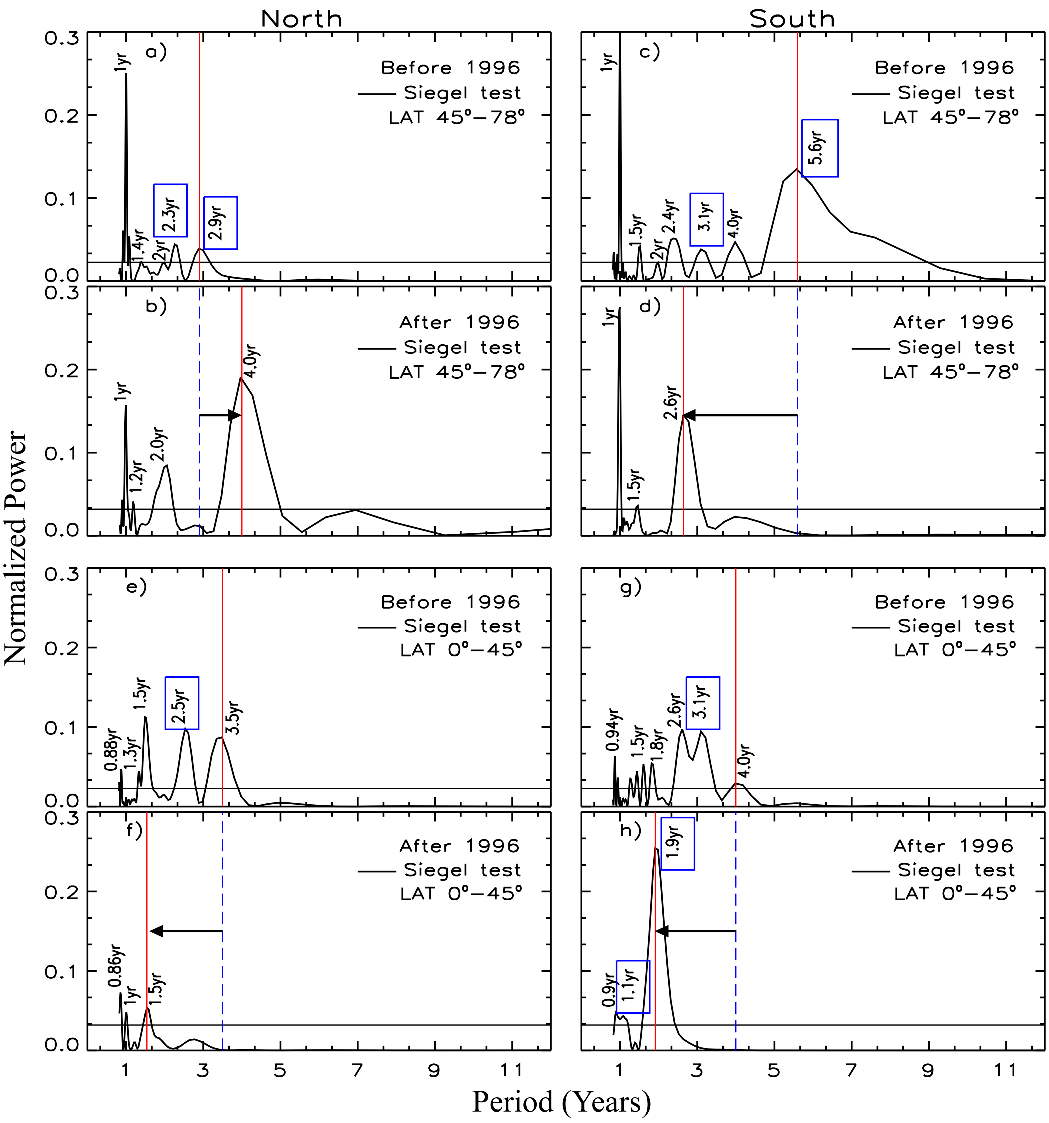

Figure 4 Normalized Fourier power distribution with the periodicity for photospheric fields in the North (left column) and South (right column) before [(a), (c), (e), (g)] and after [(b), (d), (f), (h)] 1996. The solid-red vertical lines demarcate the highest period in each of the four panels, the dotted-blue vertical line and direction of the black arrow in each panel are used to show the shift in the periodicity of the longest periods. The solid-horizontal lines depict significance levels as determined by the Siegel test. The new periodicities from our analysis are boxed in blue.

combination with the Welch-Overlapped-Segment-Averaging (WOSA) procedure (Welch, 1967). The spectral power derived from this analysis is generally normalized with respect to the total power contained in all the Fourier components taken together. This procedure makes the relative distribution of the spectral power independent of the spectral windowing used in the algorithm. Such normalized power spectra are referred to as normalized Fourier periodograms, or simply normalized periodograms.

3.1. High-Latitude Fields

Normalized periodograms obtained from the Fourier analysis are shown in Figure 4. Figures 4(a) – (d) represent the high-latitude fields, Figures 4(e) – (h) represent the low-latitude fields. The upper four panels (high-latitude fields) show the normalized periodograms before and after 1996 in the North (panels (a) and (b)), and before and after 1996 in the South (panels (c) and (d)). In a similar fashion, the lower four panels (low-latitude fields) show the normalized periodograms in the North before and after 1996 (panels (e) and (f)) and in the South before and after 1996 (panels (g) and (h)). The significant periodic components were determined using the Siegel test statistics (Siegel, 1980); these are the components with power levels above the black horizontal line drawn in each panel of Figure 4. The Siegel test is an extension of the Fisher test (Fisher, 1929). While the Fisher test attempts to spot the single dominant periodicity in a time series that has maximum power in the periodogram and is above the critical level defined by the Fisher-test statistics, the Siegel test relaxes this stringent condition a little and considers two to three dominant periodic components above the critical level. These test statistics and the process of determining the confidence/significance level are discussed by Percival and Walden (1993) and also briefly by Schultz and Stattegger (1997). We chose a 95 % confidence level (or 5 % significance level). This is equivalent to the $\pm 2\sigma$ level in the FFT method. The choice of this confidence level decides the critical level of the Siegel-test statistics (Schultz and Stattegger, 1997).

Although the Fourier components obtained from the analysis range in periods from 54 days to 12 years corresponding to 214 nHz to 2.6 nHz in frequency, Figure 4 only shows the components with periods in the range 300 days to 12 years, *i.e.* the low-frequency range. Normalized periodograms containing Fourier components with periods shorter than 300 days are discussed later.

The red vertical lines in each panel of Figure 4 are drawn through the peak of the component with the longest period. A shift in the periodicities can be seen after 1996 when compared to those before 1996. It must be emphasized that we are not interested in the actual periodicities themselves, but rather in the manner in which the longest periodicities shift between the time interval prior to and after 1996. It can be seen from Figure 4 that, in addition to the shift in periodicity of the high-latitude fields in the two hemispheres before and after 1996, the spectral power also differs significantly before and after 1996. The longer periods after 1996 have more spectral power than the longer periods prior to 1996. If we denote the longest periods for the high-latitude fields in the North before 1996 as T_1 and that after 1996 as T_2, we find that $T_2 > T_1$ for high-latitude fields in the North.

For the southern hemisphere, the shift in periodicities, as indicated by the direction of the black arrow in Figure 4, is in the opposite direction from the northern hemisphere. If we denote the longest periods for the high-latitude fields in the South before 1996 and after 1996 as T_3 and T_4 respectively, we find that $T_4 < T_3$ for the high-latitude fields in the South. As for the northern hemisphere, the distribution of spectral power in various periodicities is also significantly different in the periods before and after 1996.

Thus, a North–South asymmetry is seen in the distribution of periodicities for the high-latitude fields along with significant changes in the power of various periodic components. Since the normalized periodograms are generated from measurements of magnetic fields, it is a proxy for the behavior of the photospheric magnetic fields and a North–South asymmetry would imply a similar asymmetry in photospheric magnetic fields toward higher solar latitudes before and after 1996.

3.2. Low-Latitude Fields

In contrast to the behavior of the high-latitude fields, the low-latitude fields shown in Figure 4(e) – (h) show no asymmetry in the manner in which the longest periods shift in the periodograms prior to and after 1996. The shift in the longest periods in the North and South low-latitude fields before and after 1996 is depicted in the lower four panels of Figure 4 in a similar fashion to that of the upper four panels. The vertical solid-red line is drawn through the peak of the component with the longest period, and the dotted-blue line and a black arrow in each panel indicate the direction of the shift.

Denoting the longest period for the low-latitude fields in the North before and after 1996 as T_5 and T_6, respectively, we find that $T_5 > T_6$. In the southern hemisphere, denoting the longest period for the low-latitude fields prior to 1996 and after 1996 as T_7 and T_8, respectively, it is clear that $T_7 > T_8$. Hence, the longest periods show a shift in the same direction, indicating that there is no asymmetry in the distribution of the low-latitude fields before and after 1996.

4. Latitudinal Profile for the Fourier Power Spectrum

To examine how the Fourier spectrum for the high-latitude fields varies as a function of latitude, the residuals for the high-latitude fields were subdivided into 15°-wide latitude bins and a Fourier analysis was carried out for the data in each latitude bin. This was done to examine the changes, if any, in the spectral distribution with latitude and because the strength and distribution of photospheric magnetic fields changes with solar latitudes. It would therefore be interesting to see if the North–South asymmetry in the high-latitude fields persists across all latitude bins. Figure 5 shows normalized periodograms in the latitude range 30° to 75° in latitude steps of 15°. Figure 5(a) – (d), (e) – (h), and (i) – (k) represent normalized periodograms showing the distribution of Fourier periodicities in latitude ranges of 30° – 45°, 45° – 60°, and 60° – 75°. The latitude ranges are indicated at the top right-hand corner of each panel. Starting from the top, each of the left-column panels of Figure 5 represents the power spectra for the northern hemisphere in each latitude bin in pairs before and after 1996. Similarly, the right-column panels of Figure 5 represent power spectra obtained for each latitude bin in the southern hemisphere in pairs before and after 1996. It can be seen from Figure 5 that the North–South asymmetry is present only in the 45° – 60° bin. Although this is not shown in Figure 5, we verified that the asymmetry is also absent from the latitude bins of 0° to 15° and 15° to 30°.

In the 60° – 75° bin (bottom four panels of the Figure 5), the shift of the longest periods before and after 1996 shows no North–South asymmetry. However, the spectral powers in the longest periods are significantly different before and after 1996. The spectral power in the longest-period component increases significantly after 1996 for the northern hemisphere, but decreases for the southern hemisphere.

It is important to note here that the latitude band 45° – 60° in both hemispheres is dominated by surges or tongues of magnetic flux that is carried poleward by the meridional flow. These surges are a direct surface manifestation of the meridional flow, which is in turn governed by an internal solar dynamo. Beyond 60° in latitude, the high-latitude flux in both hemispheres saturates and can be best seen along with the magnetic surges in the 45° – 60° latitude band in a magnetic butterfly-diagram, which is described in the following section.

4.1. The Magnetic Butterfly-Diagram and Polar Surges

It is generally believed that the emergence and evolution of a magnetic field in the solar photosphere is tied to a solar dynamo in the solar interior. In particular, the toroidal field manifests itself as solar-surface bipolar active regions with sunspots migrating toward the

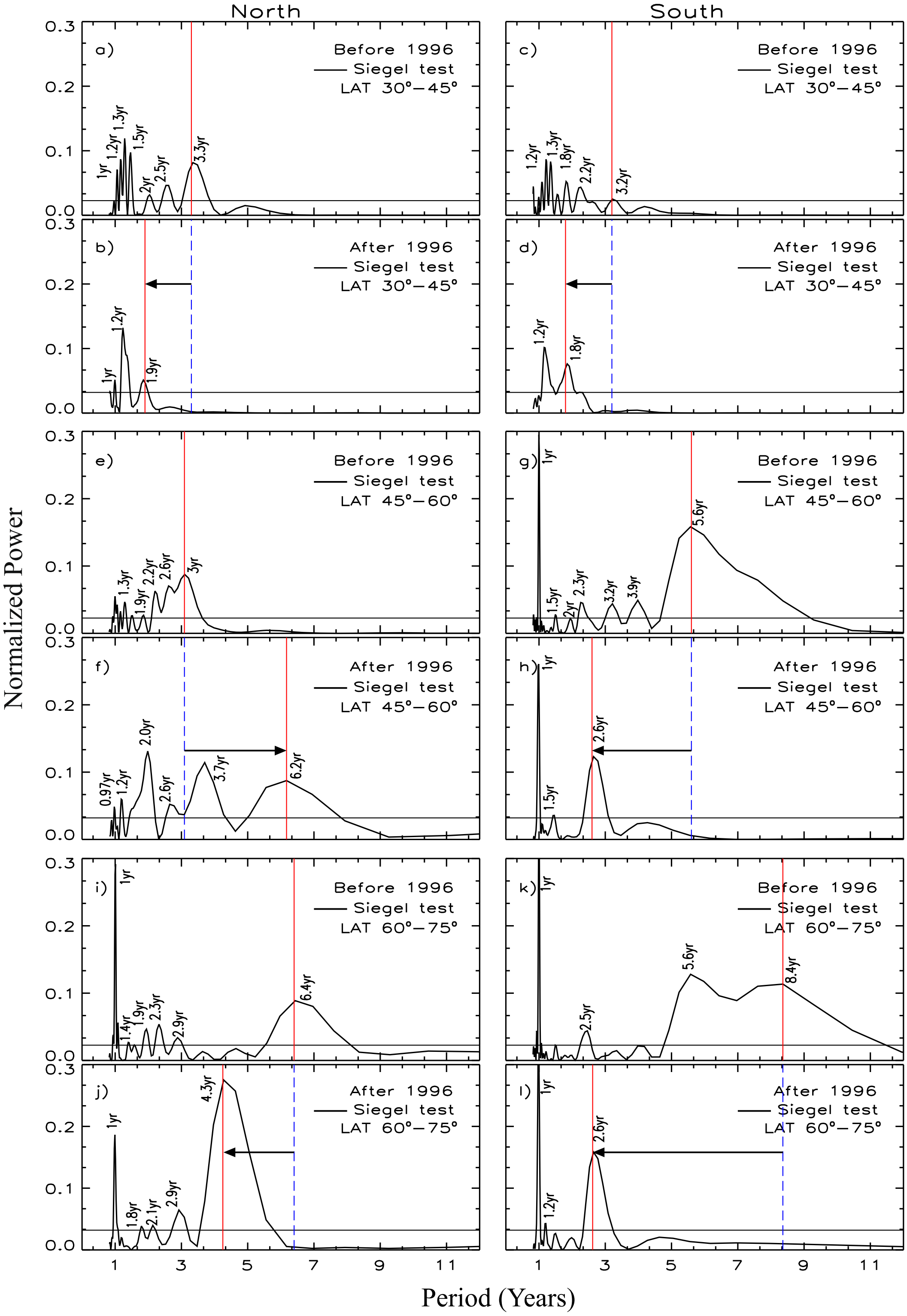

Figure 5 Normalized Fourier periodograms in the North (left column) and South (right column) before [(a), (c), (e), (g), (i), (k)] and after [(b), (d), (f), (h), (j), (l)] 1996 for the photospheric fields in latitude ranges of $30° - 45°$, $45° - 60°$, and $60° - 75°$. The solid-red vertical line, the dotted-blue vertical line, and the black arrow in each panel are used to show the shift in periodicity and the spectral power of the fields before and after 1996 in the northern and southern hemisphere. The solid horizontal lines depict significance levels as determined by the Siegel test.

Equator as the solar cycle progresses. This migration gives rise to the well-known butterfly diagram, which is basically a map of longitudinally averaged magnetic fields in time. Solar-dynamo models that explain the main features of solar magnetic activity consider the strong toroidal field as being generated by the shearing of a pre-existing weak poloidal field by solar differential rotation (ω-effect). Subsequently, the regeneration and inversion of polar fields, at the maximum of each solar cycle, is caused by the cancellation of sunspot fields at the Equator along with a net poleward surface flux that is transported via meridional circulation to reach the poles and reverse the pre-existing polar fields (Babcock–Leighton type-α effect).

We generated a butterfly diagram from the NSO/Kitt Peak synoptic maps by using longitudinally averaged photospheric fields derived from the synoptic maps described in Section 2. Figure 6(a) shows a butterfly diagram for Solar Cycles 21, 22, and 23 covering the period from 19 February 1975 to 09 November 2009 (1975.14 – 2009.86). The leading and following polarity fluxes in Figure 6(a) are shown in red and green for the northern hemisphere in Cycle 21, with the derived flux values indicated in a color-coded bar at the top of the figure. Leading and following polarity fluxes will be reversed in the southern hemisphere and will again flip from cycle to cycle and hemisphere to hemisphere.

To obtain better contrast, the fluxes in Figure 6(a) were limited to the range ± 30 G. The poleward motion of the trailing polarity fluxes above the latitudes $\pm 45°$, known as polar surges, are episodic in nature (Wang, Nash, and Sheeley, 1989) and can be clearly seen as tongues of red and green bands in Figure 6(a). For a better view of the polar surges, the middle and lower panels of Figure 6 show variations of intensity as a function of time in each 1° strip of latitude in the latitude range 45° – 60° for the northern (Figure 6(b)) and southern hemisphere (Figure 6(c)). The solar field for each degree of latitude is shown after smoothing over three Carrington rotations. An example of a surge in the North and South is highlighted in red.

Knaack, Stenflo, and Berdyugina, 2005 reported a periodicity of 1.3 years in the photospheric fields that is correlated with these polar surge motions. We see an approximate periodicity of one year in the polar surge flows in the lower two panels of Figure 6. This agrees with the strong one-year periodicity seen in Figure 4 and 5. Furthermore, a variation in the strength and occurrence rate of surges prior to and after 1996 can be seen from a careful inspection of Figure 6. In the latitude bin $\pm 45° – \pm 60°$, we find that the frequency of these surges is greater during the years 1996 – 2009, while the surges are less frequent during the years 1986 – 1995.

5. Fourier Periodicity – Low- and High-Frequency Periods

The harmonic analysis yielded Fourier components with periods ranging from 54 days to 12 years, corresponding to a frequency range of 2.6 nHz to 214 nHz. The significant periodic components, as determined by the Siegel test, were grouped into low-frequency periods in the frequency range 38.5 nHz (300 days) to 2.6 nHz (12 years) and high-frequency periods in the frequency range 214 nHz (54 days) to 38.5 nHz (300 days). These periods are listed in Table 1 (long periods) and Table 2 (short periods). Many of these periodicities have previously been reported, but we discovered a few new periodicities in our analysis. These are listed in boldface in Tables 1 and 2 and are boxed in blue in Figures 4 and 7.

5.1. The Low-Frequency Periods

In the low-frequency range, 38.5 nHz (300 days) to 2.6 nHz (12 years), we restricted our analysis to periodicities in the range of 305 days to 5.6 years. Periods longer than 5.6 years

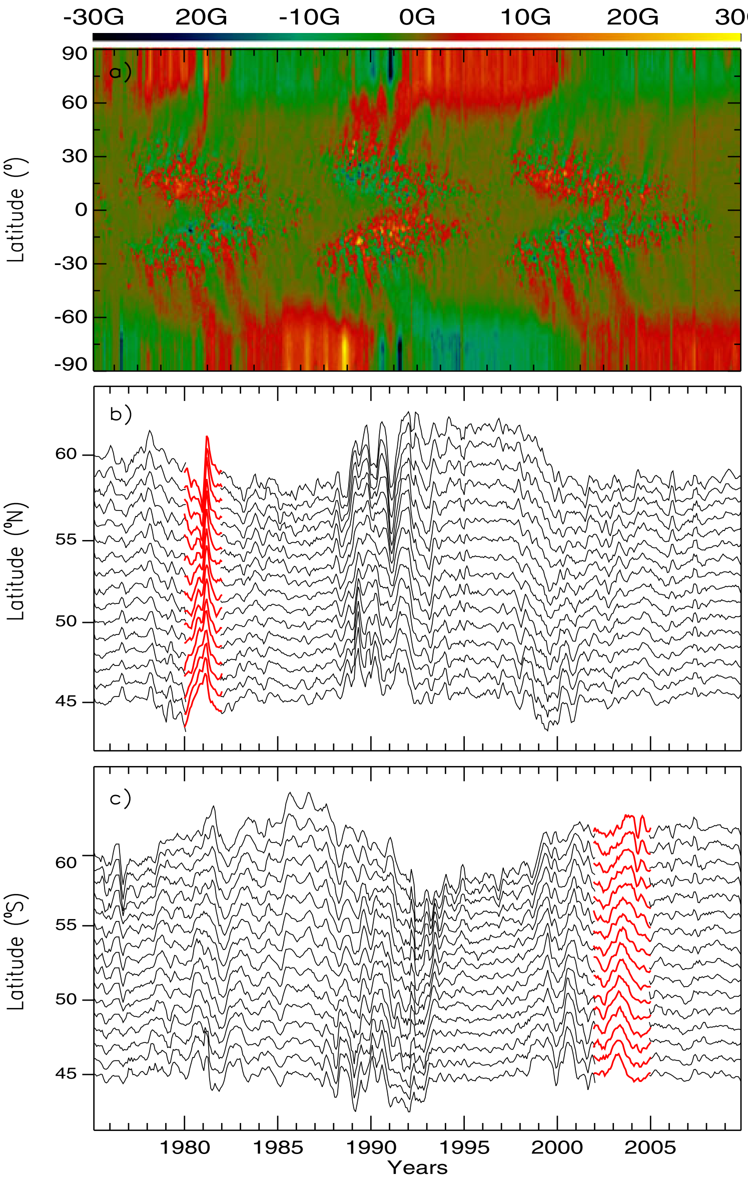

Figure 6 The top panel labeled (a) shows a magnetic butterfly-diagram generated using NSO/Kitt Peak magnetograms and depicts the net photospheric magnetic-flux distribution on the Sun for Solar Cycles 21, 22, and 23. For better contrast, the magnetic flux has been limited to ± 30 Gauss. The positive and negative polarities are shown in red and green. Polar surges or lateral motions of magnetic flux moving poleward above latitudes of $\pm 45°$ are seen as tongues of red and green bands. The lower two panels labeled (b) and (c) show the variation of the magnetic field after smoothing over three Carrington rotations for each degree of latitude in the range of 45° to 60°. An example of a surge is highlighted in red in the bottom two panels, representing the northern and southern hemisphere, respectively.

were excluded; they are inaccurately determined because we had to divide the time series. The periodicities are listed in Table 1, where the upper half lists periodicities for high-latitude fields in the North and South grouped before and after 1996, while the lower half lists periodicities for low-latitude fields in a similar fashion.

For photospheric fields in the high-latitude range we found periodicities of 305 days (0.84 years), 325 days (0.89 years), 339 days (0.92years), 341 days (0.93 years), 1 year,

Table 1 The Fourier periods in the frequency range 38.5 nHz to 2.6 nHz (low-frequency zone), are listed with their Fourier power in the upper and lower half of the table for high- and low-latitude fields in the North and South before and after 1996.

North high-latitude field				South high-latitude field			
Before 1996		After 1996		Before 1996		After 1996	
Period [yr]	Power	Period [yr]	Power	Period [yr]	Power	Period [yr]	Power
2.9	**0.04**	4.0	0.19	**5.6**	**0.13**	2.6	0.15
2.3	**0.04**	2.0	0.08	4.0	0.05	1.5	0.04
2.0	0.02	1.2	0.04	**3.1**	**0.04**	1.0	0.28
1.4	0.02	1.0	0.16	2.4	0.05	–	–
1.0	0.25	0.89	0.04	2.0	0.02	–	–
0.93	0.06	–	–	1.5	0.04	–	–
–	–	–	–	1.0	0.02	–	–
–	–	–	–	0.92	0.03	–	–
–	–	–	–	0.89	0.02	–	–
–	–	–	–	0.84	0.04	–	–
–	–	–	–	–	–	–	–

North low-latitude field				South low-latitude field			
Before 1996		After 1996		Before 1996		After 1996	
Period [yr]	Power	Period [yr]	Power	Period [yr]	Power	Period [yr]	Power
3.5	0.09	1.5	0.05	4.0	0.03	**1.9**	**0.25**
2.5	**0.10**	1.0	0.04	**3.1**	**0.09**	**1.1**	**0.04**
1.5	0.11	0.86	0.07	2.6	0.1	0.90	0.05
1.3	0.04	–	–	1.8	0.05	–	–
0.88	0.04	–	–	1.5	0.05	–	–
–	–	–	–	1.44	0.04	–	–
–	–	–	–	1.27	0.04	–	–
–	–	–	–	0.94	0.04	–	–
–	–	–	–	0.87	0.06	–	–

1.2 years, 1.4 years, 1.5 years, 2 years, 2.4 years, 2.6 years, and 4 years, while for photospheric fields in the low-latitude range we found periods of 312 days (0.86 years), 318 days (0.87 years), 321 days (0.88 years), 327 days (0.9 years), and 343 days (0.94 years), 1 year, 1.27 years, 1.3 years, 1.44 years, 1.5 years, 1.8 years, 2.6 years, 3.5 years, and 4 years. All of these quasi-periodicities in various types of solar activity have been reported previously (Howe *et al.*, 2000; Krivova and Solanki, 2002; Knaack, Stenflo, and Berdyugina, 2005; Mendoza, Velasco, and Valdés-Galicia, 2006; Chowdhury, Khan, and Ray, 2009). Knaack, Stenflo, and Berdyugina, 2005) had discussed a North–South asymmetry in quasi-periodic variations in unsigned photospheric flux with periods of 1.3 years, 1.5 years, and 2.6 years.

In addition to these known periodicities, we found some new periodicities in the high-latitude fields with periods of 2.3 years, 2.9 years, 3.1 years, and 5.6 years, and in the low-latitude fields with periods 1.1 years, 1.9 years, 2.5 years, and 3.1 years. These new periodicities are shown in boldface in Tables 1 and 2. Although the periodicity of one year has been reported previously, we found this periodicity to be the prominent periodicity observed in both the North and South high-latitude fields before and after 1996. The Fourier power in the

Table 2 The Fourier periods with their Fourier spectral power in the frequency range 214 nHz to 38.5 nHz (high-frequency zone) are listed in the upper and lower half of the table for high- and low-latitude fields in the North and South before and after 1996.

North high-latitude field				South high-latitude field			
Before 1996		After 1996		Before 1996		After 1996	
Period [day]	Power	Period [day]	Power	Period [day]	Power	Period [day]	Power
294	**0.02**	**253**	**0.04**	288	0.037	184	0.07
278	0.06	183	0.061	184	0.06	–	–
263	0.04	–	–	–	–	–	–
240	0.02	–	–	–	–	–	–
183	0.04	–	–	–	–	–	–
157	0.04	–	–	–	–	–	–

North low-latitude field				South low-latitude field			
Before 1996		After 1996		Before 1996		After 1996	
Period [day]	Power	Period [day]	Power	Period [day]	Power	Period [day]	Power
288	0.02	**257**	**0.04**	283	0.04	–	–
278	0.03	181	0.08	248	0.02	–	–
261	0.03	172	0.11	228	0.03	–	–
–	–	147	0.04	157	0.03	–	–
–	–	–	–	151	0.03	–	–
–	–	–	–	145	0.03	–	–
–	–	–	–	–	–	–	–
–	–	–	–	–	–	–	–

one-year period is comparatively higher in the North and South before 1996 than after 1996. On the other hand, although the one-year period is present in the low-latitude fields both in the North and South, it is only present after 1996. Additionally, periods of 1.2 – 1.6 years are common to both the North and South low-latitude fields and have significant power.

The periodicity most often discussed and reported is the 1.3-year periodicity (Krivova and Solanki, 2002; Knaack, Stenflo, and Berdyugina, 2004; Knaack, Stenflo, and Berdyugina, 2005). It has been linked to polar surges that can be seen most clearly in the latitude band of 45° to 60° (Wang, Nash, and Sheeley, 1989; Knaack, Stenflo, and Berdyugina, 2005) in the magnetic butterfly-diagrams, as depicted in Figure 6. The 1.3-year periodicity has also been linked to the variation of the rotation rate near the base of the convection zone (Howe *et al.*, 2000).

5.2. The High-Frequency Periods

In the high-frequency range we have frequencies ranging from 214 nHz (54 days) to 38.5 nHz (300 days). These periodicities are listed in Table 2 for the high- and low-latitude fields. The upper half of Table 2 lists periodicities for the high-latitude fields with periods ranging between 157 days to 294 days. Some of these periodicities with their Fourier spectral power are shown in the top four panels (a), (b), (c), and (d) in Figure 7. Similarly, the lower half of Table 2 lists significant periodicities for the low-latitude fields with periods ranging between 134 days to 288 days. The bottom four panels (e), (f), (g), and (h) in

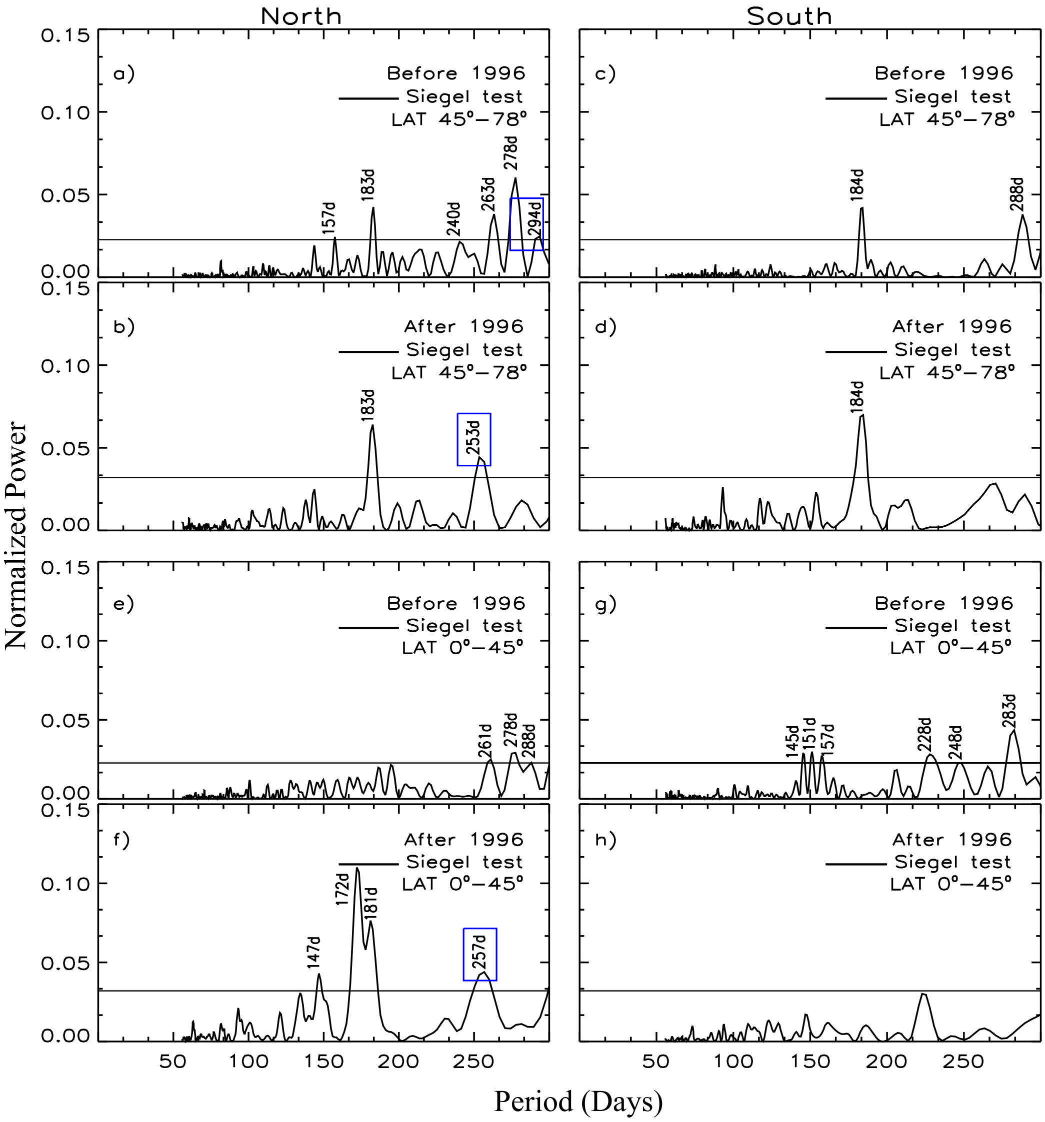

Figure 7 Normalized Fourier periodograms in the North (left column) and South (right column) before [(a), (c), (e), (g)] and after [(b), (d), (f), (h)] 1996 for high- (top panel) and low-latitude fields (bottom panel) for the high-frequency periods in the frequency range 214 nHz to 38.5 nHz. The new periodicities from our analysis are boxed in blue.

Figure 7 show a few of these periodicities with their spectral power. As stated earlier, the significant periodic components were determined using the Siegel-test statistics; they are the periodic components with power levels above the black horizontal line drawn in each panel of Figure 7.

The known periodicities in the high-latitude zone include those with periods of 157 days, 183 days, 184 days, 240 days, 263 days, 278 days, and 288 days, and the new periodicities, *viz.* with periods of 253 days and 294 days not previously reported in the literature, are shown in boldface in the upper part of Table 2.

The Rieger periodicity of 157 days is a well-known fundamental periodicity that we found only in the high-latitude fields in the northern hemisphere prior to 1996. In addition, the periodicity of 182 – 184 days is seen to be always present, and the Fourier power corresponding to this periodicity does not vary much in the North and South fields at high latitudes both before and after 1996. These high-frequency periods in the high-latitude fields do not show much variation in their normalized Fourier power, and we see no North–South asymmetry in these high-latitude fields.

On the other hand, in the low-latitude zone, shown in the lower part of Table 2, we report periodicities of 145 days, 147 days, 151 days, 157 days, 172 days, 228 days, 248 days, 261 days, 278 days, 283 days, and 288 days that have previously been reported (Oliver, Ballester, and Baudin, 1998; Krivova and Solanki, 2002; Knaack, Stenflo, and Berdyugina, 2005; Chowdhury, Khan, and Ray, 2009). The new periodicity from our analysis was 257 days and is shown in boldface in the lower half of Table 2. The Rieger periodicity of 157 days is only seen in the South low-latitude field before 1996. Likewise, the semi-annual period variation of 181 days is observed only in North low-latitude fields.

6. Discussion and Conclusion

Our wavelet analysis shows a transition occurring around 1996 in the distribution of power and periodicities of photospheric fields. When the data were divided into intervals prior to and after 1996, a hemispheric asymmetry became clear in the derived Fourier periodicities of the solar magnetic activity above latitudes of $\pm 45°$. A more detailed analysis showed that this asymmetry is confined to the latitude band $45° - 60°$ in both hemispheres. This latitude band is primarily dominated by strong, episodic poleward surges or tongues of magnetic flux in the two hemispheres, which, as stated earlier, are a direct surface manifestation of the meridional flow and the internal solar dynamo. In the $60° - 75°$ latitude band we found an asymmetry in the distribution of spectral power in the longer periods because the photospheric surface fields have saturated in this band. The observed and localized asymmetry, which is confined to the $45° - 60°$ latitude zone in the hemispheres, together with the fact that the solar fields and the micro-turbulence levels in the inner heliosphere have been decreasing since the early to mid-1990s suggests that active changes occurred around this time in the solar dynamo that governs the underlying basic processes in the Sun. These changes in turn probably initiated the build-up to one of the deepest solar minima, at the end of Cycle 23, experienced in the past 100 years.

The magnetic time-series in the two solar hemispheres exhibit a multitude of periodicities with significant variation in the spectral power of midterm (one – two years) periodicities before and after 1996. These prominent periods in the lower solar latitudes, below $\pm 45°$, are thought to be generated by stochastic processes caused by the periodic emergence of surface magnetic flux (Wang and Sheeley, 2003) as the solar cycle progresses. As stated earlier, Howe *et al.* (2000) have reported a 1.3-year periodicity at the base of the solar convection zone, which has also been detected in sunspot areas and sunspot number time-series studied using wavelet transforms (Krivova and Solanki, 2002; Chowdhury and Dwivedi, 2011). These findings have led to the conclusion that the mid-term fluctuations in the solar fields are surface manifestations of changes in the magnetic fluxes generated deep inside the Sun.

Polar surges above latitudes $\pm 45°$ show significant variations in their occurrence rates and strength in each cycle and are therefore manifested as a variation in spectral power and periods. A comparison of polar surges in the last three Solar Cycles, *viz.* 21, 22, and 23, revealed that they are somewhat stronger after the solar maximum.

Although we have restricted our analysis to data from Cycles 21, 22, and 23 in the period from $\approx 1975 – 2010$, an examination of data more recent than 2010 shows an asymmetry in

Figure 8 The solar magnetic field in the northern (top) and southern (bottom) hemispheres in the latitude range of 45° to 78° for Solar Cycles 22 and 23. It is clear that the North solar field has reversed while the South solar field still has to do so. The reversal time of the North solar field is indicated by a small blue arrow.

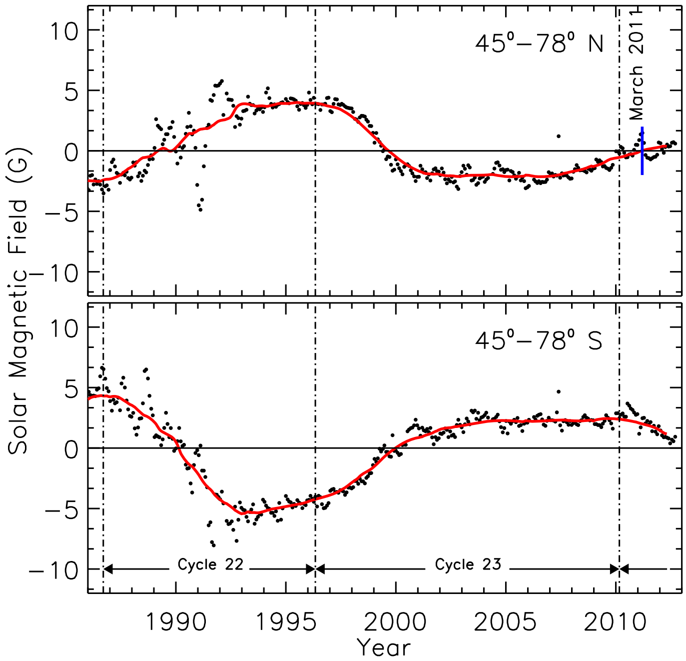

the solar field reversal at high latitudes. Figure 8 shows the reversal of the northern high-latitude field in Cycle 24 in March 2011. However, the southern hemisphere is yet to undergo a reversal. The filled black dots in Figure 8 are the actual measurements while the solid-red line is a smoothed curve. The reversal of the solar polar field occurs at times when the red curve passes through zero and is indicated for Cycle 24 by a thin blue line in the northern hemisphere. While it is known from earlier cycles that the two hemispheres do not reverse polarities at the same time, the time lag between the reversal of the northern and southern hemisphere has, to the best of our knowledge, never been as long.

In addition, Dikpati *et al.* (2010) and Dikpati (2011), using the theory of meridional circulation, have reported an asymmetry in the latitudinal extent of the Sun's meridional flow belt in Cycles 22 and 23, wherein surface meridional flows in Cycle 22 extend to latitudes of $\pm 60°$, while in Cycle 23 they extended all the way to the Poles. Thus, the meridional flow in Cycle 23 took a longer time, thereby causing a slower return flow, which in turn led to the extended solar minimum in Cycle 23. Recent work, using helioseismic data from the *Birmingham Solar Oscillation Network* (BiSON), an instrument that is very sensitive in probing the solar interior close to the solar surface, has shown that the behavior of solar oscillation frequencies in the sub-surface magnetic layers during the descending phase of Cycle 23 was significantly different from that during Cycle 22 (Basu *et al.*, 2012). Basu and co-authors went on to state that the peculiar solar minimum at the end of Cycle 23 could have been predicted long before it happened. The present work, showing a North–South asymmetry around the mid-1990s in the quasi-periodic variations of photospheric fields at high-latitudes, shows that changes were initiated at this time in the basic underlying solar dynamo processes such as the meridional flow rates and the magnetic-flux emergence that eventually led to the prolonged and deep minimum that we have just witnessed.

The current understanding of the solar dynamo is that it operates through the Babcock–Leighton mechanism to produce poloidal fields through the decay of tilted bipolar sunspots (Choudhuri, Chatterjee, and Jiang, 2007; Jiang, Chatterjee, and Choudhuri, 2007). The strength of the polar field at each solar maximum then depends upon the tilt angle in bipolar sunspots which, in turn, is determined by the Coriolis force acting on magnetic-flux tubes that reach the surface by rising through the turbulent convection zone (D'Silva and Choudhuri, 1993). This process generates a large scatter in the average tilt-angle, causing the polar field to be randomly weaker or stronger than in the previous cycle (Longcope and Choudhuri, 2002). We have observed a decline in fields above 45° for the past ≈ 15 years, which implies that weak polar fields are generated in two successive solar cycles, *viz.* Cycles 22 and 23. A continuation of this declining trend beyond 22 years would imply a third successive weak polar field produced by the Babcock–Leighton mechanism. This is unlikely because the polar field is generated by a random process, and if this does happen, it would have serious implications for our current understanding of the solar dynamo. Moreover, two of the eight strongest geomagnetic storms in the last 150 years have occurred during Solar Cycles 13 and 14, which were both relatively weak cycles. Therefore, continued observations and measurements of solar magnetic fields are extremely important.

Acknowledgements NSO/Kitt Peak data used here produced cooperatively by NSF/NSO, NASA/GSFC, and NOAA/SEL. This work uses SOLIS data obtained by the NSO Integrated Synoptic Program (NISP), managed by the National Solar Observatory, which is operated by the Association of Universities for Research in Astronomy (AURA), Inc. under a cooperative agreement with the National Science Foundation. The wavelet software was provided by C. Torrence and G. Compo and is available at URL: atoc.colorado.edu/research/wavelets/

References

Ananthakrishnan, S., Balasubramanian, V., Janardhan, P.: 1995, Latitudinal variation of solar wind velocity. *Space Sci. Rev.* **72**, 229 – 232. doi:10.1007/BF00768784.

Ananthakrishnan, S., Coles, W.A., Kaufman, J.J.: 1980, Microturbulence in solar wind streams. *J. Geophys. Res.* **85**, 6025 – 6030. doi:10.1029/JA085iA11p06025.

Bai, T.: 1987, Periodicities of the flare occurrence rate in solar cycle 19. *Astrophys. J. Lett.* **318**, L85 – L91. doi:10.1086/184943.

Bai, T.: 2003, Periodicities in solar flare occurrence: analysis of cycles 19 – 23. *Astrophys. J.* **591**, 406 – 415. doi:10.1086/375295.

Basu, S., Broomhall, A.-M., Chaplin, W.J., Elsworth, Y.: 2012, Thinning of the Sun's magnetic layer: the peculiar solar minimum could have been predicted. *Astrophys. J.* **758**, 43. doi:10.1088/0004-637X/758/1/43.

Choudhuri, A.R., Chatterjee, P., Jiang, J.: 2007, Predicting solar cycle 24 with a solar dynamo model. *Phys. Rev. Lett.* **98**(13), 131103. doi:10.1103/PhysRevLett.98.131103.

Chowdhury, P., Dwivedi, B.N.: 2011, Periodicities of sunspot number and coronal index time series during solar cycle 23. *Solar Phys.* **270**, 365 – 383. doi:10.1007/s11207-011-9738-1.

Chowdhury, P., Khan, M., Ray, P.C.: 2009, Intermediate-term periodicities in sunspot areas during solar cycles 22 and 23. *Mon. Not. Roy. Astron. Soc.* **392**, 1159 – 1180. doi:10.1111/j.1365-2966.2008.14117.x.

Chowdhury, P., Khan, M., Ray, P.C.: 2010, Short-term periodicities in sunspot activities during the descending phase of solar cycle 23. *Solar Phys.* **261**, 173 – 191. doi:10.1007/s11207-009-9478-7.

Chowdhury, P., Ray, P.C.: 2006, Periodicities of solar electron flare occurrence: analysis of cycles 21 – 23. *Mon. Not. Roy. Astron. Soc.* **373**, 1577 – 1589. doi:10.1111/j.1365-2966.2006.11120.x.

Dikpati, M.: 2011, Comparison of the past two solar minima from the perspective of the interior dynamics and dynamo of the Sun. *Space Sci. Rev.* 143. doi:10.1007/s11214-011-9790-z.

Dikpati, M., Gilman, P.A., de Toma, G., Ulrich, R.K.: 2010, Impact of changes in the Sun's conveyor-belt on recent solar cycles. *Geophys. Res. Lett.* **37**, 14107. doi:10.1029/2010GL044143.

Droege, W., Gibbs, K., Grunsfeld, J.M., Meyer, P., Newport, B.J., Evenson, P., Moses, D.: 1990, A 153 day periodicity in the occurrence of solar flares producing energetic interplanetary electrons. *Astrophys. J. Suppl.* **73**, 279 – 283. doi:10.1086/191463.

D'Silva, S., Choudhuri, A.R.: 1993, A theoretical model for tilts of bipolar magnetic regions. *Astron. Astrophys.* **272**, 621.

Fisher, R.A.: 1929, Tests of significance in harmonic analysis. *Proc. Roy. Soc. London Ser. A, Math. Phys. Sci.* **125**, 54 – 59.

Forrest, D.J., Chupp, E.L., Ryan, J.M., Cherry, M.L., Gleske, I.U., Reppin, C., Pinkau, K., Rieger, E., Kanbach, G., Kinzer, R.L.: 1980, The gamma ray spectrometer for the Solar Maximum Mission. *Solar Phys.* **65**, 15 – 23. doi:10.1007/BF00151381.

Hathaway, D.H., Rightmire, L.: 2010, Variations in the Sun's meridional flow over a solar cycle. *Science* **327**, 1350. doi:10.1126/science.1181990.
Howard, R.: 1974, Studies of solar magnetic fields. II – The magnetic fluxes. *Solar Phys.* **38**, 59 – 67. doi:10.1007/BF00161823.
Howe, R., Christensen-Dalsgaard, J., Hill, F., Komm, R.W., Larsen, R.M., Schou, J., Thompson, M.J., Toomre, J.: 2000, Dynamic variations at the base of the solar convection zone. *Science* **287**, 2456 – 2460. doi:10.1126/science.287.5462.2456.
Janardhan, P., Bisoi, S.K., Gosain, S.: 2010, Solar polar fields during cycles 21 – 23: correlation with meridional flows. *Solar Phys.* **267**, 267 – 277. doi:10.1007/s11207-010-9653-x.
Janardhan, P., Bisoi, S.K., Ananthakrishnan, S., Tokumaru, M., Fujiki, K.: 2011, The prelude to the deep minimum between solar cycles 23 and 24: interplanetary scintillation signatures in the inner heliosphere. *Geophys. Res. Lett.* **382**, 20108. doi:10.1029/2011GL049227.
Jian, L.K., Russell, C.T., Luhmann, J.G.: 2011, Comparing solar minimum 23/24 with historical solar wind records at 1 AU. *Solar Phys.* 69. doi:10.1007/s11207-011-9737-2.
Jiang, J., Chatterjee, P., Choudhuri, A.R.: 2007, Solar activity forecast with a dynamo model. *Mon. Not. Roy. Astron. Soc.* **381**, 1527 – 1542. doi:10.1111/j.1365-2966.2007.12267.x.
Jiang, J., Cameron, R.H., Schmitt, D., Schussler, M.: 2011, Can surface flux transport account for the weak polar field in cycle 23? *Space Sci. Rev.* 136. doi:10.1007/s11214-011-9783-y.
Kile, J.N., Cliver, E.W.: 1991, A search for the 154 day periodicity in the occurrence rate of solar flares using Ottawa 2.8 GHz burst data, 1955 – 1990. *Astrophys. J.* **370**, 442 – 448. doi:10.1086/169831.
Kiliç, H.: 2008, Midrange periodicities in sunspot numbers and flare index during solar cycle 23. *Astron. Astrophys.* **481**, 235 – 238. doi:10.1051/0004-6361:20078455.
Kirk, M.S., Pesnell, W.D., Young, C.A., Hess Webber, S.A.: 2009, Automated detection of EUV polar coronal holes during solar cycle 23. *Solar Phys.* **257**, 99 – 112. doi:10.1007/s11207-009-9369-y.
Knaack, R., Stenflo, J.O., Berdyugina, S.V.: 2004, Periodic oscillations in the North–South asymmetry of the solar magnetic field. *Astron. Astrophys.* **418**, L17 – L20. doi:10.1051/0004-6361:20040107.
Knaack, R., Stenflo, J.O., Berdyugina, S.V.: 2005, Evolution and rotation of large-scale photospheric magnetic fields of the Sun during cycles 21 – 23. periodicities, North–South asymmetries and r-mode signatures. *Astron. Astrophys.* **438**, 1067 – 1082. doi:10.1051/0004-6361:20042091.
Krivova, N.A., Solanki, S.K.: 2002, The 1.3-year and 156-day periodicities in sunspot data: wavelet analysis suggests a common origin. *Astron. Astrophys.* **394**, 701 – 706. doi:10.1051/0004-6361:20021063.
Lean, J.: 1990, Evolution of the 155 day periodicity in sunspot areas during solar cycles 12 to 21. *Astrophys. J.* **363**, 718 – 727. doi:10.1086/169378.
Livingston, W.: 2002, Sunspots observed to physically weaken in 2000 – 2001. *Solar Phys.* **207**, 41 – 45.
Lomb, N.R.: 1976, Least-squares frequency analysis of unequally spaced data. *Astrophys. Space Sci.* **39**, 447 – 462. doi:10.1007/BF00648343.
Longcope, D., Choudhuri, A.R.: 2002, The orientational relaxation of bipolar active regions. *Solar Phys.* **205**, 63 – 92. doi:10.1023/A:1013896013842.
McComas, D.J., Ebert, R.W., Elliott, H.A., Goldstein, B.E., Gosling, J.T., Schwadron, N.A., Skoug, R.M.: 2008, Weaker solar wind from the polar coronal holes and the whole Sun. *Geophys. Res. Lett.* **35**, L18103. doi:10.1029/2008GL034896.
Mendoza, B., Velasco, V.M., Valdés-Galicia, J.F.: 2006, Mid-term periodicities in the solar magnetic flux. *Solar Phys.* **233**, 319 – 330. doi:10.1007/s11207-006-4122-2.
Nandy, D., Muñoz-Jaramillo, A., Martens, P.C.H.: 2011, The unusual minimum of sunspot cycle 23 caused by meridional plasma flow variations. *Nature* **471**, 80 – 82. doi:10.1038/nature09786.
Oliver, R., Ballester, J.L.: 1994, The North–South asymmetry of sunspot areas during solar cycle 22. *Solar Phys.* **152**, 481 – 485. doi:10.1007/BF00680451.
Oliver, R., Ballester, J.L., Baudin, F.: 1998, Emergence of magnetic flux on the Sun as the cause of a 158-day periodicity in sunspot areas. *Nature* **394**, 552 – 553. doi:10.1038/29012.
Penn, M.J., Livingston, W.: 2006, Temporal changes in sunspot umbral magnetic fields and temperatures. *Astrophys. J. Lett.* **649**, L45 – L48. doi:10.1086/508345.
Percival, D.B., Walden, A.T.: 1993, *Spectral Analysis for Physical Applications*, Cambridge University Press, Cambridge.
Rieger, E., Kanbach, G., Reppin, C., Share, G.H., Forrest, D.J., Chupp, E.L.: 1984, A 154-day periodicity in the occurrence of hard solar flares? *Nature* **312**, 623 – 625. doi:10.1038/312623a0.
Savitzky, A., Golay, M.J.E.: 1964, Smoothing and differentiation of data by simplified least squares procedures. *Anal. Chem.* **36**, 1627 – 1639.
Scargle, J.D.: 1982, Studies in astronomical time series analysis. II – Statistical aspects of spectral analysis of unevenly spaced data. *Astrophys. J.* **263**, 835 – 853. doi:10.1086/160554.
Scargle, J.D.: 1989, Studies in astronomical time series analysis. III – Fourier transforms, autocorrelation functions, and cross-correlation functions of unevenly spaced data. *Astrophys. J.* **343**, 874 – 887. doi:10.1086/167757.

Schultz, M., Stattegger, K.: 1997, Spectrum: spectral analysis of unevenly spaced paleoclimatic time series. *Comp. Geosci.* **23**, 929 – 945.
Siegel, A.F.: 1980, Testing for periodicity in a time series. *J. Am. Stat. Assoc.* **75**, 345 – 348.
Torrence, C., Compo, G.P.: 1998, A practical guide to wavelet analysis. *Bull. Am. Meteorol. Soc.* **79**, 61 – 78.
Verma, V.K.: 1987, On the increase of solar activity in the Southern Hemisphere during solar cycle 21. *Solar Phys.* **114**, 185 – 188.
Verma, V.K., Joshi, G.C.: 1987, On the periodicities of sunspots and solar strong hard X-ray bursts. *Solar Phys.* **114**, 415 – 418. doi:10.1007/BF00167358.
Wang, Y.-M., Sheeley, N.R. Jr.: 2003, On the fluctuating component of the Sun's large-scale magnetic field. *Astrophys. J.* **590**, 1111 – 1120. doi:10.1086/375026.
Wang, Y.-M., Nash, A.G., Sheeley, N.R. Jr.: 1989, Evolution of the Sun's polar fields during sunspot cycle 21 – poleward surges and long-term behavior. *Astrophys. J.* **347**, 529 – 539. doi:10.1086/168143.
Wang, Y.-M., Robbrecht, E., Sheeley, N.R. Jr.: 2009, On the weakening of the polar magnetic fields during solar cycle 23. *Astrophys. J.* **707**, 1372 – 1386. doi:10.1088/0004-637X/707/2/1372.
Welch, P.D.: 1967, The use of fast Fourier transform for the estimation of power spectra: a method based on time averaging over short, modified periodograms. *IEEE Trans. Audio Electroacoust.* **15**, 70 – 73.

The prelude to the deep minimum between solar cycles 23 and 24: Interplanetary scintillation signatures in the inner heliosphere

P. Janardhan,[1] Susanta Kumar Bisoi,[1] S. Ananthakrishnan,[2] M. Tokumaru,[3] and K. Fujiki[3]

Received 10 August 2011; revised 28 September 2011; accepted 28 September 2011; published 29 October 2011.

[1] Extensive interplanetary scintillation (IPS) observations at 327 MHz obtained between 1983 and 2009 clearly show a steady and significant drop in the turbulence levels in the entire inner heliosphere starting from around ~1995. We believe that this large-scale IPS signature, in the inner heliosphere, coupled with the fact that solar polar fields have also been declining since ~1995, provide a consistent result showing that the buildup to the deepest minimum in 100 years actually began more than a decade earlier. **Citation:** Janardhan, P., S. K. Bisoi, S. Ananthakrishnan, M. Tokumaru, and K. Fujiki (2011), The prelude to the deep minimum between solar cycles 23 and 24: Interplanetary scintillation signatures in the inner heliosphere, *Geophys. Res. Lett.*, *38*, L20108, doi:10.1029/2011GL049227.

1. Introduction

[2] The sunspot minimum at the end of cycle 23, has been one of the deepest we have experienced in the past 100 years with the first spots of the new cycle 24 appearing only in March 2010 instead of December 2008 as was expected. Also, the number of spotless days experienced in 2008 and 2009 was over 70%. Apart from this, Cycle 23 has shown a slower than average field reversal, a slower rise to maximum than other odd numbered cycles, and a second maximum during the declining phase that is unusual for odd-numbered cycles. Though these deviations from "normal" behaviour could be significant in understanding the evolution of magnetic fields on the Sun, they do not yield any direct insights into the onset of the deep minimum experienced at the end of cycle 23. This is because predictions of the strength of solar cycles and the nature of their minima are strongly dictated by both the strength of the ongoing cycle [*Dikpati et al.*, 2006; *Choudhuri et al.*, 2007] and changes in the flow rates of the meridional circulation [*Nandy et al.*, 2011].

[3] Ulysses, the only spacecraft to have explored the mid- and high-latitude heliosphere, in its three solar orbits, provided the earliest indications of the global changes taking place in the solar wind. A significant result from the Ulysses mission came from observations of $|B_r|$, the radial component of the interplanetary magnetic field (IMF), as a function of the heliographic distance r which showed that the product $|B_r|r^2$ is independent of the heliographic latitude [*Smith et al.*, 2003; *Lockwood et al.*, 2009]. This result has far reaching consequences in that it essentially enables one to use *in situ*, single-point observations to quantify the open solar flux entering the heliosphere. The second Ulysses orbit, covering the rising to maximum phase of cycle 23, found the solar wind dynamic pressure (momentum flux) to be significantly lower in the post maximum phase of cycle 23 than during its earlier orbit, spanning the declining phase of cycle 22 [*Richardson et al.*, 2001; *McComas et al.*, 2003]. Finally, the third Ulysses orbit (2004–2008) found a global reduction of open magnetic flux and showed an ~20% reduction in both solar wind mass flux and dynamic pressure in cycle 23 as compared to the earlier two cycles [*McComas et al.*, 2008]. In addition, a study using solar wind measurements between 1995–2009 [*Jian et al.*, 2011] has shown that the solar minimum in 2008–2009 has experienced the slowest solar wind with the weakest solar wind dynamic pressure and magnetic field as compared to the earlier 3 cycles. Figure 1 shows the solar magnetic field in the latitude range 45°–78° computed from ground based magnetograms. The filled dots in Figure 1 represent the actual measurements and the open circles are the yearly means with 1σ error bars. The solid line is a smoothed curve. The vertically oriented dashed parallel lines demarcate cycles 22, and 23, respectively and the shaded gray area indicates the time between the expected minimum in cycle 23 and the time when the first spots in cycle 24 actually began to appear.

[4] The method adopted in computing solar magnetic fields shown in Figure 1 and details of the database used has been described by *Janardhan et al.* [2010]. It is clear from Figure 1 that there has been a continuous decline in the magnetic field starting from around 1995. Since the IMF is basically the result of photospheric magnetic fields being continuously swept out into the heliosphere one would expect to see this reflected in the solar wind and interplanetary medium. Due to the fact that the solar wind undergoes an enormous change in densities ranging from ~10^9 cm^{-3} at the base of the corona [*Mann et al.*, 2003] to ~10 cm^{-3} at 1 AU, different techniques are needed to study different regions of the solar wind. However, IPS is the only technique that can probe the entire inner-heliosphere using ground based radio telescopes operating at meter wavelengths.

2. The IPS Methodology

[5] IPS is a scattering phenomenon in which one observes distant extragalactic radio sources to detect random temporal variations of their signal intensity (scintillation) which are caused by the scattering suffered when plane electromagnetic radiation from the radio source passes through the turbulent and refracting solar wind [*Hewish et al.*, 1964; *Ananthakrishnan et al.*, 1980; *Asai et al.*, 1998; *Manoharan*, 2010a; *Tokumaru et al.*, 2010]. Though IPS measures only small-scale (~150 km sized) fluctuations in density and not

[1]Astronomy and Astrophysics Division, Physical Research Laboratory, Ahmedabad, India.
[2]Electronics Science Department, Pune University, Pune, India.
[3]Solar-Terrestrial Environment Laboratory, Nagoya University, Toyokawa, Japan.

0094-8276/11/2011GL049227

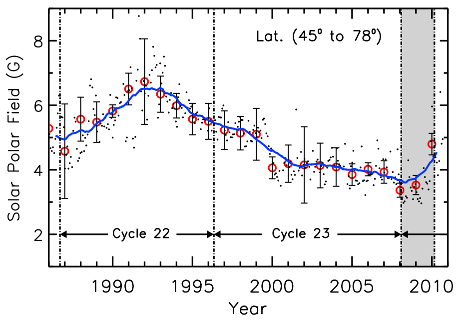

Figure 1. Shows the absolute value of the solar polar field, in the latitude range 45–78°, as a function of time in years for solar cycles 22 and 23.

the bulk density itself, *Hewish et al.* [1985] showed that there was no evidence for enhanced or decreased IPS that was not associated with corresponding variations in density. They went on to derive a relation between a normalized scintillation index denoted 'g' and the density given by g = $(\mathrm{Ncm}^{-3}/9)^{0.52\pm0.05}$. Thus, whenever interplanetary disturbances, containing either enhanced or depleted rms electron density fluctuations (Δn_e) as compared to the background solar wind, cross the line-of-sight (LOS) to the observed source they exhibit themselves as changes in the levels of scintillation (m), i.e., higher or lower than expected m, where $m = \Delta S/\langle S\rangle$ is the ratio of the scintillating flux ΔS to the mean source flux $\langle S\rangle$. In other words, whenever turbulence levels change in the solar wind, they will be reflected in IPS measurements as changes in m. The main advantage of the IPS technique is that, it can probe a very large region of the inner heliosphere, ranging from about 0.2 AU to 0.8 AU and it is extremely sensitive to small changes in Δn_e. In fact IPS is so sensitive to changes in Δn_e that it has been used to probe Δn_e fluctuations in tenuous cometary ion tails well downstream of the nucleus [*Janardhan et al.*, 1992] and to study solar wind disappearance events wherein average densities at 1 AU drop to values below 0.1 cm^{-3} [*Janardhan et al.*, 2005]. In a typical IPS observation, the angle between the Sun the Earth and the observed radio source is known as the solar elongation (ϵ). Please refer to Figure 1 of *Balasubramanian et al.* [2003] for details of the IPS observing geometry. Since the solar wind density beyond ~0.2 AU is inversely proportional to r^2 [*Bird et al.*, 1994] where, r = sin(ϵ), measurements of m in the direction of a given radio source will increase with decreasing ϵ or distance 'r' from the Sun, until a certain ϵ. After this point m falls off sharply with further reduction in ϵ. The ϵ at which m turns over is dependent on frequency and at 327 MHz it lies between 10° and 14°. The region at ϵ larger than the turnover defines the region of weak scattering where the approximation of scattering by a thin screen is valid [*Salpeter*, 1967]. For an ideal point source, m will be unity at an ϵ of ~12° and drop to values below unity with increasing distance r. For sources, with finite compact component sizes (>0 milli arcsec (mas)), m will be < unity at the turnover.

[6] For the steady state solar wind, values of m can be computed by obtaining theoretical temporal power spectra using a solar wind model assuming weak scattering and a power law distribution of density irregularities in the IP medium for any given source size and distance r of the LOS from the Sun [*Marians*, 1975]. The set of six curves (labeled 'A') in Figure 2 show the theoretically expected m as a function of ϵ for various source sizes in mas, assuming weak scattering at 327 MHz. To remove the ϵ or distance dependence of m, each observation of m has to be normalized by that of a point source at the corresponding ϵ. It has been shown that the source 1148-001 is ≤10 mas in angular extent at 327 MHz. Thus, 1148-001 can be treated as a nearly ideal point source, with most of its flux contained in a scintillating compact component [*Venugopal et al.*, 1985]. Normalizing all observations of m in this manner will yield an ϵ or distance independent value of m as shown for three source sizes (labeled 'B') in Figure 2. It must be noted that the curves in Figure 2 imply that the radial fall off rate is slightly different for different source sizes. Thus, the m for the larger source sizes will be over-corrected at large distances. However, most of the observed IPS sources are strong scintillators with sizes ≤250 mas and will not suffer from this normalization.

3. The Observations and Data Reduction

[7] The three-station IPS facility, operated by the Solar-Terrestrial Environment Laboratory (STEL), Japan, and used for the observations described in this paper, can carry out IPS observations at 327 MHz on about 200 compact extragalactic, radio sources on a regular basis, to derive solar wind velocities and m. In 1994, a fourth antenna was added to the system to form a four-station network that could provide more robust estimates of the solar wind speed owing to the redundancy in the baseline geometry obtained by having an additional station. We have taken data from 1983 to 2009, which had a one year data gap in 1994 owing to the development of the fourth IPS station, and have chosen sources which had at least 400 individual observations over this period of 27 years. We also ensured that there were no significant data gaps in any given year, apart from the one year gap in 1994. Of the total of 215 sources observed, we were finally left with 26 sources covering the entire 24 hour range of source right ascensions and a wide range of source

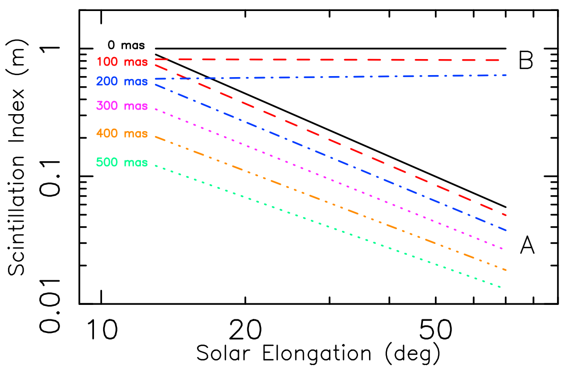

Figure 2. Curves (labeled 'A') of theoretically expected m as a function of ϵ for various source sizes. Curves (labeled 'B') corresponding to source sizes of 0 mas, 100 mas, and 200 mas, have been normalized by the point source m at the corresponding ϵ.

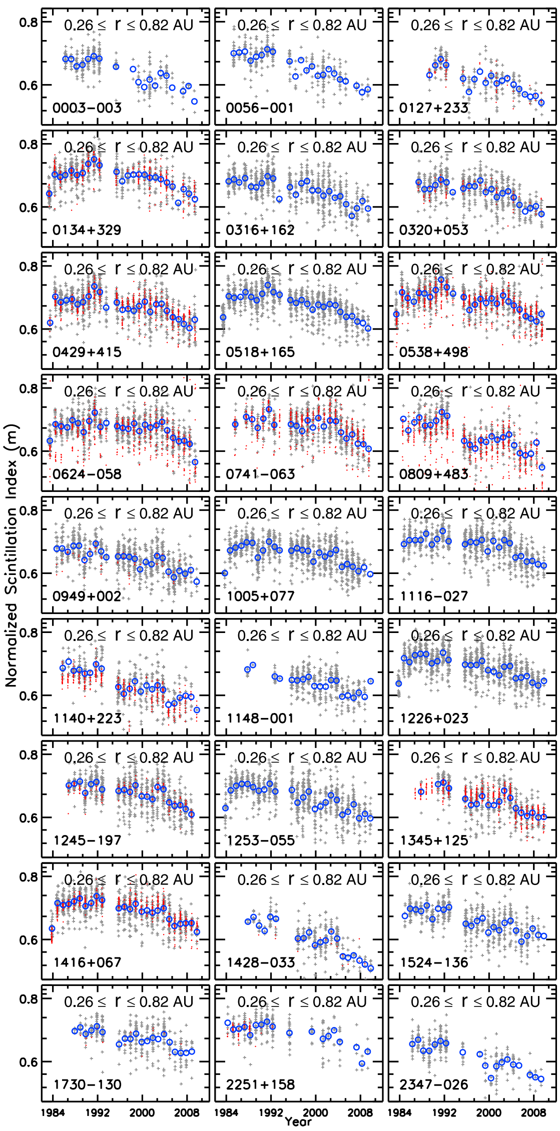

Figure 3. Plots m as a function of time in years for 27 sources after m has been made independent of distance from the Sun by normalizing each observation by the value of m for the source 1148-001. The grey crosses are observations at source helio latitudes ≤45° while the fine red dots are observations at source heliolatitudes >45°. The open circles are yearly averages by excluding the high latitude observations. The IAU name of each source is indicated at the bottom left in each panel.

declinations. The source 1148-001 was included as the 27th source even though it had some data gaps and therefore did not fully comply with our selection criteria. The data set was first normalized by the highest value so that the range of m was between 0 and unity. The distance dependence of m was then removed by normalizing every individual observation for each source by the value of m for the source 1148-001 at the corresponding ϵ. Figure 3 shows plots of m as a function of time in years for the 27 chosen sources lying in the distance range 0.26 to 0.82 AU. The grey crosses are measurements when the source heliolatitude is ≤45° while the fine red dots are measurements when the source heliolatitude is >45°. The large, blue, open circles are yearly averages taken without the high latitude observations. The reason for dropping the high latitude observations from the yearly averages is because IPS observations have shown [*Tokumaru et al.*, 2000] that the solar wind structure changes with the solar cycle, being more or less symmetric at solar maximum and considerably asymmetric during solar minimum. This asymmetry could change the way m falls off with radial distance. Since our IPS measurements mix measurements distant from the Sun near the solar equator with measurements at small ϵ at high solar latitude, we drop the high latitude observations from the yearly averages in order not to affect the yearly means. In addition, long term and gradual changes in the antenna sensitivity caused by degradation in the efficiency of the system, could cause some changes in the IPS measurements over time. Such changes are very difficult to quantify but every effort has been made to maintain the system stability and we believe that these changes cannot account for or explain the systematic drop in m starting from around 1995. It can be seen from Figure 3 that all the sources show a steady decline in m starting from around ~1995 implying a reduction in solar wind turbulence levels. The drop in m ranges between 10% and 25% when the annual means are taken considering all observations and it ranges between 10% and 22% when the annual means are taken without including the high latitude observations. The average drop is therefore around 16%. One must note however that only 16 of the 27 sources go to latitudes above 45° while the remaining 11 sources have all observations at heliolatitudes ≤45°. In order to achieve greater clarity and to avoid any confusion caused by showing a large number of panels in Figure 3 the yearly means of each source (blue open circles) are shown again, in Figure 4, as a composite plot of m as a function of time in years. The steady drop in m from ~1995 can be unambiguously seen in Figure 4.

4. Discussion and Conclusions

[8] We have seen that the turbulence levels, as indicated by reduced scintillation levels in the IP medium, have dropped steadily since ~1995. In addition, $|B_r|$ has been lower during the recent minima than in the past three

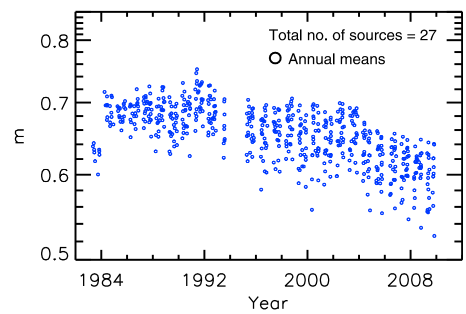

Figure 4. Shows the annual means of m as a function of time for each of the 27 sources shown in Figure 3.

minima [*Smith and Balogh*, 2008] and solar polar fields have also shown a steep decline since ~1995. Since solar polar fields supply most of the heliospheric magnetic flux during solar minimum conditions [*Svalgaard et al.*, 2005], weaker polar fields imply that the IMF will also be significantly lower. A causal relationship between stronger magnetic fields and turbulence in this region also implies a decrease in turbulence levels over the solar poles since ~1995. It has been shown that the solar wind turbulence is related to both the rms electron density fluctuations (Δn_e) and large scale magnetic field fluctuations in fast solar wind streams [*Ananthakrishnan et al.*, 1980]. Similarly, it is possible that a global reduction in the IMF is being reflected as a large scale global reduction in m (or microturbulence) as shown by our observations. As opposed to our method, IPS observations of the change in the turnover distance of m, which defines the minimum distance (from the sun) at which the weak scattering regime starts, have shown a steady decrease in the scattering diameter of the corona since 2003 [*Manoharan*, 2010b].

[9] A great deal of work has been done in modeling the solar dynamo and predicting the strength of future solar cycles. It has been argued [*Dikpati et al.*, 2006] that since the meridional circulation period is between 17–21 years in length, the strength of the polar fields during the ongoing cycle minimum and the preceding two solar minima will influence the strength of the next cycle. Another view point is that of *Choudhuri et al.* [2007] who claim that only the value of the polar field strength in the ongoing cycle minimum is important in predicting the next cycle. Very recently, *Nandy et al.* [2011] used a kinematic dynamo simulation model that adjusted the flow speeds in each half of the cycle to reproduce the extended minimum in cycle 23. Their model showed that the changes in the meridional flow speeds that led to the extended minimum began as early as the mid to late 1990's and also predicted that very deep minima are generally associated with weak polar fields. On the other hand, using observations, from cycles 21, 22 and 23, of the drift of Fe XIV emission features over time at high latitudes, referred to as "rush to the poles" *Altrock* [2011] was able to show that the solar maximum occurs approximately 1.5 years prior to the rush-to-the-poles reaching the solar poles.

[10] In conclusion, our observations have shown that turbulence levels in the inner heliosphere have shown a steady decline since the mid 90's. The fact that the change in the meridional flow that regulates the solar dynamo began in the mid 1990's coupled with the fact that solar polar fields have been declining since ~1995 and our IPS observations all provide a consistent result showing that the buildup to the deepest minimum in 100 years actually began more than a decade earlier.

[11] **Acknowledgments.** IPS observations were carried out under the solar wind program of STEL, Japan. We thank the two anonymous referees whose comments have improved the paper significantly. One of the authors (JP) thanks Bill Coles, Mike Bird and Murray Dryer for their critical comments.
[12] The Editor thanks two anonymous reviewers for their assistance in evaluating this paper.

References

Altrock, R. C. (2011), Coronal Fe XIV emission during the whole heliosphere interval campaign, *Sol. Phys.*, doi:10.1007/s11207-011-9714-9, in press.
Ananthakrishnan, S., W. A. Coles, and J. J. Kaufman (1980), Microturbulence in solar wind streams, *J. Geophys. Res.*, *85*, 6025–6030.
Asai, K., M. Kojima, M. Tokumaru, A. Yokobe, B. V. Jackson, P. L. Hick, and P. K. Manoharan (1998), Heliospheric tomography using interplanetary scintillation observations: 3. Correlation between speed and electron density fluctuations in the solar wind, *J. Geophys. Res.*, *103*, 1991–2001.
Balasubramanian, V., P. Janardhan, S. Srinivasan, and S. Ananthakrishnan (2003), Interplanetary scintillation observations of the solar wind disappearance event of May 1999, *J. Geophys. Res.*, *108*(A3), 1121, doi:10.1029/2002JA009516.
Bird, M. K., H. Volland, M. Paetzold, P. Edenhofer, S. W. Asmar, and J. P. Brenkle (1994), The coronal electron density distribution determined from dual-frequency ranging measurements during the 1991 solar conjunction of the ULYSSES spacecraft, *Astrophys. J.*, *426*, 373–381.
Choudhuri, A. R., P. Chatterjee, and J. Jiang (2007), Predicting solar cycle 24 with a solar dynamo model, *Phys. Rev. Lett.*, *98*(13), 131103, doi:10.1103/PhysRevLett.98.131103.
Dikpati, M., G. de Toma, and P. A. Gilman (2006), Predicting the strength of solar cycle 24 using a flux-transport dynamo-based tool, *Geophys. Res. Lett.*, *33*, L05102, doi:10.1029/2005GL025221.
Hewish, A., P. F. Scott, and D. Wills (1964), Interplanetary scintillation of small diameter radio sources, *Nature*, *203*, 1214–1217.
Hewish, A., S. J. Tappin, and G. R. Gapper (1985), Origin of strong interplanetary shocks, *Nature*, *314*, 137–140.
Janardhan, P., S. K. Alurkar, A. D. Bobra, O. B. Slee, and D. Waldron (1992), Power spectral analysis of enhanced scintillation of quasar 3C459 due to Comet Halley, *Aust. J. Phys.*, *45*, 115–126.
Janardhan, P., K. Fujiki, M. Kojima, M. Tokumaru, and K. Hakamada (2005), Resolving the enigmatic solar wind disappearance event of 11 May 1999, *J. Geophys. Res.*, *110*, A08101, doi:10.1029/2004JA010535.
Janardhan, P., S. K. Bisoi, and S. Gosain (2010), Solar polar fields during cycles 21–23: Correlation with meridional flows, *Sol. Phys.*, *267*, 267–277.
Jian, L. K., C. T. Russell, and J. G. Luhmann (2011), Comparing solar minimum 23/24 with historical solar wind records at 1 AU, *Sol. Phys.*, doi:10.1007/s11207-011-9737-2, in press.
Lockwood, M., M. Owens, and A. P. Rouillard (2009), Excess open solar magnetic flux from satellite data: 1. Analysis of the third perihelion Ulysses pass, *J. Geophys. Res.*, *114*, A11103, doi:10.1029/2009JA014449.
Mann, G., A. Klassen, H. Aurass, and H. Classen (2003), Formation and development of shock waves in the solar corona and the near-Sun interplanetary space, *Astron. Astrophys.*, *400*, 329–336.
Manoharan, P. K. (2010a), Ooty interplanetary scintillation—Remote-sensing observations and analysis of coronal mass ejections in the heliosphere, *Sol. Phys.*, *265*, 137–157.
Manoharan, P. K. (2010b), Peculiar current solar-minimum structure of the heliosphere, *Highlights Astron.*, *15*, 484–487.
Marians, M. (1975), Computed scintillation spectra for strong turbulence, *Radio Sci.*, *10*, 115–119.
McComas, D. J., H. A. Elliott, N. A. Schwadron, J. T. Gosling, R. M. Skoug, and B. E. Goldstein (2003), The three-dimensional solar wind around solar maximum, *Geophys. Res. Lett.*, *30*(10), 1517, doi:10.1029/2003GL017136.
McComas, D. J., R. W. Ebert, H. A. Elliott, B. E. Goldstein, J. T. Gosling, N. A. Schwadron, and R. M. Skoug (2008), Weaker solar wind from the polar coronal holes and the whole Sun, *Geophys. Res. Lett.*, *35*, L18103, doi:10.1029/2008GL034896.
Nandy, D., A. Muñoz-Jaramillo, and P. C. H. Martens (2011), The unusual minimum of sunspot cycle 23 caused by meridional plasma flow variations, *Nature*, *471*, 80–82.
Richardson, J. D., C. Wang, and K. I. Paularena (2001), The solar wind: From solar minimum to solar maximum, *Adv. Space Res.*, *27*, 471–479.
Salpeter, E. E. (1967), Interplanetary scintillations. I. Theory, *Astrophys. J.*, *147*, 433.
Smith, E. J., and A. Balogh (2008), Decrease in heliospheric magnetic flux in this solar minimum: Recent Ulysses magnetic field observations, *Geophys. Res. Lett.*, *35*, L22103, doi:10.1029/2008GL035345.
Smith, E. J., et al. (2003), The Sun and heliosphere at solar maximum, *Science*, *302*, 1165–1169.
Svalgaard, L., E. W. Cliver, and Y. Kamide (2005), Sunspot cycle 24: Smallest cycle in 100 years?, *Geophys. Res. Lett.*, *32*, L01104, doi:10.1029/2004GL021664.
Tokumaru, M., M. Kojima, Y. Ishida, A. Yokobe, and T. Ohmi (2000), Large-scale structure of solar wind turbulence near solar activity minimum, *Adv. Space Res.*, *25*, 1943–1946.
Tokumaru, M., M. Kojima, and K. Fujiki (2010), Solar cycle evolution of the solar wind speed distribution from 1985 to 2008, *J. Geophys. Res.*, *115*, A04102, doi:10.1029/2009JA014628.

Venugopal, V. R., S. Ananthakrishnan, G. Swarup, A. V. Pynzar, and V. A. Udaltsov (1985), Structure of PKS 1148-001, *Mon. Not. R. Astron. Soc.*, *215*, 685–689.

S. Ananthakrishnan, Electronics Science Department, Pune University, Pune, Maharashtra 411 007, India. (subra.anan@gmail.com)

K. Fujiki and M. Tokumaru, Solar-Terrestrial Environment Laboratory, Nagoya University, Honohara 3-13, Toyokawa, Aichi 442-8507, Japan. (fujiki@stelab.nagoya-u.ac.jp; tokumaru@stelab.nagoya-u.ac.jp)

P. Janardhan and S. K. Bisoi, Astronomy and Astrophysics Division, Physical Research Laboratory, Ahmedabad, Gujarat 380 009, India. (jerry@prl.res.in; susanta@prl.res.in)

Solar Polar Fields During Cycles 21??? 23: Correlation with Meridional Flows

Solar Physics
A Journal for Solar and Solar-Stellar Research and the Study of Solar Terrestrial Physics

ISSN 0038-0938
Volume 267
Number 2

Sol Phys (2010) 267:267-277
DOI 10.1007/s11207-010-9653-x

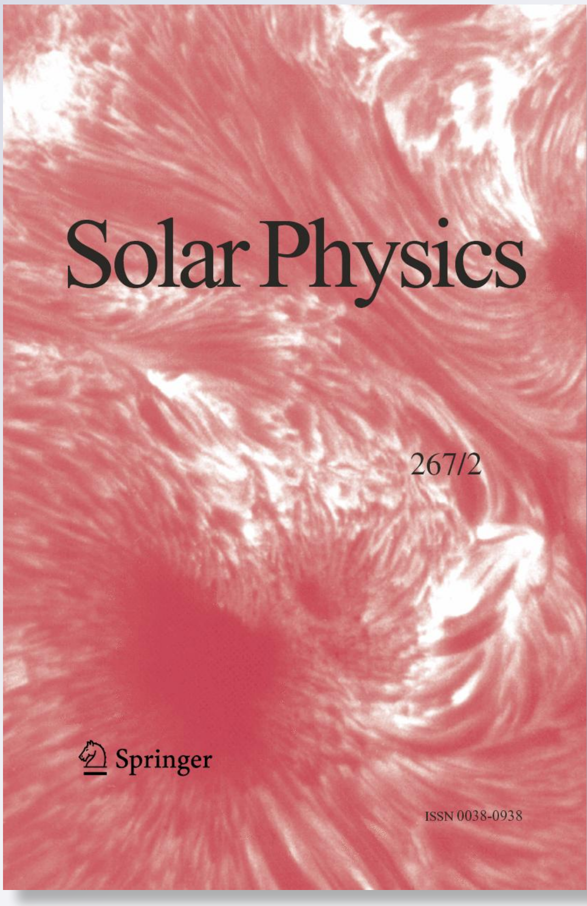

Solar Phys (2010) 267: 267–277
DOI 10.1007/s11207-010-9653-x

Solar Polar Fields During Cycles 21 – 23: Correlation with Meridional Flows

P. Janardhan · Susanta K. Bisoi · S. Gosain

Received: 16 April 2010 / Accepted: 29 September 2010 / Published online: 2 November 2010

Abstract We have examined polar magnetic fields for the last three solar cycles, *viz*. Cycles 21, 22, and 23 using NSO/Kitt Peak synoptic magnetograms. In addition, we have used SOHO/MDI magnetograms to derive the polar fields during Cycle 23. Both Kitt Peak and MDI data at high latitudes (78° – 90°) in both solar hemispheres show a significant drop in the absolute value of polar fields from the late declining phase of the Solar Cycle 22 to the maximum of the Solar Cycle 23. We find that long-term changes in the absolute value of the polar field, in Cycle 23, are well correlated with changes in meridional-flow speeds that have been reported recently. We discuss the implication of this in influencing the extremely prolonged minimum experienced at the start of the current Cycle 24 and in forecasting the behavior of future solar cycles.

Keywords Polar magnetic fields · Meridional flows · Solar cycle · MDI magnetograms

1. Introduction

Detailed study of solar magnetic features is an important area of research not only for its intrinsic interest, but also because solar magnetic fields have a profound and far-reaching influence on the Earth's near-space environment. With society's increased dependence on space-based technology, much of which is at risk due to solar activity that waxes and wanes

P. Janardhan (✉) · S.K. Bisoi · S. Gosain
Physical Research Laboratory, Astronomy & Astrophysics Division, Navrangpura,
Ahmedabad 380009, India
e-mail: jerry@prl.res.in

S.K. Bisoi
e-mail: susanta@prl.res.in

S. Gosain
e-mail: sgosain@prl.res.in

S. Gosain
Udaipur Solar Observatory, P.O. Box 198, Dewali, Udaipur 313001, India

with the sunspot cycle, it is imperative that we understand the solar magnetic cycle and its effects on the near-space environment. In addition, due to the reported anthropogenic influence on climate change that has occurred in recent times, it is becoming increasingly important to distinguish and delineate the degree to which the solar cycle can affect terrestrial climate.

The evolution of the large-scale solar magnetic field is attributed to a solar magnetohydrodynamic dynamo operating inside the Sun which involves three basic processes. The generation of toroidal fields by shearing pre-existing poloidal fields (the Ω effect), the regeneration of poloidal fields by twisting toroidal flux tubes (the α effect), and finally, flux transport by meridional circulation to carry background magnetic fields polewards from the Equator (Parker, 1955a, 1955b; Steenbeck and Krause, 1969; Wang, Sheeley, and Nash, 1991; Choudhuri, Schussler, and Dikpati, 1995; Dikpati and Charbonneau, 1999) are considered.

With the measurement of the Sun's polar field (Babcock and Babcock, 1955) and the subsequent proposal of polar-field reversal during the maximum of each solar cycle (Babcock, 1959), research on solar magnetic fields and their effect on subsequent cycles was channelled in a new direction. Since then, many investigations have been carried out to explore the relation between evolution of large-scale magnetic fields and their association with polar-field structures (Fox, McIntosh, and Wilson, 1998; Benevolenskaya, Kosovichev, and Scherrer, 2001; Benevolenskaya, Kosovichev, and Scherrer, 2002; Gopalswamy *et al.*, 2003).

The current sunspot minimum, which we have seen at the end of Cycle 23, has been one of the deepest minima that we have experienced in recent times with roughly 71–73% of the days in 2008 and 2009, respectively, being entirely spotless. Apart from this, Cycle 23 has shown several other peculiarities, such as a second maximum during the declining phase that is unusual for odd-numbered cycles, a slower rise to maximum than other odd-numbered cycles, and a slower than average polar reversal. Such departures from "normal" behavior need to be studied and understood as they could be significant in the context of understanding the evolution of magnetic fields on the Sun.

In this article, we have examined the solar polar-field behavior for the last few cycles and the following sections will discuss our findings.

2. Magnetic-Field Data

2.1. Low-resolution NSO/Kitt Peak Data

Magnetic-field data are available as standard FITS format files from the National Solar Observatory, Kitt Peak, USA (NSO/Kitt Peak) synoptic magnetogram database (ftp://nsokp.nso.edu/kpvt/synoptic/mag/). These synoptic maps are in the form of 180×360 arrays starting from Carrington Rotation (CR) CR1625 through CR2006 corresponding to years 1975.13 through 2003.66. For the period covering the years from 2003.66 through 2009.11, synoptic maps were obtained from the *Vector Spectro Magnetograph* (VSM) of the NSO/*Synoptic Optical Long-term Investigations of the Sun* (SOLIS) facility for solar observations over a long time frame (NSO/SOLIS): (ftp://solis.nso.edu/synoptic/level3/vsm/merged/carr-rot/). A few data gaps during CR1640 – CR1644, CR1854, CR1890, CR2015, CR2016, CR2040, and CR2041 were filled in by interpolated values while making the plots.

The resolution of the synoptic maps is 1° in both longitude (1° to 360°) and latitude (−90° to 90°). A typical Carrington synoptic map is produced from full-disk magnetograms spanning an entire Carrington rotation period. Each individual magnetogram is first remapped into latitude and longitude coordinates and then added together to produce the final synoptic map for each CR. All synoptic magnetogram maps, represented as an $i \times j$ data array with i and j representing the latitude and longitude respectively, for any given CR number n, contain magnetic flux density $[\phi_{i,j,n}]$, in units of Gauss averaged over equal areas of the Sun. The actual flux units are then obtained by multiplying by the appropriate area.

Since we are interested in the variation of photospheric magnetic fields with latitude, data are processed by taking longitudinal averages for each latitude bin of 1° by converting the data to a one dimensional array of 180×1. Any latitude element i, for a given CR, $[n]$ will contain the averaged magnetic field represented by Equation (1),

$$\phi_{i,n} = \frac{\sum_{j=1}^{360} \phi_{i,j,n}}{360} \tag{1}$$

Now, the averaged magnetic field for a range of latitudes in any CR is obtained by averaging $\phi_{i,n}$, as shown by Equation (2),

$$\phi_n = \frac{\sum_{i=k}^{p} \phi_{i,n}}{p-k+1} \tag{2}$$

Here k and p are the row numbers corresponding to a latitude bin. Using the above procedure, we have obtained average magnetic fields in each solar hemisphere for three different latitude bins between ranges:

- 0° and 45°, representing the equatorial or toroidal fields.
- 45° and 78°, representing the mid-latitude fields.
- 78° and 90°, representing polar fields in each hemisphere.

2.2. High-Resolution MDI Data

Line-of-sight magnetograms from the *Michelson Doppler Interferometer* (MDI: Scherrer *et al.*, 1995), onboard the *Solar and Heliospheric Observatory* (SOHO: Domingo, Fleck, and Poland, 1995), are available from 1996 onwards. High-resolution (3600×1080 pixels) MDI synoptic images beginning from CR1911 through CR2080 are used, with data gaps for CR1938 – CR1942, CR1945, and CR2073. It must, however, be noted that there are occasions that the inclination of the Earth's orbit to the Sun's Equator will cause one of the poles of the Sun to not be clearly visible. We have used MDI synoptic magnetograms available at http://soi.stanford.edu/magnetic/index6.html, which have been corrected for this effect.

Since MDI measurements are considered to be more reliable, as they are more frequent and stable as compared to Kitt Peak observations, we have compared the two data sets for the period after 1996 to check if the results agree with each other. Also, data gaps, when present, for example from CR1938 to CR1941, were dealt with by replacing them with interpolated values, and these have been indicated in the figures. Finally, the resolution of the MDI data was degraded (by averaging) to the resolution of the NSO/Kitt Peak data so as to be able to compare the results. It may be noted that for the MDI data, only the latitude bin between 78° and 90° was considered.

3. Magnetic-Field Measurements

As mentioned earlier, meridional circulation is the primary poloidal-flux-transport agent in the Sun. A polewards meridional flow at the solar surface has been shown to exist, with average speeds in the range 10 $\mathrm{m\,s^{-1}}$ – 20 $\mathrm{m\,s^{-1}}$ (Duvall, 1979; Hathaway, 1996; Hathaway *et al.*, 1996). The amplitude of this surface flow is more than an order of magnitude weaker than other surface flows, such as granulation, supergranulation and differential rotation. Therefore, the effects of this meridional circulation can best be studied at high solar latitudes, where the modulation due to the solar cycle is negligible or absent.

Figure 1 shows the measurements of the magnetic field in each solar hemisphere as a function of time in the two latitude ranges 0° – 45° and 45° – 78°. While the upper two panels of Figure 1 show the absolute value of the field in the latitude range 0° – 45° for the northern and southern hemisphere, respectively, the lower two panels show the absolute value of the magnetic field in the latitude range 45° – 78° for the northern and southern hemisphere, respectively. The filled dots represent the actual measurements derived from the NSO/Kitt Peak data base, while the solid line is a smoothed curve representing the data. The vertically oriented dashed parallel lines demarcate Cycles 21, 22, and 23. It can be seen from Figure 1 (upper two panels) that there is a strong solar-cycle modulation present in the latitude range ±0° – ±45°, while the solar-cycle modulation is much weaker and barely discernable in the latitude range ±45° – ±78° for Cycles 21 and 22; it is not seen for Cycle 23.

Figure 2 shows the actual (signed) measurements of magnetic field, in each solar hemisphere, as a function of time in years in the latitude range 78° – 90°. While the upper panel of Figure 2 shows the magnetic field for the northern hemisphere, the lower panel shows the value of the magnetic field for the southern hemisphere. The filled dots, with 1σ error bars, represent the measurements derived from the NSO/Kitt Peak data, while the thick, solid, blue line is a smoothed curve. Points where data gaps were filled by interpolation are shown by red open circles. A comparison of the polar field during Cycles 22 and 23 from Figure 2 shows that the longitude-averaged polar magnetic field between ±78° – ±90° during the current extended minimum leading up to the current Cycle 24 is weaker than the corresponding minimum period in Cycles 21 and 22. Also, a comparison of the fields in the two hemispheres in Cycle 23 shows that the south polar field is weaker than the north polar field. In a detailed analysis of sunspot data and longitude-averaged photospheric magnetic flux, Dikpati *et al.* (2004) have also pointed out several peculiarities during Cycle 23 such as the slow buildup of the polar field after the occurrence of the polar-field reversal, the asymmetry in polar reversal for the North and South Pole, and the steady behavior of the north polar field in comparison to the south polar field from the late declining phase of Cycle 22 to early rising phase of Cycle 23. All of these features can also clearly be seen in Figure 2 for the period of Cycle 23.

The two panels of Figure 3 show the variation in the absolute value of the polar magnetic field in the latitude range 78° – 90° for the north and south solar hemisphere as a function of years for Solar Cycles 21 – 23. Measurements from NSO/Kitt Peak data are shown by filled dots, while the thick, blue, solid line is a smoothed curve. During Cycle 23, MDI data are shown by red crosses to enable comparison between NSO/Kitt Peak data and MDI data. Marked by open black circles are points where MDI data gaps were filled in by interpolation. It may be noted that the MDI high-resolution data were reduced, by averaging, to that of the NSO/Kitt Peak data for comparison. A striking feature in Figure 3 is a steep and continuous drop of the average polar field (in both NSO and MDI data) from the late declining phase of Cycle 22 to the maximum of Cycle 23 in both the hemispheres. A slow continuous drop of ≈ 13 G from 1994 to 2001 is seen in the northern hemisphere, while a sharp continuous drop of ≈ 9 G from 1995 to 2002 is seen in the southern hemisphere. Cycles 21 and 22, however, showed no such drop. The recent and extended minimum at the end of Cycle 23 is also interesting in that the average polar-field behavior showed no variation and remained steady from 2004 onwards in both hemispheres as seen from both NSO and MDI data. The MDI data however, are systematically lower than the NSO/Kitt Peak values throughout Cycle 23.

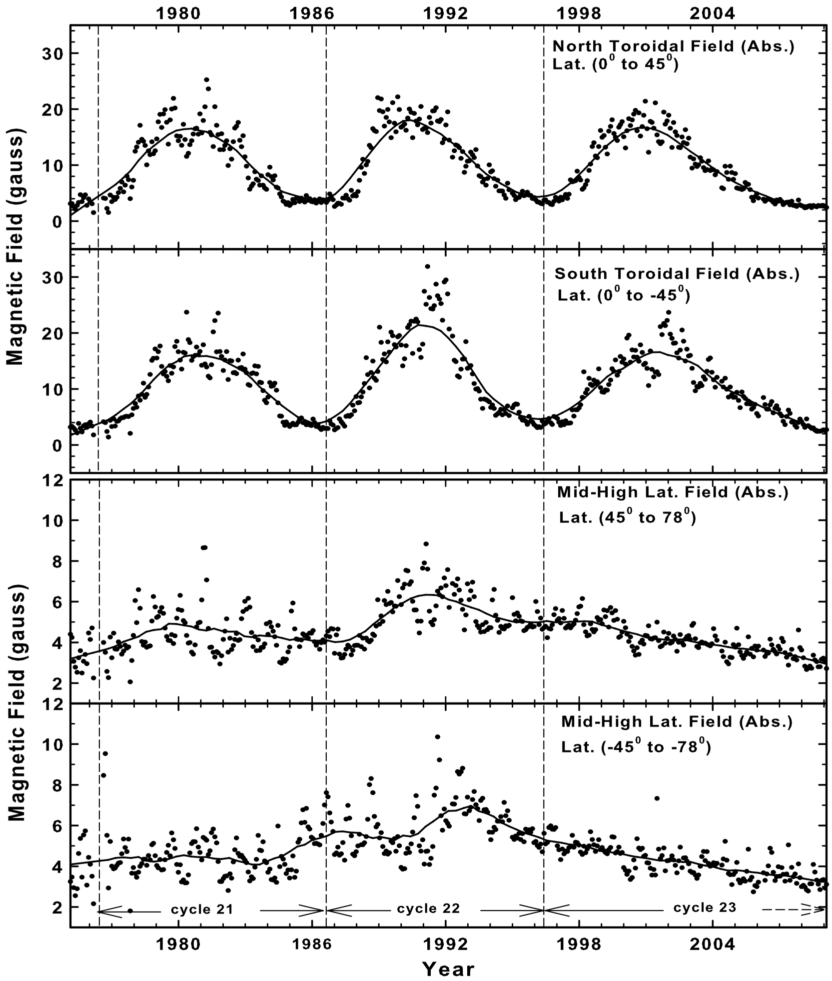

Figure 1 The four panels, in pairs starting from the top, show the variations in the magnetic field in the north and south solar hemisphere respectively, as a function of years for Solar Cycles 21 – 23. The absolute value of the magnetic field in the latitude range $0° - \pm 45°$ is shown in the first pair of panels, while the second pair of panels show the absolute value of magnetic field in the latitude range $45° - 78°$. The filled dots represent the actual measurements, while the solid line is a smoothed curve. The vertically oriented dashed parallel lines demarcate Cycles 21, 22, and 23, respectively.

4. Polar Fields and Meridional-Flow Speeds

4.1. Cycle 23

The Sun's meridional flow, which is directed polewards at the surface of the Sun, is an axis-symmetric flow of the order of $10 - 20\ \mathrm{m\,s^{-1}}$. This meridional flow is responsible for carrying background magnetic fields polewards from the Equator and plays an important

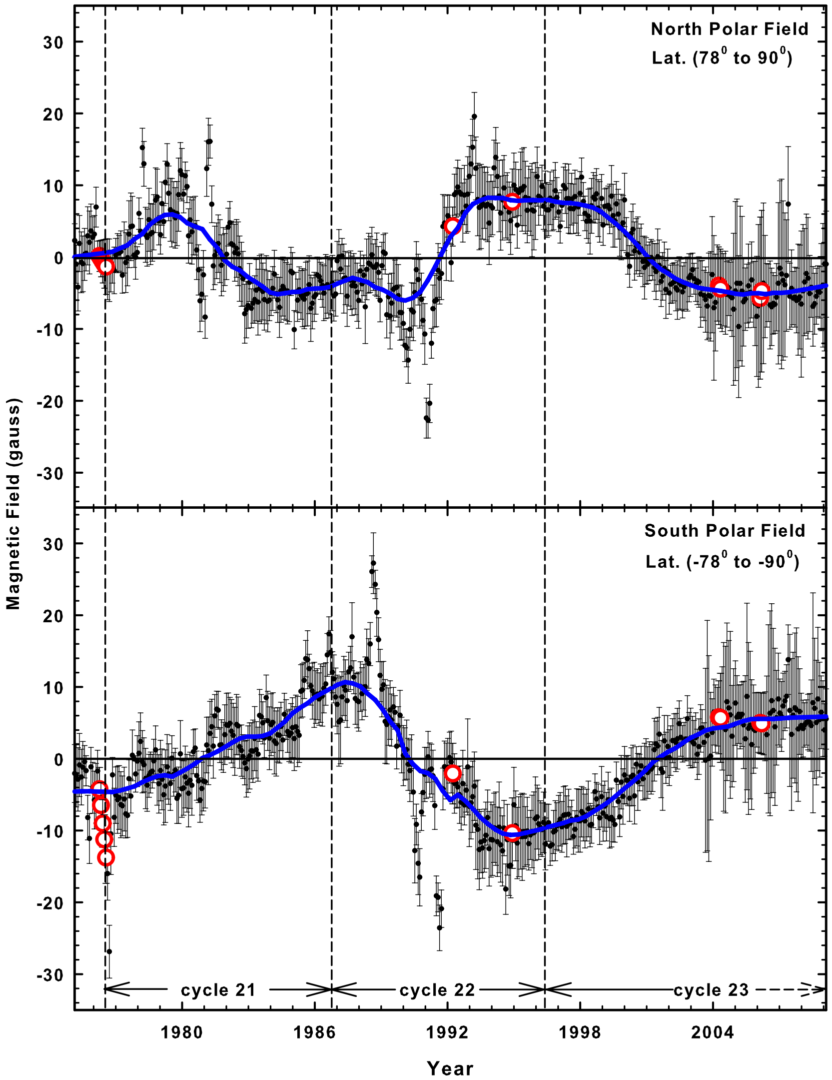

Figure 2 Variations in the magnetic field in the northern (upper panel) and southern solar hemisphere (lower panel) as a function of years for Solar Cycles 21 – 23. The actual (signed) value of magnetic field in the latitude range 78° – 90° is shown (filled dots) with 1σ error bars, while the thick, blue, solid line is a smoothed curve. The vertically oriented, dashed, parallel lines demarcate Cycles 21, 22, and 23, respectively. Points where data gaps were filled by interpolation are shown by red open circles

role in determining the strength of the solar polar field and the intensity of sunspot cycles (see, *e.g.*, Hathaway and Rightmire, 2010). There have been some attempts to infer surface meridional-flow speeds using the helioseismic technique of ring-diagram analysis applied

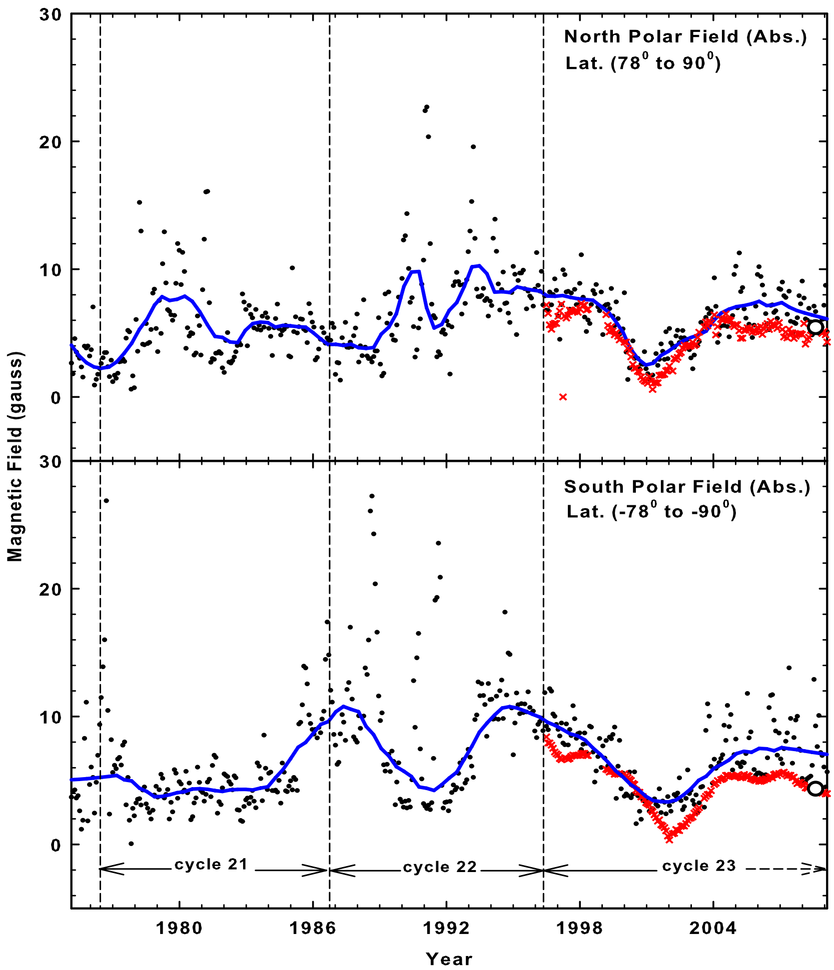

Figure 3 Variations in the absolute value of the polar magnetic field in the latitude range 78° – 90° for the north and south solar hemisphere as a function of years for the Solar Cycles 21 – 23. The measurements derived from the NSO/Kitt Peak data base are shown by filled dots, while the thick, blue, solid line is a smoothed curve. MDI data for Cycle 23 (for comparison) are shown by red crosses. The vertically oriented, dashed, parallel lines demarcate Cycles 21, 22, and 23 respectively. Points where MDI data gaps were filled by interpolation are shown by black open circles.

to MDI data (Haber *et al.*, 2002). However, a more recent and detailed study using MDI images of the line-of-sight magnetic fields (Hathaway and Rightmire, 2010) has reported measurements of the surface meridional-flow speed in the latitude range ±75° in Cycle 23. These measurements have shown a lot of variation in the meridional-flow speeds in Cycle 23. These authors determined a meridional-flow speed of 11.5 m s^{-1} at the minimum of Cycle 23 in 1996 – 1997 which then dropped to 8.5 m s^{-1} at the maximum in 2000 – 2001. It must be noted here that this drop in the flow speed coincides with the steep drop in the absolute value of the magnetic field that is seen in both the NSO/Kitt Peak and MDI data (Figure 3). In fact, the MDI data in the southern hemisphere continue to drop until 2002, after which they rise again. Between 2001 and 2004, the measured meridional-flow speed again increased to 13.0 m s^{-1} and remained constant at this value thereafter. Again, from Figure 3 we can see a corresponding steep increase in the absolute value of the polar field between 2001 and 2004. After this, the absolute value of the magnetic field remains constant in both hemispheres until 2009. From Figure 3 it is clear that the polar-field strength since 2004, as seen by both NSO/Kitt Peak and MDI has remained constant. Figure 4 shows a comparison between the averaged absolute magnetic fields determined from NSO/Kitt Peak synoptic magnetogram maps and MDI synoptic magnetogram maps for the northern (upper panel) and southern (lower panel) hemispheres for Solar Cycle 23. While the solid line is a smoothed curve representing the NSO data, the dashed line is a smoothed curve representing the MDI data. The meridional-flow speeds, as reported by Hathaway and Rightmire (2010), are indicated at the bottom of each panel and demarcated by vertically oriented, dashed parallel lines. It may be noted again that the MDI high-resolution data (3600×1080 pixels) were averaged and reduced to that of the NSO/Kitt Peak data (360×180 pixels) for comparison. The recent and extended minimum at the end of Cycle 23 is also interesting in that the average polar-field behavior showed no variation and remained steady from 2004 onwards in both hemispheres as seen from Figure 4. The magnetic field of MDI data, however, are systematically lower than the NSO/Kitt Peak values throughout Cycle 23, and in the southern hemisphere, the MDI data show a steep drop between 1997 – 2002.

4.2. Strength of Upcoming Solar Cycle 24

In trying to predict the strength of future solar cycles, magnetic persistence or the Sun's memory of the polar-field strength at minimum in the previous cycle has been postulated as the influencing factor. Some authors have used this method to try and predict the strength of upcoming cycles through magnetic persistence or the Sun's memory (Schatten *et al.*, 1978; Layden *et al.*, 1991; Schatten and Sofia, 1996). Later, it was postulated that magnetic persistence is itself governed by the meridional-flow speed (Hathaway, 1996; Haber *et al.*, 2002; Basu and Antia, 2003) with slower meridional flows resulting in longer memory. In addition, a slower meridional-flow speed would also determine the cycle period.

Two different views were postulated to predict the strength of Solar Cycle 24. The first predicted the new Solar Cycle 24 to be a strong cycle compared to Cycle 23 (Dikpati, de Toma, and Gilman, 2006). These authors used the sunspot area of the last three cycles based on a flux-transport-dynamo model as the source term for generating the poloidal field. The second predicted the new Solar Cycle 24 to be a weak one (Choudhuri, Chatterjee, and Jiang, 2007). These authors used only inputs from the last solar cycle, since the generation of poloidal fields involved randomness and indeterministic behavior.

4.3. Discussion and Conclusions

Although a great deal of progress has been made in our understanding of meridional flows and their role in determining the strength of the polar field and the amplitude of the following cycles, there seems to be a basic disagreement between flux-transport-dynamo models and surface-flux-transport models. Fast meridional flows, in the flux-transport-dynamo models, produce stronger polar fields and a short cycle, as compared to the observations of surface-flux-transport model, which give rise to weak polar fields and a long solar cycle. While the dynamo models have fields of one polarity centred on the sunspot latitudes, surface-flux-transport models have bands of opposite magnetic polarity on either side of the sunspot

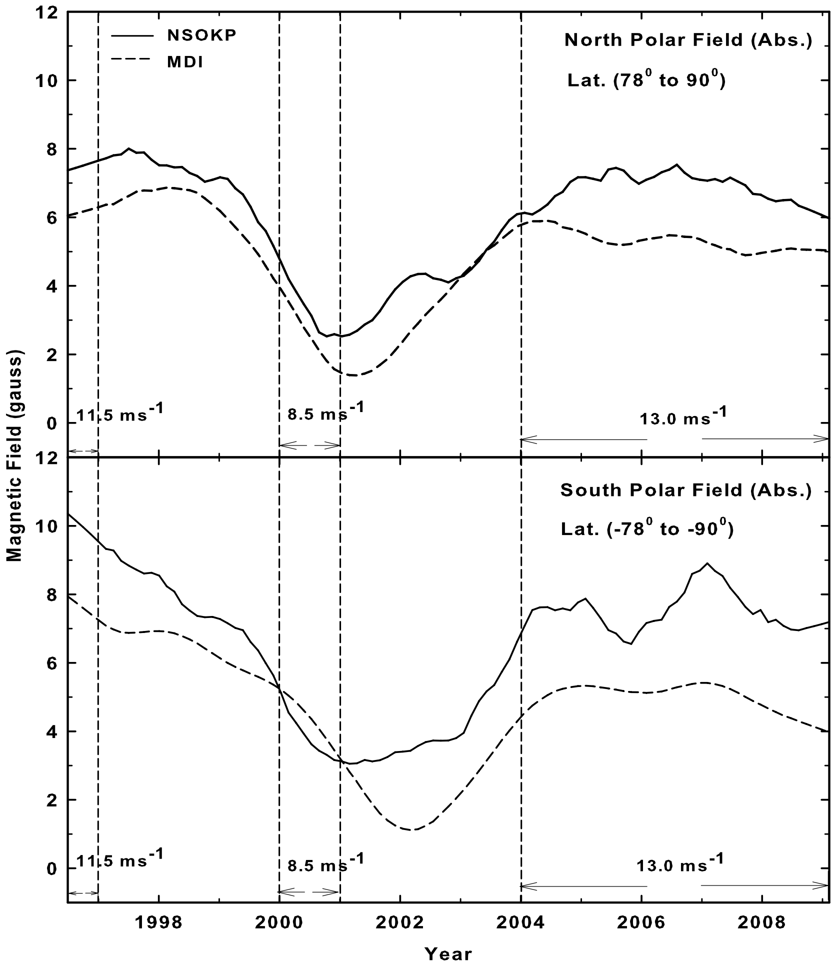

Figure 4 Comparison between Kitt Peak/NSO data and MDI data in Cycle 23 for the two hemispheres. The northern hemisphere is shown in the upper panel, while the southern hemisphere is shown in the lower panel. The meridional-flow speeds as reported by Hathaway and Rightmire (2010) have been indicated between vertically oriented dashed parallel lines.

latitudes. The cause for the difference in these two models is mainly the above difference in the latitudinal distribution of magnetic polarities, and this has been explained by Hathaway and Rightmire (2010); see also the references therein.

The observations of Hathaway and Rightmire (2010) support the surface-flux-transport model, wherein fast meridional flows inhibit opposite polarities from cancelling each other across the Equator. Thus, elements of both polarities will be carried to the poles, and a longer time would be required to reverse the old polar fields. This would in turn result in weaker polar fields of the new or reversed polarity. Such a mechanism would support our observations of weaker polar fields at solar maximum. We have seen from our data that we have a large and unusual drop in the absolute value of the polar fields during Cycle 23 compared to previous cycles (Section 3) and we also see its association with a similar behavior in the meridional-flow speed (Section 4.1). In addition, Hathaway and Rightmire (2010) have shown that the meridional flow generally shows a decrease from minimum to maximum, as has also been reported for earlier solar cycles (Komm, Howard, and Harvey, 1993), although with greater uncertainty and poorer temporal resolution than for Cycle 23, where high-resolution MDI data are available. The minimum leading up to the start of Cycle 24 has been very deep and prolonged, and we have seen that the corresponding polar fields have been at their lowest compared to Cycles 21 and 22. We believe that the "memory" of this very weak polar field in Cycle 23 is the cause of the extended solar minimum we have witnessed. Since the Sun's memory depends on the polar-field strength we believe that the upcoming Cycle 24 will be a much weaker cycle than Cycle 23, which is in accordance with the later prediction proposed by Choudhuri, Chatterjee, and Jiang (2007).

We have seen above that the absolute value of the polar magnetic field in the latitude range $78° – 90°$ virtually mirrors the change in the meridional-flow speeds in Cycle 23, with meridional-flow speeds dropping when the absolute value of the field drops. Unlike Cycles 21 and 22, the absolute values of the polar magnetic fields in Cycle 23 showed similar trends in both hemispheres. Since high-resolution MDI data are available only from 1996, this approach cannot be used to compute meridional flows for Cycles 21 and 22 noted that in both Cycles 21 and 23 the behavior of the absolute value of the polar fields is different in each hemisphere. If we assume that the correlation between the absolute value of the polar fields and the meridional-flow velocities holds good for all solar cycles, then this would imply that the field reversals occurred at different times in the two hemispheres in Cycles 21, 22, and 23.

The study of polar magnetic fields might thus provide good clues to the nature of the meridional flows in each hemisphere. Such inputs would be important in predicting the behavior of the future solar cycles. In addition to such measurements, other inputs from radio measurements of circular polarization that are sensitive to the line-of-sight component of the coronal magnetic field will also be very useful. The same is true for interplanetary scintillation measurements at high latitudes that can indicate the change in turbulence levels due to changes in polar fields (Ananthakrishnan, Balasubramanian, and Janardhan, 1995). Finally, high-resolution high-dynamic-range quiet-Sun radio imaging (Mercier *et al.*, 2006) of the Sun at low frequencies that can examine the changes in polar coronal-hole boundaries may be useful.

Acknowledgements The authors are thankful for the free-use data policy of the National Solar Observatory and acknowledge the MDI consortium for providing the data in the public domain via the world wide web. SOHO is a project of international collaboration between ESA and NASA. One of the authors (JP) would like to thank Murray Dryer for his critical comments on the manuscript.

References

Ananthakrishnan, S., Balasubramanian, V., Janardhan, P.: 1995, Latitudinal variation of solar wind velocity. *Space Sci. Rev.* **72**, 229 – 232. doi:10.1007/BF00768784.

Babcock, H.D.: 1959, The Sun's polar magnetic field. *Astrophys. J.* **130**, 364. doi:10.1086/146726.

Babcock, H.W., Babcock, H.D.: 1955, The sun's magnetic field, 1952 – 1954. *Astrophys. J.* **121**, 349. doi:10.1086/145994.

Basu, S., Antia, H.M.: 2003, Changes in solar dynamics from 1995 to 2002. *Astrophys. J.* **585**, 553 – 565. doi:10.1086/346020.

Benevolenskaya, E.E., Kosovichev, A.G., Scherrer, P.H.: 2001, Detection of high-latitude waves of solar coronal activity in extreme-ultraviolet data from the Solar and Heliospheric Observatory EUV Imaging Telescope. *Astrophys. J. Lett.* **554**, L107 – L110. doi:10.1086/320925.

Benevolenskaya, E.E., Kosovichev, A.G., Scherrer, P.H.: 2002, Evolution of large-scale coronal structure with the solar cycle from EUV data. In: Favata, F., Drake, J.J. (eds.) *Stellar Coronae in the Chandra and XMM-NEWTON Era* **CS-277**, Astron. Soc. Pac., San Fransisco, 419.

Choudhuri, A.R., Schussler, M., Dikpati, M.: 1995, The solar dynamo with meridional circulation. *Astron. Astrophys.* **303**, L29.

Choudhuri, A.R., Chatterjee, P., Jiang, J.: 2007, Predicting solar cycle 24 with a solar dynamo model. *Phys. Rev. Lett.* **98**(13), 131103. doi:10.1103/PhysRevLett.98.131103.

Dikpati, M., Charbonneau, P.: 1999, A Babcock – Leighton flux transport dynamo with solar-like differential rotation. *Astrophys. J.* **518**, 508 – 520. doi:10.1086/307269.

Dikpati, M., de Toma, G., Gilman, P.A.: 2006, Predicting the strength of solar cycle 24 using a flux-transport dynamo-based tool. *Geophys. Res. Lett.* **33**, 5102. doi:10.1029/2005GL025221.

Dikpati, M., de Toma, G., Gilman, P.A., Arge, C.N., White, O.R.: 2004, Diagnostics of polar field reversal in solar cycle 23 using a flux transport dynamo model. *Astrophys. J.* **601**, 1136 – 1151. doi:10.1086/380508.

Domingo, V., Fleck, B., Poland, A.I.: 1995, The SOHO mission: an overview. *Solar Phys.* **162**, 1 – 2. doi:10.1007/BF00733425.

Duvall, T.L., Jr.: 1979, Large-scale solar velocity fields. *Solar Phys.* **63**, 3 – 15. doi:10.1007/BF00155690.

Fox, P., McIntosh, P., Wilson, P.R.: 1998, Coronal holes and the polar field reversals. *Solar Phys.* **177**, 375 – 393.

Gopalswamy, N., Lara, A., Yashiro, S., Howard, R.A.: 2003, Coronal mass ejections and solar polarity reversal. *Astrophys. J. Lett.* **598**, L63 – L66. doi:10.1086/380430.

Haber, D.A., Hindman, B.W., Toomre, J., Bogart, R.S., Larsen, R.M., Hill, F.: 2002, Evolving submerged meridional circulation cells within the upper convection zone revealed by ring-diagram analysis. *Astrophys. J.* **570**, 855 – 864. doi:10.1086/339631.

Hathaway, D.H.: 1996, Doppler measurements of the Sun's meridional flow. *Astrophys. J.* **460**, 1027. doi:10.1086/177029.

Hathaway, D.H., Rightmire, L.: 2010, Variations in the Suns meridional flow over a solar cycle. *Science* **327**, 1350. doi:10.1126/science.1181990.

Hathaway, D.H., Gilman, P.A., Harvey, J.W., Hill, F., Howard, R.F., Jones, H.P., Kasher, J.C., Leibacher, J.W., Pintar, J.A., Simon, G.W.: 1996, GONG observations of solar surface flows. *Science* **272**, 1306 – 1309. doi:10.1126/science.272.5266.1306.

Komm, R.W., Howard, R.F., Harvey, J.W.: 1993, Meridional flow of small photospheric magnetic features. *Solar Phys.* **147**, 207 – 223. doi:10.1007/BF00690713.

Layden, A.C., Fox, P.A., Howard, J.M., Sarajedini, A., Schatten, K.H.: 1991, Dynamo-based scheme for forecasting the magnitude of solar activity cycles. *Solar Phys.* **132**, 1 – 40. doi:10.1007/BF00159127.

Mercier, C., Subramanian, P., Kerdraon, A., Pick, M., Ananthakrishnan, S., Janardhan, P.: 2006, Combining visibilities from the giant meterwave radio telescope and the Nancay radio heliograph. High dynamic range snapshot images of the solar corona at 327 MHz. *Astron. Astrophys.* **447**, 1189 – 1201. doi:10.1051/0004-6361:20053621.

Parker, E.N.: 1955a, Hydromagnetic dynamo models. *Astrophys. J.* **122**, 293. doi:10.1086/146087.

Parker, E.N.: 1955b, The formation of sunspots from the solar toroidal field. *Astrophys. J.* **121**, 491. doi:10.1086/146010.

Schatten, K., Sofia, S.: 1996, Forecasting solar activity and cycle 23 outlook. *Bull. Am. Astron. Soc.* **28**, 1347.

Schatten, K.H., Scherrer, P.H., Svalgaard, L., Wilcox, J.M.: 1978, Using dynamo theory to predict the sunspot number during solar cycle 21. *Geophys. Res. Lett.* **5**, 411 – 414. doi:10.1029/GL005i005p00411.

Scherrer, P.H., Bogart, R.S., Bush, R.I., Hoeksema, J.T., Kosovichev, A.G., Schou, J., Rosenberg, W., Springer, L., Tarbell, T.D., Title, A., Wolfson, C.J., Zayer, I., MDI Engineering Team: 1995, The solar oscillations investigation – Michelson Doppler Imager. *Solar Phys.* **162**, 129 – 188. doi:10.1007/BF00733429.

Steenbeck, M., Krause, F.: 1969, On the dynamo theory of stellar and planetary magnetic fields. I. AC dynamos of solar type. *Astron. Nachr.* **291**, 49 – 84.

Wang, Y., Sheeley, N.R., Jr., Nash, A.G.: 1991, A new solar cycle model including meridional circulation. *Astrophys. J.* **383**, 431 – 442. doi:10.1086/170800.

JOURNAL OF GEOPHYSICAL RESEARCH, VOL. 115, A12110, doi:10.1029/2010JA015708, 2010

Unique observations of a geomagnetic $SI^+ - SI^-$ pair: Solar sources and associated solar wind fluctuations

R. G. Rastogi,[1] P. Janardhan,[1] K. Ahmed,[2] A. C. Das,[1] and Susanta K. Bisoi[1]

Received 21 May 2010; revised 30 August 2010; accepted 20 September 2010; published 21 December 2010.

[1] This paper describes the occurrence of a pair of oppositely directed sudden impulses (SI) in the geomagnetic field (ΔX) at ground stations, called $SI^+ - SI^-$ pairs, that occurred between 1835 UT and 2300 UT on 23 April 1998. The $SI^+ - SI^-$ pair was closely correlated with corresponding variations in the solar wind density, while solar wind velocity and the southward component of the interplanetary magnetic field (*Bz*) did not show any correspondence. Further, this event had no source on the visible solar disk. However, a rear-side partial halo coronal mass ejection (CME) and an M1.4 class solar flare behind the west limb took place on 20 April 1998, the date corresponding to the traceback location of the solar wind flows. This event presents empirical evidence, which to our knowledge is the most convincing evidence for the association of specific solar events to the observations of an $SI^+ - SI^-$ pair. In addition, it shows that it is possible for a rear-side solar flare to propagate a shock toward the Earth.

Citation: Rastogi, R. G., P. Janardhan, K. Ahmed, A. C. Das, and S. K. Bisoi (2010), Unique observations of a geomagnetic $SI^+ - SI^-$ pair: Solar sources and associated solar wind fluctuations, *J. Geophys. Res.*, *115*, A12110, doi:10.1029/2010JA015708.

1. Introduction

[2] It is well known that space weather events observed at 1 AU are all linked to the dynamic evolution of the solar photospheric magnetic field. This evolution, in conjunction with solar rotation, drives space weather through the continuously changing conditions of the solar wind and the interplanetary magnetic field (IMF) within it. In spite of the fact that there have been substantial observations and discussions on the close correspondence between solar wind parameters at 1 AU and ground-based geomagnetic field variations [*Dungey*, 1961; *Heppner and Maynard*, 1987; *Goodrich et al.*, 1998; *Lu et al.*, 1998], it is not straightforward under this broad framework to pinpoint either the solar origins of specific space weather events or to find specific correlations between solar wind parameters at 1 AU and ground-based magnetic observations. This is because such signatures are generally weak and are usually washed out or masked by the large variety of interactions that can take place both in the interplanetary medium and within the Earth's magnetosphere. Space weather events are, however, often preceded by the arrival at 1 AU of strong interplanetary (IP) shocks. Since such storms can have adverse effects on human technologies, the study of IP shocks can yield important inputs for numerical models that simulate the propagation of solar-initiated IP disturbances out to 1 AU and beyond.

[1]Physical Research Laboratory, Astronomy & Astrophysics Division, Ahmedabad, India.
[2]Indian Institute of Geomagnetism, Navi Mumbai, India.

0148-0227/10/2010JA015708

[3] On the other hand, solar sources of space weather events can range from coronal mass ejections (CME), very energetic solar flares, filament eruptions, and corotating interaction regions (CIR). Though a vast majority of such events are caused by explosive and energetic solar events such as CMEs and flares, some recent studies have unambiguously associated large space weather events at 1 AU, such as "solar wind disappearance events," to small transient midlatitude corona holes butting up against large active regions at central meridian [*Janardhan et al.*, 2005, 2008a, 2008b]. These studies have provided the first observational link between the Sun and space weather effects at 1 AU, arising entirely from nonexplosive solar events.

[4] Though the very first observations, by the Mariner 2 spacecraft in 1962, of interplanetary shock waves showed the possibility of the existence of double-shock ensembles in the interplanetary medium [*Sonett et al.*, 1964], the existence of such shock pairs was firmly established only some years later, by the careful analysis of plasma and magnetic field measurements associated with shocks [*Burlaga*, 1970; *Lazarus et al.*, 1970]. However, the very unusual plasma and field variations associated with these structures prompted *Sonett and Colburn* [1965] to suggest that the first or forward shock would give rise to a positive *H*-component at ground-based observatories while the second or reverse shock would cause an oppositely directed or negative change in the *H*-component of the Earth's horizontal field, as measured along the local geomagnetic meridian (H). These impulses, referred to in the rest of the paper as sudden impulse or $SI^+ - SI^-$ pairs, were typically separated by a few hours in time and were hypothesized, as already stated, to be caused by the arrival at 1 AU of the forward and reverse shock pair convected toward the Earth by the solar wind. *Razdan et al.* [1965] described

worldwide occurrences of such $SI^+ - SI^-$ pairs and suggested that they were associated with solar disturbances driving interplanetary shocks at highly oblique angles to the solar wind streaming direction. They did not, however, find any solar activity or associated occurrences of solar radio emission during the period of $SI^+ - SI^-$ pairs. In a more recent study of a number of $SI^+ - SI^-$ pairs, covering the period 1995–1999, *Takeuchi et al.* [2002] concluded that the observed SI^- (or negative impulses) in their sample were not associated with reverse shocks and showed no preferential association to any particular kind of solar wind structure, such as high- and low-speed stream interface discontinuities or front boundaries of interplanetary magnetic clouds.

[5] Early theoretical support came from *Dryer* [1970, 1972], who introduced the physics of finite electrical conductivity within the forward and reverse shock pairs, to derive reasonable first-order predictions for the observed distribution of solar wind speed, density, and temperature, and this was followed up by several other early papers [*Eviatar and Dryer*, 1970; *Shen and Dryer*, 1972; *Dryer et al.*, 1975] along similar lines. In more recent times, there have been a number of theoretical models that have used inputs from solar data to predict the arrival of IP shocks and IP CMEs at Earth [*Odstrcil*, 2003; *Vandegriff et al.*, 2005; *Tóth et al.*, 2005; *Detman et al.*, 2006], including the well-known Hakamada-Akasofu-Fry model (HAFV2) [*Fry et al.*, 2003], which is the only model to date to have been substantially validated in an operational forecasting environment [*Smith et al.*, 2009a, 2009b] during solar cycle 23.

2. The $SI^+ - SI^-$ Pair of 23 April 1998

[6] An $SI^+ - SI^-$ pair was identified at three Indian geomagnetic observatories on 23–24 April 1998. Figure 1 (bottom) shows the tracings of H magnetograms (projected onto the X or geographic north direction and marked ΔX in Figure 1) on 23–24 April 1998 at the three Indian stations Gulmarg, Alibag, and Trivandrum, respectively. A sudden positive impulse in H was recorded at all three Indian observatories at 1835 UT (23 April 2335 LT), followed by a sudden negative impulse at 2300 UT (24 April 0430 LT). During the time interval between the SI^+ impulse and the SI^- impulse, the amplitude of H first decreased and then attained a peak of 44 nT at Trivandrum that progressively increased to 54 nT at Alibag and 76 nT at Gulmarg. Between 2100 and 2300 UT, large fluctuations were recorded at all stations. The fluctuations in H at all stations were remarkably similar with the amplitude increasing from Trivandrum to Gulmarg. Also shown in Figure 1 (starting from the top and going down) are the corresponding variations of the solar wind velocity, the IMF-*Bz*, the interplanetary electric field, the solar wind flow pressure, the solar wind density, and the symmetrical H Field, respectively. The curve for the solar wind density, as observed by the Advanced Composition Explorer (ACE; *Stone et al.* [1998]) has been shaded in Figure 1 in the region between the $SI^+ - SI^-$ pair. The vertically oriented dashed parallel lines in all parts of Figure 1 demarcates the time interval between the SI^+ impulse and the SI^- impulse. It is to be noted that the symmetric H field (SYM/H), characterizing the mean variation of H at all middle latitude stations around the world, too had remarkably similar variations as the H at Indian stations. This therefore implies that the $SI^+ - SI^-$ pair was a global event.

[7] *Rastogi and Patel* [1975] showed that solar plasma moving toward the Earth's magnetosphere with the velocity, V, and having a frozen-in magnetic field normal to the ecliptic (IMF-*Bz*) is equivalent to an electric field, $E_{sw} = (-V \times Bz)$, which is transmitted without any time delay to the polar region and then to the low-latitude ionosphere. This belongs to a process known as overshielding electric field in the magnetosphere, which has been extensively studied [*Nishida*, 1968; *Vasyliunas*, 1970; *Spiro et al.*, 1988; *Wolf et al.*, 2001; *Goldstein et al.*, 2002]. Prompt penetration occurs owing to the slow response of the shielding electric field at the inner edge of the ring current that opposes the time varying convection field in the presence of an IMF-*Bz*. The time scale of this process is generally of the order of an hour but can sometimes be longer [*Vasyliunas*, 1970; *Senior and Blanc*, 1984]. During a period of sudden northward turning of the IMF, from a steady southward configuration, the convective electric field shrinks while the shielding electric field takes a longer time to decay and produce a residual electric field, known as the overshielding electric field. The direction of this field is opposite to the normal direction of the ionospheric electric field. The E_{sw} has a direction of dusk-to-dawn for positive IMF-*Bz* and dawn-to-dusk for negative IMF-*Bz*.

[8] It can be seen from Figure 1 that ΔX at Indian stations just after the SI^+ at 1835 UT (around local midnight) had gradually decreased until 2000 UT. This effect is due to the prompt penetration of the electric field when the IMF-*Bz* is negative during the period. At around 2000 UT, ΔX again increased suddenly to values much above the first impulse level. Correspondingly, it can be seen that IMF-*Bz* turned from southward to northward at this instant, implying that it is due to the overshielding condition described above. After this, the level of ΔX went down, with some oscillations, and finally came down to normal level at 2300 UT. It is interesting to note that the fluctuations in ΔX between 2130 and 2200 UT were very well correlated with the solar wind density rather than with the IMF-*Bz* or the solar wind speed. The SI^+ at 1835 UT was associated with a sudden increase of both the solar wind density and speed causing a sudden pressure on the magnetosphere (as first suggested by *Gold* [1959]). The SI^- at 2300 UT was associated with the sudden decrease of solar wind density.

2.1. Global Geomagnetic Fields

[9] Figure 2 shows the variation of ΔX from 11 low-latitude stations around the world on 23–24 April 1998. The stations, starting from Alibag (ABG − Lat. 18.64; Long. 72.87) (uppermost curve), and arranged in increasing order of geographic longitude are, respectively, Gnangara (GNA − Lat. −31.78; Long. 115.95), Esashi (ESA − Lat. 39.24; Long. 141.35), Honolulu (HON − Lat. 21.32; Long. 202.00), Fresno (FRN − 37.10; Long. 240.30), Del Rio (DLR − Lat. 29.49; Long. 259.08), Kourou (KOU − Lat. 2.21; Long. 307.27), Ascension Island (ASC − Lat. −7.95; Long. 345.62), Hermanus (HER − Lat. −34.42; Long. 19.23), Addis Ababa (AAE − Lat. 9.02; 38.77), and Tananarive (TAN − Lat. −18.92; Long. 47.55). The geographic longitude of the ground stations is indicated at the left of each curve in

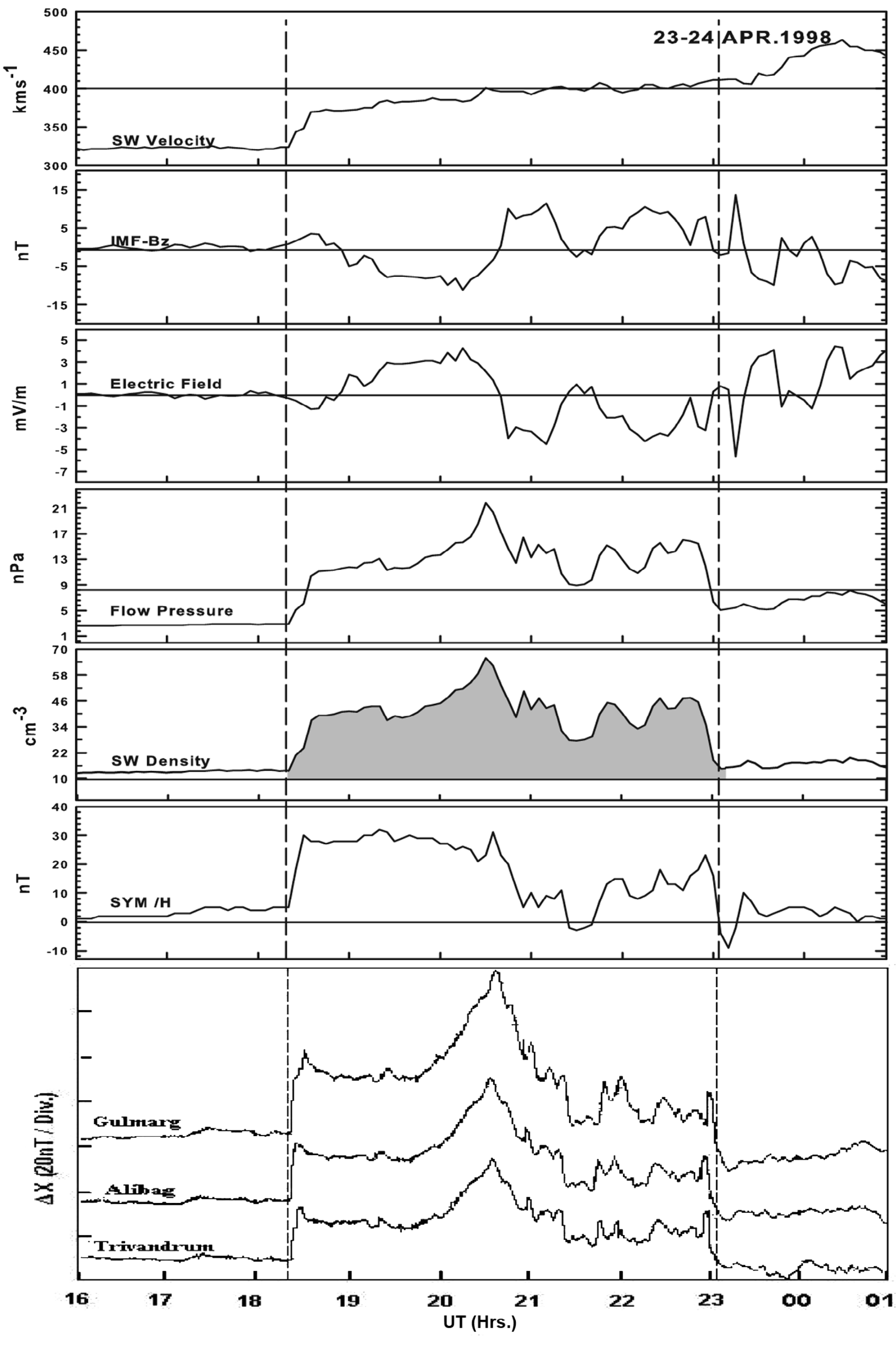

Figure 1. The first six parts starting from the top show the variations as a function of time in UT on 23–24 April 1998 of the solar wind velocity, *Bz*, the electric field, the solar wind flow pressure, the solar wind density (shaded), and the the symmetrical H field, respectively. Observations of the H field at Indian geomagnetic stations Gulmarg, Alibag, and Trivandrum are shown at the bottom. The pair of dashed vertically oriented parallel lines in all parts demarcate the times 1835 UT and 2300 UT. These times correspond, respectively, to the times of the SI^+ impulse and the SI^- impulse in the H field that were observed at Indian stations.

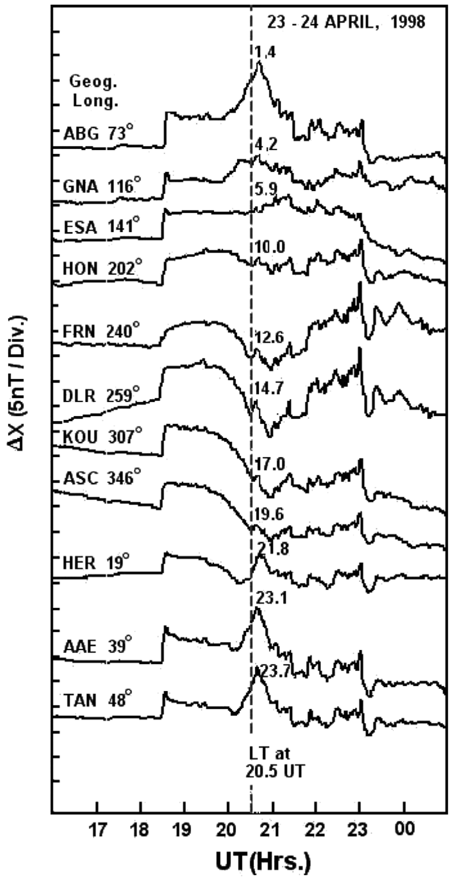

Figure 2. Variation of the horizontal component of the geomagnetic field projected onto the x-direction at 11 low-latitude stations around the world on 23–24 April 1998. The vertical dashed line is marked at 20.5 UT, and shown alongside it, for each curve, is the corresponding local time at each station. Also indicated on the left of each curve is the geographic longitude of the station.

Figure 2. Also indicated to the right of the vertical dashed line (marked at 20.5 hours UT in Figure 2) for each curve is the local time at 20.5 hours UT. The stations chosen range from geographic longitudes of 19° to 346° corresponding to local times of ~22 hours through the midnight, dawn, noon to dusk (20 hours).

[10] The negative IMF-*Bz* between 1835 and 2000 UT caused a decrease of ΔX at stations in the night sectors (HER, AAE, and TAN) and an increase at stations in the midday sector (FRN, DLR, KOU, and ASC). Around 20.50 UT, ΔX showed strong positive peaks at AAE, TAN, and ABG, no change at ESA and HON, and negative peaks at FRN, DLR, and KOU. These data conform very well with the process of prompt penetration and overshielding electric field [*Nishida*, 1968; *Vasyliunas*, 1970; *Rastogi and Patel*, 1975; *Spiro et al.*, 1988] wherein a southward IMF-*Bz* (between 1835 and 2000 UT) would cause a decrease of ΔX at nightside stations and an increase of ΔX at dayside stations of the Earth while a northward turning of IMF-*Bz* would produce a strong positive ΔX at stations in the night sector and negative ΔX at stations in the dayside sector owing to the imposition of either a dusk-to-dawn or dawn-to-dusk electric field. The fluctuations in ΔX between 2130 and 2300 UT are synchronous at all stations in the day as well as in night sectors, suggesting that the effect is due to solar wind flow pressure and not to the IMF-*Bz*. It is important to note here that the solar wind density fluctuations virtually mirror those seen in ΔX at ground stations, thereby implying that the solar wind density was the main key or driver for this event. Qualitatively, the fluctuations seem to be independent of the latitude. The dominant parameter is the solar wind pressure that makes the magnetosphere shrink and expand self-similarly, with some scaling factor depending on the pressure. This is reflected in the magnetic field data at all latitudes and longitudes in a configuration where the IMF appears to have no role to play. Thus, this was a unique space weather event in which one could unambiguously associate solar wind density variations with variations in ΔX at ground stations while no such changes were seen in the solar wind speed or magnetic field.

3. Solar Source Locations

[11] It is well known that owing to the rotation of the Sun (Ω = 1.642 × 10^{-4} deg s^{-1}), a radially directed outflow of solar wind from the sun will trace out an Archimedean spiral through the interplanetary medium. For a steady state solar wind with a velocity of 430 km s^{-1}, the tangent to this spiral, at 1 AU, will make an angle of 45° with the radial vector from the Sun [*Schwenn*, 1990]. As a consequence, the longitudinal offset (ϕ_R) of a solar wind stream with a velocity v, when traced backward from a distance R_1 (say, 1 AU) to a distance R_2, will be $\phi_R = \Omega(R_1 - R_2)/v$. We can thus project the observed solar wind velocities back to the Sun to determine the sources of the solar wind flows at the Sun. The earliest instance of using such a technique to trace solar wind outflows back to the sun was by *Rickett* [1975]. For the present event, we have back-projected the observed ACE velocities along Archimedean spirals to the source surface at 2.5 $R_\odot$ to determine its solar source location. Though this method is generally applicable to a steady-state flow of the solar wind, it has also been applied in cases when the solar wind outflows were not steady state and highly nonradial. For example, during the well-known disappearance event of 11 May 1999, the work by *Janardhan et al.* [2005] and *Janardhan* [2006] has shown that solar source locations determined by the traceback technique, using constant velocities along Archimedean spirals, do not have significant errors, even though the solar wind flows were known to be highly nonradial during that period. In the case under discussion, the solar wind flows would have been highly kinked and nonradial due to the propagating forward and reverse shocks arising from the optically occulted flare and the rear side CME. Therefore, if the $SI^+ - SI^-$ pair had a source on the solar disk, the ambiguity about the location of the source region would be within reasonable errors as shown by *Janardhan et al.* [2005] and *Janardhan* [2006]. Figure 3 shows a map of the solar photosphere indicating the locations of the active regions. The back-projected region of the solar wind

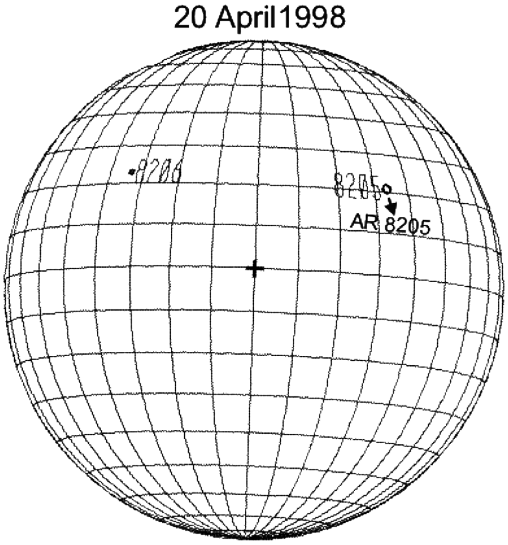

Figure 3. Map of the solar photosphere on 20 April 1998 corresponding to the back-projected region of the solar wind flows observed at 1 AU. The map shows the locations of the large active regions with active region AR8205 indicated by an arrow for convenience.

flows go back to the vicinity of the large active region AR8205 located at N21W25, to the west of central meridian on 20 April 1998 and indicated by a solid arrow in Figure 3. Typically, the solar disk shows a large number of active regions during the rising phase of the solar cycle. A detailed theoretical study by *Schrijver and DeRosa* [2003], has shown that solar wind outflows from active regions comprise ≤10% during solar minimum and up to 30–50% during solar maximum. However, the visible solar disk on 20 April 1998 showed no activity in terms of flares or CMEs and had only two active regions AR8206 and AR8205 as shown in Figure 3. The active region AR8206 was smaller than AR8205, being around 245 millionths of the solar disk in size as compared to 312 millionths of the solar disk for AR8205. Also, AR8205 was less than 30° west of the central meridian as compared to over 40° east of the central meridian for AR8206. It may be noted that a central meridian location would imply that any activity like a large CME or flare would be Earth-directed. However, there was no flare or CME on the entire visible solar disk on 20 April. Images from the Extreme-ultraviolet Imaging Telescope (EIT; *Delaboudinière et al.* [1995]) and the Michelson Doppler Imager (MDI; *Scherrer et al.* [1995]) onboard the Solar and Heliospheric Observatory (SoHO; *Domingo et al.* [1995]) were also examined carefully to confirm that there were no other possible source regions on the solar disk on 20 April 1998.

3.1. The Rear Side CME and Optically Occulted Flare of 20 April 1998

[12] On 20 April 1998, a rear side, fast (~1850 km s^{-1}) partial halo CME occurred in association with an optically occulted GOES M1.4 class flare which took place just behind the limb at S43W90. It must be pointed out here that most forecasters of space weather events generally ignore the possibility that a limb or backside solar explosive event could propagate a disturbance toward the Earth. However, there have been some instances where such cases have been studied and reported in recent times [*McKenna-Lawlor et al.*, 2006; *Smith et al.*, 2009a, 2009b].

[13] The GOES M1.4 flare at S43W90 was first detected in 1–8 Å band at 0915 UT on 20 April 1998 and reached its maximum at 1021 UT. The rear side partial halo CME was first seen in the LASCO coronograph C2, at 1004:51 UT on 20 April 1998, as a bright, sharply defined loop structure spanning ~80° in latitude and extending to ~3.1 $R_\odot$. The same was first observed by C3 at 1045:22 UT. Both the CME and the flare have been extensively studied and reported [*Bastian et al.*, 2001; *Simnett*, 2000, 2002], and it has been shown that the CME, which was radio loud [*Gopalswamy*, 2000], actually pushed aside preexisting streamers while moving beyond the LASCO C3 field of view. Since this was a rear side CME, the shock front that it drove would have been in a direction away from the Earth. In a study of the arrival time of flare-driven shocks at 1 AU and beyond [*Smart and Shea*, 1985; *Janardhan et al.*, 1996], it was assumed that the trailing edges of flare-driven shock waves travel at roughly half the velocity of the shock in the flare radial direction. It is therefore not unreasonable to assume that the trailing edges of the CME-driven reverse shock would be much slower and could be convected outward toward the Earth by the solar wind. The flare and the rear side CME would thus provide the forward and reverse shocks to cause the SI^+ and SI^- pair. Figure 4 shows hourly averaged value of the absolute magnitude of the magnetic field, as observed by the ACE spacecraft, as a function of time in UT. It is expected that the strength of the magnetic field would increase at the forward shock or SI^+ impulse and decrease at the reverse shock or SI^- impulse. It can be easily seen in Figure 4 that there is a sharp increase in the magnetic field at around 1835 UT, corresponding to the

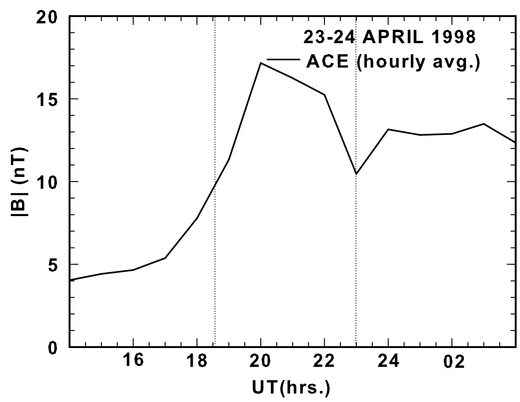

Figure 4. Hourly averaged total magnetic field as a function of time in UT as observed by the ACE spacecraft located at the L1 Lagrangian point at 1 AU. The vertically oriented dashed parallel lines at 1835 UT and 2300 UT correspond to the time of the SI^+ and SI^- impulse, respectively.

arrival of the forward shock associated with the SI^+ impulse, and a decrease in the magnetic field at 2300 UT, corresponding to the arrival of the reverse shock associated with the SI^- impulse. The vertically oriented dashed parallel lines in Figure 4 are marked at 1835 UT and 2300 UT, the time corresponding to the SI^+ and SI^- impulse, respectively.

4. Discussion and Conclusions

[14] From an observational point of view, the present work has been able to link interplanetary structure during this particular event with worldwide magnetospheric response, using the Indian magnetic observatories to provide the first clue. In particular, this event has been unique in that the solar wind density variations have played a key role, as seen through the close correspondence between the fluctuations in the solar wind densities and the ΔX at ground stations while no such changes were seen in the solar wind speed or magnetic field. Though there has been a large body of work over the past four decades that has addressed the issues concerned with forward/reverse shock pairs, their manifestation at 1 AU, and their relation to specific solar events, we believe that this paper presents empirical evidence, which to our knowledge is the most convincing evidence for the association of specific solar events to the observations of an $SI^+ - SI^-$ pair. In addition, it shows that it is possible for a rear side solar event to propagate a shock toward the Earth.

[15] We have seen that the SI^+ impulse 1835 UT was associated with a sudden increase of both the solar wind density and speed causing a sudden pressure on the magnetosphere while the SI^- at 2300 UT was associated with the sudden decrease of solar wind density. The southward IMF-*Bz* between 1835 and 2000 UT caused a decrease of ΔX at nightside stations and a increase of ΔX at dayside stations of the Earth owing to the imposition of a sudden electric field caused by the prompt penetration of electric field to low latitudes. As stated earlier, a northward turning of IMF-*Bz* produces a strong positive ΔX at stations in a night sector and negative ΔX at stations in the day side sector due to the effect of overshield electric field which is in a direction opposite to the normal electric field in the ionosphere. Between 2015 and 2300 UT, the fluctuations in ΔX were similar at all stations in the day or night sectors and were well correlated with the fluctuations in solar wind flow pressure, reflecting the shrinking and expansion of the magnetopause as a result of strong solar wind pressure variation.

[16] The solar event lasting only for some 4–5 hours showed signatures of all mechanisms involving solar-magnetosphere-ionosphere relationships. The arrival at 1 AU of the forward and reverse shock pair associated with the SI^+ and SI^-, respectively, is clearly seen in the behavior of the hourly averaged values of the total magnetic field, which shows a sharp increase at ~1835 UT and a decrease at ~2300 UT. The effect of sudden changes in the solar flow pressure due to a change of only the solar wind density has been clearly identified. The effect of the slowly varying IMF-*Bz* has been shown to impose dusk-to-dawn or dawn-to-dusk electric field globally, depending on the southward or northward turning of the IMF-*Bz*. Though theoretical first-order predictions for the observed distribution of solar wind speed, density, and temperature (as in Figure 1) during the propagation of forward and reverse shock pairs were derived four decades ago [*Dryer*, 1970, 1972], the analysis of the event has been rewarding owing to the relatively quiet solar conditions prevailing as it allowed us to identify specific solar sources as the possible drivers of the SI^+ and SI^- pair. The only activity on the Sun was the rear side CME and the associated solar flare. This is thus a very unique observation wherein a pair of SI events have been shown to be associated with corresponding changes in the solar wind density while no such changes are seen in the solar wind speed or magnetic field. Many more such events need to be observed, retrieved, and studied, both from archival records and future observations, before a clearer understanding of the exact nature and physics behind such events is obtained. High resolution, high dynamic range radio imaging techniques [*Mercier et al.*, 2006] can also provide useful information in this regard.

[17] **Acknowledgments.** The authors thank the two referees for their very constructive suggestions that have gone a long way in improving this paper. One of the authors (JP) thanks Murray Dryer for specific and focused comments. The authors thank J. H. King and N. Papatashvilli, of Adnet Systems, NASA, GSFC, the CDAWeb team, the ACE SWEPAM instrument team, the ACE Science Center, and the EIT and MDI consortia for making data available in the public domain via the World Wide Web. SoHO is a project of international collaboration between ESA and NASA.

[18] Philippa Browning thanks Murray Dryer and another reviewer for their assistance in evaluating this paper.

References

Bastian, T. S., M. Pick, A. Kerdraon, D. Maia, and A. Vourlidas (2001), The coronal mass ejection of 1998 April 20: Direct imaging at radio wavelengths, *Astrophys. J.*, *558*, L65–L69.

Burlaga, L. F. (1970), A reverse hydromagnetic shock in the solar wind, *Cosmic Electrodyn.*, *1*, 233–238.

Delaboudinière, J.-P., et al. (1995), EIT: Extreme-Ultraviolet Imaging Telescope for the SOHO Mission, *Sol. Phys.*, *162*, 291–312.

Detman, T., Z. Smith, M. Dryer, C. D. Fry, C. N. Arge, and V. Pizzo (2006), A hybrid heliospheric modeling system: Background solar wind, *J. Geophys. Res.*, *111*, A07102, doi:10.1029/2005JA011430.

Domingo, V., B. Fleck, and A. I. Poland (1995), The SOHO Mission: An overview, *Sol. Phys.*, *162*, 1–2.

Dryer, M. (1970), Some effects of finite electrical conductivity on solar flare-induced interplanetary shock waves., *Cosmic Electrodyn.*, *1*, 348–370.

Dryer, M. (1972), Interplanetary double-shock ensembles with anomalous electrical conductivity, *Solar Wind 2*, *NASA SP-308* (C. P. Sonett, P. J. Coleman Jr., and J. M. Wilcox, Eds.), *2*, 453.

Dryer, M., Z. K. Smith, T. Unti, J. D. Mihalov, B. F. Smith, J. H. Wolfe, D. S. Colburn, and C. P. Sonett (1975), Pioneer 9 and OGO 5 observations of an interplanetary multiple shock ensemble on February 2, 1969, *J. Geophys. Res.*, *80*, 3225–3234.

Dungey, J. W. (1961), Interplanetary magnetic field and the auroral zones, *Phys. Rev. Lett.*, *6*, 47–48.

Eviatar, A., and M. Dryer (1970), Finite conductivity and interplanetary piston-driven shock waves, *Cosmic Electrodyn.*, *1*, 371–379.

Fry, C. D., M. Dryer, Z. Smith, W. Sun, C. S. Deehr, and S. Akasofu (2003), Forecasting solar wind structures and shock arrival times using an ensemble of models, *J. Geophys. Res.*, *108*(A2), 1070, doi:10.1029/2002JA009474.

Gold, T. (1959), Motions in the magnetosphere of the Earth, *J. Geophys. Res.*, *64*, 1219–1224, doi:10.1029/JZ064i009p01219.

Goldstein, J., R. W. Spiro, P. H. Reiff, R. A. Wolf, B. R. Sandel, J. W. Freeman, and R. L. Lambour (2002), IMF-driven overshielding electric field and the origin of the plasmaspheric shoulder of May 24, 2000, *Geophys. Res. Lett.*, *29*(16), 1819, doi:10.1029/2001GL014534.

Goodrich, C. C., J. G. Lyon, M. Wiltberger, R. E. Lopez, and K. Papadopoulos (1998), An overview of the impact of the January 10–11, 1997 magnetic cloud on the magnetosphere via global MHD simulation, *Geophys. Res. Lett.*, *25*, 2537–2540, doi:10.1029/98GL01159.

Gopalswamy, N. (2000), Type II solar radio bursts, in *Radio Astronomy at Long Wavelengths*, edited by R. G. Stone, K. W. Weiler, M. L. Goldstein, & J.-L. Bougeret, p. 123.

Heppner, J. P., and N. C. Maynard (1987), Empirical high-latitude electric field models, *J. Geophys. Res.*, *92*, 4467–4489, doi:10.1029/JA092iA05p04467.

Janardhan, P. (2006), Enigmatic solar wind disappearance events: Do we understand them?, *J. Astrophys. Astron.*, *27*, 193.

Janardhan, P., V. Balasubramanian, S. Ananthakrishnan, M. Dryer, A. Bhatnagar, and P. S. McIntosh (1996), Travelling interplanetary disturbances detected using interplanetary scintillation at 327 MHz, *Sol. Phys.*, *116*, 379–401.

Janardhan, P., K. Fujiki, M. Kojima, M. Tokumaru, and K. Hakamada (2005), Resolving the enigmatic solar wind disappearance event of 11 May 1999, *J. Geophys. Res.*, *110*, A08101, doi:10.1029/2004JA010535.

Janardhan, P., K. Fujiki, H. S. Sawant, M. Kojima, K. Hakamada, and R. Krishnan (2008a), Source regions of solar wind disappearance events, *J. Geophys. Res.*, *113*, A03102, doi:10.1029/2007JA012608.

Janardhan, P., D. Tripathi, and H. E. Mason (2008b), The solar wind disappearance event of 11 May 1999: Source region evolution, *Astron. Astrophys. Lett.*, *448*, L1–L4.

Lazarus, A. J., K. W. Ogilvie, and L. F. Burlaga (1970), Interplanetary shock observations by Mariner 5 and Explorer 34, *Sol. Phys.*, *13*, 232–239.

Lu, G., et al. (1998), Global energy deposition during the January 1997 magnetic cloud event, *J. Geophys. Res.*, *103*, 11,685–11,694, doi:10.1029/98JA00897.

McKenna-Lawlor, S. M. P., M. Dryer, M. D. Kartalev, Z. Smith, C. D. Fry, W. Sun, C. S. Deehr, K. Kecskemety, and K. Kudela (2006), Near real-time predictions of the arrival at Earth of flare-related shocks during Solar Cycle 23, *J. Geophys. Res.*, *111*, A11103, doi:10.1029/2005JA011162.

Mercier, C., P. Subramanian, A. Kerdraon, M. Pick, S. Ananthakrishnan, and P. Janardhan (2006), Combining visibilities from the giant meter-wave radio telescope and the Nancay radio heliograph: High dynamic range snapshot images of the solar corona at 327 MHz, *Astron. Astrophys.*, *447*, 1189–1201.

Nishida, A. (1968), Coherence of geomagnetic DP 2 fluctuations with interplanetary magnetic variations, *J. Geophys. Res.*, *73*, 5549–5559, doi:10.1029/JA073i017p05549.

Odstrcil, D. (2003), Modeling 3-D solar wind structure, *Adv. Space Res.*, *32*, 497–506.

Rastogi, R. G., and V. L. Patel (1975), Effect of the interplanetary magnetic field on the ionosphere over the magnetic equator., *Proceedings of the Indian National Science Academy Part A*, *82*, 121–141.

Razdan, H., D. S. Colburn, and C. P. Sonett (1965), Recurrent $SI^+ - SI^-$ impulse pairs and shock structure in M-region beams, *Planet. Space Sci.*, *13*, 1111.

Rickett, B. J. (1975), Disturbances in the solar wind from IPS measurements in August 1972, *Sol. Phys.*, *43*, 237–247.

Scherrer, P. H., et al. (1995), The solar oscillations investigation: Michelson Doppler Imager, *Sol. Phys.*, *162*, 129–188.

Schrijver, C. J., and M. L. DeRosa (2003), Photospheric and heliospheric magnetic fields, *Sol. Phys.*, *212*, 165–200.

Schwenn, R. (1990), Large-scale structure of the interplanetary medium, in R. Schwenn and E. Marsch, *Physics of the Inner Physics of the Inner Heliosphere 1*(9), pp. 99–181, Springer-Verlag, Berlin.

Senior, C., and M. Blanc (1984), On the control of magnetospheric convection by the spatial distribution of ionospheric conductivities, *J. Geophys. Res.*, *89*, 261–284, doi:10.1029/JA089iA01p00261.

Shen, W. W., and M. Dryer (1972), Magnetohydrodynamic theory for the interaction of an interplanetary double-shock ensemble with the Earth's bow shock, *J. Geophys. Res.*, *77*, 4627–4644, doi:10.1029/JA077i025p04627.

Simnett, G. M. (2000), The relationship between CMEs and prominence eruptions, *JASTP*, *62*, 1479–1487.

Simnett, G. M. (2002), The acceleration and release of solar energetic particles in events from April 20–May 9, 1998, *Adv. Space Res.*, *29*, 1493–1500.

Smart, D. F., and M. A. Shea (1985), A simplified model for timing the arrival of solar flare-initiated shocks, *J. Geophys. Res.*, *90*, 183–190, doi:10.1029/JA090iA01p00183.

Smith, Z. K., M. Dryer, S. M. P. McKenna-Lawlor, C. D. Fry, C. S. Deehr, and W. Sun (2009a), Operational validation of HAFv2's predictions of interplanetary shock arrivals at Earth: Declining phase of Solar Cycle 23, *J. Geophys. Res.*, *114*, A05106, doi:10.1029/2008JA013836.

Smith, Z. K., R. Steenburgh, C. D. Fry, and M. Dryer (2009b), Predictions of interplanetary shock arrivals at Earth: Dependence of forecast outcome on the input parameters, *Space Weather*, *7*, S12005, doi:10.1029/2009SW000500.

Sonett, C. P., and D. S. Colburn (1965), The $SI^+ - SI^-$ pair and interplanetary forward-reverse shock ensembles, *Planet. Space Sci.*, *13*, 675.

Sonett, C. P., D. S. Colburn, L. Davis, E. J. Smith, and P. J. Coleman (1964), Evidence for a collision-free magnetohydrodynamic shock in interplanetary space, *Phys. Rev. Lett.*, *13*, 153–156.

Spiro, R. W., R. A. Wolf, and B. G. Fejer (1988), Penetrating of high-latitude-electric-field effects to low latitudes during SUNDIAL 1984, *Ann. Geophys.*, *6*, 39–49.

Stone, E. C., A. M. Frandsen, R. A. Mewaldt, E. R. Christian, D. Margolies, J. F. Ormes, and F. Snow (1998), The advanced composition explorer, *Space Sci. Rev.*, *86*, 1–22.

Takeuchi, T., T. Araki, A. Viljanen, and J. Watermann (2002), Geomagnetic negative sudden impulses: Interplanetary causes and polarization distribution, *J. Geophys. Res.*, *107*(A7), 1096, doi:10.1029/2001JA900152.

Tóth, G., et al. (2005), Space weather modeling framework: A new tool for the space science community, *J. Geophys. Res.*, *110*, A12226, doi:10.1029/2005JA011126.

Vandegriff, J., K. Wagstaff, G. Ho, and J. Plauger (2005), Forecasting space weather: Predicting interplanetary shocks using neural networks, *Adv. Space Res.*, *36*, 2323–2327.

Vasyliunas, V. M. (1970), Mathematical models of magnetospheric convection and its coupling to the ionosphere, in *Particles and Field in the Magnetosphere*, vol. 17 of *Astrophysics and Space Science Library*, p. 60.

Wolf, R. A., T. W. Garner, J. Goldstein, S. Sazykin, and R. W. Spiro (2001), Storm-time magnetospheric effects on electric fields in the subauroral ionosphere, *AGU Fall Meeting Abstracts*, p. A12.

K. Ahmed, Indian Institute of Geomagnetism, Navi Mumbai, 410218, India.

A. C. Das, S. K. Bisoi, P. Janardhan, and R. G. Rastogi, Physical Research Laboratory, Astronomy & Astrophysics Division, Ahmedabad 380 009, India. (jerry@prl.res.in)